

THERMODYNAMIC MODELING AND EXPERIMENTAL ANALYSIS OF OXIDATION/  
SULFIDATION OF NI-CR-AL MODEL ALLOY COATINGS

By

ERIK M. MUELLER

A DISSERTATION PRESENTED TO THE GRADUATE SCHOOL  
OF THE UNIVERSITY OF FLORIDA IN PARTIAL FULFILLMENT  
OF THE REQUIREMENTS FOR THE DEGREE OF  
DOCTOR OF PHILOSOPHY

UNIVERSITY OF FLORIDA

2007

© 2007 Erik M. Mueller

This dissertation is dedicated to all hard-working graduate students.

## ACKNOWLEDGMENTS

I would like to thank my supervisory committee chair, Dr. Wolfgang Sigmund, for all his support and last-minute assistance on this dissertation. I would also like to thank my former advisor, Dr. Hans Seifert, for not only starting me on and supporting me with this project financially, but for the invaluable help in teaching the Thermo-Calc computational software as well as the challenging goals set to enable me to finish this project. I would like to thank Damian Cupid for his help with the thermodynamic software and his insight into unique approaches to the problems encountered in computational thermodynamics.

I would also like to thank Dr. L. Amelia Dempere for her support and use of the characterization equipment at the Major Analytical Instrumentation Center. Wayne Acree should be credited with the operating the electron microprobe. Dr. Gerhard Fuchs' high-temperature materials courses were also instrumental in exposing me to this subject area in metallurgy. Dr. W. Greg Sawyer and Dr. Gerald Bourne also assisted in this project by serving on my supervisory committee.

Finally, I would also like to thank the University of Florida and the Materials Science and Engineering Department for use of their facilities and for affording me the opportunity to complete this degree with financial assistance.

## TABLE OF CONTENTS

	<u>page</u>
ACKNOWLEDGMENTS .....	iv
LIST OF TABLES .....	vii
LIST OF FIGURES .....	viii
ABSTRACT .....	1
1 INTRODUCTION .....	2
2 LITERATURE REVIEW .....	5
2.1 Turbine Engine Considerations .....	5
2.2 Turbine Blade Materials .....	6
2.2.1 Superalloys .....	6
2.2.2 Coatings for Turbine Blades .....	7
2.4 The Al-Cr-Ni Ternary System .....	9
2.5 Oxidation of Al-Ni-Cr Alloys .....	17
2.5.1 General Oxidation Mechanism .....	17
2.5.1.1 Oxidation of Ni .....	19
2.5.1.2 Oxidation of Al .....	20
2.5.1.3 Oxidation of Cr .....	22
2.5.2 Oxidation of Ni-Al Alloys .....	23
2.5.3 Oxidation in Al-Cr-Ni Ternary and NiCrAlY Coatings .....	26
2.6 Sulfidation and Hot Corrosion .....	28
2.6.1 Hot Corrosion .....	28
2.6.2 Sulfidation on Metals .....	29
2.6.3 Sulfidation on Metal Oxides .....	31
2.6.4 Sulfidation in Ni-Cr-Al Coatings .....	33
2.7 Calculations of Oxidation/Sulfidation .....	34
3 METHODS AND MATERIALS .....	36
3.1 Thermodynamic Modeling and Simulations .....	36
3.1.1 The CALPHAD Approach .....	36
3.1.2 Databases and Software .....	37
3.2 Materials and Sample Preparation .....	38
3.3 Thermogravimetric Analysis .....	39
3.4 Characterization .....	43
3.4.1 X-Ray Diffraction .....	44
3.4.2 Scanning Electron Microscopy .....	44
3.4.3 Electron Microprobe .....	45
4 THERMODYNAMIC CALCULATION RESULTS .....	46

4.1 Calculations of Ni-Cr-Al Alloys and Mixtures using Phase Diagrams .....	46
4.1.1 Binary Systems .....	46
4.1.2 Ternary Systems .....	49
4.2 Calculations of Temperature-Potential Diagrams .....	53
4.2.1 Calculations with O <sub>2</sub> -SO <sub>2</sub> Interactions .....	53
4.2.2 Calculations of Metal-Gas Interactions .....	57
4.3 Calculations of Potential Diagrams .....	58
4.4 Phase Fraction Diagrams .....	73
5 EXPERIMENTAL RESULTS .....	81
5.1 TGA Experiments .....	81
5.1.1 Oxidation Experiments in Air .....	81
5.1.2 Oxidation Experiments in He + 0.21 O <sub>2</sub> + 0.02 SO <sub>2</sub> .....	88
5.1.3 Oxidation Experiments in He + 0.21 O <sub>2</sub> + 0.10 SO <sub>2</sub> .....	91
5.2 Phase Identification .....	95
5.3 Surface Imaging .....	106
5.3.1 Untested Alloy Specimens .....	106
5.3.2 Oxidized Ni and Ni-Al Specimens .....	113
5.3.3 Oxidized Ni-8Cr-6Al Specimens .....	113
5.3.3.1 Ni-8Cr-6Al Oxidized in Air .....	113
5.3.3.2 Ni-8Cr-6Al Oxidized in He + 0.21 O <sub>2</sub> + 0.02 SO <sub>2</sub> .....	118
5.3.3.3 Ni-8Cr-6Al Oxidized in He + 0.21 O <sub>2</sub> + 0.10 SO <sub>2</sub> .....	121
5.3.4 Oxidized Ni-22Cr-11Al Specimens .....	124
5.3.4.1 Ni-22Cr-11Al Oxidized in Air .....	124
5.3.4.2 Ni-22Cr-11Al Oxidized in He + 0.21 O <sub>2</sub> + 0.02 SO <sub>2</sub> .....	126
5.3.4.3 Ni-8Cr-6Al Oxidized in He + 0.21 O <sub>2</sub> + 0.10 SO <sub>2</sub> .....	129
5.4 Cross-Sectional Analysis .....	131
5.4.1 Ni and Ni-Al Specimens .....	131
5.4.2 Ni-8Cr-6Al Specimens .....	133
5.4.3 Ni-22Cr-11Al Specimens .....	137
5.4.4 Electron Microprobe (EPMA) Analysis .....	139
6 DISCUSSION AND ANALYSIS .....	142
6.1 Mechanisms of Scale Formation .....	142
6.2 Comparison of Experimental Results and Calculations .....	148
7 CONCLUSIONS .....	156
LIST OF REFERENCES .....	158
BIOGRAPHICAL SKETCH .....	167

## LIST OF TABLES

<u>Table</u>	<u>page</u>
2-1. List of common alloying elements in Ni-base superalloys.....	7
2-2. List of phases described in calculations of the Al-Cr-Ni ternary. ....	14
2-3. The phases present in the Ni-22Cr-11Al and Ni-8Cr-6Al (weight percent) alloys at room temperature and 1000°C. ....	17
2-4. Descriptions and crystallographic information on different phases of Al <sub>2</sub> O <sub>3</sub> [49-50]. ....	21
3-1. List of experimental conditions performed for oxidation of alloys for 100 hr in 1 bar of gas at 25 mL/min. ....	43
4-1. Comparison of equilibria computed between two databases SPOT3 and SPIN4 at a pressure of 1 bar and T = 1073 K for Ni-22Cr-11Al alloy (by mass) with a P <sub>O<sub>2</sub></sub> of 0.22 bar. This table compares number of moles of each phase, along with the composition (in weight fraction) of each phase.....	58
4-2. Comparison of gas species (at mole fractions > 10 <sup>-10</sup> ) present in the unstable equilibrium regions of Figure 4-19 at low P <sub>O<sub>2</sub></sub> and high P <sub>O<sub>2</sub></sub> . These mole fractions are calculated based on ideal gas behavior. ....	60
5-1. List of the parabolic rate constants obtained from steady-state oxidation of Ni, Ni-13.6Al, NiAl, Ni-8Cr-6Al, and Ni-22Cr-11Al alloys.....	94
5-2. Table summarizing the phases identified using XRD for all cast, heat-treated alloys oxidized.....	107
6-1. Table showing the equilibrium partial pressures of gases that evolve upon various mixtures of O <sub>2</sub> and SO <sub>2</sub> at various temperatures, calculated from the SPOT3 database.....	146

## LIST OF FIGURES

<u>Figure</u>	<u>page</u>
2-1. Schematic of a typical turbine engine.....	5
2-2. Schematic of coating configuration of modern turbine blades.....	9
2-3. Al-Ni binary phase diagram [H. Baker. <i>ASM Handbook Vol. 3—Alloy Phase Diagrams</i> , ASM International: Materials Park, OH, p. 49 (1992)]......	10
2-4. Ni-Cr binary phase diagram [H. Baker. <i>ASM Handbook Vol. 3—Alloy Phase Diagrams</i> , ASM International: Materials Park, OH, p. 155 (1992)]......	10
2-5. Al-Cr binary phase diagram [H. Baker. <i>ASM Handbook Vol. 3—Alloy Phase Diagrams</i> , ASM International: Materials Park, OH, p. 43 (1992)]......	11
2-6. Liquidus projection of the Al-Ni-Cr ternary system [P. Rogl. “Al-Cr-Ni,” <i>Ternary Alloys: A Comprehensive Compendium of Evaluated Constitutional Data and Phase Diagrams: Al-Cd-Ce to Al-Cu-Ru</i> . 4 p. 411 (1991)]......	13
2-7. Scheil reaction scheme of the Al-Cr-Ni ternary. The $\delta$ -phase refers to $\text{Ni}_2\text{Al}_3$ , the $\zeta_1$ to $\text{Al}_8\text{Cr}_5$ -hexagonal, $\zeta_2$ to $\text{Al}_8\text{Cr}_5$ -rhombohedral, and $\epsilon_1$ to $\text{Al}_9\text{Cr}_4$ . The question marks represent areas of the ternary that were not investigated.....	13
2-8. Isothermal section of Al-Cr-Ni ternary at 1025°C above the $\text{U}_4$ reaction. The green areas denote regions of two-phase equilibria [P. Rogl. “Al-Cr-Ni,” <i>Ternary Alloys: A Comprehensive Compendium of Evaluated Constitutional Data and Phase Diagrams: Al-Cd-Ce to Al-Cu-Ru</i> . 4 p. 414 (1991)]......	15
2-9. Partial Isothermal section of Al-Cr-Ni ternary at 850°C below the $\text{U}_4$ reaction. The green areas denote regions of two-phase equilibria [P. Rogl. “Al-Cr-Ni,” <i>Ternary Alloys: A Comprehensive Compendium of Evaluated Constitutional Data and Phase Diagrams: Al-Cd-Ce to Al-Cu-Ru</i> . 4 p. 413 (1991)]......	15
2-10. Plot of oxidation growth kinetics versus time. ....	18
2-11 – Arrhenius plot of parabolic growth rates versus temperature of NiO (violet) as well as $\text{Cr}_2\text{O}_3$ and $\text{Al}_2\text{O}_3$ (red) [J.L. Smialek, G.M. Meier, “High-Temperature Oxidation,” <i>Superalloys II</i> . C.T. Sims, N.S. Stolff, W.C. Hagel, eds., John Wiley & Sons: New York p. 295 (1987)]......	24
2-12. Dependence of oxidation mechanisms and scale type of Ni-Al alloys based on temperature and Al content [F.S. Pettit: <i>Transactions of the AIME</i> . 239, pp. 1296-1305 (1967)]......	25
2-13. Schematic of the stages of oxidation in Ni-Cr-Al alloys. Group I are alloys that will have a stable NiO scale, Group II will develop a stable $\text{Cr}_2\text{O}_3$ scale, and Group III	

will develop a stable Al <sub>2</sub> O <sub>3</sub> scale [F.S. Pettit: <i>Transactions of the AIME</i> . 239, pp. 1296-1305 (1967)]. .....	27
2-24. Schematic showing the formation of metal sulfides (a) under an initial metal oxide layer (b) in simultaneous oxidizing and sulfidizing conditions. The various proposed transport mechanisms are shown. ....	32
3-1. Flowchart detailing the Calculation of Phase Diagrams approach. This study is concerned mostly with the equilibrium calculations. ....	37
3-2. Schematic of the Setsys Evolution (TGA only). ....	41
4-1. Temperature-composition binary phase diagram of the Ni-Al system calculated from the SPIN4 database. ....	47
4-2. Temperature-composition binary phase diagram of the Ni-Cr system calculated from the SPIN4 database. ....	47
4-3. Temperature-composition binary phase diagram of the Al-Cr system calculated from the SPIN4 database. ....	48
4-4. Temperature-composition binary phase diagram of the Ni-Al system calculated from the SPIN4 database with the Ni <sub>3</sub> Al <sub>5</sub> low-temperature phase restored. ....	48
4-5. Isothermal section of Ni-Cr-Al ternary system at 900°C in weight fractions. This diagram is calculated from data in the SPIN4 database. ....	49
4-6. Partial isothermal section of Ni-Cr-Al ternary system at 850°C in mole fractions. The axes are chosen to compare with Figure 2-9. This diagram is calculated from data in the SPIN4 database. ....	50
4-7. Isothermal section of Ni-Cr-Al ternary system at 1025°C in mole fractions. The axes are chosen to compare with Figure 2-8. This diagram is calculated from data in the SPIN4 database. ....	50
4-8. Ternary isothermal section of the Ni-Al-O <sub>2</sub> system at 900°C. The x-axis is the composition of Al in weight percent, and the y-axis is the logarithmic partial pressure of O <sub>2</sub> in bar. This diagram is calculated from data in the SPIN4 database. ....	51
4-9. Ternary isothermal section of the Ni-Cr-O <sub>2</sub> system at 900°C. The x-axis is the composition of Cr in weight percent, and the y-axis is the logarithmic partial pressure of O <sub>2</sub> in bar. This diagram is calculated from data in the SPIN4 database. ....	51
4-10. The Ni-Al-Cr-O system shown as a series of connected ternary subsystem isotherms at 900°C. The outer axes are the logarithm of the partial pressure of O <sub>2</sub> in bar, whereas the inner axes are the weight percents of Ni, Cr, and Al. This diagram is calculated from data in the SPIN4 database. ....	52

4-11. Change in partial pressure of O <sub>2</sub> , SO <sub>2</sub> , and SO <sub>3</sub> (in bar) with temperature using the initial gas mixture of He + 0.21 O <sub>2</sub> + 0.02 SO <sub>2</sub> . The P <sub>He</sub> is omitted due to scale. The data used for calculations is taken from the SPOT3 database. ....	54
4-12. Change in partial pressure of O <sub>2</sub> , SO <sub>2</sub> , and SO <sub>3</sub> (in bar) with temperature using the initial gas mixture of He + 0.21 O <sub>2</sub> + 0.10 SO <sub>2</sub> . The P <sub>He</sub> is omitted due to scale. The data used for calculations is taken from the SPOT3 database. ....	55
4-13. The relationship between the partial pressure of SO <sub>3</sub> in an O <sub>2</sub> -SO <sub>2</sub> gas mixture, with varying temperature. All partial pressures are in bar. ....	55
4-14. The relationship between the partial pressure of S <sub>2</sub> in an O <sub>2</sub> -SO <sub>2</sub> gas mixture, with varying temperature. All partial pressures are in bar. ....	56
4-15. The relationship between the partial pressure of O <sub>2</sub> in an SO <sub>3</sub> -SO <sub>2</sub> gas mixture, with varying temperature. All partial pressures are in bar. ....	56
4-16. Stability diagram of Ni and its oxide with varying temperature and partial pressure of oxygen (in bar). ....	59
4-17. Stability diagram of Ni and its oxide with varying temperature and partial pressure of oxygen (in bar) with a constant partial pressure of sulfur dioxide at 2 mol %. ....	59
4-18. Stability diagram of Ni and its oxide with varying temperature and partial pressure of oxygen (in bar) with a constant partial pressure of sulfur dioxide at 10 mol %. ....	60
4-19. Ni potential diagrams for (a) SO <sub>2</sub> -O <sub>2</sub> and (b) S <sub>2</sub> -O <sub>2</sub> at 800°C. U.E. is an abbreviation for undefined equilibrium. Published in [170]. ....	61
4-20. Ni SO <sub>2</sub> -O <sub>2</sub> potential diagram at 900°C. U.E. is an abbreviation for undefined equilibrium. Published in [170]. ....	61
4-21. Ni SO <sub>2</sub> -O <sub>2</sub> potential diagram at 1000°C. U.E. is an abbreviation for undefined equilibrium. Published in [170]. ....	62
4-22. Al potential diagrams for (a) SO <sub>2</sub> -O <sub>2</sub> and (b) S <sub>2</sub> -O <sub>2</sub> at 800°C. Published in [170]. ....	63
4-23. Al SO <sub>2</sub> -O <sub>2</sub> potential diagram at 900°C. ....	64
4-24. Al SO <sub>2</sub> -O <sub>2</sub> potential diagram at 1000°C. ....	64
4-25. Cr potential diagrams for (a) SO <sub>2</sub> -O <sub>2</sub> and (b) S <sub>2</sub> -O <sub>2</sub> at 800°C. Published in [170]. ....	65
4-26. Cr SO <sub>2</sub> -O <sub>2</sub> potential diagram at 900°C. ....	65
4-27. Al SO <sub>2</sub> -O <sub>2</sub> potential diagram at 900°C. ....	66
4-28. Ni-13.6Al potential diagrams for (a) SO <sub>2</sub> -O <sub>2</sub> and (b) S <sub>2</sub> -O <sub>2</sub> at 800°C. U.E. is an abbreviation for undefined equilibrium. Published in [170]. ....	66

4-29. Ni <sub>3</sub> Al SO <sub>2</sub> -O <sub>2</sub> potential diagram at 900°C. ....	67
4-30. Ni <sub>3</sub> Al SO <sub>2</sub> -O <sub>2</sub> potential diagram at 1000°C. Published in [170]. ....	67
4-31. NiAl potential diagrams for (a) SO <sub>2</sub> -O <sub>2</sub> and (b) S <sub>2</sub> -O <sub>2</sub> at 800°C. U.E. is an abbreviation for undefined equilibrium. Published in [170]. ....	68
4-32. NiAl SO <sub>2</sub> -O <sub>2</sub> potential diagram at 900°C. ....	68
4-33. NiAl SO <sub>2</sub> -O <sub>2</sub> potential diagram at 1000°C. Published in [170]. ....	69
4-34. Ni-8Cr-6Al potential diagrams for (a) SO <sub>2</sub> -O <sub>2</sub> and (b) S <sub>2</sub> -O <sub>2</sub> at 800°C. Published in [170]. ....	70
4-35. Ni-8Cr-6Al SO <sub>2</sub> -O <sub>2</sub> potential diagram at 900°C. Published in [170]. ....	70
4-36. Ni-8Cr-6Al SO <sub>2</sub> -O <sub>2</sub> potential diagram at 1000°C. Published in [170]. ....	71
4-37. Ni-22Cr-11Al potential diagrams for (a) SO <sub>2</sub> -O <sub>2</sub> and (b) S <sub>2</sub> -O <sub>2</sub> at 800°C. Published in [170]. ....	72
4-38. Ni-22Cr-11Al SO <sub>2</sub> -O <sub>2</sub> potential diagram at 900°C. Published in [170]. ....	72
4-39. Ni-22Cr-11Al SO <sub>2</sub> -O <sub>2</sub> potential diagram at 1000°C. Published in [170]. ....	73
4-40. Phase fraction diagram of the Ni-O system showing the change in phase percent with varying oxygen partial pressure at 800°C in air. Calculated from the SPOT3 database. ....	75
4-41. Phase fraction diagram of the Ni-O-S system showing the change in phase percent with varying oxygen partial pressure at 800°C in an 0.21 O <sub>2</sub> + 0.02 SO <sub>2</sub> atmosphere. Calculated from the SPOT3 database. ....	76
4-42. Phase fraction diagram of the Ni-O-S system showing the gas evolution (in partial pressure [bar]) with varying oxygen partial pressure at 800°C in an 0.21 O <sub>2</sub> + 0.02 SO <sub>2</sub> atmosphere. Calculated from the SPOT3 database. ....	76
4-43. Phase fraction diagram of the Ni-O-S system showing activity change of each component with varying oxygen partial pressure at 800°C in an 0.21 O <sub>2</sub> + 0.02 SO <sub>2</sub> atmosphere. Calculated from the SPOT3 database. ....	77
4-44. Phase fraction diagram an Ni-8Cr-6Al alloy showing activity change of each component with varying oxygen partial pressure at 800°C in air. Calculated from the SPIN4 database. ....	77
4-45. Phase fraction diagram an Ni-8Cr-6Al alloy showing the change in phase percent with varying oxygen partial pressure at 800°C in air. Calculated from the SPIN4 database. ....	78

4-46. Phase fraction diagram an Ni-8Cr-6Al alloy at 800°C comparing the activity change calculated for Figure 4-38 using the SPIN4 database (black) and the SPOT3 database (teal). .....	78
4-48. Phase fraction diagram of an Ni-8Cr-6Al alloy showing the change in phase percent with varying oxygen partial pressure at 800°C in an 0.21 O <sub>2</sub> + 0.02 SO <sub>2</sub> atmosphere. Calculated from the appended SPIN4 database. ....	79
4-49. Phase fraction diagram of an Ni-22Cr-11Al alloy showing activity change of each component with varying oxygen partial pressure at 800°C in an 0.21 O <sub>2</sub> + 0.02 SO <sub>2</sub> atmosphere. Calculated from the appended SPIN4 database.....	80
4-50. Phase fraction diagram of an Ni-22Cr-11Al alloy showing the change in phase percent with varying oxygen partial pressure at 800°C in an 0.21 O <sub>2</sub> + 0.02 SO <sub>2</sub> atmosphere. Calculated from the appended SPIN4 database. ....	80
5-1. Plot of weight change versus time for Ni specimen at 800°C for 24 hr in air. ....	81
5-2. Plot of weight change versus square root time for Ni specimen at 800°C for 24 hr in air. The formula containing the slope and the coefficient of determination are listed.....	82
5-3. Plot of weight change versus square root time for Ni specimen at 900°C for 24 hr in air. The formula containing the slope and the coefficient of determination are listed.....	83
5-4. Arrhenius plot of the parabolic rate constant versus inverse temperature of Ni oxidized for 24 hr in air. The formula containing the slope and the coefficient of determination are listed.....	83
5-5. Plot of weight change versus square root time for a NiAl specimen at 800°C for 24 hr in air. The formula containing the slope and the coefficient of determination are listed. ....	84
5-6. Arrhenius plot of the parabolic rate constant versus inverse temperature of NiAl oxidized for 24 hr in air. The formula containing the slope and the coefficient of determination are listed.....	85
5-7. Plot of weight change versus square root time for a Ni-8Cr-6Al specimen at 1000°C for 100 hr in air. The formula containing the slope and the coefficient of determination are listed. ....	86
5-8. Plot of weight change versus square root time for a Ni-8Cr-6Al specimen at 900°C for 100 hr in air. The formula containing the slope and the coefficient of determination are listed. ....	86
5-9. Plot of weight change versus square root time for a Ni-22Cr-11Al specimen at 800°C for 100 hr in air. The formula containing the slope and the coefficient of determination are listed.....	87

5-10. Arrhenius plot of the parabolic rate constant versus inverse temperature of Ni-8Cr-6Al oxidized for 100 hr in air. ....	87
5-11. Arrhenius plot of the parabolic rate constant versus inverse temperature of Ni-22Cr-11Al oxidized for 100 hr in air. The formula containing the slope and the coefficient of determination are listed. ....	88
5-12. Plot of weight change versus square root time for a Ni-8Cr-6Al specimen at 975°C for 100 hr in He + 0.21 O <sub>2</sub> + 0.02 SO <sub>2</sub> . The formula containing the slope and the coefficient of determination are listed. ....	89
5-13. Plot of weight change versus square root time for a Ni-22Cr-11Al specimen at 975°C for 100 hr in He + 0.21 O <sub>2</sub> + 0.02 SO <sub>2</sub> . The formula containing the slope and the coefficient of determination are listed. ....	89
5-14. Arrhenius plot of the parabolic rate constant versus inverse temperature of Ni-8Cr-6Al oxidized for 100 hr in He + 0.21 O <sub>2</sub> + 0.02 SO <sub>2</sub> . The formula containing the slope and the coefficient of determination are listed.....	90
5-15. Arrhenius plot of the parabolic rate constant versus inverse temperature of Ni-22Cr-11Al oxidized for 100 hr in He + 0.21 O <sub>2</sub> + 0.02 SO <sub>2</sub> . The formula containing the slope and the coefficient of determination are listed. ....	90
5-16. Plot of weight change versus square root time for a Ni-8Cr-6Al specimen at 900°C for 100 hr in He + 0.21 O <sub>2</sub> + 0.10 SO <sub>2</sub> . The formulas containing the slopes and the coefficients of determination are listed.....	91
5-17. Arrhenius plot of the parabolic rate constant versus inverse temperature of Ni-8Cr-6Al oxidized for 100 hr in He + 0.21 O <sub>2</sub> + 0.10 SO <sub>2</sub> . The blue data and regression correspond to the initial oxidation rates, whereas the red data and regression correspond to the later stage oxidation. The formulas containing the slope and the coefficients of determination are listed.....	92
5-18. Plot of weight change versus square root time for a Ni-22Cr-11Al specimen at 800°C for 100 hr in He + 0.21 O <sub>2</sub> + 0.10 SO <sub>2</sub> . The formula containing the slope and the coefficient of determination are listed. ....	93
5-19. Arrhenius plot of the parabolic rate constant versus inverse temperature of Ni-22Cr-11Al oxidized for 100 hr in He + 0.21 O <sub>2</sub> + 0.10 SO <sub>2</sub> . The formula containing the slope and the coefficient of determination are listed. ....	93
5-20. Arrhenius plot of alloys isothermally oxidized in this study for 100 hr.....	95
5-21. Histogram of the peak intensities measured from an XRD analysis of polished, heat treated Ni-8Cr-6Al.....	96
5-22. Histogram of the peak intensities measured from an XRD analysis of Ni-8Cr-6Al oxidized in air for 100 hr at 800°C.....	96

5-23. Histogram of the peak intensities measured from an XRD analysis of Ni-8Cr-6Al oxidized in air for 100 hr at 900°C.....	97
5-24. Histogram of the peak intensities measured from an XRD analysis of Ni-8Cr-6Al oxidized in air for 100 hr at 1000°C.....	97
5-25. Histogram of the peak intensities measured from an XRD analysis of Ni-8Cr-6Al oxidized in He + 0.21 O <sub>2</sub> + 0.02 SO <sub>2</sub> for 100 hr at 800°C. ....	98
5-26. Histogram of the peak intensities measured from an XRD analysis of Ni-8Cr-6Al oxidized in He + 0.21 O <sub>2</sub> + 0.02 SO <sub>2</sub> for 100 hr at 900°C. ....	98
5-27. Histogram of the peak intensities measured from an XRD analysis of Ni-8Cr-6Al oxidized in He + 0.21 O <sub>2</sub> + 0.02 SO <sub>2</sub> for 100 hr at 975°C. ....	99
5-28. Histogram of the peak intensities measured from an XRD analysis of Ni-8Cr-6Al oxidized in He + 0.21 O <sub>2</sub> + 0.10 SO <sub>2</sub> for 100 hr at 800°C. ....	99
5-29. Histogram of the peak intensities measured from an XRD analysis of Ni-8Cr-6Al oxidized in He + 0.21 O <sub>2</sub> + 0.10 SO <sub>2</sub> for 100 hr at 900°C. ....	100
5-30. Histogram of the peak intensities measured from an XRD analysis of Ni-8Cr-6Al oxidized in He + 0.21 O <sub>2</sub> + 0.10 SO <sub>2</sub> for 100 hr at 975°C. ....	100
5-31. Histogram of the peak intensities measured from an XRD analysis of polished, heat treated Ni-22Cr-11Al.....	101
5-32. Histogram of the peak intensities measured from an XRD analysis of Ni-22Cr-11Al oxidized in air for 100 hr at 800°C.....	102
5-33. Histogram of the peak intensities measured from an XRD analysis of Ni-22Cr-11Al oxidized in air for 100 hr at 900°C.....	102
5-34. Histogram of the peak intensities measured from an XRD analysis of Ni-22Cr-11Al oxidized in air for 100 hr at 1000°C.....	103
5-35. Histogram of the peak intensities measured from an XRD analysis of Ni-22Cr-11Al oxidized in He + 0.21 O <sub>2</sub> + 0.02 SO <sub>2</sub> for 100 hr at 800°C. ....	103
5-36. Histogram of the peak intensities measured from an XRD analysis of Ni-22Cr-11Al oxidized in He + 0.21 O <sub>2</sub> + 0.02 SO <sub>2</sub> for 100 hr at 900°C. ....	104
5-37. Histogram of the peak intensities measured from an XRD analysis of Ni-22Cr-11Al oxidized in He + 0.21 O <sub>2</sub> + 0.02 SO <sub>2</sub> for 100 hr at 975°C. ....	104
5-38. Histogram of the peak intensities measured from an XRD analysis of Ni-22Cr-11Al oxidized in He + 0.21 O <sub>2</sub> + 0.10 SO <sub>2</sub> for 100 hr at 800°C. ....	105

5-39. Histogram of the peak intensities measured from an XRD analysis of Ni-22Cr-11Al oxidized in He + 0.21 O <sub>2</sub> + 0.10 SO <sub>2</sub> for 100 hr at 900°C. ....	105
5-40. Histogram of the peak intensities measured from an XRD analysis of Ni-22Cr-11Al oxidized in He + 0.21 O <sub>2</sub> + 0.10 SO <sub>2</sub> for 100 hr at 975°C. ....	106
5-41. Optical micrograph of as cast Ni-8Cr-6Al at 125X. ....	108
5-42. Optical micrograph of heat-treated Ni-8Cr-6Al at 125X. ....	108
5-43. Secondary electron (SE) micrograph of as cast Ni-8Cr-6Al microstructure at 5000X. ....	109
5-44. SE micrograph of heat-treated Ni-8Cr-6Al microstructure at 20000X. ....	109
5-45. Optical micrograph of as cast Ni-22Cr-11Al at 125X. ....	110
5-46. Optical micrograph of heat-treated Ni-22Cr-11Al at 125X. ....	111
5-47. Backscattered electron (BSE) micrograph of as cast Ni-22Cr-11Al microstructure at 5000X. ....	111
5-48. Secondary electron (SE) micrograph of heat-treated Ni-22Cr-11Al microstructure at 15000X. ....	112
5-49. X-ray map of the SE micrograph in Figure 5-46. ....	112
5-50. SE micrograph of NiO scale Ni oxidized in air at 800°C for 24 hr. ....	113
5-51. SE micrograph of NiAl oxidized at 800°C for 36 hr at 5000X. ....	114
5-52. SE micrograph of NiAl oxidized at 1000°C for 36 hr at 20000X. ....	114
5-53. SE micrograph of NiAl oxidized at 1000°C for 36 hr at 200X. ....	115
5-54. Backscattered electron (BSE) micrograph of Ni-8Cr-6Al oxidized in air for 100 hr at 900°C. ....	116
5-55. X-ray map of SE micrograph at 2500X of Ni-8Cr-6Al oxidized in air for 100 hr at 800°C. ....	116
5-56. SE micrograph of surface of Ni-8Cr-6Al after oxidation in air for 100hr at 1000°C at 10000X. ....	117
5-57. BSE micrograph of surface of Ni-8Cr-6Al after oxidation in air for 100hr at 1000°C at 5000X. ....	117
5-58. SE micrograph of surface of Ni-8Cr-6Al after oxidation in air for 0.5 hr at 800°C at 10000X. The light oxide is NiO and the dark oxide on the right is alumina. ....	118

5-59. BSE micrograph of the surface of Ni-8Cr-6Al oxidized in 2% SO <sub>2</sub> at 800°C for 100 hr at 4000X.....	119
5-60. BSE micrograph of the surface of Ni-8Cr-6Al oxidized in 2% SO <sub>2</sub> at 900°C for 100 hr at 1000X.....	119
5-61. SE micrograph of the surface of Ni-8Cr-6Al oxidized in 2% SO <sub>2</sub> at 975°C for 100 hr at 1500X.....	120
5-62. SE micrograph of the surface of Ni-8Cr-6Al oxidized in 2% SO <sub>2</sub> at 975°C for 100 hr at 1500X. In this area, the scale has spalled off revealing the bare metal surface.....	120
5-63. SE micrograph of the surface of Ni-8Cr-6Al oxidized in 10% SO <sub>2</sub> at 800°C for 100 hr at 15000X.....	121
5-64. SE micrograph of Ni-8Cr-6Al alloy oxidized in 10% SO <sub>2</sub> at 800°C for 100 hr at 1500 showing scale “blisters.”.....	122
5-65. SE micrograph of the surface of Ni-8Cr-6Al oxidized in 10% SO <sub>2</sub> at 900°C for 100 hr at 700X.....	122
5-66. SE micrograph of the overlying alumina regions of Ni-8Cr-6Al oxidized in 10% SO <sub>2</sub> at 900°C for 100 hr at 10000X.....	123
5-67. SE micrograph of the surface of Ni-8Cr-6Al oxidized in 10% SO <sub>2</sub> at 975°C for 100 hr at 5000X.....	123
5-68. SE micrograph of the surface of Ni-8Cr-6Al oxidized in 10% SO <sub>2</sub> at 975°C for 100 hr at 1500X where the scale (top) had spalled off and began to reoxidized (bottom). .....	124
5-69. SE micrograph of Ni-22Cr-11Al oxidized in air at 800°C for 100 hr at 1000X. ....	125
5-70. SE micrograph of Ni-22Cr-11Al oxidized in air at 800°C for 100 hr at 5000X. ....	125
5-71. BSE micrograph of Ni-22Cr-11Al oxidized in air at 1000°C for 100 hr at 500X.....	126
5-72. SE micrograph of Ni-22Cr-11Al oxidized in 2% SO <sub>2</sub> gas mixture at 800°C for 100 hr at 1000X.....	127
5-73. SE micrograph of Ni-22Cr-11Al oxidized in 2% SO <sub>2</sub> gas mixture at 900°C for 100 hr at 9000X.....	127
5-74. SE micrograph of Ni-22Cr-11Al oxidized in 2% SO <sub>2</sub> gas mixture at 900°C for 100 hr at 10000X.....	128
5-75. SE micrograph of Ni-22Cr-11Al oxidized in 2% SO <sub>2</sub> gas mixture at 1000°C for 100 hr at 1900X.....	128

5-76. SE micrograph of Ni-22Cr-11Al oxidized in 10% SO <sub>2</sub> gas mixture at 800°C for 100 hr at 100X.....	129
5-77. SE micrograph of Ni-22Cr-11Al oxidized in 10% SO <sub>2</sub> gas mixture at 800°C for 100 hr at 5000X.....	130
5-78. SE micrograph of Ni-22Cr-11Al oxidized in 10% SO <sub>2</sub> gas mixture at 1000°C for 100 hr at 10000X. ....	130
5-79. SE micrograph of Ni-22Cr-11Al oxidized in 10% SO <sub>2</sub> gas mixture at 900°C for 100 hr at 1500X.....	131
5-80. BSE micrograph of a Ni specimen oxidized at 800°C for 24 hr at 1900X. The top layer is the electroless Ni layer deposited for edge retention. ....	132
5-81. BSE micrograph of a NiAl specimen oxidized at 1000°C for 36 hr at 2000X. The top layer is the electroless Ni layer deposited for edge retention. ....	132
5-82. BSE micrograph of Ni-8Cr-6Al oxidized at 900°C in cross-section.....	133
5-83. SE micrograph of Ni-8Cr-6Al oxidized in 2% SO <sub>2</sub> gas mixture at 800°C for 100hr in cross-section at 10000X.....	134
5-84. BSE micrograph of Ni-8Cr-6Al oxidized in 2% SO <sub>2</sub> gas mixture at 900°C for 100hr in cross-section at 3500X.....	135
5-85. BSE micrograph of Ni-8Cr-6Al oxidized in 2% SO <sub>2</sub> gas mixture at 900°C for 100hr in cross-section at 3500X, showing an oxide deeply penetrating along a grain boundary. ....	135
5-86. BSE micrograph of Ni-8Cr-6Al oxidized in 2% SO <sub>2</sub> gas mixture at 900°C for 100hr in cross-section at 5000X, showing sulfides along a grain boundary.....	136
5-87. SE micrograph of Ni-8Cr-6Al oxidized in 2% SO <sub>2</sub> gas mixture at 800°C for 100hr in cross-section, showing sulfides along grain boundaries and pores in the oxide layer.....	136
5-88. BSE micrograph of Ni-22Cr-11Al oxidized in 2% SO <sub>2</sub> gas mixture at 975°C for 100hr in cross-section at 8000X. The top layer is a Ni-coating added for edge retention.....	138
5-89. BSE micrograph of Ni-22Cr-11Al oxidized in 2% SO <sub>2</sub> gas mixture at 800°C for 100hr in cross-section at 800X.....	138
5-90. BSE micrograph of Ni-22Cr-11Al matrix that was exposed to the 2% SO <sub>2</sub> gas mixture at 975°C for 100hr 2000X. The labeled X-numbers are areas that were probed for EDS.....	139
5-91. EPMA linescan across scale and interface in an Ni-8Cr-6Al alloy oxidized at 900°C in He + 0.21 O <sub>2</sub> + 0.02 SO <sub>2</sub> gas mixture.....	140

5-92. EPMA linescan across scale and interface in a Ni-22Cr-11Al alloy oxidized at 800°C in He + 0.21 O <sub>2</sub> + 0.02 SO <sub>2</sub> gas mixture.....	141
5-93. EPMA linescan across scale and interface in a Ni-22Cr-11Al alloy oxidized at 975°C in He + 0.21 O <sub>2</sub> + 0.02 SO <sub>2</sub> gas mixture.....	141
6-1. Comparison of phases observed in SPIN4 calculations versus an SO <sub>2</sub> -O <sub>2</sub> potential diagram of Ni-8Cr-6Al at 900°C. The blue dots correspond to calculated equilibria where the appended SPIN4 and SPOT3 databases agree. The green cubes correspond to disagreements. The dashed lines represent the alternate reaction lines determined by the appended SPIN4 database.....	150
6-2. Comparison of phases observed in SPIN4 calculations versus an SO <sub>2</sub> -O <sub>2</sub> potential diagram of Ni-22Cr-11Al at 975°C. This diagram uses the same methodology as used in Figure 6-1. ....	151
6-3. Comparison of the calculated activities from microprobe linescans with calculated values using the appended SPIN4 database for a Ni-8Cr-6Al alloy oxidized at 900°C in 0.21 O <sub>2</sub> + 0.02 SO <sub>2</sub> . ....	154
6-4. Comparison of the calculated activities from microprobe linescans with calculated values using the appended SPIN4 database for a Ni-22Cr-11Al alloy oxidized at 975°C in 0.21 O <sub>2</sub> + 0.02 SO <sub>2</sub> . ....	154

Abstract of Dissertation Presented to the Graduate School  
of the University of Florida in Partial Fulfillment of the  
Requirements for the Degree of Doctor of Philosophy

THERMODYNAMIC MODELING AND EXPERIMENTAL ANALYSIS OF OXIDATION/  
SULFIDATION OF NI-CR-AL MODEL ALLOY COATINGS

By

Erik M. Mueller

May 2007

Chair: Wolfgang Sigmund  
Major: Materials Science and Engineering

With the current focus on finding future energy sources, land-based power gas turbines offer a desirable alternative to common coal-fired steam power generation. Ni-Cr-Al-X alloys are the material basis for producing overlay bond coats for the turbine blades used in sections of the turbine engine experiencing the most extreme environments. These overlay coatings are designed to provide environmental protection for the blades and vanes. While the oxidation of such alloys has been investigated and modeled in-depth, the concurrent sulfidation attack has not. This corrosion mode is now being heavily researched with the desire to use gasified coal, biomass, and other renewable fuel sources in gas turbines that often contain significant amounts of sulfur. The purpose of this dissertation was to use thermodynamic calculations to describe and predict the oxidation/sulfidation processes of two Ni-Cr-Al model alloys regarding phase evolution, composition, and component activities. These calculations, in the form of potential and phase fraction diagrams, combined with sulfidation experiments using kinetic measurements and materials characterization techniques, were able to describe and predict the simultaneous oxidation and sulfidation that occurred in these alloys.

## CHAPTER 1 INTRODUCTION

The United States and the rest of the world today are on the verge of an energy crisis. A situation has developed in which increasing energy demands are consuming the current supply. Besides the United States, which consumes more than 25% of the world's energy resources, the growing economies of Eastern Europe, China, India, and other developing countries are taxing world energy reserves [1]. Therefore, in order to solve this growing problem, energy supply must be increased while the demand is reduced.

The solution to creating new energy supplies is not easy, especially considering the environmental and political impact of the most common source, fossil fuels [2]. Fossil fuel use has led to the production of sulfur and nitrous oxides ( $\text{SO}_x$  and  $\text{NO}_x$ , respectively) and the byproducts of incomplete combustion, carbon monoxide and excess hydrocarbons, which were the chief environmental concerns of the Environmental Protection Agency and the Department of Energy [3]. However, with the recent recognition by the White House of manmade global climate change due to carbon dioxide ( $\text{CO}_2$ ) emissions, the focus of new energy creation is finding carbon-neutral or less carbon-positive sources [4]. In essence, this entails the maximized reduction of carbon dioxide from not only fuel consumption, but also fuel production.

Current alternatives for traditional coal, oil, and natural gas combustion to power steam turbines are wide and varied. However, many of these energy sources are not available in all regions and some do not yet possess the technological development to make efficient use of their resources. Furthermore, some energy sources, such as nuclear power, have such high capital costs and political restriction, as to make them unfeasible in many regions. One currently developed and researched alternative is the use of land-based power gas turbines. The advantage of this process is that it has relatively few mechanical parts, requiring small capital investment,

reaching stable power output quickly, and achieving high thermal efficiencies [5]. This high thermal efficiency translates into more power production for less fuel consumption, resulting in a reduction in CO<sub>2</sub> emissions compared to traditional steam turbines [5]. Furthermore, the source of fuel does not have to be limited to natural gas, but can also be synthetic combustion gases derived from biomass, gasified coal, and steam reformation of liquid hydrocarbons.

However, the use of synthetic gases and even natural gas allow the inclusion of sulfur-based gases, such as SO<sub>2</sub>, SO<sub>3</sub>, and H<sub>2</sub>S, into the engine itself. In the turbine industry, research of the effects of these fuels were often overlooked since they play little role highly oxidizing conditions found in aerospace turbines. However, with the advent of fuels from less pure sources and the addition of later turbine blade stages, which operate at temperatures lower than those near the combustor chamber, this has again become a concern. The blades and vanes found in the turbine section can be attacked by these impurities, leading to catastrophic failure of the turbine and the entire engine as a whole. New research into understanding the prevention of this failure is key to making the placement of gas-based turbines in power plants more feasible and cost-effective. Experimental research and testing of the alloys in the turbine section are expensive, long, and difficult to reproduce. Therefore, efforts have been made to calculate these conditions [6-9]. However, these efforts are usually restricted to oxidation alone, or are performed on single elements, limiting their application to complex turbine alloys or their coatings.

The purpose of this dissertation was to test if thermodynamic calculations can be used to describe and predict the oxidation/sulfidation processes of two Ni-Cr-Al alloys with regard to phase evolution, composition, and component activities. In addition, the oxidation of these alloys was analyzed in situ to determine the rate of corrosion in air and synthetic air mixtures

with SO<sub>2</sub> as the sulfidizing gas. These specimens will be characterized using a variety of techniques to determine the evolution of various phases during oxidation and the mechanisms for corrosion. Information garnered from these experiments was compared and contrasted to calculations using free energy minimization software to simulate the gas corrosion conditions. The combination of these procedures was expected to determine the effects of these coatings in the environments given and suggest solutions for preventing their failure.

## CHAPTER 2 LITERATURE REVIEW

As stated in Chapter 1, the corrosion mechanisms of overlay coatings on turbine blades are the chief concern of this dissertation. This chapter introduces the turbine blade alloys and their coatings, the thermodynamics of the coatings used, and the corrosion issues characteristic of the Ni-Cr-Al systems that are published to date.

### 2.1 Turbine Engine Considerations

Turbines operate by using the power from the exhaust to drive the forward inlet compressor (Figure 2-1). Today's modern turbine engines comprise a fan, a compressor, a combustion region, and a turbine. The fan draws in the air required for eventual combustion, and in the case of bypass turbofan engines provides most of the thrust for commercial and military aviation uses. For industrial gas turbines used in power generation, the fan may be replaced by a generator to create electricity (more often, the generator is placed toward the rear).

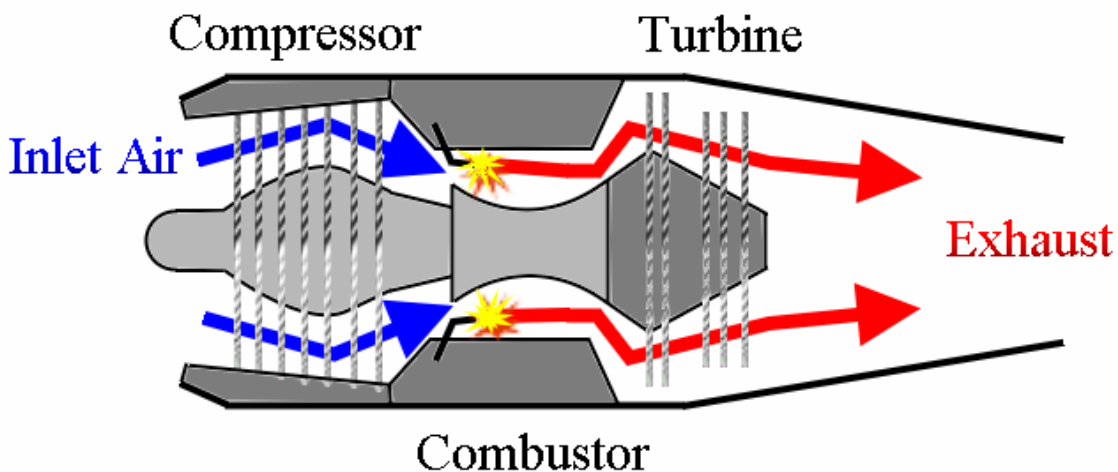


Figure 2-1. Schematic of a typical turbine engine.

The compressor region is a series of blades, rotors, and stators that draw air in and compress it in ranges upwards of 30 to 40 bar [10]. In the combustion chamber, fuel is injected into the hot compressed air, combusting spontaneously and expanding the gas mixture toward the

exhaust of the engine. This hot, expanding exhaust drives the turbine section, comprised of a series of blades and vanes, which powers the compressor and fan. As expected, the blades nearest to the combustion section experience the most severe conditions, but the later stages are greatly taxed as well. The materials contained in and the environments affecting the turbine section are the focus of this dissertation.

## **2.2 Turbine Blade Materials**

### **2.2.1 Superalloys**

Nickel base superalloys are often used for applications that require high strength at elevated temperatures, and are the material of choice for the turbine sections because, in addition to being strong and tough, they are resistant to fatigue, creep, and environmental attack. Common yield strengths for cast polycrystalline Ni-base superalloys are on the order of 700-1000 MPa at room temperature [11]. Creep rupture strength are typically 75-300 MPa at 870°C after 1000 hrs, and 60-125 MPa at 980°C after 1000 hr [11]. These properties stem from the nature of the two majority phases which have a coherent interface between the FCC  $\gamma$  structure and the  $L1_2$   $\gamma'$  structure of  $\text{Ni}_3\text{Al}$ —both having similar lattice parameters and coherent interfaces creating a low mismatch (less than 0.5% by length) [11-12]. The  $\gamma'$  phase is a superlattice that shows long-range ordering (LRO) to its melting point. This microstructure displays an increase in flow stress with increasing temperature [11-12]. Extensive and complex heat treatments, along with careful alloying, are used to create unique microstructures that will have the desired mechanical and environmental properties. The alloying elements commonly used in superalloys are listed in Table 2-1. Each of the elements has a tendency to partition during non-equilibrium solidification causing some of the elements to remain in the dendrite cores and some to be rejected into the interdendritic fluid that solidifies last. In service, these elements have a

tendency to diffuse and react with the environment. Therefore, careful balance and knowledge of the effects of each of these elements must be understood. Furthermore, complex heat treatments are employed to carefully control the microstructures, and mitigate these effects.

Table 2-1. List of common alloying elements in Ni-base superalloys.

Alloying Element	Alloying Properties	Partitioning Behavior
Al	$\gamma'$ former; increases anti-phase boundary energy ( $\gamma_{APB}$ ), increases oxidation resistance	Interdendritic / $\gamma'$
C	Carbide former; oxygen getter; grain boundary strengthener	n/a
Co	Lowers stacking fault energy ( $\gamma_{SFE}$ ); increases $\gamma'$ melting point; strengthens $\gamma$ phase	Dendrite Core / $\gamma$
Cr	Oxidation/corrosion protection, lowers $\gamma_{APB}$ ; can form topologically close-packed (TCP) phases	Dendrite Core / $\gamma$
Mo	Increase creep strength, strength in $\gamma$ ; decrease oxidation/corrosion resistance; forms TCP	Dendrite Core / $\gamma$
Nb	$\gamma''$ former; increases coherency strain, peak strength, room temperature strength	Interdendritic / $\gamma' / \gamma''$
Re	Increases creep strength, strength in $\gamma$ , modulus; decrease oxidation/corrosion resistance, forms TCP	Dendrite Core / $\gamma$
Ru	Reduces Re partitioning; delays TCP formation; increase creep strength; decreases oxidation/corrosion resistance	Dendrite Core / $\gamma$
Ta	$\gamma'$ former; increase $\gamma_{APB}$ , coherency strain, creep strength, peak strength; improves castability	Interdendritic / $\gamma'$
Ti	$\gamma'$ former; increases $\gamma_{APB}$ , coherency strain	Interdendritic / $\gamma'$
W	Increases creep strength, strength in $\gamma$ , modulus; decrease oxidation/corrosion resistance, forms TCP	Dendrite Core / $\gamma$

### 2.2.2 Coatings for Turbine Blades

There are a variety of coatings for superalloy blades and vanes, and they are applied to increase environmental stability and/or reduce the heat transmitted to the blade. Figure 2-2 shows the common coating configuration used in aerospace and industrial gas turbine (IGT) engines [16]:

- The substrate (superalloy turbine blades)
- The bond coat, which provides an environmental barrier for the substrate and a better bonding surface for the exterior coating
- The thermally grown oxide (TGO), which is sometimes manufactured before service
- The thermal barrier coating (TBC), which is a porous, columnar ceramic coating usually consisting of  $ZrO_2$  designed to reduce the heat seen by the layers underneath

The TBC effectiveness of the TBC is the change in temperature ( $\Delta T$ ) which controlled by TBC thickness ( $\delta$ ), thermal conductivity ( $k$ ), and the thermal flux ( $Q$ ) through the blade wall, via:

$$\Delta T = Q \cdot \frac{\delta}{k} \quad (2-1)$$

The  $\Delta T$  values obtained can be as high as  $150^\circ C$  [10]. The focus of this study will be on bond coats, which are generally of the MCrAlY composition design, where M is a metal base usually Ni, Co, or both. This layer, which is higher in Cr and Al than the substrate, is designed to oxidize first and protect the superalloy. This is because, even though the TBC is the outer coating, it is porous and the oxidizing/corroding elements of the atmosphere directly contact and react with the bond coat. Ni-base superalloys generally oxidize to form nickel-based oxides, which do not adhere to the substrate and cause spallation of TBC layer [13]. The layer of protection formed on the bond coat is generally designed to grow as aluminum oxide,  $\alpha-Al_2O_3$ , since it has the lowest oxygen diffusivity of the oxide of any of the elements listed in Table 2-1 [14]. The TGO is sometimes pre-grown before the coated blade is put into service but, regardless, is present upon usage in the highly oxidizing high temperature conditions. Co is can be used to increase the coating ductility, but the formation of CoO reduces the oxidation resistance because this oxide grows at a faster rate than NiO,  $Al_2O_3$ , or  $Cr_2O_3$  [10,13,15]. The thermal barrier coating is said to fail when the TGO grows to a thickness so large that it spalls. Spallation can also occur from buckling due to cyclic thermal stresses [16].

## Thermal Barrier Coating

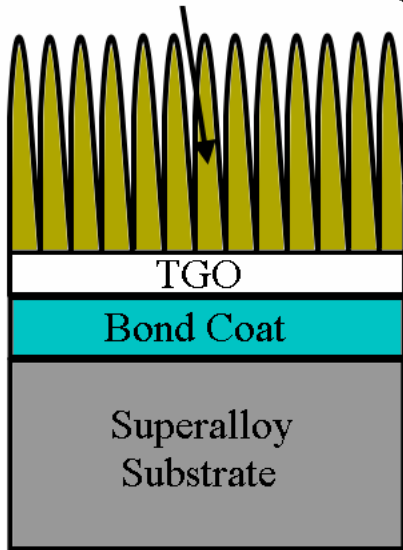


Figure 2-2. Schematic of coating configuration of modern turbine blades.

### 2.4 The Al-Cr-Ni Ternary System

The bond coats that are examined here are of the NiCrAl-type. In order to understand these coatings, the Al-Cr-Ni ternary should be discussed. The Al-Cr-Ni ternary has been studied through both experiments [17-22] and thermodynamic calculations [23-29]. Figures 2-3, 2-4, and 2-5 refer to the ASM Handbook binary phase diagrams of Al-Ni, Al-Cr, and Cr-Ni, respectively [30]. Studies of the Al-Cr-Ni ternary were undertaken—first using powder X-ray diffraction techniques [17], which were integrated with other techniques to determine thermodynamic data such as the Gibbs free energies of formation ( $\Delta G_f$ ) [18]. These other methods included diffusion couples [19-20], differential thermal analysis (DTA) [21], and electron microprobe (EPMA) [21]. The data were optimized to enable calculations of the ternary system. Since the Ni-rich area ( $X_{Ni} > 0.5$ ) is of more importance for practical applications, it has been studied in more depth than the Al or Cr-rich regions [19-20, 23, 25, 27].

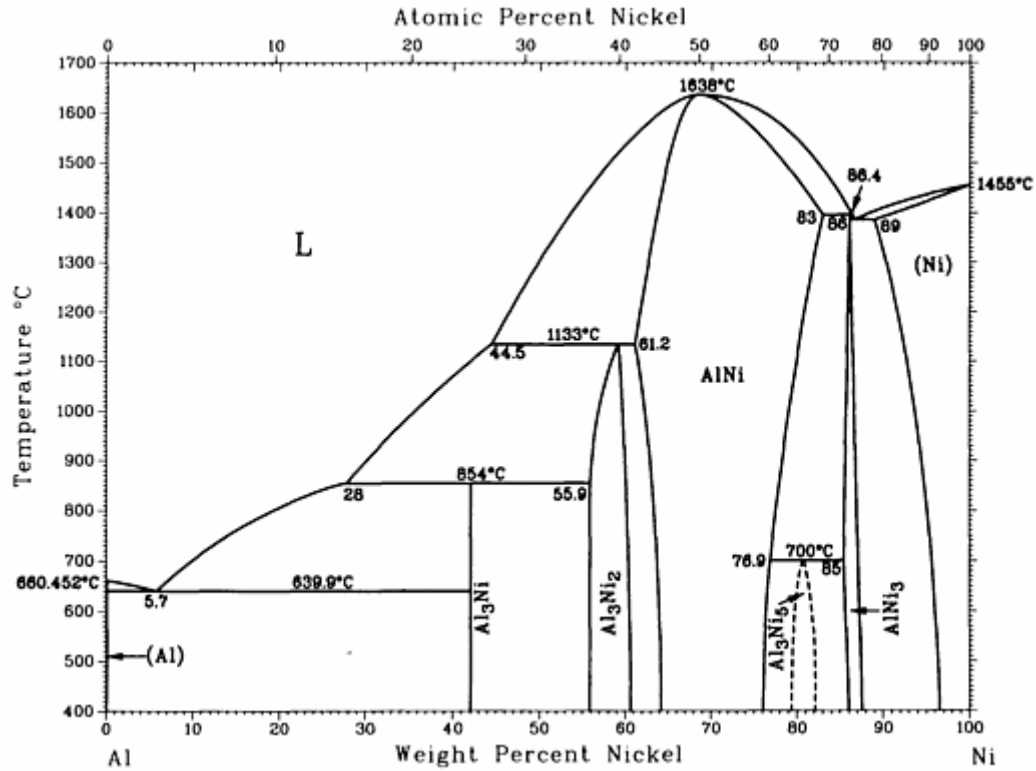


Figure 2-3. Al-Ni binary phase diagram [H. Baker. *ASM Handbook Vol. 3—Alloy Phase Diagrams*, ASM International: Materials Park, OH, p. 49 (1992)].

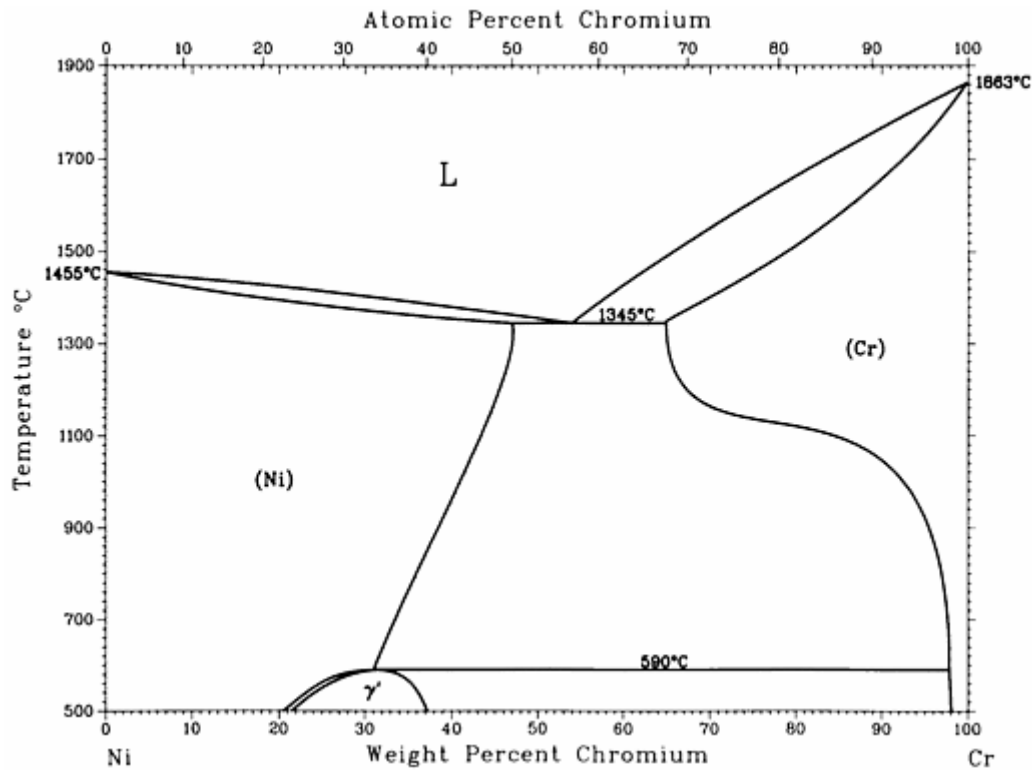


Figure 2-4. Ni-Cr binary phase diagram [H. Baker. *ASM Handbook Vol. 3—Alloy Phase Diagrams*, ASM International: Materials Park, OH, p. 155 (1992)].

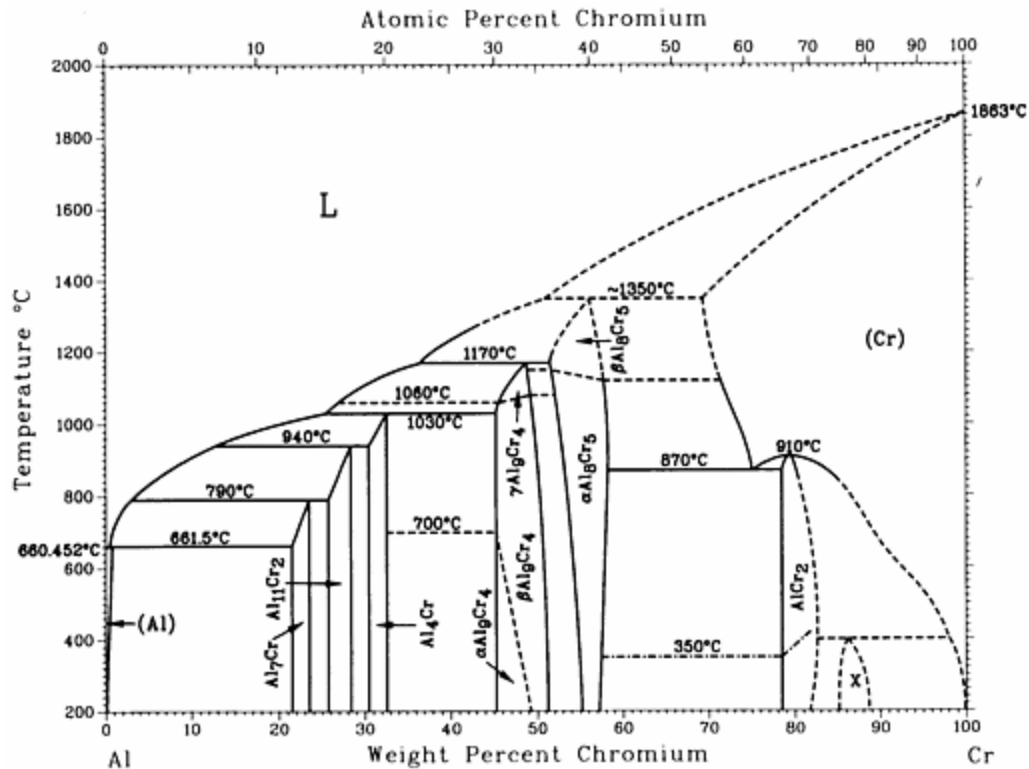


Figure 2-5. Al-Cr binary phase diagram [H. Baker. *ASM Handbook Vol. 3—Alloy Phase Diagrams*, ASM International: Materials Park, OH, p. 43 (1992)].

A recent retooling of the  $\Delta G_f$  descriptions of several of the important phases has been performed. Earlier studies described the  $\gamma$  and  $\gamma'$  phases as having separate Gibbs energy functions [23-24], but more recent studies by using new data [25] describe the  $\gamma$  and  $\gamma'$  as ordered and disordered versions of the same phase, transforming via a second-order reaction [27]. The  $\alpha$ -Cr and  $\beta$ -NiAl are also treated as having the same Gibbs energy function [26-27] as can be described by the compound energy formalism, which attempt to simplify descriptions of intermetallics and oxides using sublattices that can substitute multiple elements and vacancies [31]. This methodology is used for one of the databases accessed for ternary calculations (see Chapter 4). Debate has occurred over the exact descriptions of this sublattice model, as to whether there should be a single sublattice [23-25] or multiple [26-27]. The most recent

publications, though, [27-29, 32] agree that multiple sublattice models best describe the ordered and disordered phases present in the Al-Cr-Ni system.

The phases present in the Al-Cr-Ni ternary are listed in Table 2-2. Figure 2-6 shows the liquidus projection taken from a review of a compilation of calculated and experimental data [32]. The Scheil reaction scheme is shown in Figure 2-7. At 1445°C (labeled  $e_1$ ), a eutectic occurs in which  $\alpha$ -Cr and  $\beta$ -NiAl solidify. Eutectics also occur for  $\gamma$  and  $\gamma'$  at 1380°C ( $e_2$ ) and for  $\gamma$  and  $\alpha$  at 1345°C ( $e_3$ ). Peritectics are observed for  $L + \beta \rightarrow \gamma'$  at 1385°C ( $p_1$ ) and 1350°C for  $L + \alpha \rightarrow \zeta_1$  ( $Al_8Cr_5$ -hexagonal) ( $p_2$ ). At 1340°C,  $L\beta\gamma'$  and  $L\gamma\gamma'$  tie-triangles react in a ternary invariant reaction (Class II) to form  $L\beta\gamma$  and  $\beta\gamma\gamma'$  three-phase equilibria ( $U_1$ ). The  $L\beta\gamma$  then reacts with the  $L\alpha\beta$  and  $L\gamma\alpha$  tie-triangles at a ternary eutectic reaction (Class I) to solidify to  $\alpha + \beta + \gamma$  at 1320°C ( $E_1$ ). At 990°C, a ternary invariant reaction ( $U_4$ ) occurs in which the  $\alpha\beta\gamma$  reacts with  $\beta\gamma\gamma'$  to form  $\alpha\gamma\gamma'$  and  $\alpha\beta\gamma'$  three-phase equilibria. Figures 2-8 and 2-9 show isothermal sections of the ternary before and after reaction  $U_4$ , respectively. Other invariant reactions occur in the Cr-rich and Al-rich areas of the ternary, but these are ignored as they are not applicable to this study nor the one referenced [32].

The importance of studying this ternary is to construct model alloys of Ni-Cr-Al that can be modeled and studied as opposed to multicomponent alloys [28-29]. Results from experiments with these model alloys can be directly correlated to bond coats containing more elements such as rare-earths and Y (typically less than or equal to 1 wt%) and be related to their microstructures and corrosion results.

Overlay coatings are those in which interdiffusion is not required so that the coatings are “laid onto” the substrate. The MCrAlY compositions are designed to provide optimum oxidation or hot corrosion resistance, as well as strength, ductility, and thermal expansion match with the

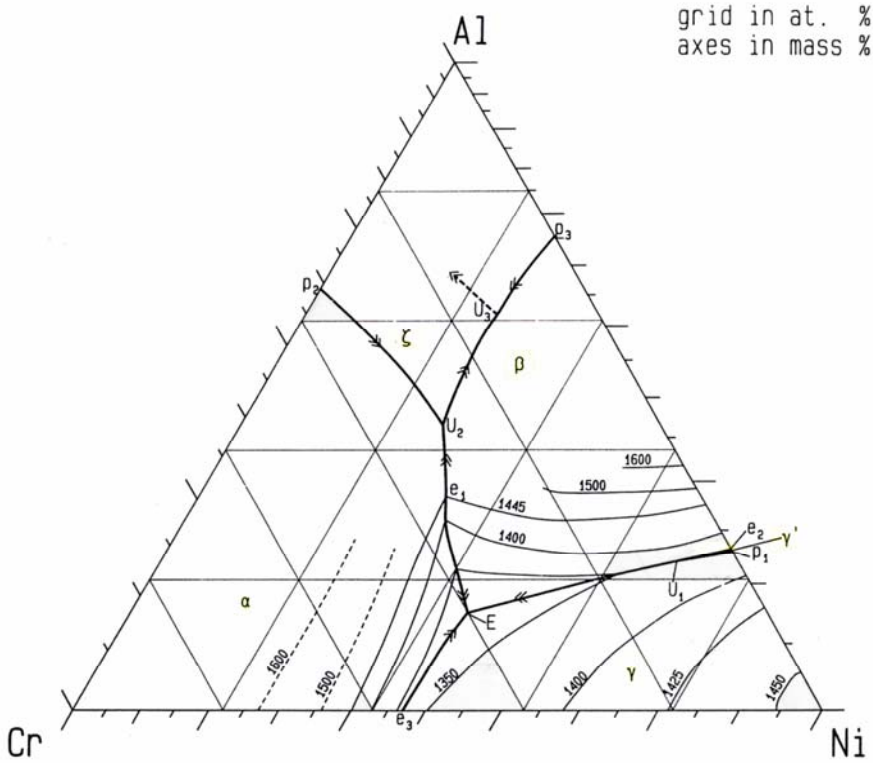


Figure 2-6. Liquidus projection of the Al-Ni-Cr ternary system [P. Rogl. "Al-Cr-Ni," *Ternary Alloys: A Comprehensive Compendium of Evaluated Constitutional Data and Phase Diagrams: Al-Cd-Ce to Al-Cu-Ru*. 4 p. 411 (1991)].

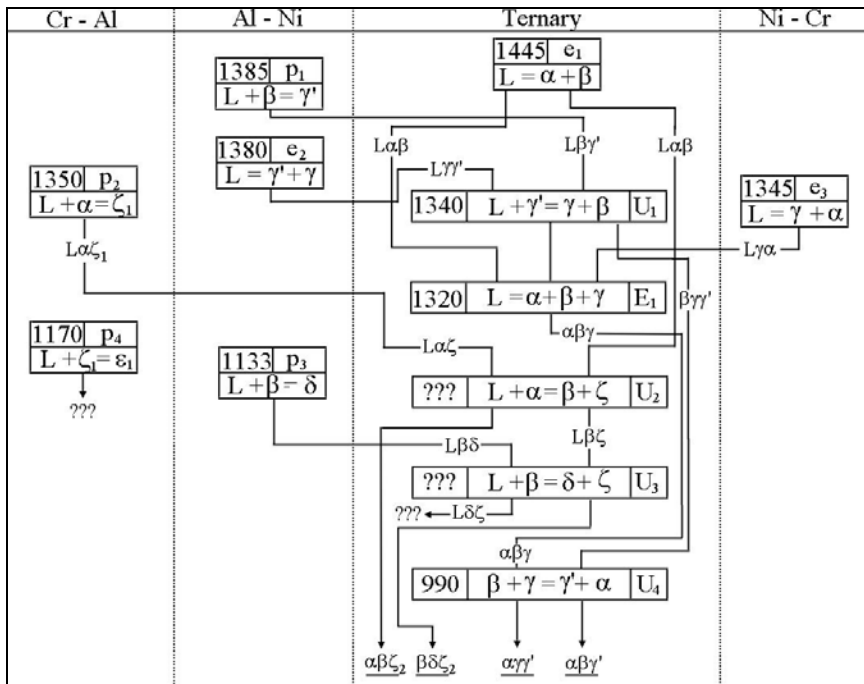


Figure 2-7. Scheil reaction scheme of the Al-Cr-Ni ternary. The  $\delta$ -phase refers to  $\text{Ni}_2\text{Al}_3$ , the  $\zeta_1$  to  $\text{Al}_8\text{Cr}_5$ -hexagonal,  $\zeta_2$  to  $\text{Al}_8\text{Cr}_5$ -rhombohedral, and  $\varepsilon_1$  to  $\text{Al}_9\text{Cr}_4$ . The question marks represent areas of the ternary that were not investigated.

Table 2-2. List of phases described in calculations of the Al-Cr-Ni ternary.

Phase	Temperature Range (°C)	Lattice Parameter (Å)	Space Group	Pearson Symbol
(Al)	< 660.45	4.049	Fm $\bar{3}$ m	cF4
$\alpha$ -Cr	< 1863	2.884	Im $\bar{3}$ m	cI2
$\gamma$ -Ni	< 1455	3.524	Fm $\bar{3}$ m	cF4
$\gamma'$ (Ni <sub>3</sub> Al)	< 1372	3.566	Pm $\bar{3}$ m	cP4
$\beta$ (NiAl)	< 1638	2.886	Pm $\bar{3}$ m	cP2
Ni <sub>2</sub> Al <sub>3</sub>	< 1133	a = 4.036 c = 4.900	P $\bar{3}$ m1	hP5
NiAl <sub>3</sub>	< 854	a = 6.611 b = 7.366 c = 4.8112	Pnma	oP16
Al <sub>13</sub> Cr <sub>2</sub>	< 791	a = 25.19 b = 7.574 c = 10.95 $\beta$ = 128.7°	C2/m	mC104
Al <sub>11</sub> Cr <sub>2</sub>	< 941	a = 12.88 b = 7.652 c = 10.639 $\beta$ = 119.3°	P2	mP48
Al <sub>4</sub> Cr	< 1031	a = 8.716 b = 23.95 c = 16.39 $\beta$ = 119.33°	P2/m	mP180
Al <sub>9</sub> Cr <sub>4</sub>	1172 – 1061	a = 9.123	Unknown	cI52
Al <sub>9</sub> Cr <sub>4</sub>	< 1050	Unknown	Unknown	[Monoclinic]
Al <sub>8</sub> Cr <sub>5</sub>	1352 – 1127	a = 9.047	Unknown	cI52
Al <sub>8</sub> Cr <sub>5</sub>	< 1127	a = 12.733 c = 7.944	R3m	hR26
AlCr <sub>2</sub>	< 911	a = 0.3004 c = 0.8648	I4/mmm	tI6
Ni <sub>2</sub> Cr	< 590	a = 2.524 b = 7.571 c = 3.568		oI6

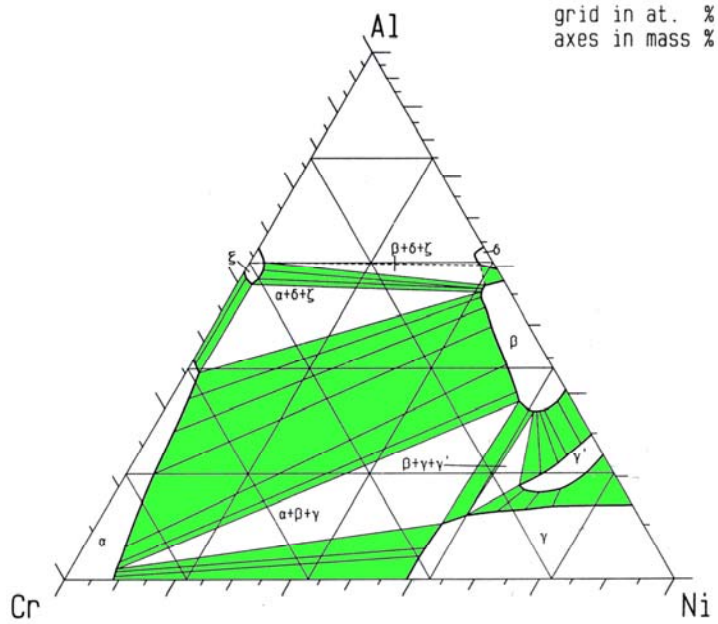


Figure 2-8. Isothermal section of Al-Cr-Ni ternary at 1025°C above the  $U_4$  reaction. The green areas denote regions of two-phase equilibria [P. Rogl. "Al-Cr-Ni," *Ternary Alloys: A Comprehensive Compendium of Evaluated Constitutional Data and Phase Diagrams: Al-Cd-Ce to Al-Cu-Ru*. 4 p. 414 (1991)].

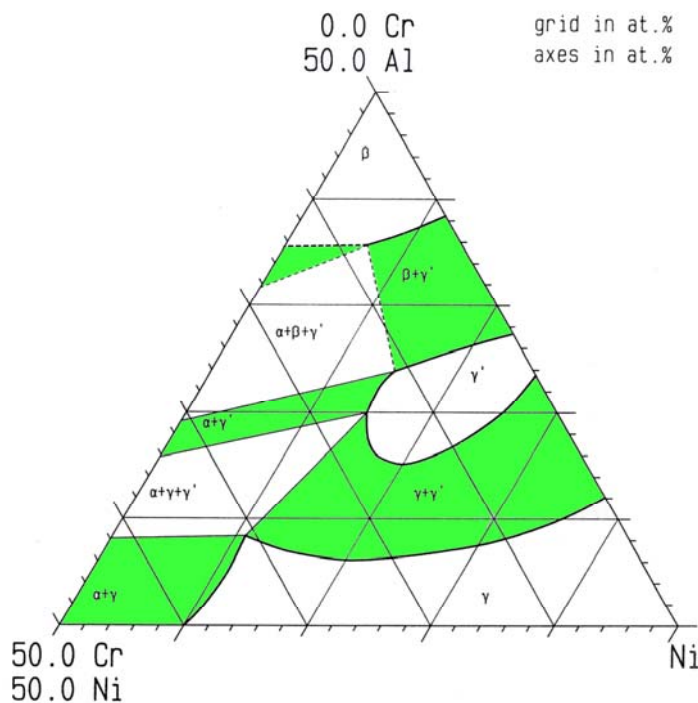


Figure 2-9. Partial Isothermal section of Al-Cr-Ni ternary at 850°C below the  $U_4$  reaction. The green areas denote regions of two-phase equilibria [P. Rogl. "Al-Cr-Ni," *Ternary Alloys: A Comprehensive Compendium of Evaluated Constitutional Data and Phase Diagrams: Al-Cd-Ce to Al-Cu-Ru*. 4 p. 413 (1991)].

given substrate. One application method is through electron beam physical vapor deposition (EB-PVD). This method allows direct deposition from a metal source to a heated metal substrate without a chemical reaction and forms a columnar structure [33]. This can also be accomplished using an electric arc [34]. Another common method, plasma spraying, involves injecting a prefabricated powder into a plasma-gas stream, which deposits melted pellets as splats on the surface [35]. This leaves few voids, but the coating has a rougher surface finish than EB-PVD. The surfaces of both coatings are often mechanically machined to create a smooth exterior and heat-treated to better bond to the substrate. Oxidative heat treatments are sometimes employed to begin TGO formation in a controlled manner in order to stabilize the coating system. Overlays can also be applied by a high-velocity oxide furnace (HVOF) in which liquid fuel and oxygen are fed at high pressure into a combustion chamber where they burn to produce a hot gas stream that accelerates powder particles onto the substrate [36].

The phases present in the overlay coating vary with the composition of the coating and can be approximated by the Ni-Cr-Al or Co-Cr-Al ternaries. Many of the coating processes do not create an equilibrium microstructure due to the rapid solidification, so they heat-treated to obtain the desired microstructure [37]. For the coatings to be used in this project, Ni-22Cr-11Al and Ni-8Cr-6Al, the phases present are shown in Table 2-3 [37]. Upon proper heat-treatment, the Ni-8Cr-6Al shows a microstructure of cuboidal  $\gamma'$  surrounded by a matrix of  $\gamma$  [28], whereas Ni-22Cr-11Al alloys show large globular  $\beta$  phases containing small  $\gamma'$  surrounded by a matrix of  $\gamma$  with small irregular  $\alpha$  [37]. At increasing temperature, the solubility of the alloying elements in the  $\gamma$  and  $\gamma'$  phases increase, reducing the number of stable phases. In this respect, there is more compositional homogeneity to more easily form a stable  $\alpha$ -Al<sub>2</sub>O<sub>3</sub> oxide film. The oxidation mechanisms and behavior of these coatings is discussed in the next section.

Table 2-3. The phases present in the Ni-22Cr-11Al and Ni-8Cr-6Al (weight percent) alloys at room temperature and 1000°C.

Alloy Composition	Phases Present (Room Temperature)	Phases Present (1000°C)
Ni-8Cr-6Al	$\gamma, \gamma'$	$\gamma$
Ni-22Cr-11Al	$\gamma, \gamma', \beta, \alpha$	$\gamma, \gamma'$

## 2.5 Oxidation of Al-Ni-Cr Alloys

### 2.5.1 General Oxidation Mechanism

In general, the oxidation of a metal in a gaseous environment involves several stages.

First, the O<sub>2</sub> molecule must adsorb (by physisorption) and dissociate onto two sites on the metal surface [39-40]. The molecule then chemisorbs with the surface, at which one or more of several processes may take place:

- Active oxidation—an M<sub>x</sub>O<sub>y</sub> molecule may desorb leaving a bare metal surface [40]
- Dissolution—the oxygen may diffuse into the metal, where it may later form internal oxides [38]
- Nucleation—oxides “islands” may nucleate and grow [38]
- Thin film formation—a thin film layer of oxide may form, passivating the metal [38-40]

This general mechanism is the mechanism of oxide growth expected for the alloys in this study.

The reaction on the surface



can be rate-limited by [38]

- Desorption (in the case of active oxidation)
- Diffusion of species through a film
- Gas transport in the substrate
- Ion transport in the substrate
- Oxide growth
- Oxide nucleation
- Surface adsorption

In the case of the formation of a thin film at lower temperatures, the rate-limiting step has been shown to be cation transfer from metal to oxide surface driven by an electric potential

across the film, as described by Mott and Cabrera [39]. The kinetics of thin film growth can be described as logarithmic

$$x = k_l \cdot \log(t + \tau) \quad (2-3)$$

or inverse logarithmic

$$\frac{1}{x} = B - k_l \cdot \log t \quad (2-4)$$

where  $x$  is film thickness,  $k_l$  is the rate constant,  $t$  is time, and  $B$  and  $\tau$  are constants. Figure 2-10 shows an example of logarithmic and inverse logarithmic growth.

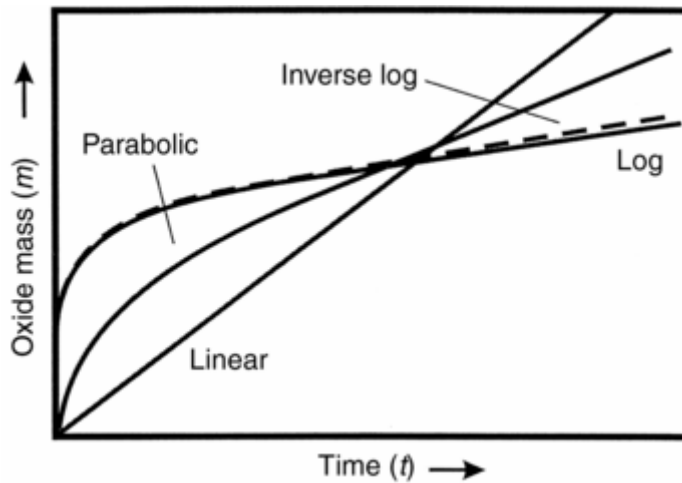


Figure 2-10. Plot of oxidation growth kinetics versus time.

At higher temperatures, and in thicknesses large enough where electric field effects are negligible ( $x > 10$  nm), parabolic kinetics usually govern film growth (Figure 2-10):

$$x^2 \approx k_p \cdot t + C \quad (2-5)$$

As described by Wagner's theory of passive oxidation of Si, thermal diffusion of cations and anions is generally the rate-limiting step in parabolic growth [40]. As the film thickness increases, the diffusion length increases slowing the growth. This observation, however, assumes a compact, adherent scale. If the oxide is porous or has poor adhesion with the metal surface, then bulk parabolic growth may not apply as short-circuit surface  $O_2$  diffusion paths

become prevalent. Bulk diffusion is usually bypassed by diffusion along grain boundaries, stacking faults, and dislocations, which increase the film growth rate [41].

Other kinetic oxidation models relevant to this study include linear growth:

$$\frac{dx}{dt} = k \quad (2-6)$$

Linear kinetics are also observed if the oxide is volatile or above its melting point. This occurs in oxides where the film is not protective, and is often porous. Other kinetic models include parabolic, cubic, and subparabolic, which describe mixed growth. These models attempt to describe transitions from one kinetic model to another (e.g. linear to parabolic) or growth limited by several simultaneous mechanisms.

The oxidation described in this section and the rest of this report deals with isothermal oxidation. Cyclic oxidation, where the temperature is varied (usually from room temperature to a maximum temperature), is not covered here as thermal expansion and residual stress factors must be taken into account, leading to more rapid failure than in isothermal conditions. For more information on cyclic oxidation, the interested reader is referred to references 10, 14, and 15.

#### 2.5.1.1 Oxidation of Ni

The oxidation of Ni is governed by gas absorption, oxide nucleation, and film growth as per the chemical reaction



NiO, or busenite, has an NaCl-type structure and appears as a black oxide (or green in high Ni contents). The oxide grows with a  $(111)_{\text{Ni}} \parallel (001)_{\text{NiO}}$ ,  $[1\bar{1}0]_{\text{NiO}} \parallel [1\bar{1}0]_{\text{Ni}}$  orientation relationship, although  $(100)_{\text{NiO}}$  and  $(211)_{\text{NiO}}$  are grown in epitaxy as well [36]. NiO is a p-type metal deficient oxide, where every cation vacancy has two  $\text{Ni}^{3+}$  pairs. In p-type metal deficient oxides, cations diffuse via vacancies in the cation sublattice to the oxide/gas surface while electrons migrate via

electron holes back toward the oxide/metal interface as determined by tracer experiments [38, 43].

Ni oxidation has been described by parabolic kinetics [43-46]. However, a recent study with pure Ni in various oxygen-argon atmospheres showed that between 700°C and 1000°C, NiO could grow “subparabolically” [44]; above 1000°C and below 600°C, parabolic growth is observed. The reason for this is that above 1000°C, bulk diffusion via cation vacancies dominates, and the scale exhibits columnar grains [47]. In the subparabolic regime, the scale exhibits a duplex structure with outer columnar grains having outward Ni cation diffusion, and inner equiaxed grains with short-circuit  $O_{2(g)}$  diffusion inward [48].

### 2.5.1.2 Oxidation of Al

Al oxidation has been widely characterized for a variety of applications. Al is highly reactive and readily ionizes at -1.662 eV [38]:



$Al_2O_3$  is considered an excellent passivating film due to its good Pilling-Bedworth (P-B) ratio (1.28) [38] and having a low  $O^{2-}$  diffusivity at sufficient thicknesses [49]. Alumina is most prevalent in the  $\alpha$ - $Al_2O_3$  corundum R3c phase, although other phases exist, as outlined in Table 2-4.

The initial stages of Al oxidation have been described using Al substrates in ultra-high vacuums. In the initial stages,  $O_2$  molecules approaching an Al surface physisorb, dissociate, and chemisorb onto the surface. This then allows for the inward diffusion of  $O^{2-}$  and the formation of  $Al_2O_3$  tetrahedra [51]. The adsorption sites are different based on the orientation of the metal surface. Initially, these original formula units of  $Al_2O_3$  exist as amorphous “islands,” which grow laterally, eventually covering most of the metal surface [52]. Initially cation-

Table 2-4. Descriptions and crystallographic information on different phases of Al<sub>2</sub>O<sub>3</sub> [49-50].

	$\alpha$ -Al <sub>2</sub> O <sub>3</sub>	$\kappa$ -Al <sub>2</sub> O <sub>3</sub>	$\gamma$ -Al <sub>2</sub> O <sub>3</sub>	$\theta$ -Al <sub>2</sub> O <sub>3</sub>	$\delta$ -Al <sub>2</sub> O <sub>3</sub>
Crystal system	Trigonal	Orthorhombic	Cubic	Monoclinic	Tetragonal
Space group	R3c	Pna2 <sub>1</sub>	Fd $\bar{3}$ m	C2/m	P $\bar{4}$ m2
Lattice parameters (Å)	a=4.7587 c= 12.9929	a=4.8351 b=8.3109 c=8.9363	a=7.92	a=11.8545 b=2.9041 c=5.6622 $\beta$ =103.837	A=5.599 c=23.657
Al atoms in unit cell	12	16	63/3	n/a	14
O atoms in unit cell	18	24	32	n/a	12
Al-co-ordination	Octahedral	75% octahedral 25% tetrahedral	n/a	n/a	n/a

deficient, the amorphous film grows outward via interstitial Al<sup>3+</sup> transport [49,52] driven by the Al concentration gradient [49,53] and E-field effects [40]. At several nanometers, when stoichiometry in the oxide is achieved [54], the amorphous alumina crystallizes into  $\gamma$ -Al<sub>2</sub>O<sub>3</sub> (sometimes preceded by a  $\gamma'$ -Al<sub>2</sub>O<sub>3</sub> [55]) due to a close orientation relationship between the oxide and the substrate (111)<sub>Al</sub>|| (111) <sub>$\gamma$ -Al<sub>2</sub>O<sub>3</sub></sub> as determined by a rigorous TEM analysis [56-57]. The  $\gamma$ -Al<sub>2</sub>O<sub>3</sub> is an anion-deficient n-type semiconductor, growing via inward chemical bulk O diffusion [58]. Short-circuit paths play a role at larger thicknesses. The growth kinetics are logarithmic at lower temperatures, and parabolic at higher temperatures.

The  $\gamma$ -phase is metastable and rarely seen above 800°C [58]. It will usually transition to the stable  $\alpha$ -phase at sufficient thicknesses, times, and temperatures. The  $\delta$  and  $\theta$  phases are sometimes seen as intermediates with whisker morphologies [58-59] and generally grow by outward cation diffusion, as determined by tracer and inert marker tests [58-60]. These transition

phases are undesirable compared to the  $\alpha$ -phase because stable  $\alpha$ -phase has a parabolic rate constant an order of magnitude lower [61] due to slow anion-diffusion along grain boundaries [56, 62]. This growth mechanism depletes the substrate less (in the case of Al-X alloys) than the cation-diffusing transition aluminas. Furthermore, the  $k_p$  of  $\gamma$ - $\text{Al}_2\text{O}_3$  is higher than that of NiO or  $\text{Cr}_2\text{O}_3$ , defeating the use of  $\text{Al}_2\text{O}_3$  as an impediment to oxidation in Ni-Cr-Al alloys [63].

### 2.5.1.3 Oxidation of Cr

The oxidation of Cr has been studied extensively due to its use as the major alloying protectant in stainless steels [64-66]. As found with tests in steels or in elemental form, Cr reacts with  $\text{O}_2$  to form  $\text{Cr}_2\text{O}_3$  via a similar reaction as Al does with  $\text{O}_2$ :



$\text{Cr}_2\text{O}_3$ , or chromia, like NiO is a p-type metal deficient semiconductor [67], and therefore grows by outward cation transport through the scale lattice [67-68] at temperatures less than  $1250^\circ\text{C}$ .  $\text{Cr}_2\text{O}_3$  is commonly used because it reacts faster with O than the elements it is alloyed with and has a low  $\text{O}_2$  diffusivity, thereby allowing a slow growth rate [69-70]. Cr oxidation is described by parabolic kinetics above  $700^\circ\text{C}$ , and shows initial logarithmic growth at lower temperatures. Above this temperature, chromia can become amphoteric, or able to transport in both directions simultaneously, and the growth rate increases rapidly [67]. Due to this defect structure, the  $\text{Cr}_2\text{O}_3$  can form a duplex structure with an inner layer where interstitial  $\text{Cr}^{3+}$  diffusion also takes place. This tends to increase the diffusion of  $\text{Cr}^{3+}$  in the inner region, which is highly dependent on the oxygen partial pressure [70]. As validated by tracer tests and diffusion coefficient findings, short-circuit diffusion through grain boundaries, cracks, and pores dominate and increase the scale growth rate [64, 69-70]. One oxidation study showed that this was the primary growth mechanism [71].

One of the problems with  $\text{Cr}_2\text{O}_3$  is the ability for the Cr cations to become hexavalent at higher  $\text{O}_2$  partial pressures, forming  $\text{CrO}_3$ , such as can be experienced in gas turbine conditions by these reactions [72]:



The formation of this gas species removes the protective chromia layer thereby making the  $\text{Cr}_2\text{O}_3$  ineffective. Volatilization also increases the Cr alloyed in the substrate, decreasing the time-to-fail of the  $\text{Cr}_2\text{O}_3$  scale. Other gas species have been studied, but are less likely to be major contributors at high temperatures and high oxygen partial pressures [72-73]. Hexavalent Cr gas species have been classified as carcinogens and the use of Cr coatings in some industries has been restricted [74].

### 2.5.2 Oxidation of Ni-Al Alloys

$\text{Al}_2\text{O}_3$  (as well as  $\text{Cr}_2\text{O}_3$ ) has a slower growth rate (Figure 2-11) and higher affinity for  $\text{O}_2$  than Ni [15]. Therefore, Al is commonly used as an alloying agent with Ni to provide an environmental protection in lieu of the unprotective NiO scale. As mentioned in Section 2.2, Al is also used to form and stabilize the intermetallics  $\gamma'$  and ( $\beta$ ).

With Ni-Al alloys, the corundum  $\alpha$ -alumina phase is the desired TGO for its slow-growth rate, low anion diffusivity, and overall smooth morphology. The  $\gamma$ -alumina phase has been shown in studies to appear first, especially at lower temperatures ( $T < 850^\circ\text{C}$ ) due to a lower activation energy to form on Ni-Al alloys [75-77].

The oxidation of dilute Ni-Al alloys begins with the formation of NiO. The formation of this oxide, though, depletes the alloy at the alloy/gas interface of Ni and reduces the  $P_{\text{O}_2}$  in relation to the gas/scale interface. This leads then to the formation of  $\text{Al}_2\text{O}_3$  [63]. Scanning

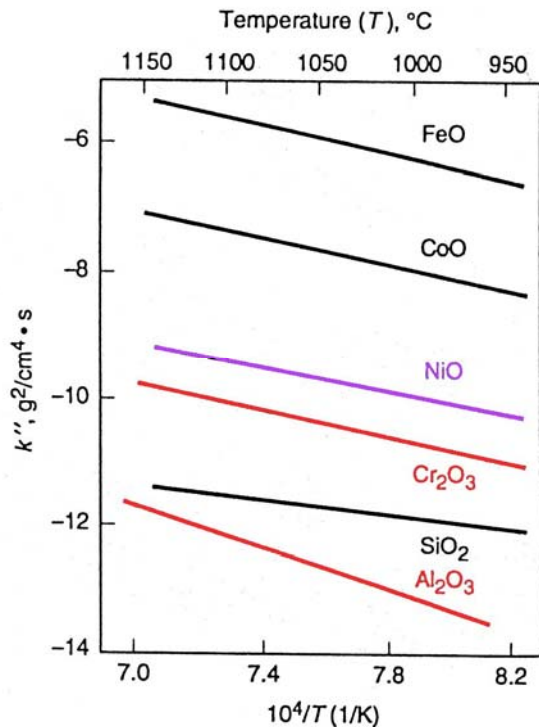


Figure 2-11 – Arrhenius plot of parabolic growth rates versus temperature of NiO (violet) as well as Cr<sub>2</sub>O<sub>3</sub> and Al<sub>2</sub>O<sub>3</sub> (red) [J.L. Smialek, G.M. Meier, “High-Temperature Oxidation,” *Superalloys II*. C.T. Sims, N.S. Stolff, W.C. Hagel, eds., John Wiley & Sons: New York p. 295 (1987)].

electron microscopy (SEM) cross-sections found that alumina scale formation will develop fastest at the grain boundaries, since these are fast diffusion paths for Al<sup>3+</sup> and O<sup>2-</sup> transport [77]. Hindam and Smeltzer described the formation of Al<sub>2</sub>O<sub>3</sub> in the presence of NiO or Ni will lead to “breakdown oxidation” of the alumina scale in which spinel is formed via [78]:



If the amount of Al present in the alloy is too little, a stable alumina scale may not be formed [78]. As graphically described by Pettit in Figure 2-12, too little Al will prevent the internal oxides of Al<sub>2</sub>O<sub>3</sub> from coalescing to form a continuous scale [76]. Furthermore, even if a stable scale is formed, the alloy must have enough Al to continually feed the oxide growth, and the flux of Al in the alloy must exceed that in the oxide. If not, the alumina scale will break down, and NiO and NiAl<sub>2</sub>O<sub>4</sub> will stabilize [76, 78-79].

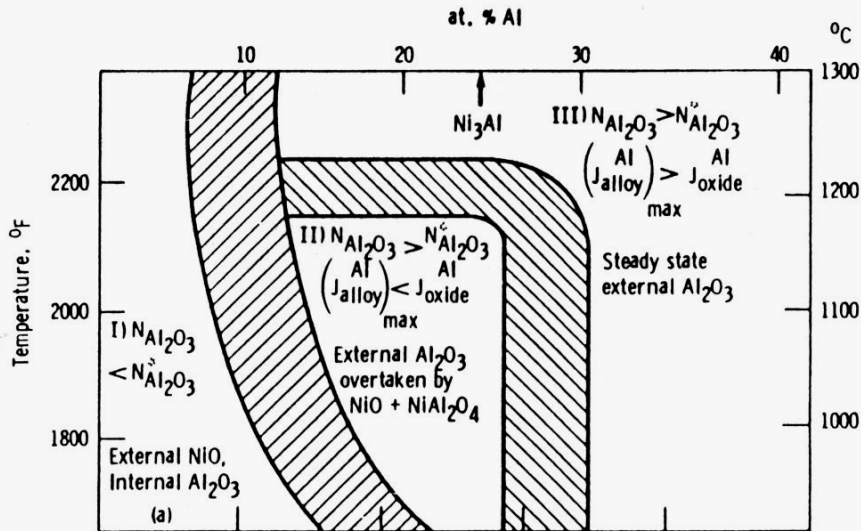


Figure 2-12. Dependence of oxidation mechanisms and scale type of Ni-Al alloys based on temperature and Al content [F.S. Pettit: *Transactions of the AIME*. 239, pp. 1296-1305 (1967)].

In two-phase alloys, oxidation rates and oxide phases can differ over a range of compositions. The addition of any Al to Ni will cause an increase in the rate of oxide growth, and a decrease in activation energy [58, 79]. This fast oxidation is due to  $\text{Al}^{3+}$  doping of the NiO and the formation of the open  $\text{NiAl}_2\text{O}_4$  spinel that allows for rapid cation diffusion [79]. In  $\gamma + \gamma'$  mixtures, the kinetics are more complex, showing a parabolic-linear-parabolic procedure whose growth rate is less than alloys with  $\text{Al} < 6 \text{ wt}\%$  [76]. This occurs because the initial  $\alpha\text{-Al}_2\text{O}_3$  scale is being overtaken by NiO growth, and eventually reaches steady-state nickel oxide parabolic growth [80]. For those oxides growing over  $\gamma\text{-Ni}$ , the only alumina seen is  $\alpha\text{-Al}_2\text{O}_3$ , and can be mixed with NiO and spinel. Transient  $\delta$  and  $\theta$  alumina phases are often seen growing first over  $\text{Ni}_3\text{Al}$  [81-82]. This is also observed on  $\gamma' + \beta$  mixtures, but kinetics are always parabolic [76, 83-84]. The presence of  $\beta$  causes the faster formation of  $\alpha\text{-Al}_2\text{O}_3$  and a slower growth rate than with more dilute Ni-Al alloys. Transient alumina phases have been observed over NiAl as well [85].

### 2.5.3 Oxidation in Al-Cr-Ni Ternary and NiCrAlY Coatings

Oxidation of Ni-Cr-Al alloys involves a complex competition of the formation and growth of NiO, Cr<sub>2</sub>O<sub>3</sub>, and Al<sub>2</sub>O<sub>3</sub>. In addition, the nickel-chromium and nickel-aluminum spinels often play a role. In general, the addition of Cr to Ni-Al alloys stabilizes the Al<sub>2</sub>O<sub>3</sub> phase [85-86]. This overall process, was first described by Pettit [76] and is shown in Figure 2-13. Upon initial oxidation, the activities of oxygen and nickel are high enough that NiO forms [87]. Any Al or Cr that oxidizes reacts with NiO to form spinel. NiCr<sub>2</sub>O<sub>4</sub> and NiAl<sub>2</sub>O<sub>4</sub> allow for faster transport of O<sup>2-</sup> anions in and Ni<sup>2+</sup> anions out. As the initial scale grows, the P<sub>O<sub>2</sub></sub> at the scale/alloy interface diminishes due to scale thickening, and the activity of Ni decreases due to Ni-depletion in the alloy below the interface [88]. This causes internal oxidation of Cr and Al in the alloy. If there are insufficient amounts of alloying elements, the Al and Cr oxides will remain as small spherical and/or rodlike internal phases (Group I). If, however, there is enough Cr, a continuous scale of Cr<sub>2</sub>O<sub>3</sub> will form and grow at the scale/alloy interface (Group II). This has the effect of further lowering the oxygen activity at the interface, which, if there is enough Al to sustain it, will form a continuous Al<sub>2</sub>O<sub>3</sub> scale that becomes rate-controlling (Group III) [86, 89-90]. In effect, Cr “getters” O<sub>2</sub> allowing the Al<sub>2</sub>O<sub>3</sub> scale to stabilize. If there is not enough Al, though, the steady-state scale that grows will be chromia (Group II) [90-92].

Kinetically, as with Ni-Al alloys, increasing the alloying elements Al and Cr in Ni-Cr-Al will cause a decrease in the parabolic growth rate [93-94]. The exception to this is in the case of dilute alloys wherein the alloying elements actually dope the oxide increasing ionic mobility by introducing lattice vacancies [88, 95].

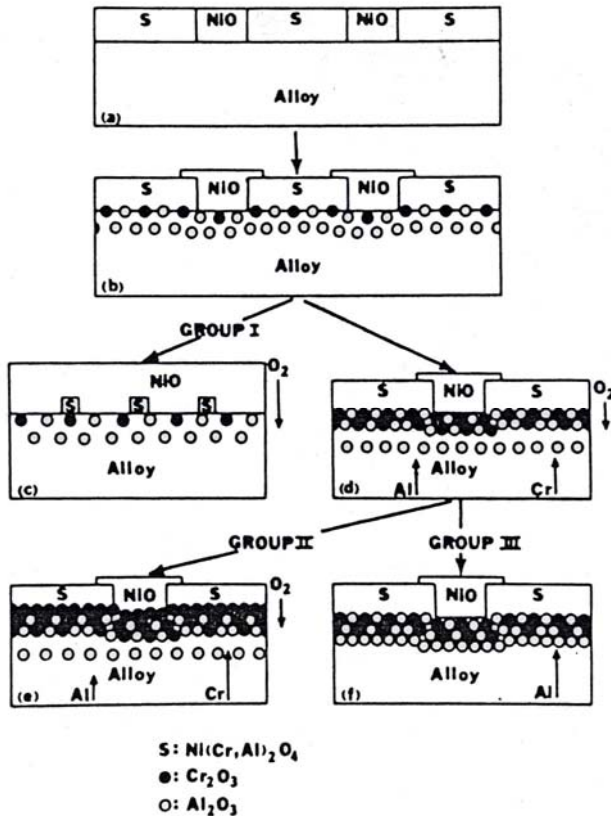


Figure 2-13. Schematic of the stages of oxidation in Ni-Cr-Al alloys. Group I are alloys that will have a stable NiO scale, Group II will develop a stable Cr<sub>2</sub>O<sub>3</sub> scale, and Group III will develop a stable Al<sub>2</sub>O<sub>3</sub> scale [F.S. Pettit: *Transactions of the AIME*. 239, pp. 1296-1305 (1967)].

The microstructure of the scale shows orientation relationships between the initial oxides formed and the metal. Similar to that of  $\gamma$ -Al<sub>2</sub>O<sub>3</sub> and Al, the relationship of the spinel and  $\gamma$ -Al<sub>2</sub>O<sub>3</sub> that forms on the alloy is  $(111)_{\text{Spinel}} \parallel (111)_{\text{NiCrAl}}$ ,  $\langle 110 \rangle_{\text{Spinel}} \parallel \langle 110 \rangle_{\text{NiCrAl}}$  [58]. The Cr<sub>2</sub>O<sub>3</sub> that grows is  $(0001)_{\text{Cr}_2\text{O}_3} \parallel (111)_{\text{NiCrAl}}$ ,  $\langle 11\bar{2}0 \rangle_{\text{Cr}_2\text{O}_3} \parallel \langle 110 \rangle_{\text{NiCrAl}}$ . However, TEM studies showed that the steady-state alumina that grows has a random orientation with the alloy and the other oxide layers [58, 61, 96]. Over time, the Cr in the alloy tends to segregate out of the NiAl into the  $\gamma$  and  $\gamma'$ . Cr<sub>2</sub>O<sub>3</sub> is seen on top of those Cr-rich regions, whereas Al<sub>2</sub>O<sub>3</sub> forms faster above the  $\beta$  [57]. As with Ni-Al with high Al contents,  $\delta$  and  $\theta$ -Al<sub>2</sub>O<sub>3</sub> are observed having a needle-like morphology [57, 97-98] that transforms to  $\alpha$  during continuous exposure to an oxidizing gas

mixture [56]. A study by Levi et. al. observed these transient aluminas formed as lumps or hills on top of the  $\beta$ , whereas the oxides over  $\gamma/\gamma'$  were seen as a smooth scale [97]. The  $\alpha$ -alumina that forms underneath (over all alloy phases) is columnar [93, 96-97]. The absence of these transient aluminas again shows a lower oxidation rate [98].

## 2.6 Sulfidation and Hot Corrosion

### 2.6.1 Hot Corrosion

Hot corrosion is an accelerated corrosive attack of molten salts that often occurs in the later stages of turbine engines where the pressure is less than those near the combustor, and when salt or ash deposits accrue on the alloy or coating surface [99]. Even for applications typically operating above 1000°C, hot corrosion can be a problem during thermal cycling—frequently occurring in salty marine areas or in operations with fuels containing S, V, and/or P. This mechanism occurs when temperatures enable molten salts such as  $\text{Na}_2\text{SO}_4$ ,  $\text{K}_2\text{SO}_4$ , and/or  $\text{NaCl}$  to be in their liquid state, in which they attack the oxide scale, and eventually penetrate into the substrate itself [99-101]. This type of corrosion can be categorized into two stages: an initiation stage, and a propagation stage. The initiation stage is marked by either parabolic growth or slow weight loss. The mechanism is similar to oxidation, except that sulfides form in the oxide from an influx of sulfur anions or  $\text{SO}_x$  gases. Once the propagation stage begins, severe weight loss is observed and rapid attack of the oxide and alloy begins. The chief reaction(s) governing this process is



These are the basis for the fluxing reactions in which basic fluxing



or acidic fluxing



occurs [102]. This attack can be categorized into either Type I, which occurs between 850 and 1000°C and is governed by basic fluxing, and Type II that occurs between 680 and 750°C [97] and is governed by acidic fluxing [103-104]. Type II corrosion displays characteristic pits can be avoided through higher Cr contents, higher temperatures, and larger gas flow velocities in the engine. The partial pressure of SO<sub>3</sub> is critical for the reaction where the sulfate dissolves the metal oxide at the scale/salt interface, which then reacts with SO<sub>3</sub> to form oxide (low P<sub>SO<sub>3</sub></sub>) or sulfate (high P<sub>SO<sub>3</sub></sub>), which then repeats the process [103-105].

Type I hot corrosion is of more concern for this study, in which the formation of metal sulfides from reactions with the sulfate create a free oxygen anion that reacts with the metal oxide to form a metal oxyanion that dissolves in the salt [105-106]. This MO<sub>x</sub><sup>2-</sup> then can react with SO<sub>2</sub> (or SO<sub>x</sub>) to form oxide particulates at the salt/gas interface that frees up oxygen anions to repeat the process [106-107]. While originally thought to be self-sustaining, other research by Goebel and Shores has shown that a constant supply of Na<sub>2</sub>SO<sub>4</sub>(l) is required to prolong the reaction [100, 108]. One of the chief drivers for this corrosive attack is the production of sulfides, and the diffusion of sulfur into the oxide itself [109]. The last sections of this chapter will examine the role of sulfidation, which is the mechanism for the initiation stage of Type I hot corrosion [103-105].

### **2.6.2 Sulfidation on Metals**

Sulfidation in metallic systems has been studied in oxygen and oxygen-free environments. Sulfur is present in unclean fuels, coal, and salts in marine environments, and behaves differently

depending on whether it is present in oxidizing environments, or those devoid of oxygen (reducing environments). Reducing environments of sulfur are often modeled in  $H_2S$  atmospheres with low oxygen partial pressures and a fixed  $H_2/H_2S$  ratio in order to fix the partial pressure of  $S_2$ . Studies involving this have shown that Ni in  $H_2/H_2S$  environments form almost exclusively  $\beta-Ni_3S_2$  which exhibits linear sulfidation behavior initially (or at lower temperatures) and then grows parabolically [110-111] due to rapid sulfur diffusion along grain boundaries [112]. In Cr-containing alloys, the sulfides come closer to a 1:1 ratio of CrS as the temperature increases as determined by XRD and TEM, with a layered structure exhibiting inward anion diffusion, and an outer layer exhibiting outward cation diffusion [113]. This duplex sulfide layer is also seen in alloys where the rate-limiting mechanisms are similar with an outer layer of  $Ni_3S_2$  and an inner layer mix of nickel, chromium, and aluminum sulfides [114-115] due to decreased the sulfur activity.

In sulfidation experiments performed in oxidizing conditions, which are the focus of this study, either  $SO_2$  is mixed with the oxidizing atmosphere (usually air or  $O_2$ ),  $SO_2$  is used alone, or  $H_2S$  is added to oxygen. In all these situations, the  $P_{O_2}$  is usually high enough to begin initial oxidation of the metal, and sulfides are absent since these conditions are above their dissolution pressure [116-117]. In oxidation, the role of S is initially one of an impurity dopant that accelerates oxidation through the creation of vacancies [118-119]. Sulfur can diffuse rapidly through grain boundaries, pores, and other high surface energy defects and stabilize them, allowing fast transport of other ions [122-124]. This can be accelerated by the dissociation of  $SO_2$  in these defects, which increases the oxygen and sulfur partial pressures [125-127]. However, sulfur can build up at sufficient scale thicknesses to cause sulfide formation. This will be elaborated upon in section 2.6.3.

Whenever SO<sub>2</sub> and O<sub>2</sub> are present below 700°C, they can react to form SO<sub>3</sub> [125], a gas above 45°C, via the reaction



The formation of SO<sub>3</sub> causes different reactions with the metal, as it is more oxidizing [128] and therefore sulfidizing [129] than its dioxide counterpart. These conditions make it more likely to form sulfates, which, as with hot corrosion, can rapidly attack the oxide or metal [130-131].

However, the effects of SO<sub>3</sub> are minimal above 800°C in that it becomes unstable and will readily decompose into SO<sub>2</sub> and O<sub>2</sub>. SO<sub>3</sub> also chemisorbs on the oxide surface slower than SO<sub>2</sub> [128]. Furthermore, the reaction on Equation 2-16 occurs at slow rates, requiring a platinum catalyst to stabilize the reaction at higher temperatures [128]. Therefore, the effects of SO<sub>3</sub> may only be relevant in specific service conditions in modeling Type I hot corrosion.

### **2.6.3 Sulfidation on Metal Oxides**

In metal oxide scales adherent to metal alloys, sulfur has been shown to migrate towards the scale/alloy interface. Sulfur is also present in pores, cracks, and grain boundaries [127, 132-135]. At the scale/alloy interface at extended times, the amount of sulfur continues to build up while the scale/gas interface moves further away relative to the scale/alloy interface due to oxide growth [136-139]. This reduces the amount of oxygen near the interface [140]. When the P<sub>S<sub>2</sub></sub> is high enough, and the P<sub>O<sub>2</sub></sub> is low enough, sulfide phases begin to stabilize and their growth becomes faster than that of the oxide [126-127, 130-131, 139, 140-146]. The formation of these sulfides destabilizes the scale adherence to the substrate [135], causing the formation of cracks and pores, which leads to scale spallation [120, 127, 133, 138, 140]. These cracks allow the gas species to migrate faster to the interface, accelerating corrosion. Due to the complex and open structures of these sulfides, ionic species are able to diffuse faster through the sulfide, which also increases the oxidation rate [111, 121, 126, 133, 147]. This mechanism of premature oxide

failure because of sulfur buildup at the oxide/alloy interface has been dubbed the “sulfur effect” by Lees and Fox and is illustrated in Figure 2-14 [120, 139]. If enough  $\text{Ni}_3\text{S}_2$  is present, it can react with Ni to form a low melting liquid eutectic, exacerbating the situation [130, 146].

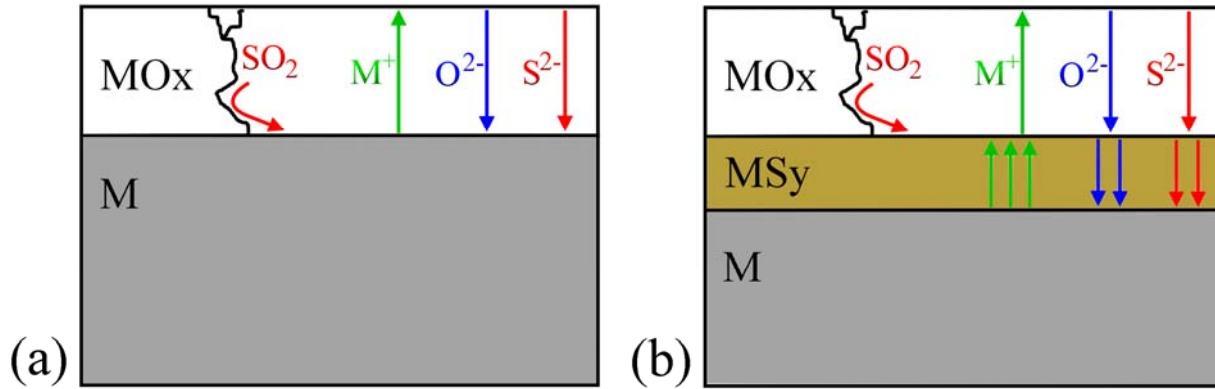


Figure 2-14. Schematic showing the formation of metal sulfides (a) under an initial metal oxide layer (b) in simultaneous oxidizing and sulfidizing conditions. The various proposed transport mechanisms are shown.

While it is clear that sulfur migrates towards the scale/alloy interface, the mechanism behind this process is not entirely agreed upon. Two schools of thought have developed as drawn in Figure 2-14. Originally, it was believed that sulfur diffused as  $\text{S}^{2-}$  anions through the lattice, accumulating at the interface [119, 122, 142, 144, 148-149]. However, other studies have rejected this notion stating that diffusion rate is too slow for this to be seen in experiments [118, 130] and, with  $\text{Cr}_2\text{O}_3$ , the solubility of S or  $\text{S}_2$  is too low [134]. Furthermore, the  $\text{S}^{2-}$  anions would eventually have to climb up a concentration gradient as the  $P_{\text{S}_2}$  required to form sulfides is significantly higher that of the corrosive gas at the gas/scale interface [138, 141].

The other theory is that the sulfur migrates by gaseous diffusion of  $\text{SO}_2$  [118, 123-124, 130, 132, 134, 138, 140-141]. The  $\text{SO}_2$  would flow via cracks and pores, or along high-angle grain boundaries to the scale/alloy interface where one of three reactions are possible [150]:

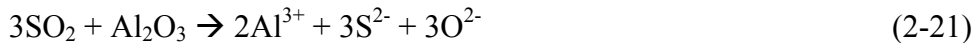




This third reaction is unlikely to occur, while the first allows for the formation of free sulfur, which increases the  $P_{S_2}$ , and the second causes sulfide formation (although it does raise the  $P_{O_2}$ , which is generally counteractive to sulfide formation). Indeed, in SEM studies with Cr and Ni-Cr alloys exposed to  $SO_2$  that developed compact chromia scales, no sulfide formation took place at the scale/alloy interface, while porous scales developed sulfides [117, 134]. This mechanism is disputed by other studies stating that gaseous diffusion is unlikely due to the size of the  $SO_2$  molecule [142], and studies with high S contents at grain boundaries absent of voids still formed sulfides at the scale/alloy interface [122, 139].

#### 2.6.4 Sulfidation in Ni-Cr-Al Coatings

As has been shown, sulfur can reduce the effectiveness of bond coats, even in highly oxidizing conditions. As described by previous publications, sulfidation processes for these coatings resemble the initiation stage of Type I hot corrosion [90, 99, 107, 130]. Ni-Cr-Al alloys have been designed to resist against sulfidation attack and are relatively high in Al and Cr, mainly because the S and O diffusivities in  $Al_2O_3$  and  $Cr_2O_3$  are lower than in NiO [120, 143, 148, 151]. In sulfidation attacks,  $Al_2O_3$  is slightly more susceptible to  $SO_2$  attack [99] by



Therefore, some applications, especially those experiencing hot corrosion, are designed to allow for  $Cr_2O_3$  protective scales rather than  $Al_2O_3$  to grow, even though chromia grows faster [73].

In addition, rare earth elements, yttrium, and silicon are commonly added as getters for O and S. These elements have been shown to decrease corrosion rates as well as spallation and scale degradation in sulfidizing environments [124, 133, 151]. This occurs when reactive-element grain boundaries phases such as  $Ni_5Y$ , which react with S first [152], prevent the sulfidation of the other alloying elements.

## 2.7 Calculations of Oxidation/Sulfidation

Thermodynamic calculations have been used to describe and predict a variety of materials applications, especially the development of phase diagrams. Calculations of the Al-Cr-Ni ternary have already been performed (see Section 2.4). The study of oxidation by calculations for this system was limited until recent publications compiled and optimized thermodynamic data. Previous studies of the  $\text{Al}_2\text{O}_3$ - $\text{Cr}_2\text{O}_3$  system used the quasichemical model for non-gaseous phases and modeled the phases as a single solid solution with a miscibility gap [153]. The quasichemical model was used for the Cr-Ni-O system [154], and, combined with the sublattice model descriptions of the Cr-Ni-O and Al-Ni-O systems [43, 155], an  $\text{Al}_2\text{O}_3$ - $\text{Cr}_2\text{O}_3$ -NiO ternary was constructed [6]. Saltykov's analysis of these ternaries allowed one of the more comprehensive descriptions of the Al-Ni-Cr-O quaternary system using free energy minimization [156] software to produce multiple plots that graphically described the system [6]. This approach was also used by Seifert et. al. to assess the AlNi-Cr-Ni-O system [7]. However, little work has been done to model sulfidation attacks of this system.

M-O-S systems for Fe, Ni, Co, and Cr were developed using Gibbs energy minimization techniques with  $\text{CO}_2/\text{H}_2$  and  $\text{H}_2\text{S}/\text{H}_2$  ratios to set the  $P_{\text{O}_2}$  and  $P_{\text{S}_2}$ , respectively [8]. The idea of using M-O-S type diagrams was also approached in previous publications [127, 142]. An attempt to produce Na-M-O-S quaternaries of Fe, Cr, and Al for Type II hot corrosion applications was also performed by Li and Gesmundo [157] based on previous techniques of overlaying "quasi-ternaries" and finding stable quadruple points [158-159]. Through all these publications, no work has been done to attempt to describe alloys or even their mechanical mixtures. This dissertation will fill these gaps by calculating the stability of Ni-Cr-Al alloys and their mechanical mixtures in oxidizing and sulfidizing atmospheres. These diagrams will be plotted as potential diagrams, described by Yokokawa [160], which plot chemical potential

instead of composition (a traditional phase diagram). Potential diagrams are useful for showing diffusion paths, which are straight lines on potential diagrams, and for visualizing phases present based on the changing activities of various reacting elements of an oxidizing and/or sulfidizing system [160]. The chemical potentials can also be plotted as activities or partial pressures, for easier interpretation. The exact methodology of these calculations will be described in Section 3.1.

## CHAPTER 3 METHODS AND MATERIALS

This chapter discusses the methods and materials used in this study. This includes the calculation of phase diagrams approach (CALPHAD) for the development of potential diagrams, as well as the experimental design for the kinetic tests and the characterization of the materials of this study.

### **3.1 Thermodynamic Modeling and Simulations**

#### **3.1.1 The CALPHAD Approach**

In performing simulations by thermodynamic modeling, the CALPHAD approach was used. This approach is shown as a flowchart in Figure 3-1. Here, one combines the information obtained by theoretical development with that of experimental measurements and estimates to create data that are stored as analytical expressions of thermodynamic functions with adjustable parameters [156]. These descriptions are then optimized using a least squares regression to get the best possible thermodynamic data [156]. From this, the data are compiled into stored databases, from which the desired information for a particular study can be obtained. This method prevents the use of a “black box” design and allows the data to be adjusted, as opposed to some other calculation methodologies [161].

From these databases, one can then use a thermodynamic software program to obtain the desired information. This is done by computing an equilibrium and then graphically presenting the phase diagram from the initial equilibrium. These diagrams are then compared and contrasted with the existing experimental data to determine if database adjusting is needed. Lastly, the calculated diagrams are utilized for developing and designing applications in industry and research. This study will stress this last part of the CALPHAD approach—the calculation of diagrams from previously developed databases.

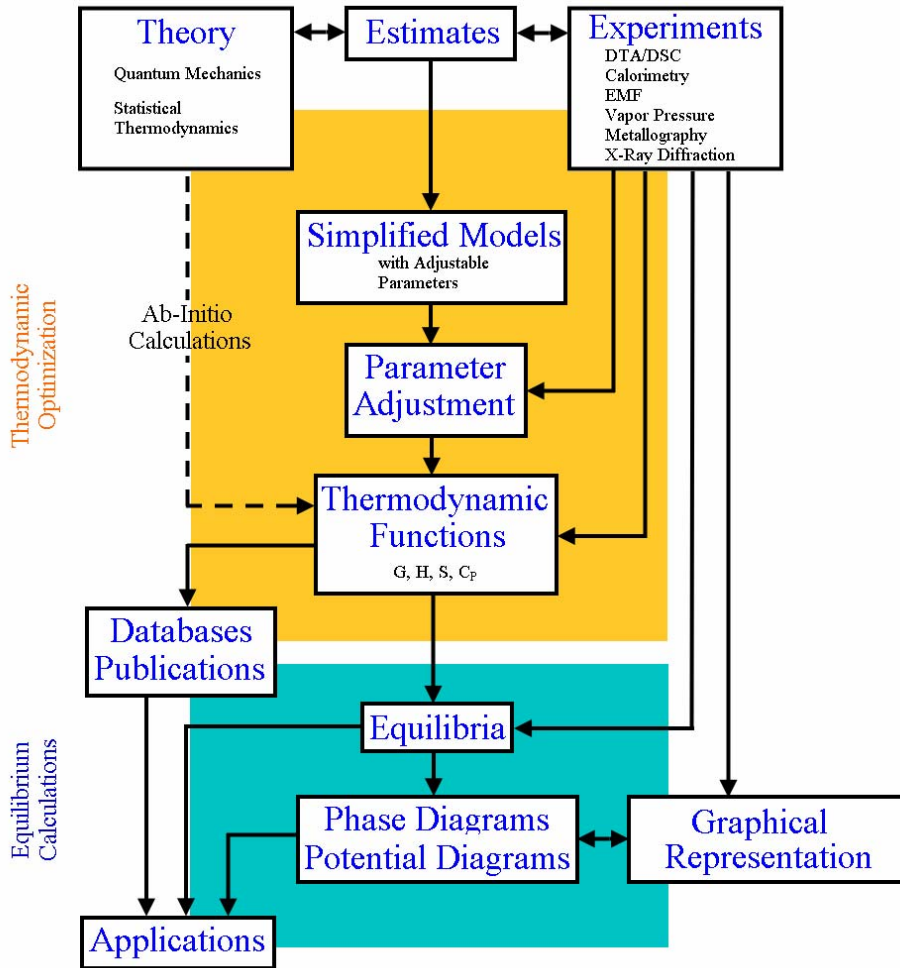


Figure 3-1. Flowchart detailing the Calculation of Phase Diagrams approach. This study is concerned mostly with the equilibrium calculations.

### 3.1.2 Databases and Software

The databases used in this particular study were the Scientific Group Thermodata Europe (SGTE) Standard Potential Database (SPOT3) obtained from the Russian Academy of Sciences (TCRAS) and other sources [162-165], as well as the SPIN4 database, developed from previous Ni-Cr-Al-O studies [6-7]. Both databases contain thermodynamic descriptions of Ni, Cr, Al, and O. However, only the SPOT3 database contained descriptions for S and its sulfide and sulfate phases. The SPOT3 database, though, only takes into account thermochemical reactions between stoichiometric compounds that allow for no solutions—a mechanical mixture—whereas

the SPIN4 database allows for solution phases. The use of mechanical mixtures to model a system has been previously published [166]. An attempt was made to append the SPIN4 database with the SPOT3 descriptions for the sulfur, sulfide, and sulfates phases.

The Gibbs' free energy minimization software used for this study is Thermo-Calc version

Q. Using this software, the desired phase or potential diagrams was obtained by:

1. Selecting the desired elements
2. Accessing the relevant thermodynamic information on each element and compound formed between each element
3. Setting conditions for each degree of freedom (eg. temperature, pressure, composition) so as to satisfy Gibbs' Phase Rule:

$$P + F = C + 2 \quad (3-1)$$

4. Computing an equilibrium using Gibbs' free energy minimization algorithms
5. Assigning one condition per axis of the desired diagram
6. Mapping from the initial computed equilibrium along each axis to determine phase stability regions.

From this method, graphical plots of phase and potential diagrams were created.

### 3.2 Materials and Sample Preparation

The materials used for the experimental aspects of this dissertation were obtained from Alfa Aesar with the purity determined by chemical analyses from the company. The metals used are

- Ni slugs: 99.98% metals basis
- Al shot: 99.999% metals basis
- Cr granules: 99.999% metals basis

These metals were measured by weight and combined into either the Ni-8Cr-6Al or Ni-22Cr-11Al alloys, which were approximately 12.5 g for Ni-8Cr-6Al and 7.5 g for the Ni-22Cr-11Al alloys. The mixtures were placed in a Centorr chilled-copper arc-melter that used a non-consumable tungsten electrode. The chamber was evacuated and backfilled with argon gas three times. Titanium getters were melted initially, followed by the mixture of interest. The melted

and solidified button was flipped and remelted four times in order to ensure homogeneity. These arc-melted buttons were then heat-treated at 1200°C for 4 hours in vacuum (better than 10<sup>-4</sup> torr) using an Elatec Technology Corporation vacuum furnace, using a He(g) quench. In addition, some of the Ni slugs as well as arc-melted Ni-13.6Al and NiAl were used in the oxidation studies. The compositions were checked by energy dispersive spectroscopy.

The specimens were then sliced using an Allied Techcut 4 diamond saw at low speeds (< 300 RPM). The slices, approximately 0.7 mm in thickness, were ground with SiC abrasive paper of 60, 180, 320, 600, 800, and 1200 grit on all sides. They were then polished on velcloth with 1 μm polycrystalline diamond suspension. The polished slices were measured using calipers to measure the various dimensions of each specimen to determine the surface area of each specimen. The surface area was approximately 1.7 to 2.8 cm<sup>2</sup>. Each polished sample was ultrasonically cleaned in acetone and then methanol for 10 minutes each. Some specimens to be characterized were etched with aqua regia for macroetching and/or equal parts HCl and ethanol for microetching.

Some specimens had a strip of Pt paint applied to one surface. This is to allow for the classic Pt-marker experiment to be conducted in which the movement of the scale/alloy interface can be measured [41].

### **3.3 Thermogravimetric Analysis**

The thermogravimetric analysis (TGA) was performed using a Setaram Setsys Evolution. Figure 3-2 shows a schematic of the TGA used for this study. The Setsys TGA works by having a balance whose deflection in either direction was measured using a laser. Each cleaned, polished specimen was placed in a silica crucible suspended by a series of quartz hooks from the balance. A counterweight is used to balance the weight. The following gas mixtures were used:

- Air
- He + 0.21 O<sub>2</sub> + 0.02 SO<sub>2</sub>
- He + 0.21 O<sub>2</sub> + 0.10 SO<sub>2</sub>

In the case of air, the gas flowed over the specimen chamber and the instrument head. In the case of the O<sub>2</sub> + SO<sub>2</sub> mixtures, ultra-high purity (4.5 Grade) He was passed through the instrumentation head and into the specimen chamber via the anti-convection tube. The O<sub>2</sub> + SO<sub>2</sub> mixture was made possible by using analog volumetric flowmeters, which were then flowed through the auxiliary gas inlet to the specimen chamber and mixed with the He. The Setsys had its own digital flow controllers, so the desired gas mixture could be established. The total gas flow used was 25 mL/min, which is the Setaram recommended flow rate for this instrument. This flow rate was selected to prevent turbulence in the furnace chamber. The flow of the He carrier gas was also greater than that of the corrosive auxiliary gas to prevent attack of the instrumentation head. The gas then passed out of the chamber through an exhaust outlet. A type S thermocouple, encased in alumina was inserted into the chamber adjacent to the specimen crucible in order to measure the temperature of the specimen.

Each sample run was performed by flowing only carrier gas (He) through the entire chamber at 200 mL/min for 10 minutes to remove most of the reacting oxygen and other species in air. The flow was then decreased to 20 mL/min to allow for the measure weight of the specimen to equilibrate for 10 minutes. The chamber, with the carrier gas still flowing, was then raised to the desired temperature for the experimental run (either 800, 900, or 975°C) at 50°C/min. Those samples not exposed to sulfidizing gases did not require a silica crucible and

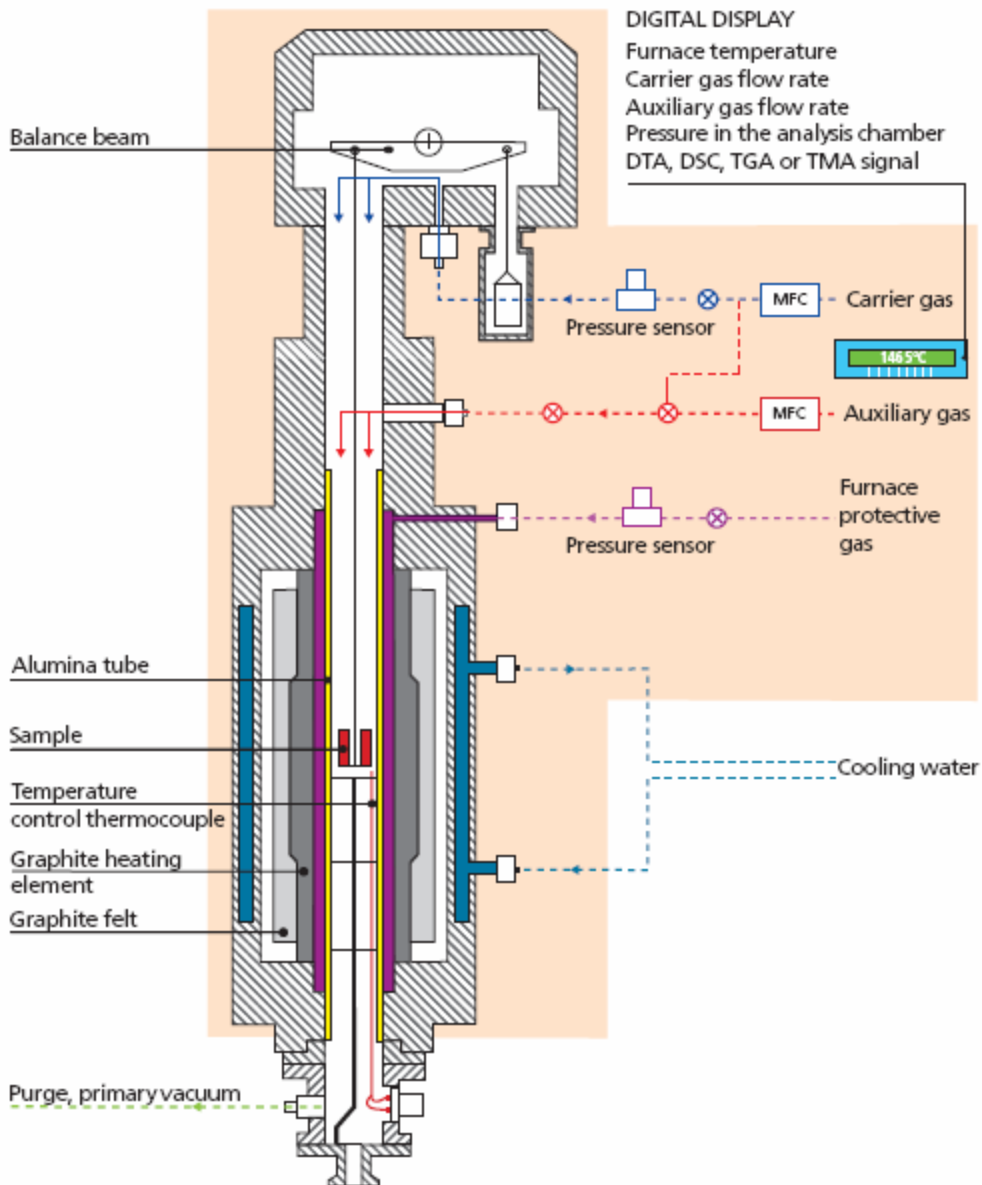


Figure 3-2. Schematic of the Setsys Evolution (TGA only).

were heated to 1000°C instead of 975°C in a Pt crucible. Upon reaching the desired temperature, the chamber was held for 2 minutes to allow the specimen to reach the temperature of the furnace, and to allow for the buoyancy of the carrier gas to equilibrate for the specimen. After this, the desired auxiliary gas was added. In the case of those specimens in air, the carrier and auxiliary gases were both switched to air. Each experiment was run this way for 100 hr. At the conclusion of the test, the auxiliary gas was shut off, and the chamber was cooled at 99°C/min.

No baseline calculations were performed since the desired measurement was a weight change at a constant temperature. In addition, some oxidation tests were carried out in a Lindberg/Blue 1200°C tube furnace to test specimens for less than 100 hr.

The data obtained from the TGA experiments were analyzed to determine the parabolic, or other rate constants, gained from the growth of oxides and/or sulfides on each specimen. In the previous publications on high temperature oxidation discussed in Chapter 2, the weight change of the specimen is normalized by dividing by the surface area exposed. This way, sample of different size and surface area can be properly compared. The specimens used in this study were made from arc-melted buttons, as described in Section 3.2. Each specimen cut from each button was elliptical in nature, and the resulting surface area being

$$A = 2\pi \cdot a \cdot b + P \cdot t \quad (3-2)$$

where A is the surface area, a is the half-length of the longer dimension, b is the half-length of the shorter dimension, t is the thickness, and P is the perimeter of the specimen as described by

$$P = 2\pi\sqrt{\frac{1}{2}(a^2 + b^2)} \quad (3-3)$$

In analyzing the growth rate constants of any oxidation study, the normalized weight change is plotted on one axis and the time on the other so that the slope of a linear regression of the experimental data is growth rate constant. If growth is occurring linearly, plotting normalized weight change over time will yield a straight line with a slope equal to  $k_L$ . In most studies of oxidation and sulfidation, normalized weight change is plotted squared against time, revealing  $k_p$ . However, a study by Pieraggi argues that this method can only be used for pure metals or simple alloys [167]. His study plots normalized weight change over the square root of time to determine the initial kinetics and differentiate that from the steady-state  $k_p$ , which is desired. This study follows Pieraggi's method. Lastly, the parabolic rate constants for each

composition and condition were plotted Arrheniusly in order to determine what, if any, activation energy could be garnered from these experiments. Table 3-1 lists the experiments for the alloys in this study.

Table 3-1. List of experimental conditions performed for oxidation of alloys for 100 hr in 1 bar of gas at 25 mL/min.

Alloy (Weight Percent)	Atmosphere (bar)	Temperature (°C)
Ni	Air	800
Ni	Air	900
Ni	Air	1000
Ni	Air	1100
Ni-13.6Al	Air	800
Ni-13.6Al	Air	900
Ni-13.6Al	Air	1000
Ni-22Cr-11Al	Air	800
Ni-22Cr-11Al	Air	900
Ni-22Cr-11Al	Air	1000
Ni-22Cr-11Al	He + 0.21 O <sub>2</sub> + 0.02 SO <sub>2</sub>	800
Ni-22Cr-11Al	He + 0.21 O <sub>2</sub> + 0.02 SO <sub>2</sub>	900
Ni-22Cr-11Al	He + 0.21 O <sub>2</sub> + 0.02 SO <sub>2</sub>	975
Ni-22Cr-11Al	He + 0.21 O <sub>2</sub> + 0.10 SO <sub>2</sub>	800
Ni-22Cr-11Al	He + 0.21 O <sub>2</sub> + 0.10 SO <sub>2</sub>	900
Ni-22Cr-11Al	He + 0.21 O <sub>2</sub> + 0.10 SO <sub>2</sub>	975
Ni-31Al	Air	800
Ni-31Al	Air	900
Ni-31Al	Air	1000
Ni-8Cr-6Al	Air	800
Ni-8Cr-6Al	Air	900
Ni-8Cr-6Al	Air	1000
Ni-8Cr-6Al	He + 0.21 O <sub>2</sub> + 0.02 SO <sub>2</sub>	800
Ni-8Cr-6Al	He + 0.21 O <sub>2</sub> + 0.02 SO <sub>2</sub>	900
Ni-8Cr-6Al	He + 0.21 O <sub>2</sub> + 0.02 SO <sub>2</sub>	975
Ni-8Cr-6Al	He + 0.21 O <sub>2</sub> + 0.10 SO <sub>2</sub>	800
Ni-8Cr-6Al	He + 0.21 O <sub>2</sub> + 0.10 SO <sub>2</sub>	900
Ni-8Cr-6Al	He + 0.21 O <sub>2</sub> + 0.10 SO <sub>2</sub>	975

### 3.4 Characterization

This section details the methods and procedures of materials characterization for each specimen. Data obtained from these various techniques was used to identify the microstructures formed from and mechanisms of oxidation and sulfidation on these alloys.

### **3.4.1 X-Ray Diffraction**

Each polished and oxidized specimen was analyzed using X-Ray diffraction (XRD). The specimens were adhered to a glass slide using double-sided tape and placed in a Philips APD 3720 XRD. The specimens were exposed from 10 to 90° 2 $\theta$  at a rate of 0.5 s per step using 40 kV and 20 mA from a Cu K $\alpha$  radiation source. The patterns were then treated according to the software protocol of the APD 3720 to determine the d-spacings detected. These were then compared to the files from the JCPDS International Center for Diffraction database to determine the phases diffracting at those 2 $\theta$  angles.

### **3.4.2 Scanning Electron Microscopy**

After XRD, the specimens were then analyzed using Scanning Electron Microscopy (SEM). First, each sample, whether oxidized or not, was affixed onto an aluminum mount using a small amount of carbon paint and analyzed from the top of the surface. The SEM used was a JEOL SEM 6400 equipped with Oxford Link ISIS energy dispersive spectroscopy (EDS) and Oxford OPAL electron backscattered secondary electron detector (EBSD), operated at 15 kV. Semi-quantitative analysis was performed using correction matrices for atomic number, absorption, and fluorescence (ZAF) [166]. The grain size of the substrate materials was determined by using line-intercept stereology methods from optical light micrographs taken from a Leco Neophot 21 optical microscope.

After this analysis, the specimens were viewed in cross-section. This was performed applying an electroless Ni layer between 1 and 5  $\mu\text{m}$  thick using Buehler Edgemet chemical system for scale adhesion and edge retention. Next, the specimens were held upright using stainless steel clips, cast into an epoxy mixture, and allowed to cure overnight at room temperature. These epoxy-mounted specimens were then sectioned using the Allied TechCut 4

and ground using 600, 800, and 1200 grit SiC abrasive paper on the Allied MetPrep3 with an AP-3 autopolisher. They were then polished using 3  $\mu\text{m}$  diamond suspension on nylon, 1  $\mu\text{m}$  diamond suspension on velcloth, and 0.1  $\mu\text{m}$  diamond suspension on Chem-Pol B cloth. Lastly, the specimens were thermally carbon coated in order to make the surface electrically conductive, and were analyzed on the SEM.

### **3.4.3 Electron Microprobe**

Some of the cross-sectioned epoxy-mounted specimens were analyzed using wavelength dispersive spectroscopy (WDS) in a JEOL Superprobe 733 electron microprobe (EPMA). These were performed using a 1  $\mu\text{m}$  size beam at approximately 1 nA that was scanned at various intervals (usually 1  $\mu\text{m}$ ) to detect the change in composition, not only from phase to phase, but across the scale and alloy depletion zones. The compositions were calculated using the ZAF correction technique also used for EDS.

The activities of the elements from each of the line scan were calculated from the Thermo-Calc software using the appended SPIN4 database with S descriptions. This was performed by entering the microprobe data from each point of a line scan into the software at the temperature the sample was oxidized and computing an equilibrium to determine the equilibrium activities at each probe.

## CHAPTER 4 THERMODYNAMIC CALCULATION RESULTS

This section shows the diagrams created using the Thermo-Calc software. This chapter is divided into three sections that detail the development of various phase diagrams of the Ni-Cr-Al system, the temperature-potential diagrams, and potential diagrams at fixed temperatures and pressures. Phase fraction diagrams are also included throughout the chapter to give a better visual understanding of mechanisms and reactions occurring.

### **4.1 Calculations of Ni-Cr-Al Alloys and Mixtures using Phase Diagrams**

#### **4.1.1 Binary Systems**

Before attempting to analyze the more complex systems, it is important to validate the simpler binary systems that will be the basis for later calculations. Using the SPIN4 database, the Ni-Al, Ni-Cr, and Al-Cr binaries were calculated as shown in Figures 4-1, 4-2, and 4-3, respectively. The green lines represent various tie lines of two-phase equilibria. These diagrams agree with those found in the ASM Handbooks as seen in Figures 2-3, 2-4, and 2-5 for Al-Ni, Cr-Ni, and Al-Cr, respectively [30]. Differences include some of the solubility ranges for several phases including the Al-Cr diagram, where all the intermetallic phases are stoichiometric compounds with no solubility, unlike in Figure 2-5. It should be noted that the  $\text{Al}_{13}\text{Cr}_2$  and  $\text{Al}_{11}\text{Cr}_2$  intermetallics in Figure 4-3 are the same as  $\text{Al}_7\text{Cr}$  and  $\text{Al}_5\text{Cr}$ , respectively, in Figure 2-5. It should also be noted that the Ni-Al diagram calculated in Figure 4-4 was done without the low-temperature  $\text{Ni}_3\text{Al}_5$  phase. In Figure 4-4, this is restored. However, its position differs from that of Figure 2-3. Since this phase is only stable at temperatures lower than the experiments to be performed in this study, and since it is rarely discussed in literature, it will not be used for further calculations. Lastly, the SPOT3 database was not used to describe these binaries since each phase has no solubility for other elements, the liquids of each element are immiscible, and

the diagrams merely show a series of lines. However, the SPOT3 potential database contains information on the solid-gas reactions that will be elaborated upon in Sections 4.2 and 4.3.

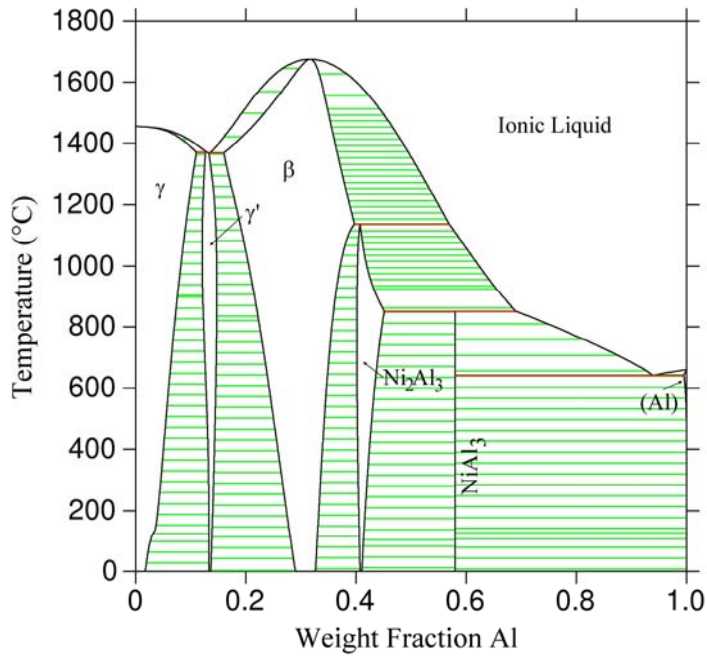


Figure 4-1. Temperature-composition binary phase diagram of the Ni-Al system calculated from the SPIN4 database.

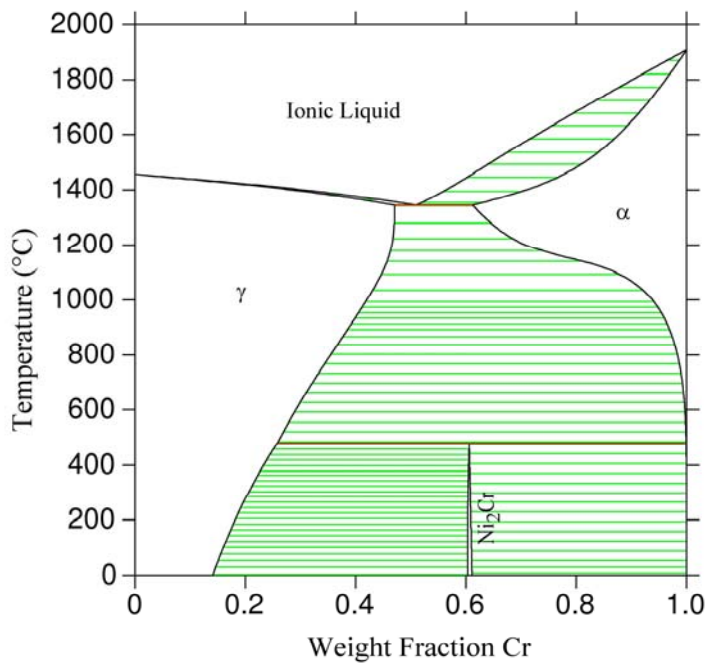


Figure 4-2. Temperature-composition binary phase diagram of the Ni-Cr system calculated from the SPIN4 database.

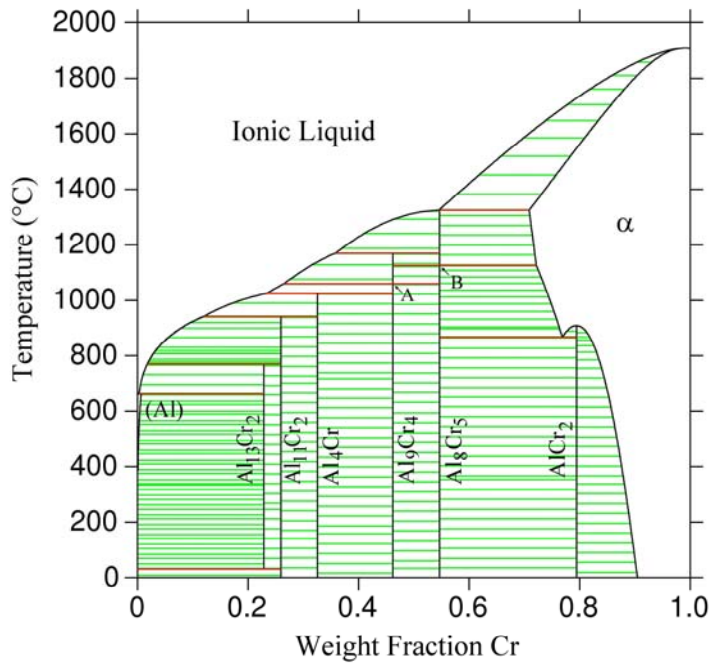


Figure 4-3. Temperature-composition binary phase diagram of the Al-Cr system calculated from the SPIN4 database.

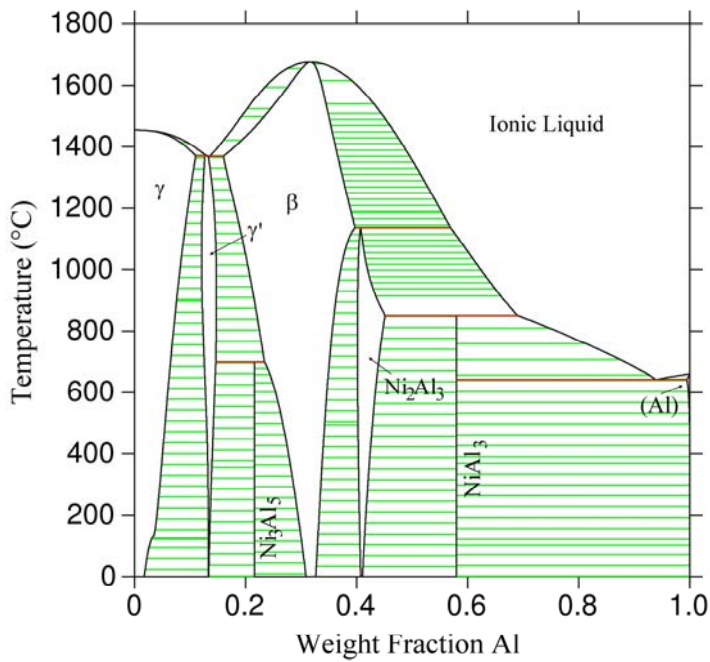


Figure 4-4. Temperature-composition binary phase diagram of the Ni-Al system calculated from the SPIN4 database with the  $\text{Ni}_3\text{Al}_5$  low-temperature phase restored.

### 4.1.2 Ternary Systems

The ternary phase diagrams were calculated using the thermodynamic data in the SPIN4 database. Figure 4-5 shows the complete Ni-Cr-Al ternary isothermal section for 900°C, where the weight percents of the Cr and Al elements are plotted. This can be compared to the ternary calculated by Dupin in Figures 2-9 and 2-8 with that calculated in Figure 4-6, which is in mole percent at 850°C and in Figure 4-7 in weight percent at 1025°C. The fields of stability are often different in size and shape in comparing the isotherms, and Figure 4-7 is more complete in showing the Al rich regions of the phase diagram.

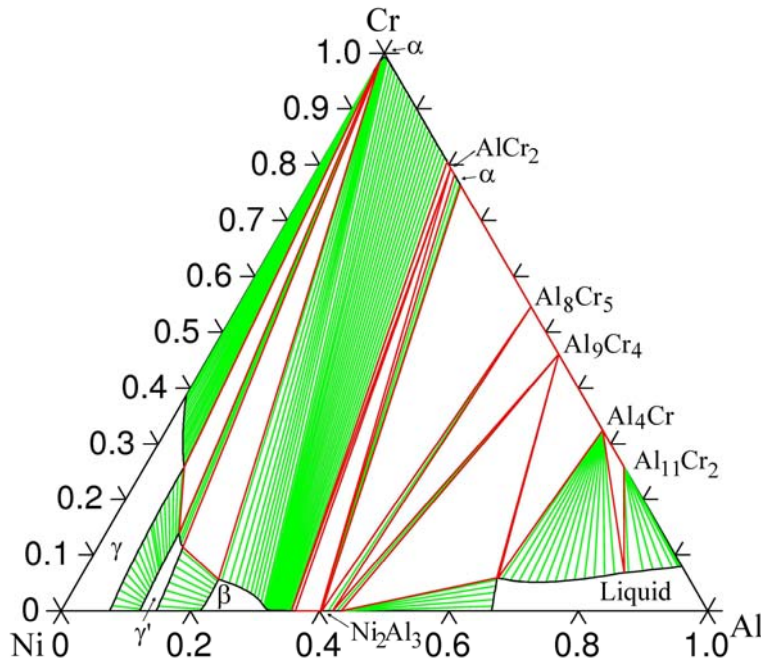


Figure 4-5. Isothermal section of Ni-Cr-Al ternary system at 900°C in weight fractions. This diagram is calculated from data in the SPIN4 database.

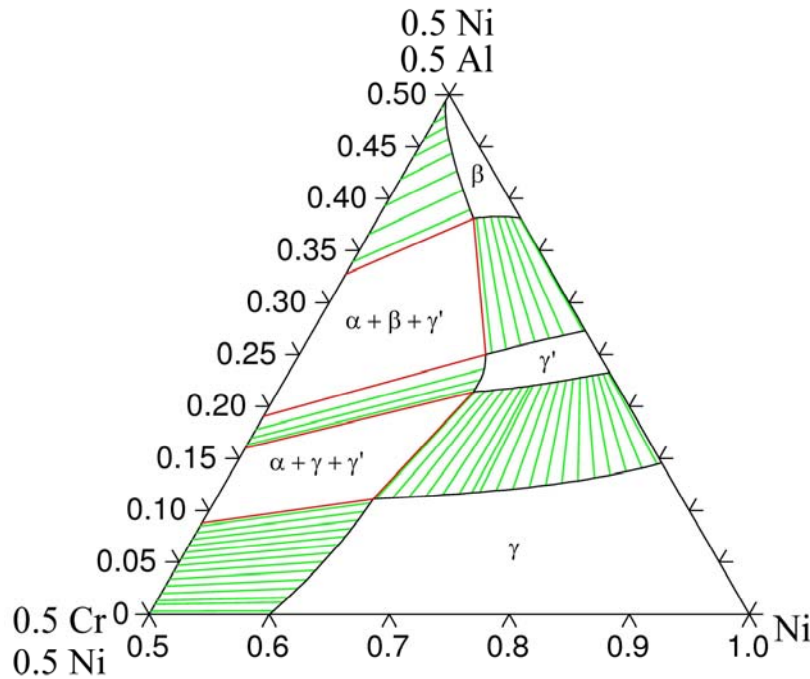


Figure 4-6. Partial isothermal section of Ni-Cr-Al ternary system at 850°C in mole fractions. The axes are chosen to compare with Figure 2-9. This diagram is calculated from data in the SPIN4 database.

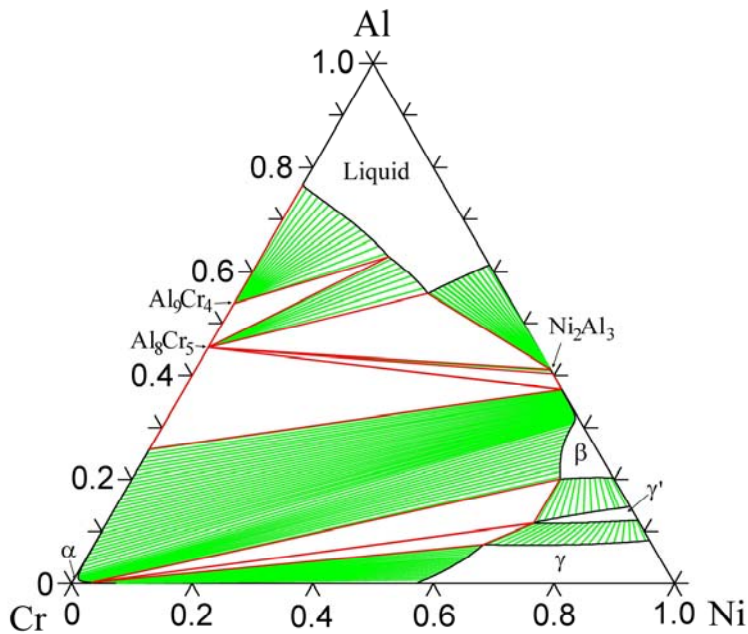


Figure 4-7. Isothermal section of Ni-Cr-Al ternary system at 1025°C in mole fractions. The axes are chosen to compare with Figure 2-8. This diagram is calculated from data in the SPIN4 database.

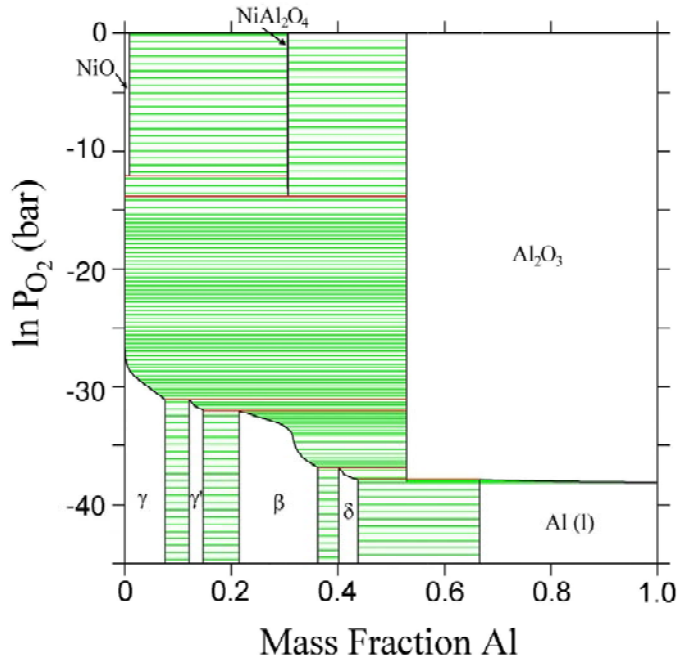


Figure 4-8. Ternary isothermal section of the Ni-Al-O<sub>2</sub> system at 900°C. The x-axis is the composition of Al in weight percent, and the y-axis is the logarithmic partial pressure of O<sub>2</sub> in bar. This diagram is calculated from data in the SPIN4 database.

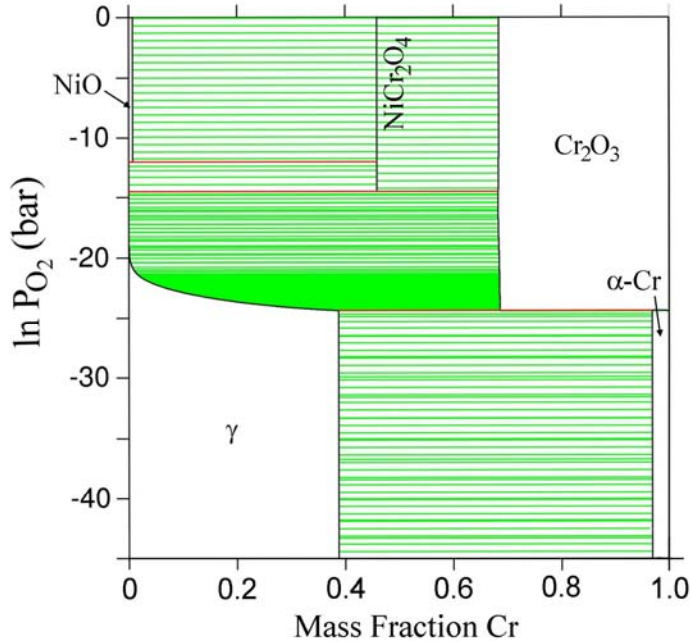


Figure 4-9. Ternary isothermal section of the Ni-Cr-O<sub>2</sub> system at 900°C. The x-axis is the composition of Cr in weight percent, and the y-axis is the logarithmic partial pressure of O<sub>2</sub> in bar. This diagram is calculated from data in the SPIN4 database.



## 4.2. Calculations of Temperature-Potential Diagrams

Calculations were performed using the SPOT3 database to develop diagrams that would show the reactions occurring with change in temperature and the chemical potential (or activity). These and all further diagrams show axes labeled as the partial pressure of a certain gas, in bar. This is found by converting either the natural log of activity or chemical potential into units of  $\log_{10}$  bar by

$$P_x = \frac{\ln(a_x)}{\ln 10} \quad (4-1)$$

$$P_x = \frac{\mu(X)}{R \cdot T \cdot \ln(10)} \quad (4-2)$$

where  $a$  is the activity of a certain gas species  $X$ ,  $P$  is the partial pressure of the gas species,  $\mu(X)$  is the chemical potential of a gas species (in J/mol),  $R$  is the gas constant of 8.314 J/mol K, and  $T$  is the temperature in K.

### 4.2.1 Calculations with O<sub>2</sub>-SO<sub>2</sub> Interactions

For the physical experiments used in this study, the reacting gases used were air, oxygen (O<sub>2</sub>) and sulfur dioxide (SO<sub>2</sub>). These results are discussed in Chapter 5, but in this section are dealt with by thermodynamic calculations. As discussed in Chapter 2, an environment mixing O<sub>2</sub> and SO<sub>2</sub> will cause a reaction that can create sulfur trioxide (SO<sub>3</sub>) and other products. Using the conditions for the experiments

1. He + 0.21 O<sub>2</sub> + 0.02 SO<sub>2</sub>
2. He + 0.21 O<sub>2</sub> + 0.10 SO<sub>2</sub>

calculations were performed to determine how the gases react with change in temperature. The calculations for condition 1 are shown in Figure 4-11, and condition 2 are shown in Figure 4-12. These are shown in a similar manner to CO<sub>2</sub>/CO diagrams illustrating isobars of O<sub>2</sub> [167]. With both diagrams, at temperatures below approximately 600°C, the reaction



occurs readily and  $\text{SO}_3$  is the more stable sulfur-based gas species. However, it is of much less consequence above  $900^\circ\text{C}$ . Between the two temperatures, the stability of  $\text{SO}_2$  and  $\text{SO}_3$  change rapidly with a major vapor transition point occurring at  $707^\circ\text{C}$ . He is used in the calculations as “filler” so that the total number of moles can remain constant at unity. However, due to scale its partial pressure is omitted.

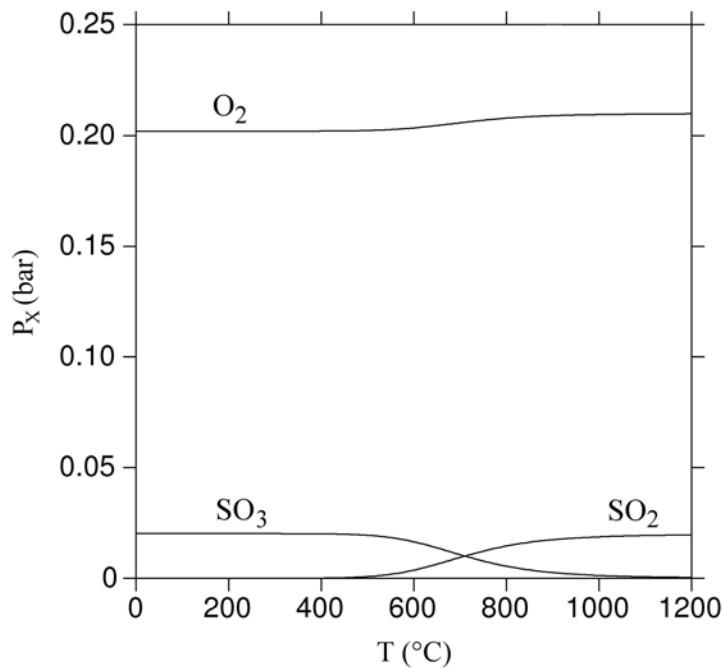


Figure 4-11. Change in partial pressure of  $\text{O}_2$ ,  $\text{SO}_2$ , and  $\text{SO}_3$  (in bar) with temperature using the initial gas mixture of  $\text{He} + 0.21 \text{O}_2 + 0.02 \text{SO}_2$ . The  $P_{\text{He}}$  is omitted due to scale. The data used for calculations is taken from the SPOT3 database.

As well as these calculations, diagrams were calculated of isobaric lines of one gas in relation to a ratio of the partial pressures of two other gases with changing temperature. For example, Figure 4-13 shows lines of constant partial pressure of sulfur trioxide based of the ratio of partial pressure of oxygen over sulfur dioxide. The region labeled as “unstable gas,” occurring at high  $\text{SO}_2$  and low  $\text{O}_2$  at higher temperatures, could not be calculated due to the

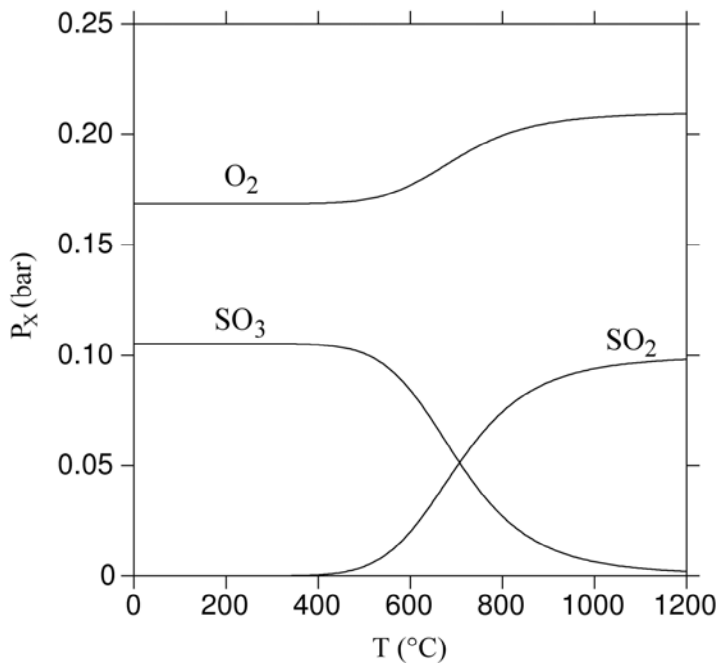


Figure 4-12. Change in partial pressure of  $O_2$ ,  $SO_2$ , and  $SO_3$  (in bar) with temperature using the initial gas mixture of  $He + 0.21 O_2 + 0.10 SO_2$ . The  $P_{He}$  is omitted due to scale. The data used for calculations is taken from the SPOT3 database.

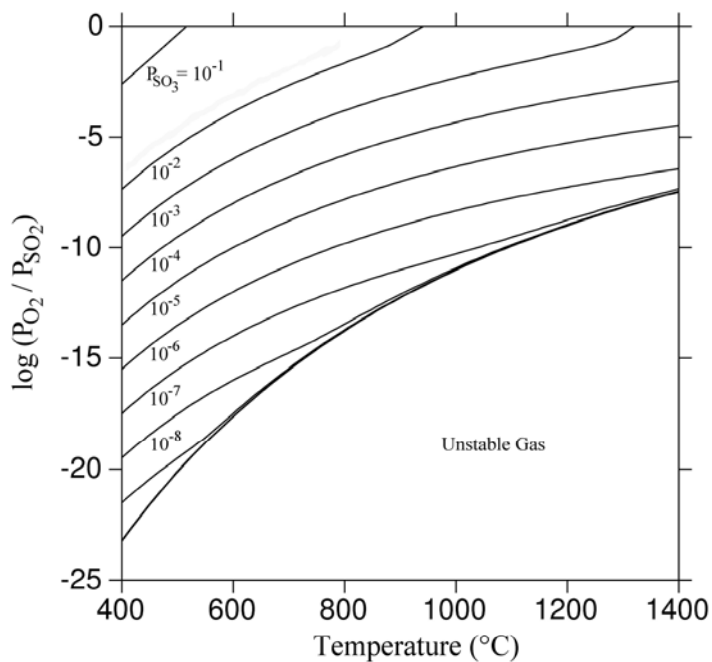


Figure 4-13. The relationship between the partial pressure of  $SO_3$  in an  $O_2$ - $SO_2$  gas mixture, with varying temperature. All partial pressures are in bar.

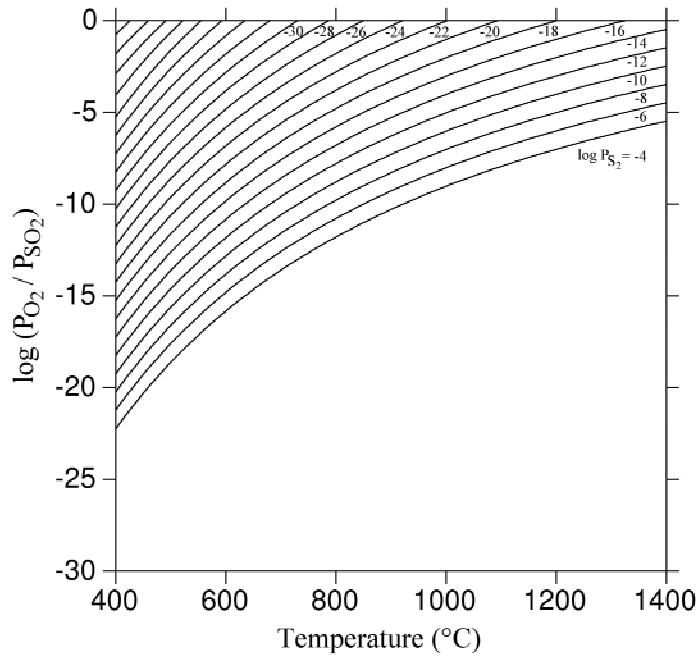


Figure 4-14. The relationship between the partial pressure of S<sub>2</sub> in an O<sub>2</sub>-SO<sub>2</sub> gas mixture, with varying temperature. All partial pressures are in bar.

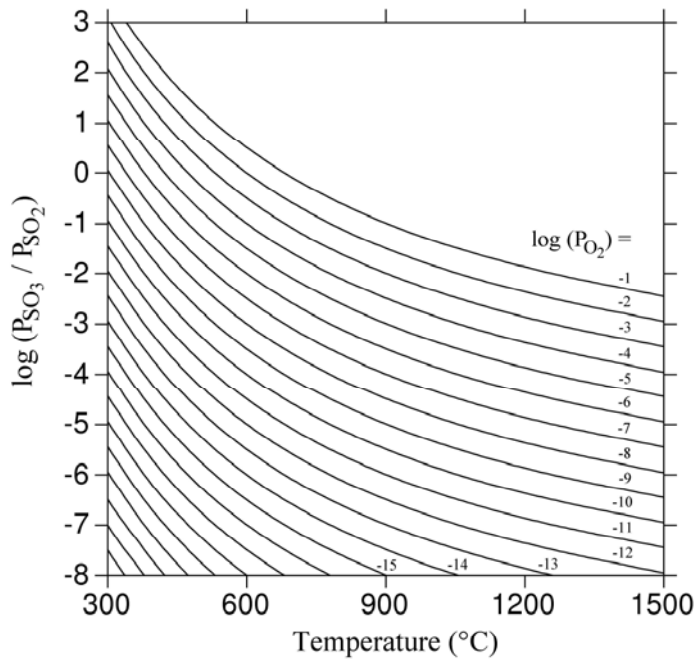


Figure 4-15. The relationship between the partial pressure of O<sub>2</sub> in an SO<sub>3</sub>-SO<sub>2</sub> gas mixture, with varying temperature. All partial pressures are in bar.

evolution of more than three phases in equilibrium. In CO/CO<sub>2</sub>/O<sub>2</sub> systems, this corresponds with the deposition of graphite [157]. Here, it may correspond with the deposition of liquid sulfur, but this could not be calculated and was not confirmed by any experiments. This is continued in Figures 4-14 and 4-15, which show the isobars of S<sub>2</sub> and O<sub>2</sub> based on ratios of O<sub>2</sub>/SO<sub>2</sub> and SO<sub>3</sub>/SO<sub>2</sub>, respectively.

#### 4.2.2 Calculations of Metal-Gas Interactions

Thermodynamic equilibria were calculated for several metal mechanical mixtures (meant to represent specific phases or alloys) between 800 and 1000°C by fixing the number of conditions so that the degrees of freedom were zero. Then, a range of activities or chemical potentials of the components O<sub>2</sub> and SO<sub>2</sub> were defined, and the diagrams were mapped in that range. The diagrams are plotted at various temperatures using the partial pressures of either O<sub>2</sub> and SO<sub>2</sub>, or O<sub>2</sub> and S<sub>2</sub>, which can be defined from their activities or chemical potentials, as axes.

The mixtures for which calculations were performed are:

- Ni
- Ni<sub>3</sub>Al (γ')
- NiAl (β)
- Ni-8Cr-6Al
- Ni-22Cr-11Al

Since no solubility in the solid state is described per the SPOT3 database, the equilibria calculated were compared to a proprietary database that allows for solubility, SPIN4. This database was not accessed for this study because it has no description for S. However, in using a Ni-Cr-Al-O system, the calculated equilibria are in good agreement between the two databases and are shown in Table 4-1.

Figure 4-16 shows the temperature-potential diagram of Ni in an environment with only oxygen and some inert gas. Here, one can see that at higher partial pressures of O<sub>2</sub>, NiO becomes more stable than Ni. However, this oxide stability decreases with increasing

Table 4-1. Comparison of equilibria computed between two databases SPOT3 and SPIN4 at a pressure of 1 bar and  $T = 1073$  K for Ni-22Cr-11Al alloy (by mass) with a  $P_{O_2}$  of 0.22 bar. This table compares number of moles of each phase, along with the composition (in weight fraction) of each phase.

Database	Phases	Moles	W(Ni)	W(Cr)	W(Al)	W(O <sub>2</sub> )
SPOT3	NiO	0.134	0.786	0	0	0.214
	NiAl <sub>2</sub> O <sub>4</sub>	0.424	0.332	0	0.305	0.362
	NiCr <sub>2</sub> O <sub>4</sub>	0.441	0.259	0.459	0	0.362
SPIN4	Halite (NiO)	0.138	0.777	9.87e-4	4.75e-3	0.217
	Spin3 Ni[Cr,Al] <sub>2</sub> O <sub>4</sub> )	0.862	0.290	0.263	0.131	0.216

temperature. Figures 4-17 and 4-18 show the same conditions as that for 4.16, except for the addition of 2 mol % SO<sub>2</sub> and 10 mol % SO<sub>2</sub>, respectively. It is plain to see that the stability of the Ni and the nickel oxide decrease dramatically with even small sulfur dioxide additions. At higher partial pressures of oxygen at lower temperatures, the nickel sulfate becomes stable, and at lower oxygen partial pressures, the nickel sulfides become stable—Ni<sub>3</sub>S<sub>2</sub> is the most stable, but NiS, Ni<sub>3</sub>S<sub>4</sub>, and NiS<sub>2</sub> can also be present. The areas labeled “unstable equilibrium” are areas where the software could not calculate, and therefore not map, a stable equilibrium. This is likely due to the evolution of some gas, which creates too many phases to calculate a stable equilibrium. These conditions are mostly observed at high  $P_{O_2}$  at low temperatures, or high  $P_{SO_2}$  at high temperatures. Diagrams for mixtures of Ni, O<sub>2</sub>, and other metals (Al and/or Cr) were not able to be calculated and are not shown.

### 4.3 Calculations of Potential Diagrams

The results for the calculations of Ni in SO<sub>2</sub>/O<sub>2</sub> environments at 800, 900, and 1000°C are shown in Figures 4-19a, 4-20, and 4-21, respectively. Figure 4-19b also shows the S<sub>2</sub>-O<sub>2</sub> potential diagram for Ni at 800°C for comparison with Figure 4-19a. As with section 4.2, all calculations were performed using data from the SPOT3 database unless otherwise noted. At high  $P_{O_2}$  and low  $P_{SO_2}$ , the NiO becomes stable from the oxidation of Ni. Increasing SO<sub>2</sub> can cause the

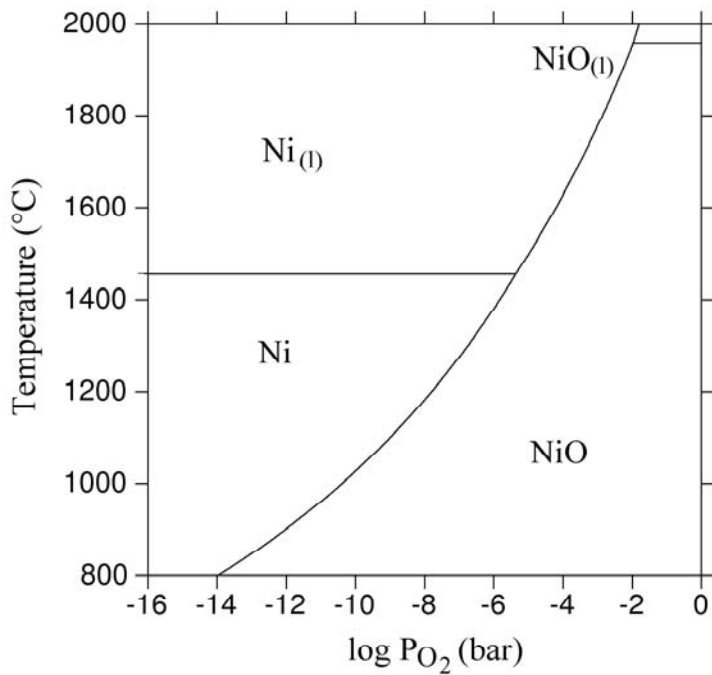


Figure 4-16. Stability diagram of Ni and its oxide with varying temperature and partial pressure of oxygen (in bar).

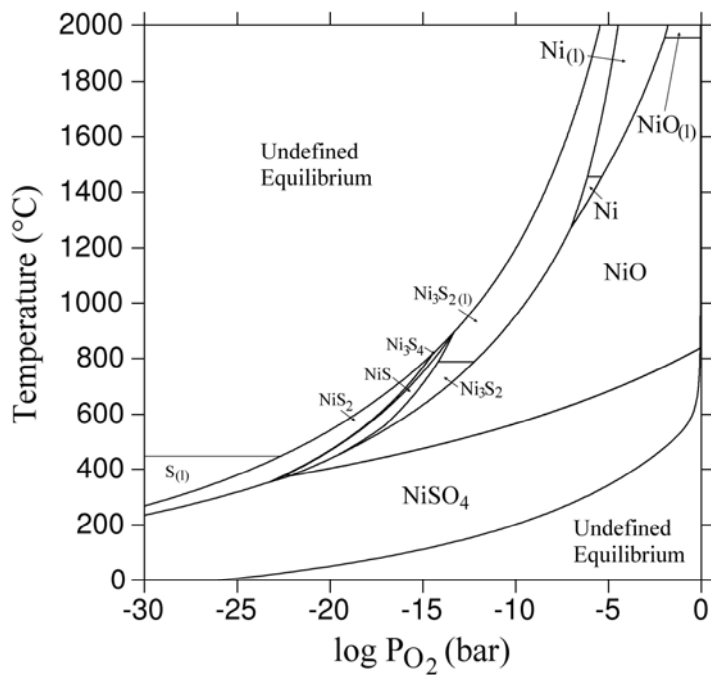


Figure 4-17. Stability diagram of Ni and its oxide with varying temperature and partial pressure of oxygen (in bar) with a constant partial pressure of sulfur dioxide at 2 mol %.

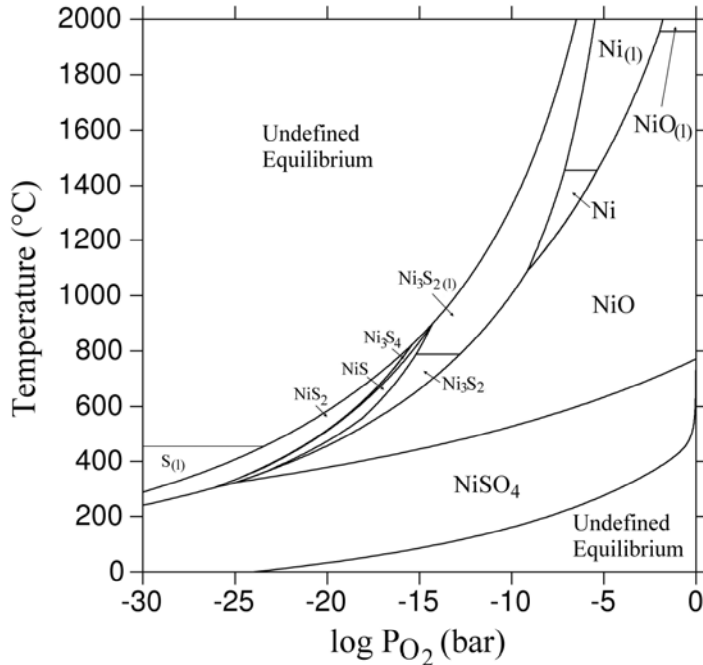


Figure 4-18. Stability diagram of Ni and its oxide with varying temperature and partial pressure of oxygen (in bar) with a constant partial pressure of sulfur dioxide at 10 mol %.

formation of NiSO<sub>4</sub>. Decreasing O<sub>2</sub> at higher SO<sub>2</sub> contents cause the formation of Ni sulfides—Ni<sub>3</sub>S<sub>2</sub>, NiS, Ni<sub>3</sub>S<sub>4</sub>, and NiS<sub>2</sub> at increasing P<sub>SO<sub>2</sub></sub>. The Ni<sub>3</sub>S<sub>2</sub> is a liquid at these temperatures. At high P<sub>SO<sub>2</sub></sub> and high or low P<sub>O<sub>2</sub></sub>, no stable equilibrium could be calculated. It is possible that this is a gas phase, which at low P<sub>O<sub>2</sub></sub> is almost entirely SO<sub>2</sub>, whereas the gas at high P<sub>O<sub>2</sub></sub> is a mixture of SO<sub>2</sub>, O<sub>2</sub>, and SO<sub>3</sub> (see Table 4-2). As temperature is increased, the resistance of Ni to oxidize decreases, but attack by sulfur species is more prevalent.

Table 4-2. Comparison of gas species (at mole fractions > 10<sup>-10</sup>) present in the unstable equilibrium regions of Figure 4-19 at low P<sub>O<sub>2</sub></sub> and high P<sub>O<sub>2</sub></sub>. These mole fractions are calculated based on ideal gas behavior.

Gas Species (low P <sub>O<sub>2</sub></sub> )	Mole Fraction	Gas Species (High P <sub>O<sub>2</sub></sub> )	Mole Fraction
SO <sub>2</sub>	0.999	SO <sub>2</sub>	0.356
SO	4.59e-6	O <sub>2</sub>	0.356
SO <sub>3</sub>	4.14e-6	SO <sub>3</sub>	0.288
S <sub>2</sub> O	8.92e-7		
S <sub>2</sub>	3.84e-7		

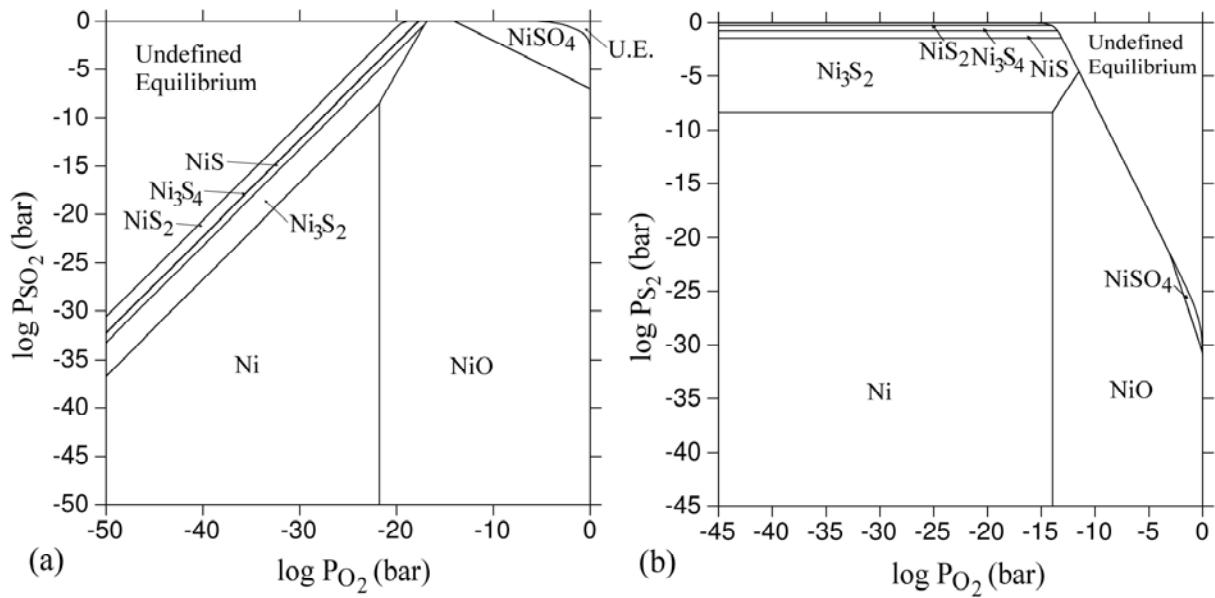


Figure 4-19. Ni potential diagrams for (a) SO<sub>2</sub>-O<sub>2</sub> and (b) S<sub>2</sub>-O<sub>2</sub> at 800°C. U.E. is an abbreviation for undefined equilibrium. Published in [170].

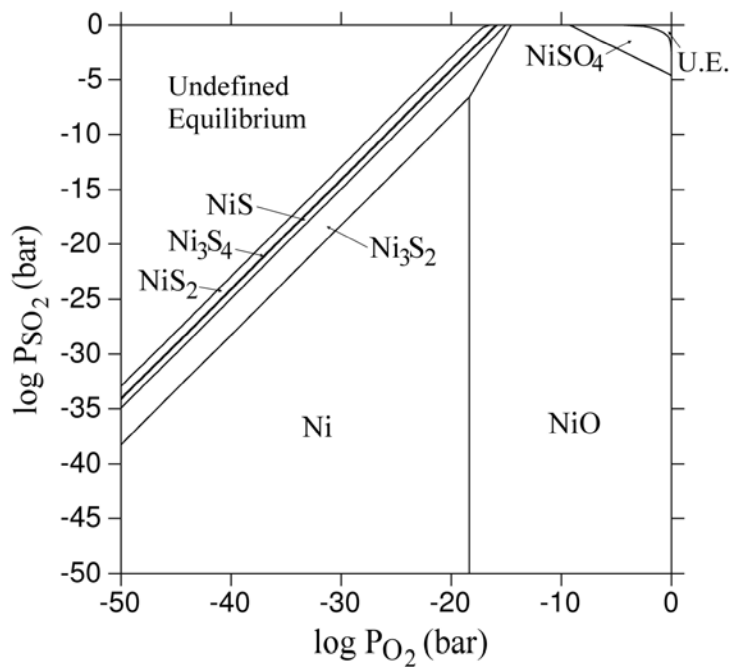


Figure 4-20. Ni SO<sub>2</sub>-O<sub>2</sub> potential diagram at 900°C. U.E. is an abbreviation for undefined equilibrium. Published in [170].

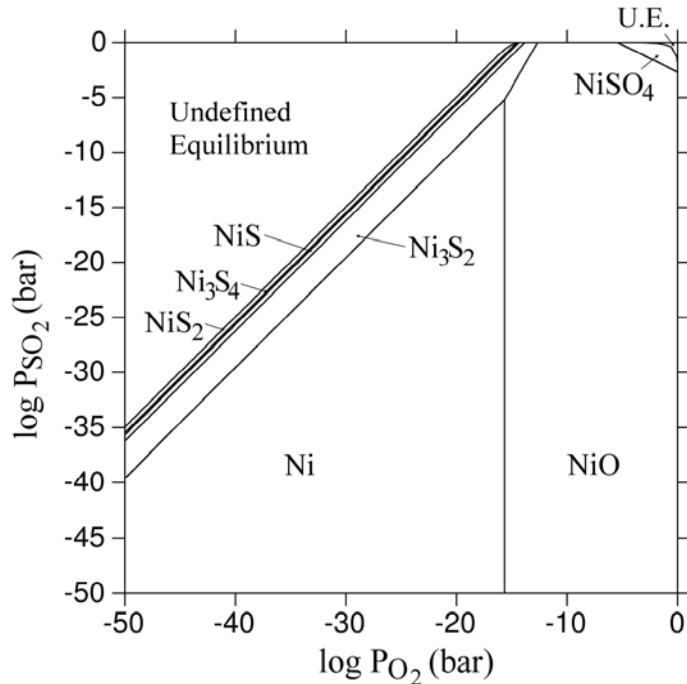


Figure 4-21. Ni SO<sub>2</sub>-O<sub>2</sub> potential diagram at 1000°C. U.E. is an abbreviation for undefined equilibrium. Published in [170].

Figures 4-22a, 4-23, and 4-24 show the SO<sub>2</sub>-O<sub>2</sub> potential diagrams for Al at 800, 900, and 1000°C, respectively. Figures 4-25a, 4-26, and 4-27 show the SO<sub>2</sub>-O<sub>2</sub> potential diagrams for Cr at the same respective temperatures. Figures 4-22b and 4-25b show the S<sub>2</sub>-O<sub>2</sub> potential diagrams for Al and Cr, respectively. Comparing these diagrams with those for Ni, one can tell that Cr and especially Al have greater affinities for O<sub>2</sub> as they will oxidize at a lower P<sub>O<sub>2</sub></sub> than Ni. In addition, Al and Cr will also sulfidize at lower S activities, and these sulfides will oxidize at lower P<sub>O<sub>2</sub></sub>. Al and Cr were calculated as having only one sulfidation product each, as opposed to the four exhibited by Ni at these temperatures. Figures 4-28, 4-29, and 4-30 show calculations of Ni<sub>3</sub>Al, or γ', at 800, 900, and 1000°C, respectively. Due to the Gibbs' Phase Rule (Equation 3-1), each phase field contains two phases. At low partial pressures of both gases, the γ' phase was calculated and, to satisfy the phase rule, Al is in equilibrium as excess in the intermetallic. In this system, Al is the more reactive element, and reacts with S and/or O at lower partial

pressures. In all cases, the  $\text{Al}_2\text{O}_3$  phase is  $\alpha$ . Increasing the  $\text{O}_2$  eventually depletes the  $\gamma'$  phase of Al, causing it to form the  $\gamma$  (Ni) phase. Further increasing  $P_{\text{O}_2}$  causes the alumina to react with the  $\gamma$  to form a spinel phase ( $\text{NiAl}_2\text{O}_4$ ). Al forms only an  $\text{Al}_2\text{S}_3$  sulfide, and similar to what is shown in Figures 4-19-4-21, the Ni forms a variety of sulfides depending on the  $P_{\text{SO}_2}$ . At 900 and 1000°C, the  $\text{Ni}_3\text{S}_2$  becomes the most stable sulfide, as the others become degenerate cases. Figures 4-31, 4-32, and 4-33 show calculations of NiAl, or  $\beta$ , at 800, 900, and 1000°C, respectively. These diagrams are similar to those for  $\text{Ni}_3\text{Al}$ , except that  $\beta$  is the stable phase, and that there is enough Al present to keep  $\text{Al}_2\text{O}_3$  stable up to 1 bar  $P_{\text{O}_2}$ . Also, the  $\gamma'$  phase was shown to have a larger stability range than  $\beta$ .

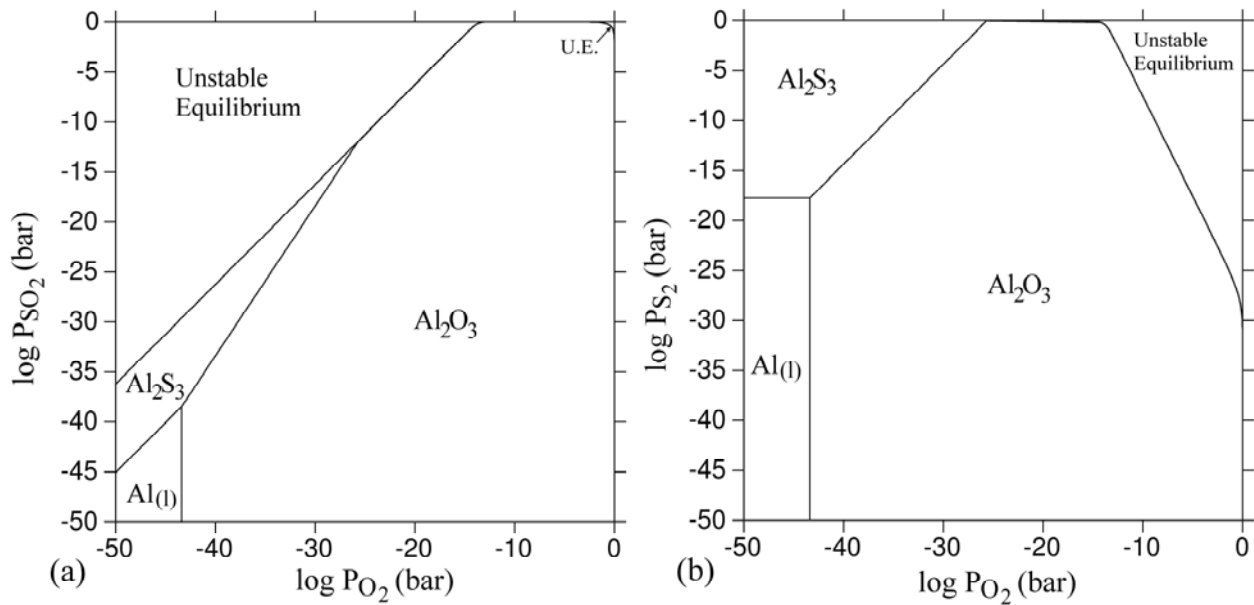


Figure 4-22. Al potential diagrams for (a)  $\text{SO}_2$ - $\text{O}_2$  and (b)  $\text{S}_2$ - $\text{O}_2$  at 800°C. Published in [170].

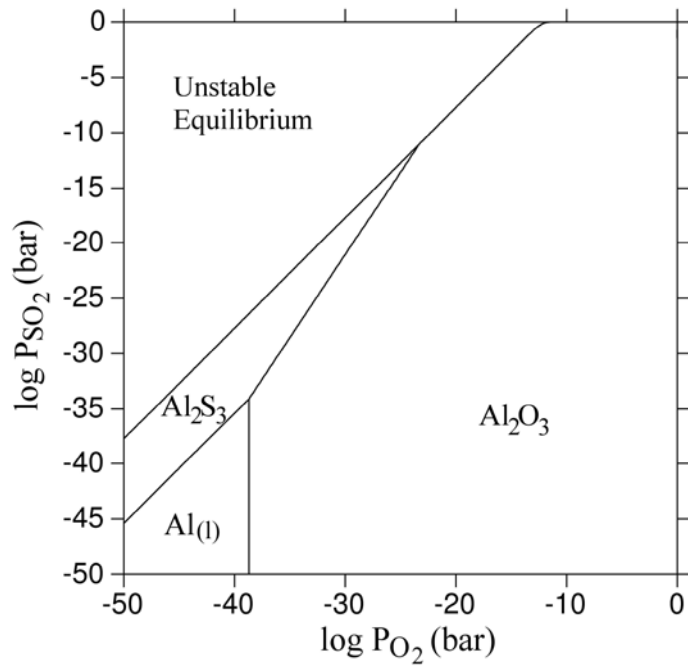


Figure 4-23. Al-SO<sub>2</sub>-O<sub>2</sub> potential diagram at 900°C.

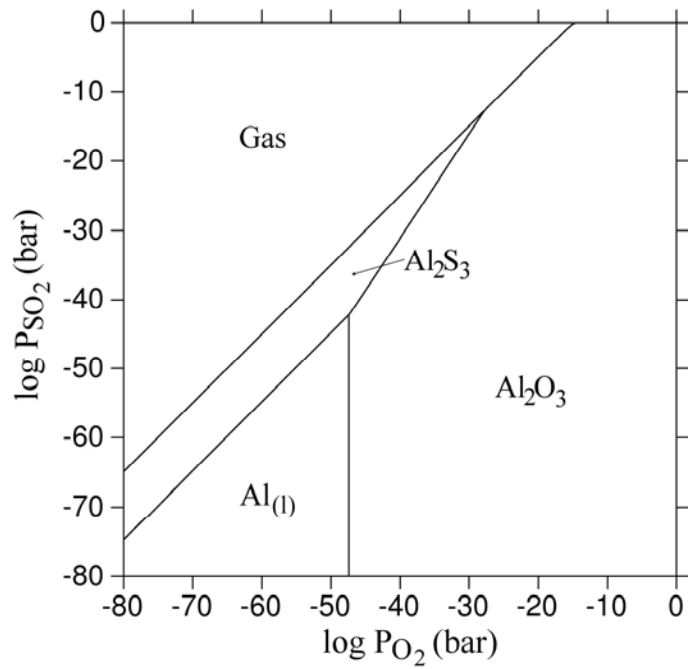


Figure 4-24. Al-SO<sub>2</sub>-O<sub>2</sub> potential diagram at 1000°C.

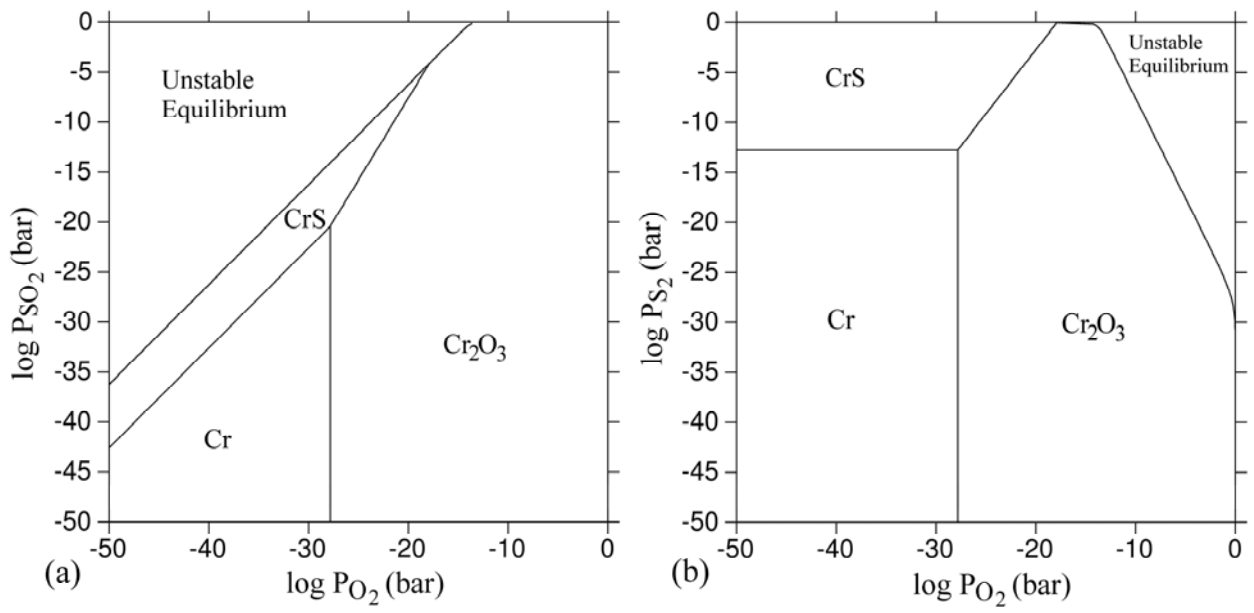


Figure 4-25. Cr potential diagrams for (a)  $SO_2-O_2$  and (b)  $S_2-O_2$  at 800°C. Published in [170].

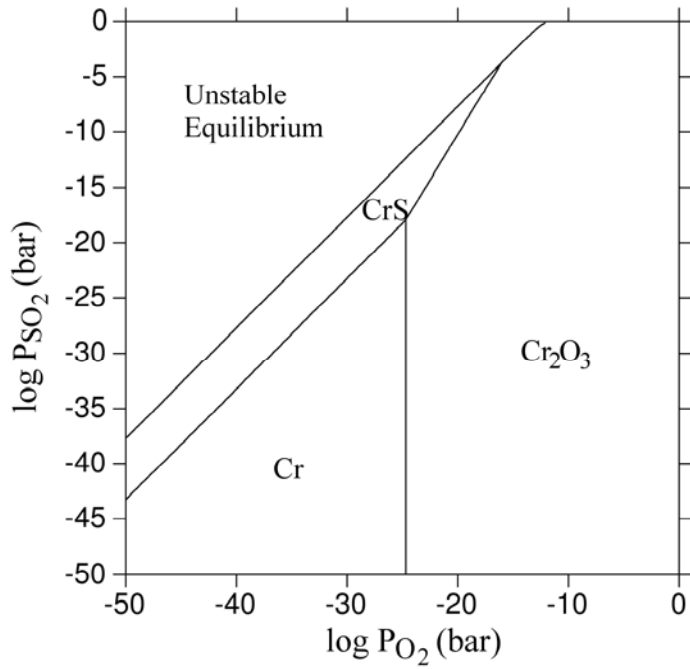


Figure 4-26. Cr  $SO_2-O_2$  potential diagram at 900°C.



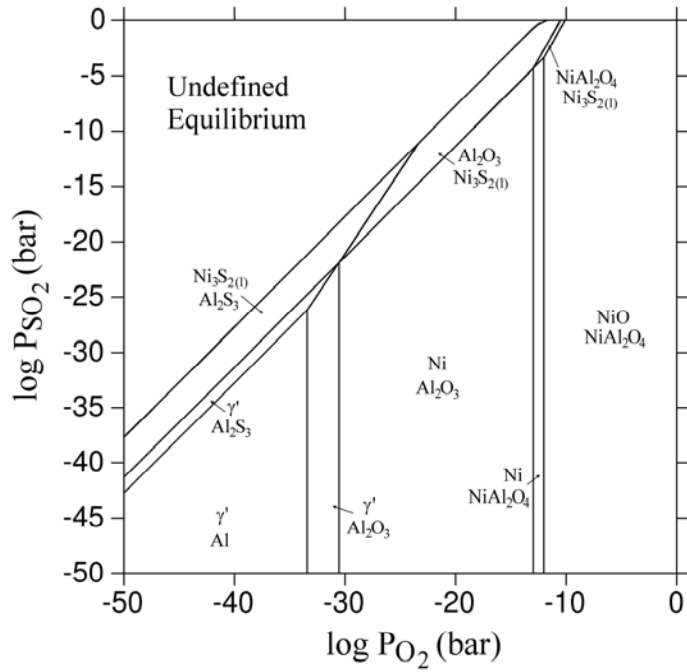


Figure 4-29. Ni<sub>3</sub>Al SO<sub>2</sub>-O<sub>2</sub> potential diagram at 900°C.

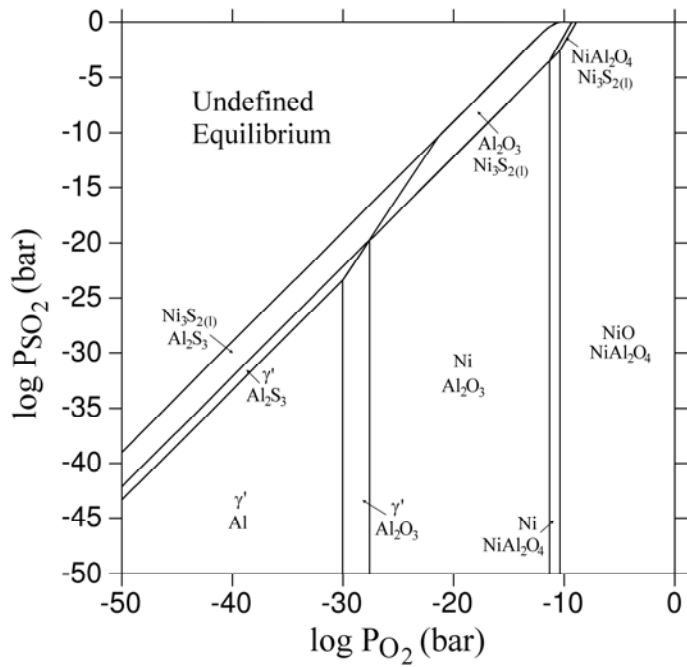


Figure 4-30. Ni<sub>3</sub>Al SO<sub>2</sub>-O<sub>2</sub> potential diagram at 1000°C. Published in [170].

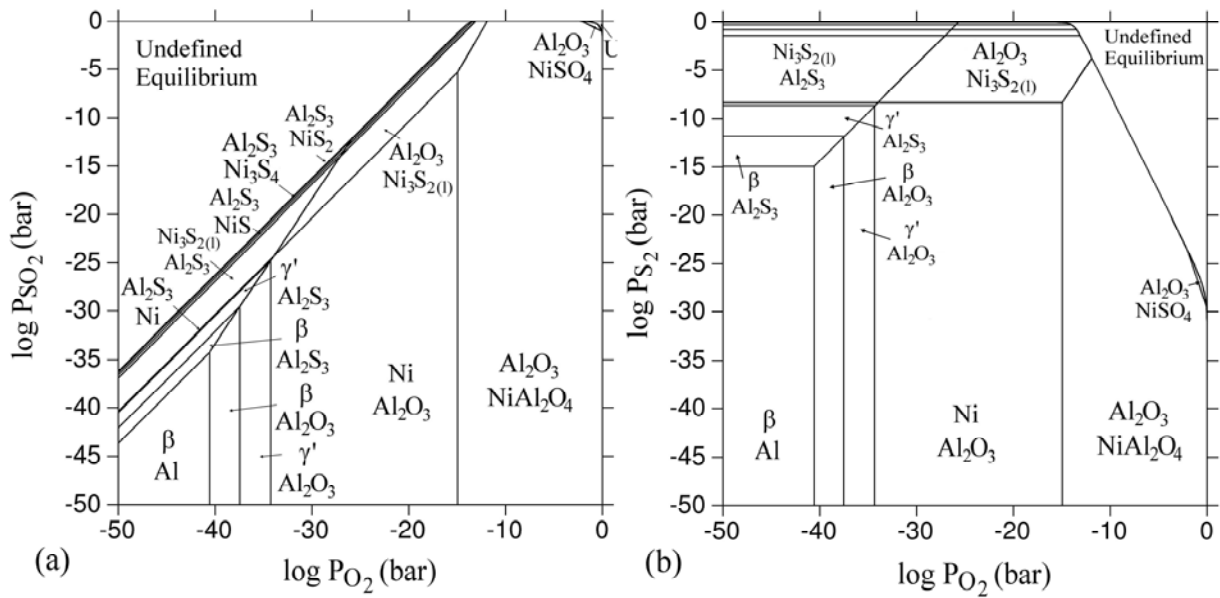


Figure 4-31. NiAl potential diagrams for (a) SO<sub>2</sub>-O<sub>2</sub> and (b) S<sub>2</sub>-O<sub>2</sub> at 800°C. U.E. is an abbreviation for undefined equilibrium. Published in [170].

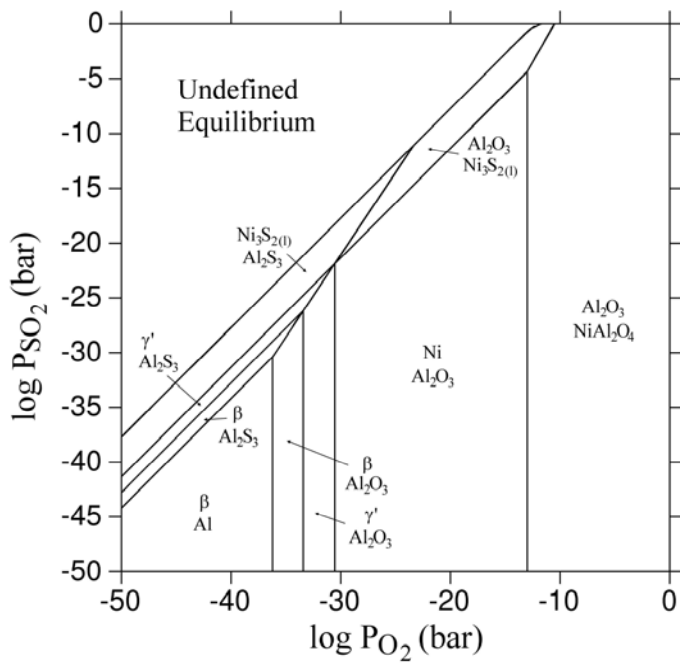
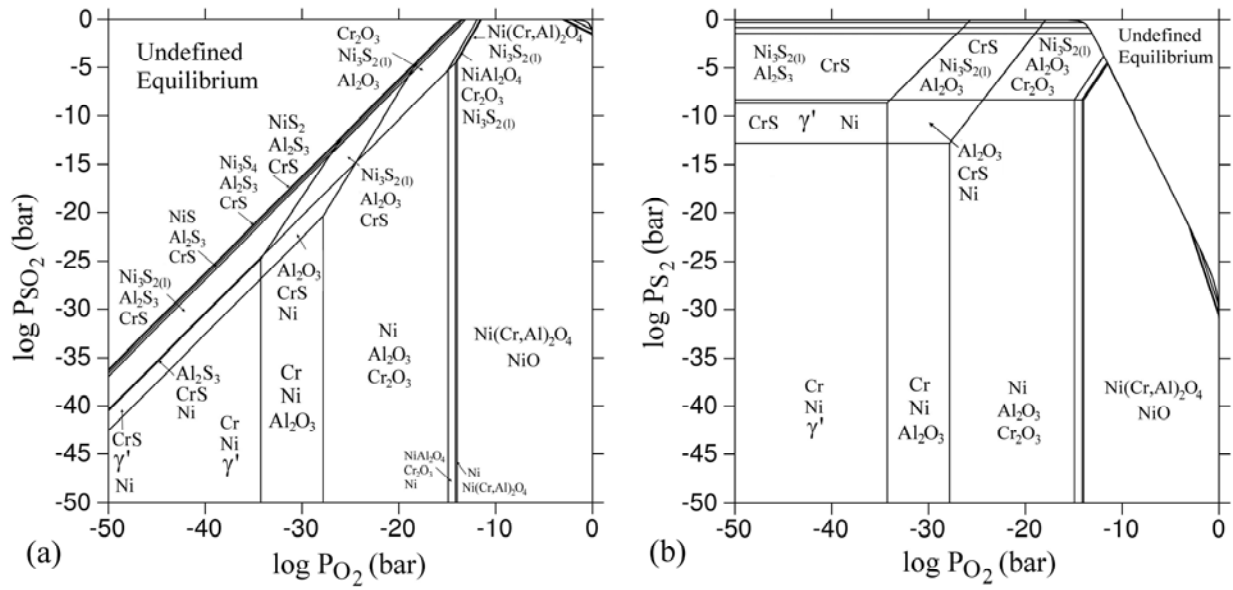


Figure 4-32. NiAl SO<sub>2</sub>-O<sub>2</sub> potential diagram at 900°C.









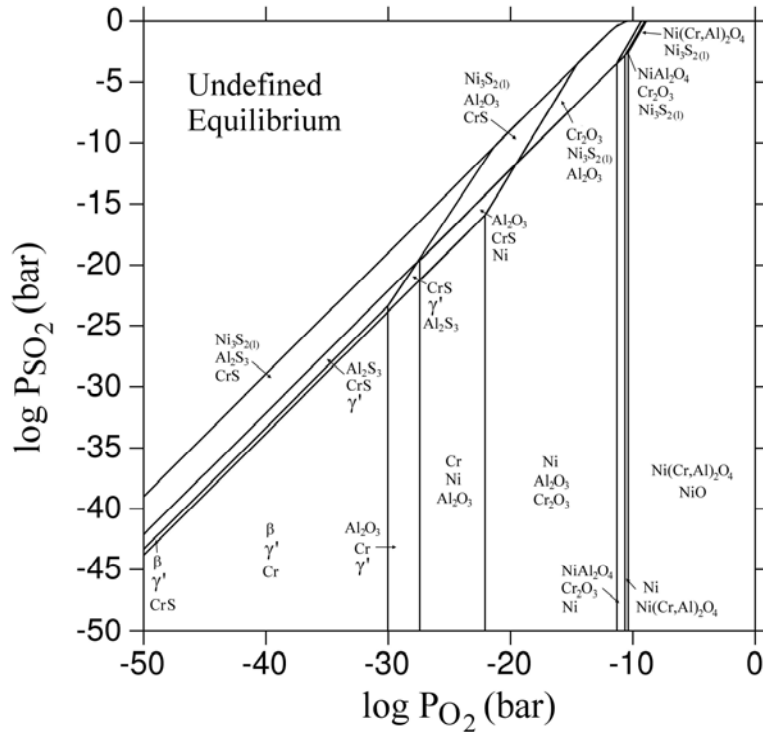


Figure 4-39. Ni-22Cr-11Al SO<sub>2</sub>-O<sub>2</sub> potential diagram at 1000°C. Published in [170].

#### 4.4 Phase Fraction Diagrams

This section shows the calculations in the form of phase fraction diagrams, which are diagrams with a potential, temperature, or composition of the x-axis, and a quantity on the y-axis. This quantity can be a generic term such as phase fraction, or can be more specific like partial pressure or composition.

Figure 4-40 shows a phase fraction diagram of the Ni-O system calculated using the SPOT3 database at 800°C with varying oxygen partial pressure. As predicted from Figure 4-16, the Ni phase is stable below a P<sub>O<sub>2</sub></sub> of 10<sup>-14</sup>, whereas the NiO is stable above this partial pressure. In essence, Figure 4-40 is slice of Figure 4-16 at a constant temperature. Figure 4-41 shows the phase fraction diagram of Ni at 800°C if 2% SO<sub>2</sub> is added. The partial pressure of S<sub>2</sub> is derived using the same methods to obtain Figures 4-11 and 4-14. The addition of S to the system causes the formation of Ni<sub>3</sub>S<sub>2</sub> at lower P<sub>O<sub>2</sub></sub> and NiSO<sub>4</sub> at higher P<sub>O<sub>2</sub></sub>. In between is a gas that stabilizes (mostly SO<sub>2</sub>), consisting of the species shown in Figure 4-42. In this calculation, Ar was added

as a component to the system to add as filler to keep the total system pressure 1 bar. An attempt was made to use the appended SPIN4 database to calculate these diagrams, but no stable equilibrium could be calculated. This was likely due to the equilibrium converging to two stable phases, which would violate the Gibbs Phase Rule for a three-component Ni-O-S system. Figure 4-43 shows the change in component activity where there is an increase in  $S_2$  activity at the oxide/metal interface. On either side of this peak, the  $P_{S_2}$  drops, especially toward increasing  $O_2$  where the S is oxidized into  $SO_2$  and  $SO_3$ .

Figure 4-44 shows the phase fraction diagram of changing activity of the constituents of the Ni-8Cr-6Al alloy in air calculated using the SPIN4 database. This diagram shows the drop in metal activities with increasing  $P_{O_2}$ , starting with the most reactive, Al, then Cr and finally Ni. Figure 4-45 shows the different phases that are stable over this range of  $P_{O_2}$ . Figure 4-46 shows a comparison of the activities obtained for this system with the SPOT3 and SPIN4 database. The two calculations agree perfectly with component activities in the  $(Al,Cr)_2O_3$  oxide and NiO. However, there is disagreement where the component are dissolved in  $\gamma$  and the spinel phase, due to the interaction parameters of elements in solution, which is not accounted for in the SPOT3 database.

The addition of sulfur to the above system and Ni-22Cr-11Al are of the most interest for this dissertation. Figure 4-47 shows the Ni-8Cr-6Al alloy in a 2%  $SO_2$  atmosphere, as calculated by the appended SPIN4 database. As with Figure 4-43, there is again a spike in  $S_2$  activity near the boundary of oxide/alloy stability. The phase fraction diagram in Figure 4-48 shows stabilization of sulfurous phases—from CrS at low  $P_{O_2}$ , to  $Ni_3S_2$  at higher  $P_{O_2}$ , and finally a gas consisting mostly of  $SO_2$  and  $O_2$ . Figure 4-49 shows the activity change for Ni-22Cr-11Al in the same environment and temperature, and Figure 4-50 shows the phase quantities. The activity

profile is similar to that of Ni-8Cr-6Al. In addition, similar phases evolve with the Ni-22Cr-11Al alloy, except with the formation of an  $\alpha$ -Cr phase at low  $P_{O_2}$ . Spinel is now the most predominant oxide at high  $P_{O_2}$ , and at intermediate partial pressures of oxygen, the oxide dominates instead of the alloy.

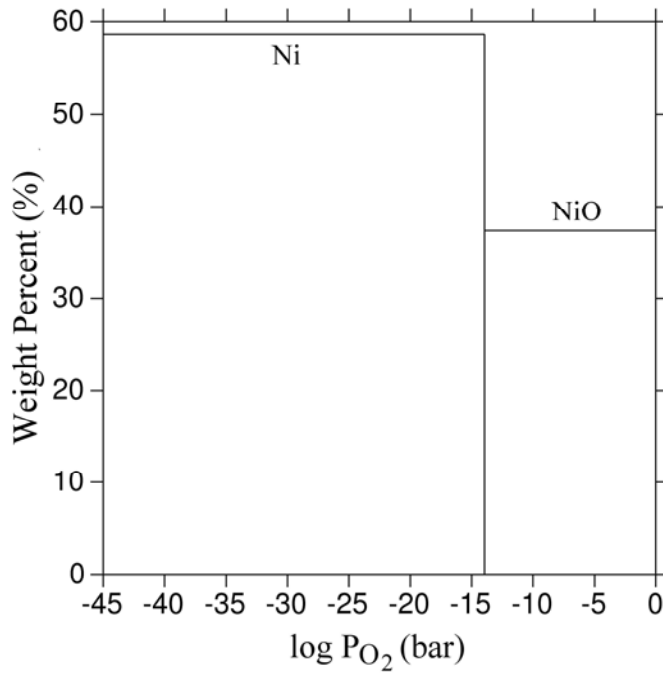


Figure 4-40. Phase fraction diagram of the Ni-O system showing the change in phase percent with varying oxygen partial pressure at 800°C in air. Calculated from the SPOT3 database.

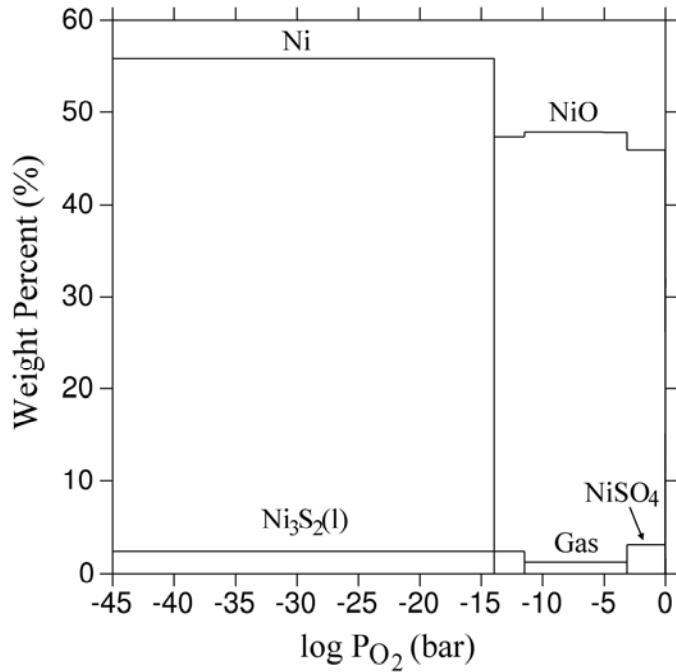


Figure 4-41. Phase fraction diagram of the Ni-O-S system showing the change in phase percent with varying oxygen partial pressure at 800°C in an 0.21 O<sub>2</sub> + 0.02 SO<sub>2</sub> atmosphere. Calculated from the SPOT3 database.

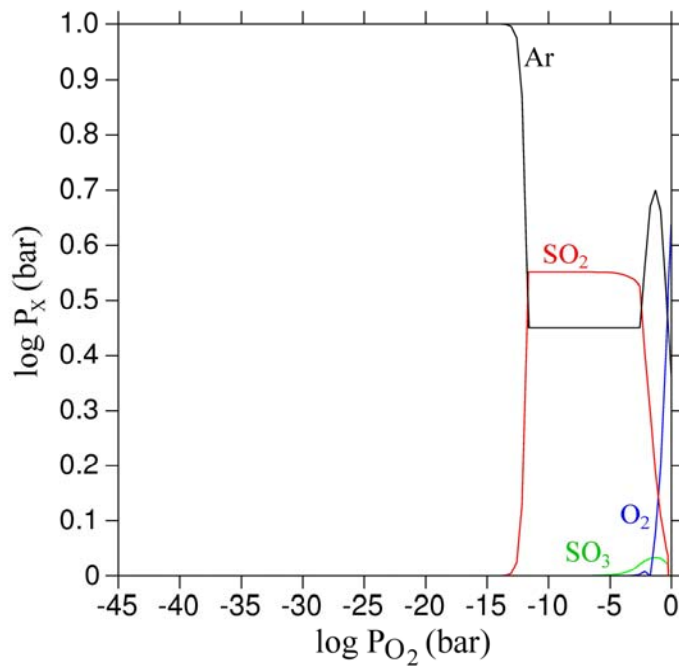


Figure 4-42. Phase fraction diagram of the Ni-O-S system showing the gas evolution (in partial pressure [bar]) with varying oxygen partial pressure at 800°C in an 0.21 O<sub>2</sub> + 0.02 SO<sub>2</sub> atmosphere. Calculated from the SPOT3 database.

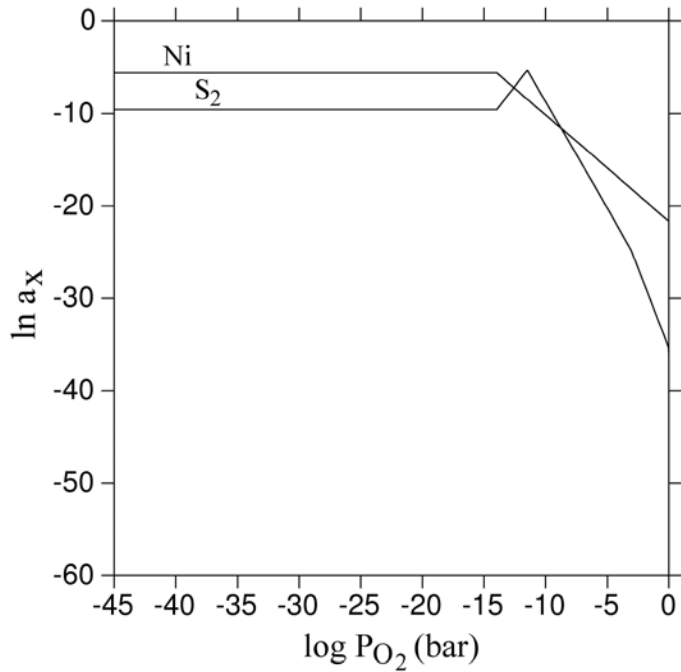


Figure 4-43. Phase fraction diagram of the Ni-O-S system showing activity change of each component with varying oxygen partial pressure at 800°C in an 0.21 O<sub>2</sub> + 0.02 SO<sub>2</sub> atmosphere. Calculated from the SPOT3 database.

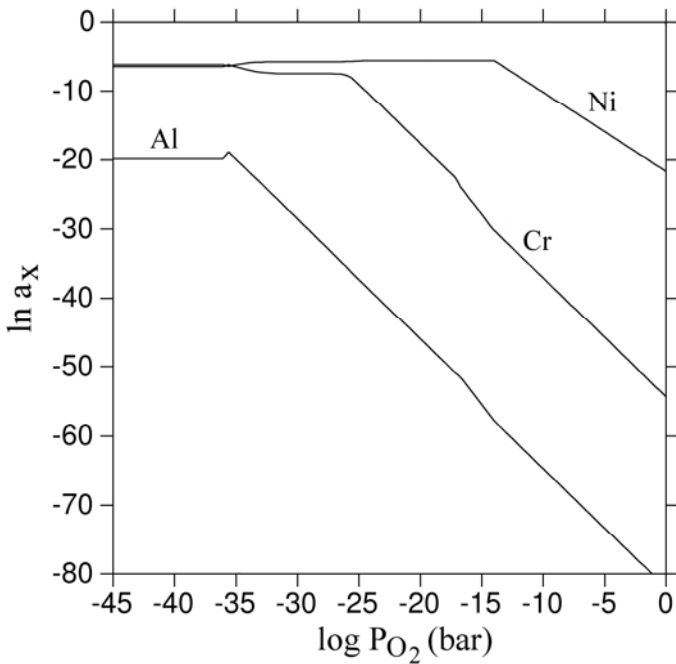


Figure 4-44. Phase fraction diagram an Ni-8Cr-6Al alloy showing activity change of each component with varying oxygen partial pressure at 800°C in air. Calculated from the SPIN4 database.

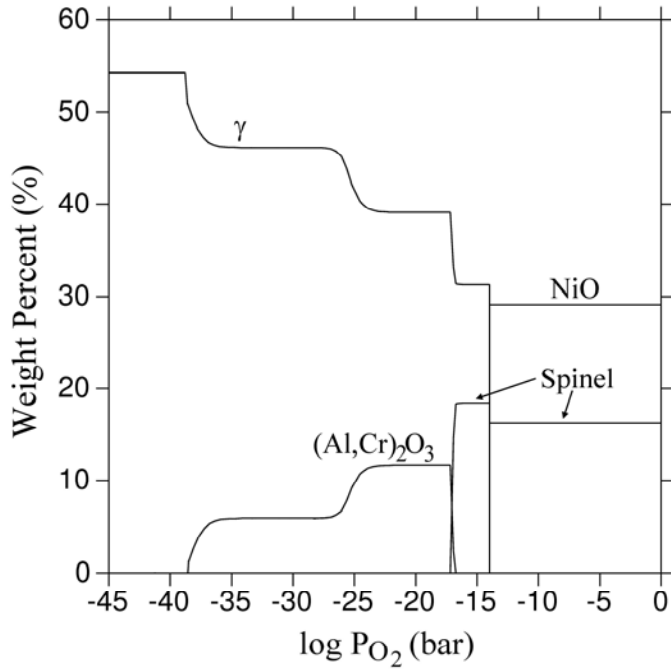


Figure 4-45. Phase fraction diagram an Ni-8Cr-6Al alloy showing the change in phase percent with varying oxygen partial pressure at 800°C in air. Calculated from the SPIN4 database.

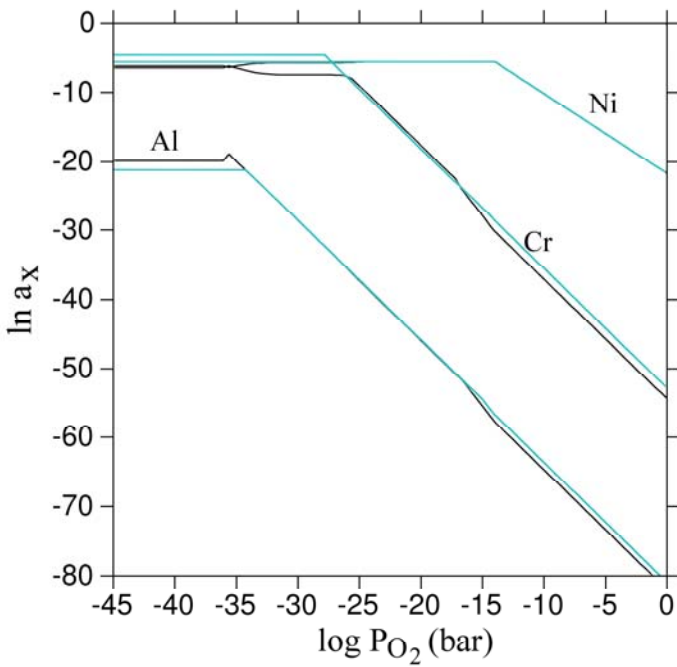


Figure 4-46. Phase fraction diagram an Ni-8Cr-6Al alloy at 800°C comparing the activity change calculated for Figure 4-38 using the SPIN4 database (black) and the SPOT3 database (teal).

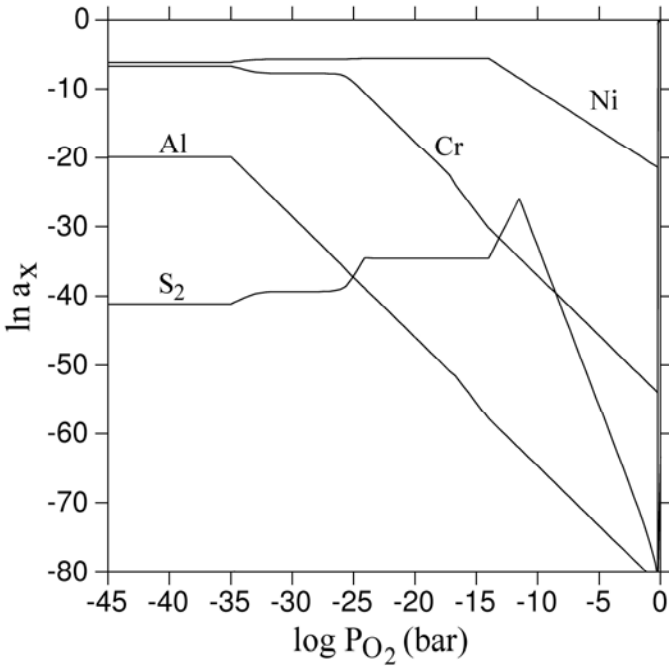


Figure 4-47. Phase fraction diagram of an Ni-8Cr-6Al alloy showing activity change of each component with varying oxygen partial pressure at 800°C in an 0.21 O<sub>2</sub> + 0.02 SO<sub>2</sub> atmosphere. Calculated from the appended SPIN4 database.

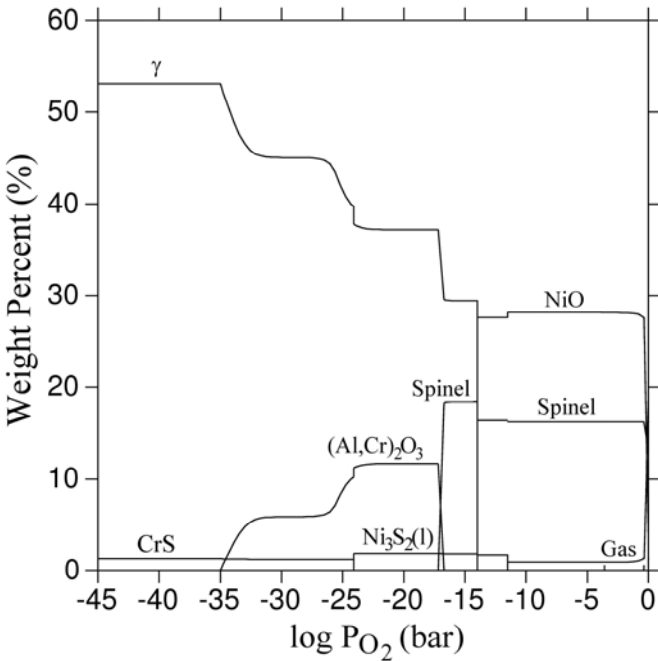


Figure 4-48. Phase fraction diagram of an Ni-8Cr-6Al alloy showing the change in phase percent with varying oxygen partial pressure at 800°C in an 0.21 O<sub>2</sub> + 0.02 SO<sub>2</sub> atmosphere. Calculated from the appended SPIN4 database.

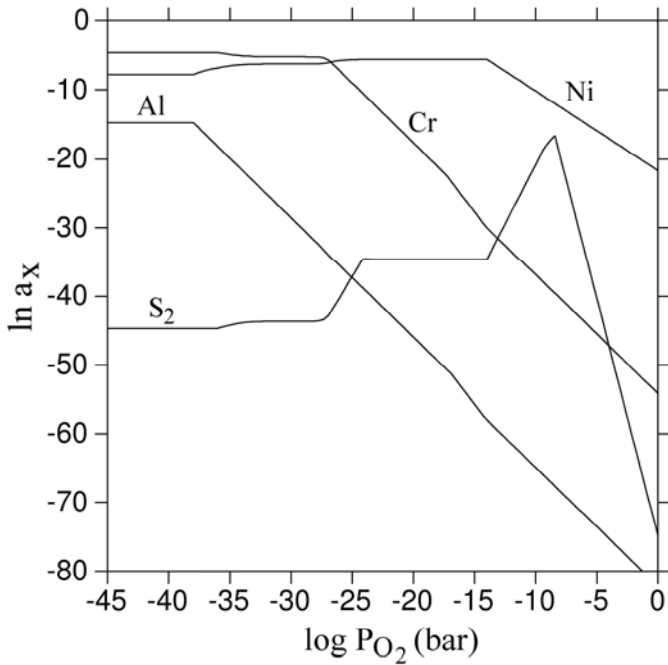


Figure 4-49. Phase fraction diagram of an Ni-22Cr-11Al alloy showing activity change of each component with varying oxygen partial pressure at 800°C in an 0.21 O<sub>2</sub> + 0.02 SO<sub>2</sub> atmosphere. Calculated from the appended SPIN4 database.

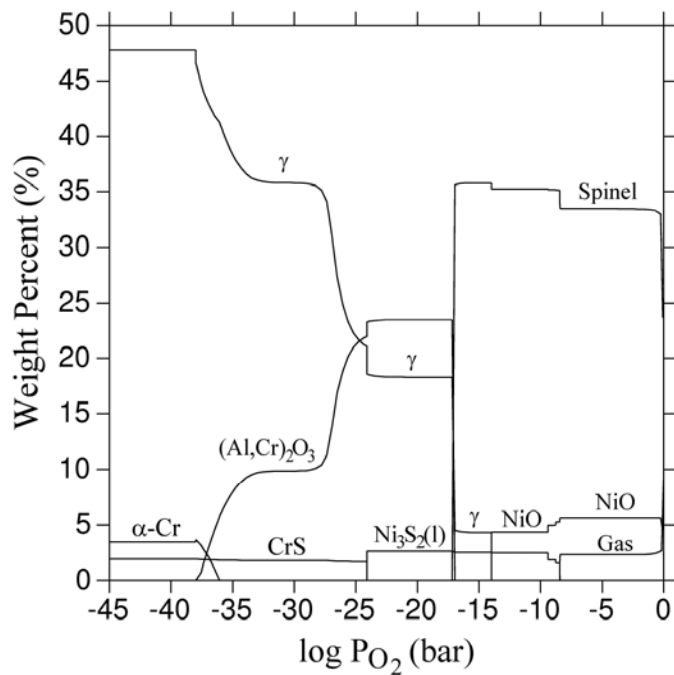


Figure 4-50. Phase fraction diagram of an Ni-22Cr-11Al alloy showing the change in phase percent with varying oxygen partial pressure at 800°C in an 0.21 O<sub>2</sub> + 0.02 SO<sub>2</sub> atmosphere. Calculated from the appended SPIN4 database.

## CHAPTER 5 EXPERIMENTAL RESULTS

This chapter will discuss the results of the kinetic experiments conducted using the methodology described in Chapter 3. The results of the kinetic analyses will be shown, and then the characterization data of the oxidized specimens will be presented.

### 5.1 TGA Experiments

#### 5.1.1 Oxidation Experiments in Air

The TG experiments were carried out as outlined in Chapter 3. Figure 5-1 shows the results of a typical oxidation run—a Ni specimen in air at 800°C for 24 hr. Here, the weight change divided by surface area (in  $\text{mg}/\text{cm}^2$ ) is plotted against the time in seconds. However, for the purpose of brevity, further results will be given to best visualize and derive the parabolic rate constant(s) of each sample run. Figure 5-2 is similar to Figure 5-1 except that the x-axis plots the square root of time, in  $\text{s}^{1/2}$ . From this figure, one can derive the parabolic rate constant,  $k_p$  in  $\text{mg}/\text{cm}^2 \cdot \text{s}^{1/2}$ , from the slope of the linear regression which is plotted on the graph. The  $R^2$  coefficient of determination is plotted as well to show the global fit of the parabolic rate model.

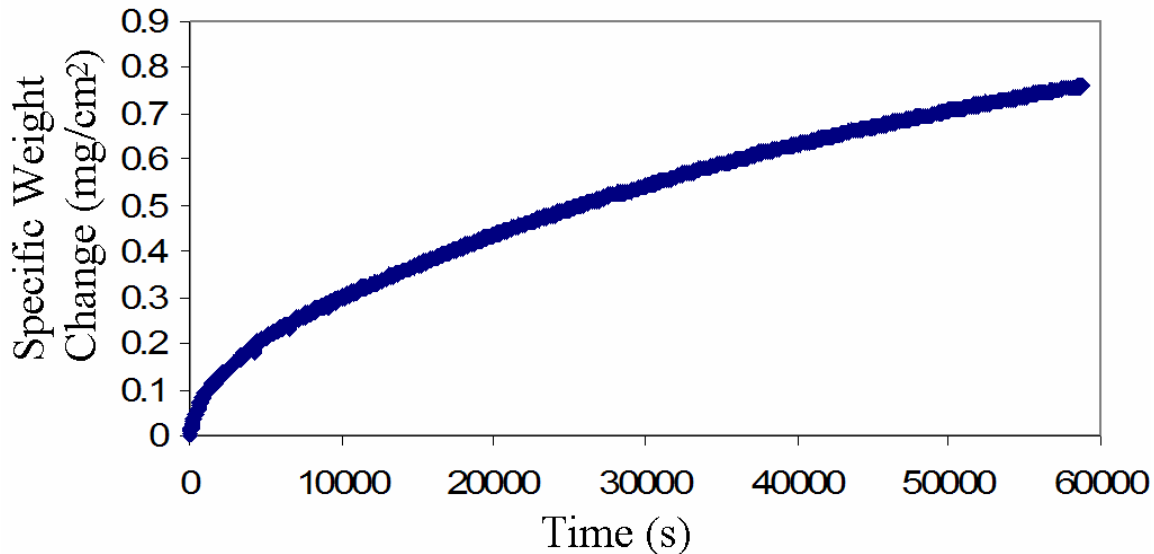


Figure 5-1. Plot of weight change versus time for Ni specimen at 800°C for 24 hr in air.

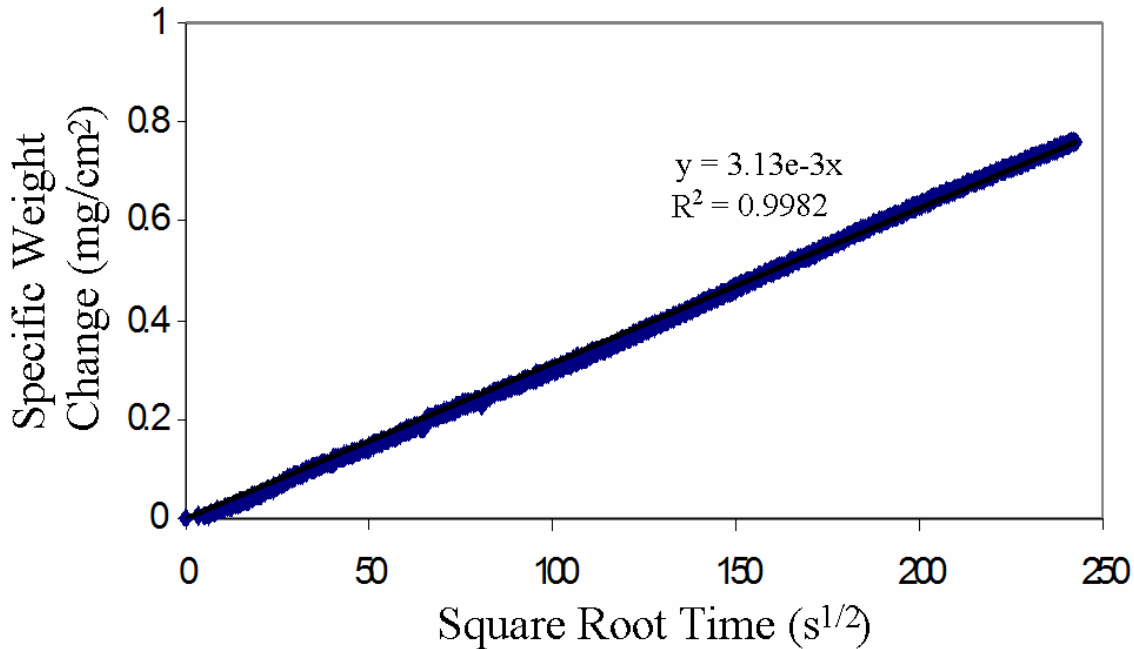


Figure 5-2. Plot of weight change versus square root time for Ni specimen at 800°C for 24 hr in air. The formula containing the slope and the coefficient of determination are listed.

Figure 5-3 shows the TG data collected for Ni oxidized at 900°C. This data is noteworthy because the oxidation growth at the beginning of the test takes on the subparabolic behavior described by Haugsrud [44]. This is also observed in the Ni specimen oxidized at 1100°C. However, it is not seen at 1000°C. To compare the growth constants for this study with those of most every other oxidation study, which plot the weight change squared versus time yielding units of  $\text{mg}^2/\text{cm}^4 \cdot \text{s}$ , the  $k_p$  values obtain were squared, and then plotted Arrheniusly against the inverse absolute temperature to determine an activation energy, as shown in Figure 5-4. The activation energy,  $Q_A$ , can be derived from the slope by:

$$Q_A = m \cdot R \quad (5.1)$$

where  $m$  is the slope of the linear regression obtained from the Arrhenius plot (in K) and  $R$  is the ideal gas constant of 8.314 J/mol·K. The oxidation of Ni specimens in this study had an activation energy of 150.74 kJ/mol.

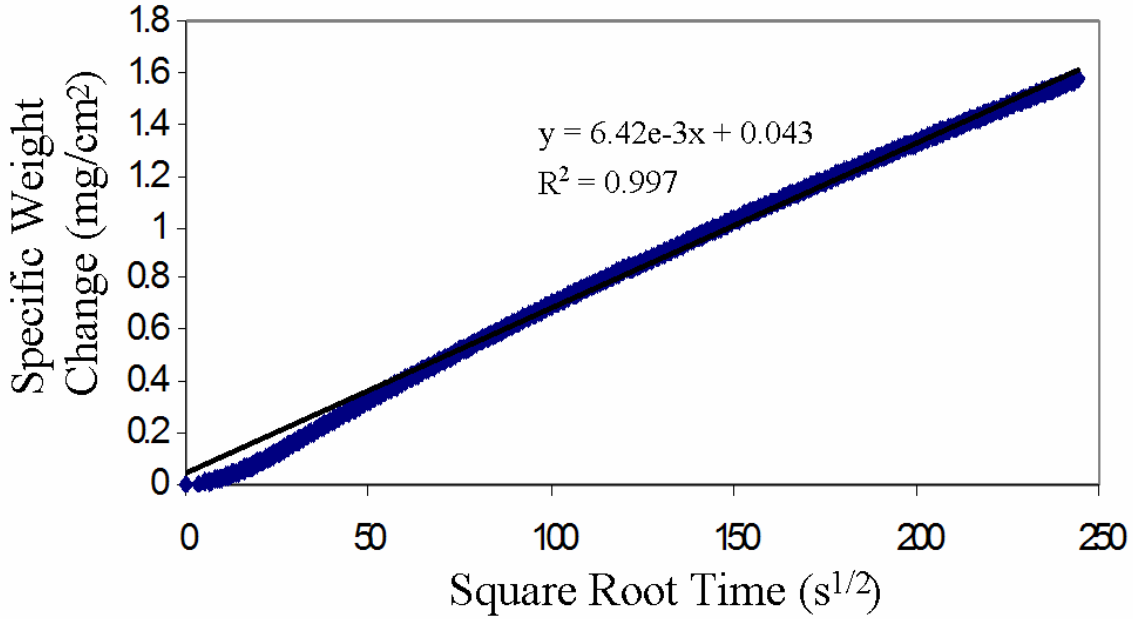


Figure 5-3. Plot of weight change versus square root time for Ni specimen at 900°C for 24 hr in air. The formula containing the slope and the coefficient of determination are listed.

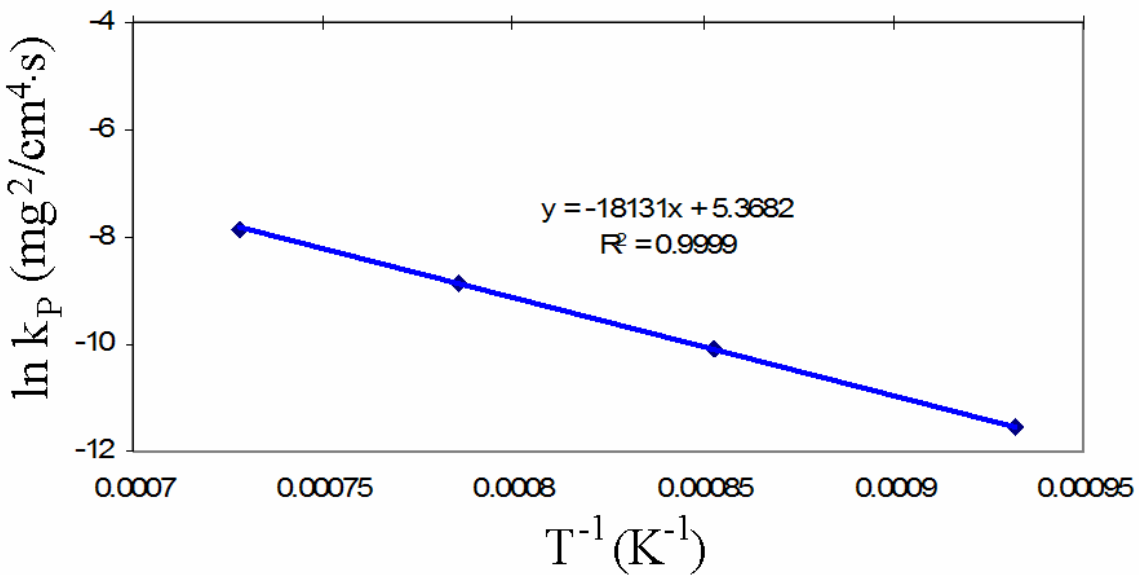


Figure 5-4. Arrhenius plot of the parabolic rate constant versus inverse temperature of Ni oxidized for 24 hr in air. The formula containing the slope and the coefficient of determination are listed.

Unlike the TG curves for pure Ni, the oxidation growth for all the other alloys was more complex. In Figure 5-5, the oxidation of NiAl at 800°C for 24 hr is plotted. This plot shows an incubation time with possibly some minor weight loss until approximately 3 hours into the test

( $105 \text{ s}^{1/2}$  on Figure 5-5), when parabolic growth occurs. This same behavior was seen for all three NiAl oxidation tests, which had incubation times of 3.1 hr, 1.5 hr, and 1.2 hr respectively for tests at 800, 900, and 1000°C. This incubation time was chosen by taking a tangent to the parabolic region of the curve, as outlined by the method developed by Pieraggi [167]. Where the slope changed there was a deviation defined by Equation 2-5 and was not considered steady-state. The parabolic rate constants for the NiAl specimens are graphed on an Arrhenius plot in Figure 5-6. The activation energy for the oxidation of NiAl, excluding the incubation time, was found to be 161.69 kJ/mol. No activation energies for these materials were calculated by literature

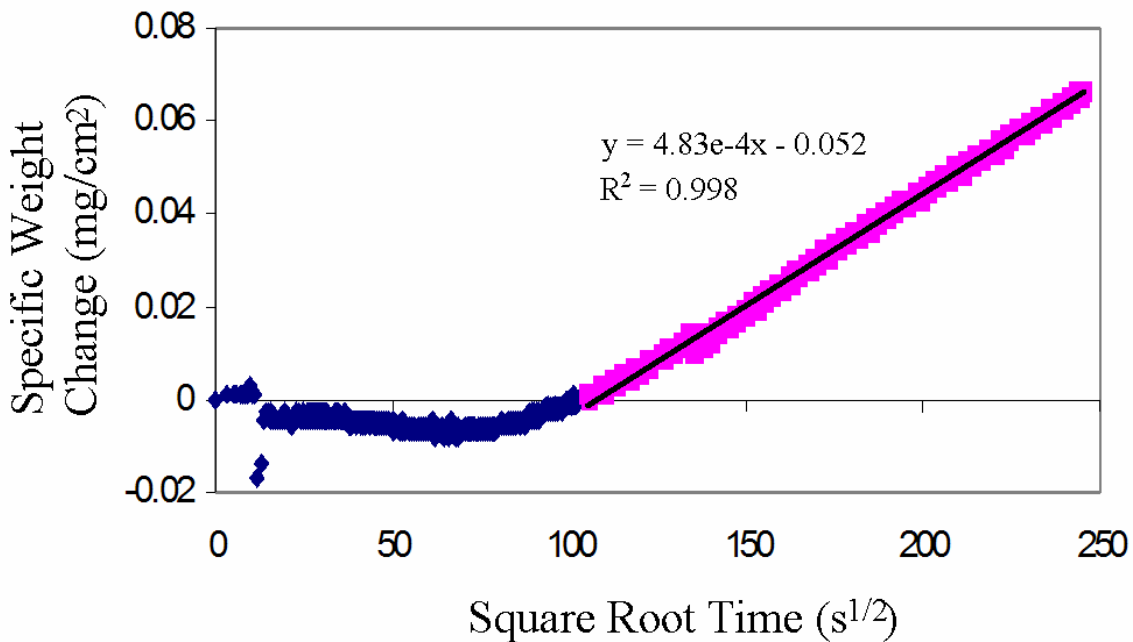


Figure 5-5. Plot of weight change versus square root time for a NiAl specimen at 800°C for 24 hr in air. The formula containing the slope and the coefficient of determination are listed.

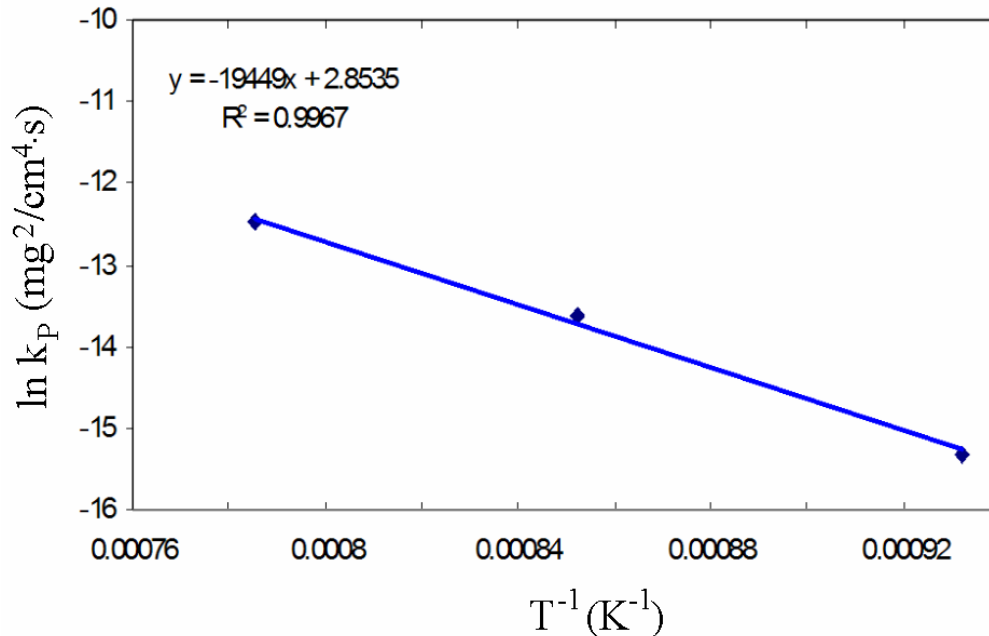


Figure 5-6. Arrhenius plot of the parabolic rate constant versus inverse temperature of NiAl oxidized for 24 hr in air. The formula containing the slope and the coefficient of determination are listed.

For the Ni-Cr-Al alloys, the TG curves were even more complex. One of the Ni-8Cr-6Al, like Figure 5-7, had a similar shape to that of Figure 5-5. Others, like Figure 5-8 had an initial oxidation growth rate that was faster than the “steady-state” parabolic growth. The oxidation plots for Ni-8Cr-6Al at 800°C has the same shape as that for 1000°C (Figure 5-7), although the initial oxidation stages are much less pronounced. The curves for the Ni-22Cr-11Al alloys were all similar to those for 100 hr at 800°C, as shown in Figure 5-9. In the experiments with these alloys, there was an initial weight gain, then a slight weight loss, and finally steady parabolic growth. The “steady-state” parabolic rate constants for Ni-8Cr-6Al and Ni-22Cr-11Al are plotted versus inverse absolute temperature as Arrhenius plots in Figures 5-10 and 5-11, respectively. No activation energy could be calculated for the Ni-8Cr-6Al alloy because there was not an Arrhenius dependency. An activation energy of 25.07 kJ/mol was calculated for the oxidation of Ni-22Cr-11Al. However, the amount of variance here cannot be explained by the Arrhenius model making this is statistic unsound.

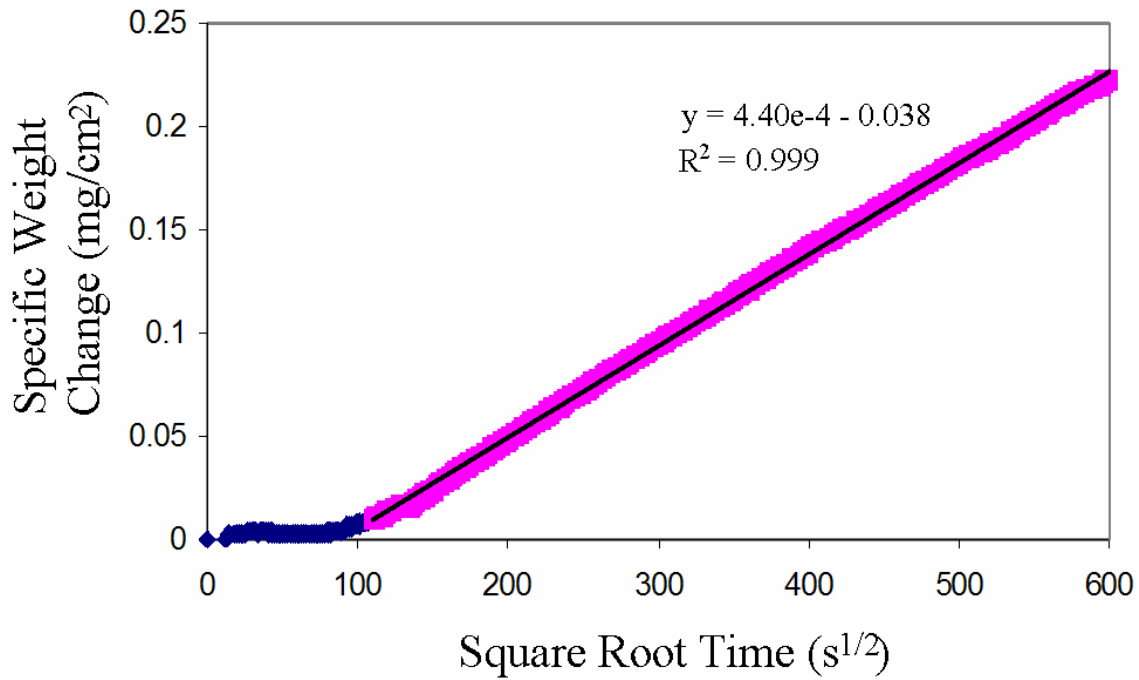


Figure 5-7. Plot of weight change versus square root time for a Ni-8Cr-6Al specimen at 1000°C for 100 hr in air. The formula containing the slope and the coefficient of determination are listed.

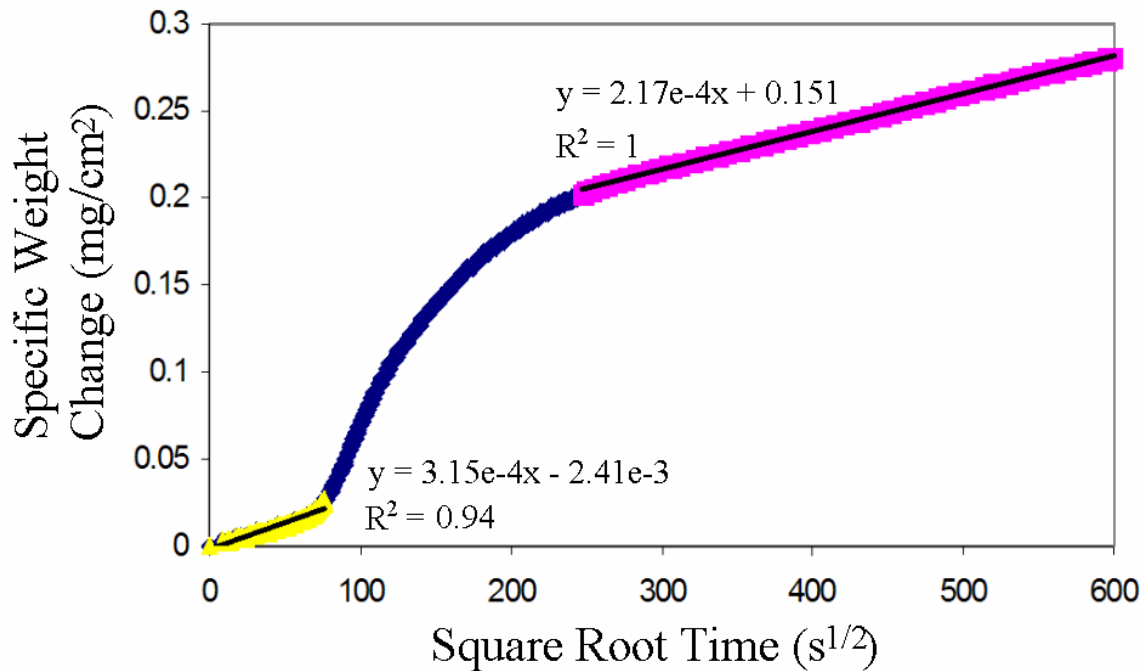


Figure 5-8. Plot of weight change versus square root time for a Ni-8Cr-6Al specimen at 900°C for 100 hr in air. The formula containing the slope and the coefficient of determination are listed.

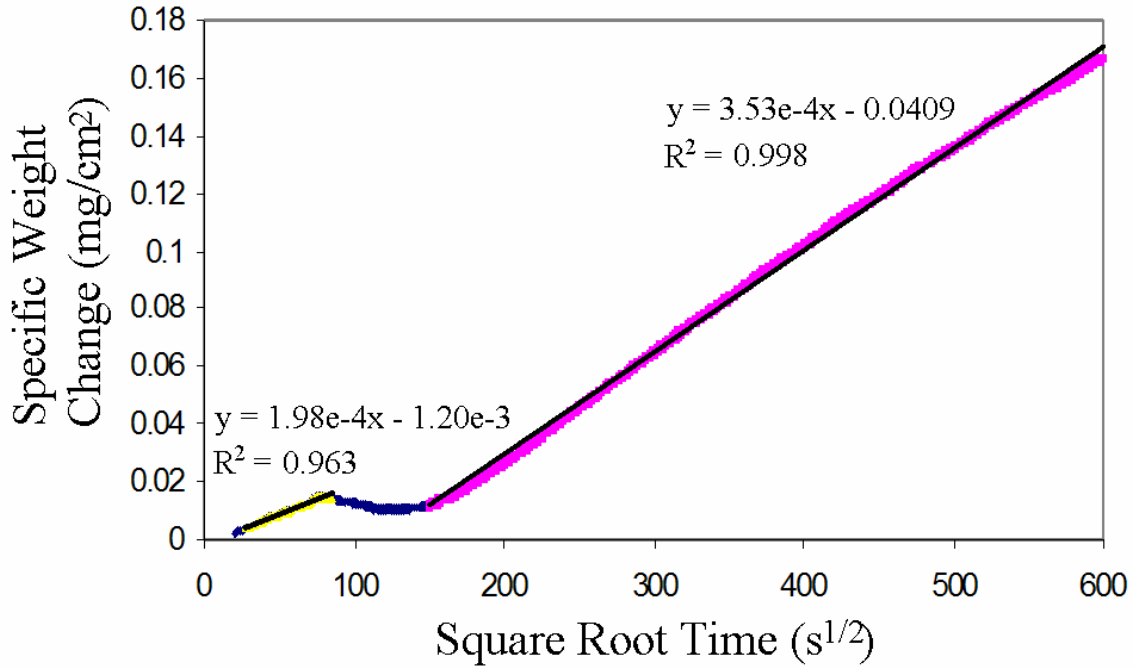


Figure 5-9. Plot of weight change versus square root time for a Ni-22Cr-11Al specimen at 800°C for 100 hr in air. The formula containing the slope and the coefficient of determination are listed.

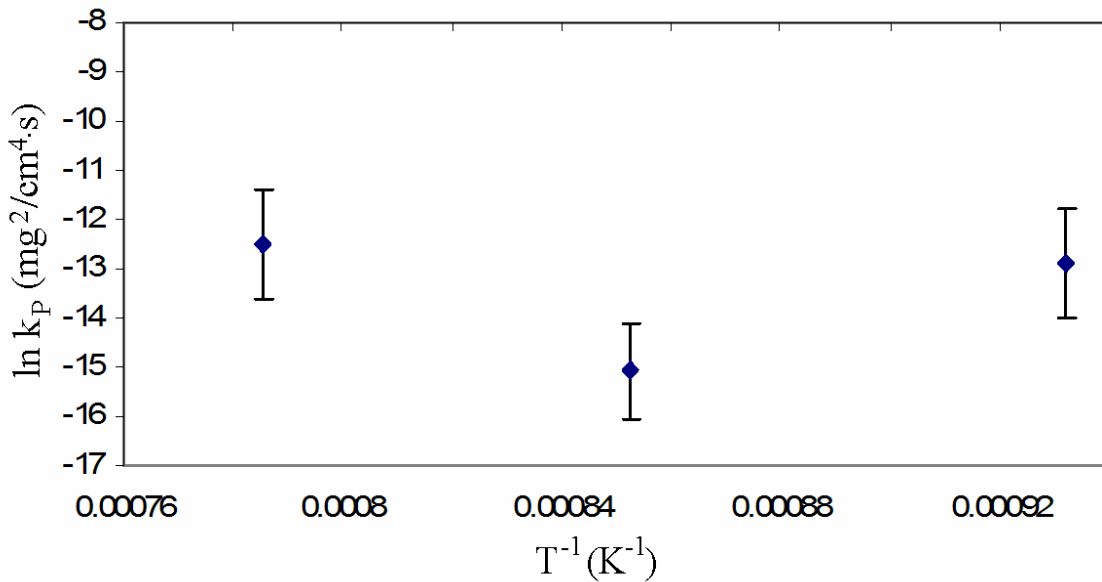


Figure 5-10. Arrhenius plot of the parabolic rate constant versus inverse temperature of Ni-8Cr-6Al oxidized for 100 hr in air.

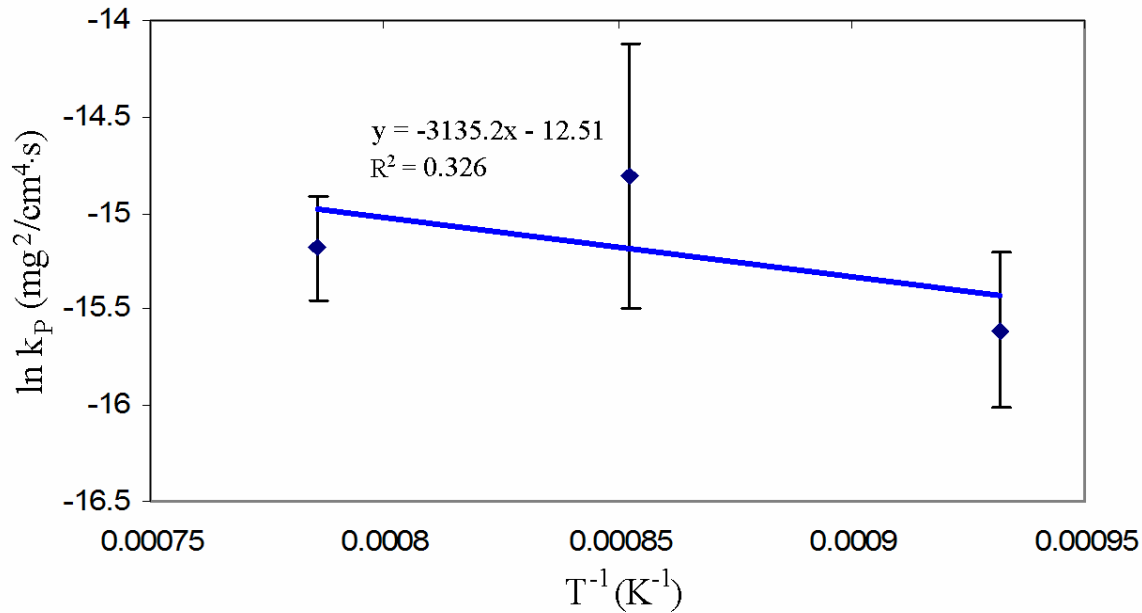


Figure 5-11. Arrhenius plot of the parabolic rate constant versus inverse temperature of Ni-22Cr-11Al oxidized for 100 hr in air. The formula containing the slope and the coefficient of determination are listed.

### 5.1.2 Oxidation Experiments in He + 0.21 O<sub>2</sub> + 0.02 SO<sub>2</sub>

The TG experiments with 2% SO<sub>2</sub> showed more scatter in the collected data, but there appeared to be less change in mechanism during the oxidation process. For Ni-8Cr-6Al, there appeared to be a faster initial stage of oxidation before transitioning to the steady parabolic rate (Figure 5-12). For all other conditions though, with this alloy and with Ni-22Cr-11Al, there appeared to be no pronounced initial oxidation stage, as shown in Figure 5-13. The Arrhenius plots for Ni-8Cr-6Al and Ni-22Cr-11Al are shown in Figures 5-14 and 5-15, respectively. The activation energy for oxidation of Ni-8Cr-6Al in He + 0.21 O<sub>2</sub> + 0.02 SO<sub>2</sub> is 415.14 kJ/mol, and for Ni-22Cr-11Al is 157.83 kJ/mol. This shows a higher activation energy for steady-state oxidation in the Ni-8Cr-6Al specimens than the Ni-22Cr-11Al. No previous literature discusses activation energies for the oxidation of these alloys.

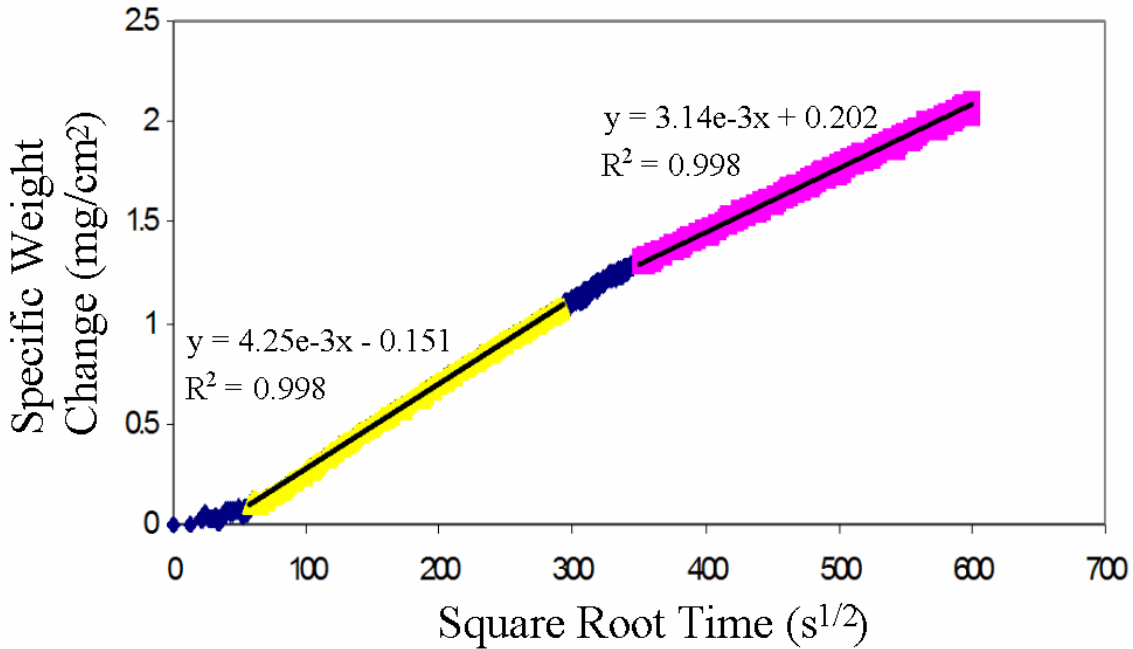


Figure 5-12. Plot of weight change versus square root time for a Ni-8Cr-6Al specimen at 975°C for 100 hr in He + 0.21 O<sub>2</sub> + 0.02 SO<sub>2</sub>. The formula containing the slope and the coefficient of determination are listed.

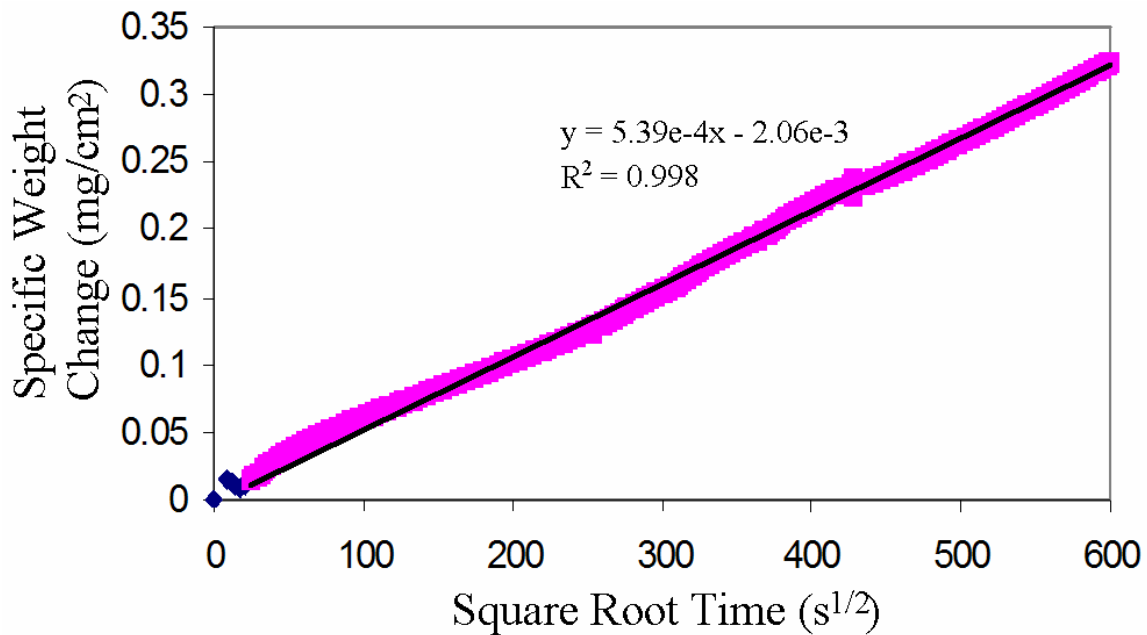


Figure 5-13. Plot of weight change versus square root time for a Ni-22Cr-11Al specimen at 975°C for 100 hr in He + 0.21 O<sub>2</sub> + 0.02 SO<sub>2</sub>. The formula containing the slope and the coefficient of determination are listed.

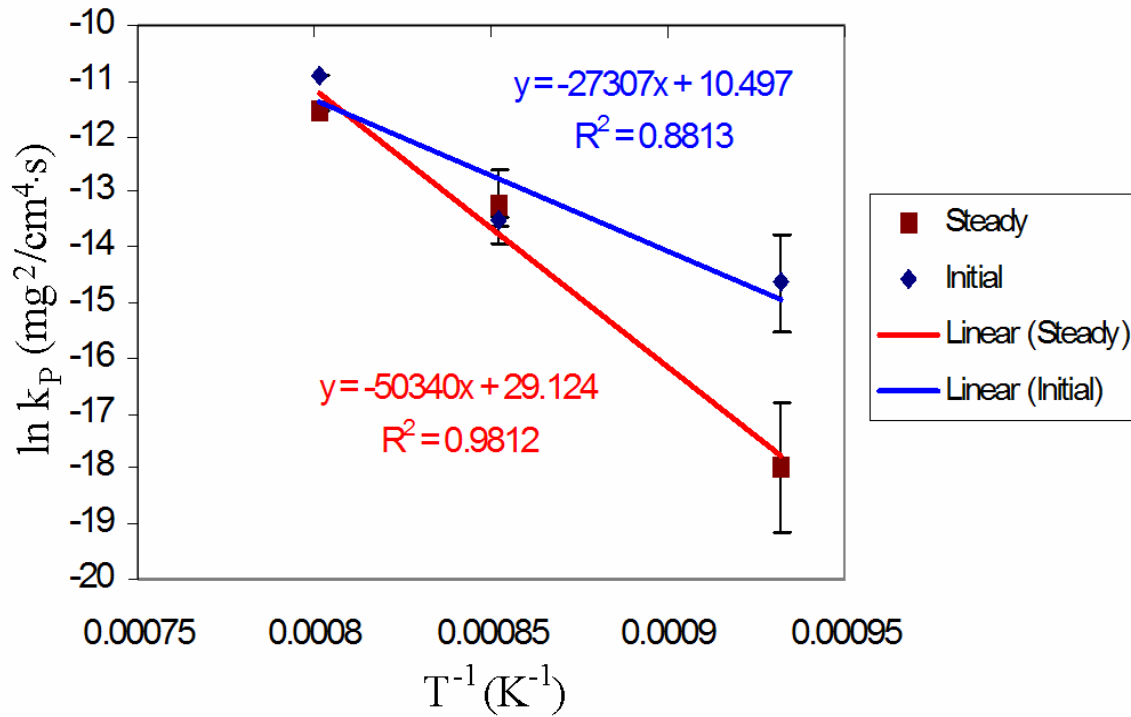


Figure 5-14. Arrhenius plot of the parabolic rate constant versus inverse temperature of Ni-8Cr-6Al oxidized for 100 hr in He + 0.21 O<sub>2</sub> + 0.02 SO<sub>2</sub>. The formula containing the slope and the coefficient of determination are listed.

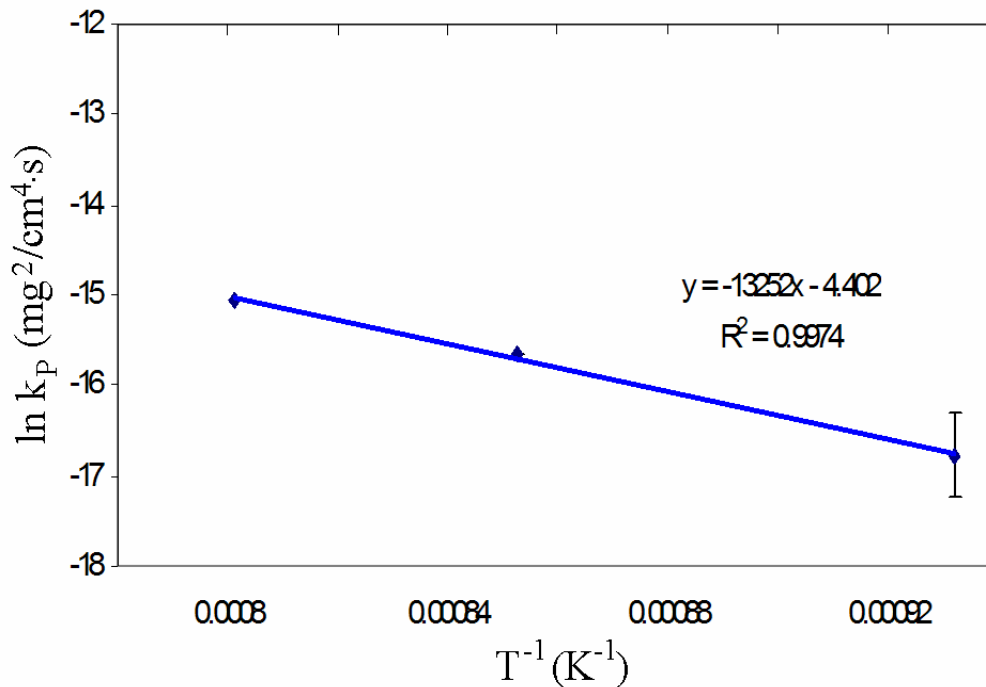


Figure 5-15. Arrhenius plot of the parabolic rate constant versus inverse temperature of Ni-22Cr-11Al oxidized for 100 hr in He + 0.21 O<sub>2</sub> + 0.02 SO<sub>2</sub>. The formula containing the slope and the coefficient of determination are listed.

### 5.1.3 Oxidation Experiments in He + 0.21 O<sub>2</sub> + 0.10 SO<sub>2</sub>

The oxidation/sulfidation TG plots of all the Ni-8Cr-6Al alloys in He + 0.21 O<sub>2</sub> + 0.10 SO<sub>2</sub> had the same shape as the plot in Figure 5-16 for 900°C. There was an initial parabolic growth rate, which at a certain time would enter a transition stage, which would then the growth would proceed at a faster parabolic rate. Therefore, there are two parabolic rate constants for each experimental temperature—one for the initial oxidation, and one for the later, “steady-state” oxidation. Figure 5-17 shows the Arrhenius plots for both oxidation stages. The activation energy for the initial oxidation in He + 0.21 O<sub>2</sub> + 0.10 SO<sub>2</sub> is 140 kJ/mol, while that of the later stage is 120 kJ/mol.

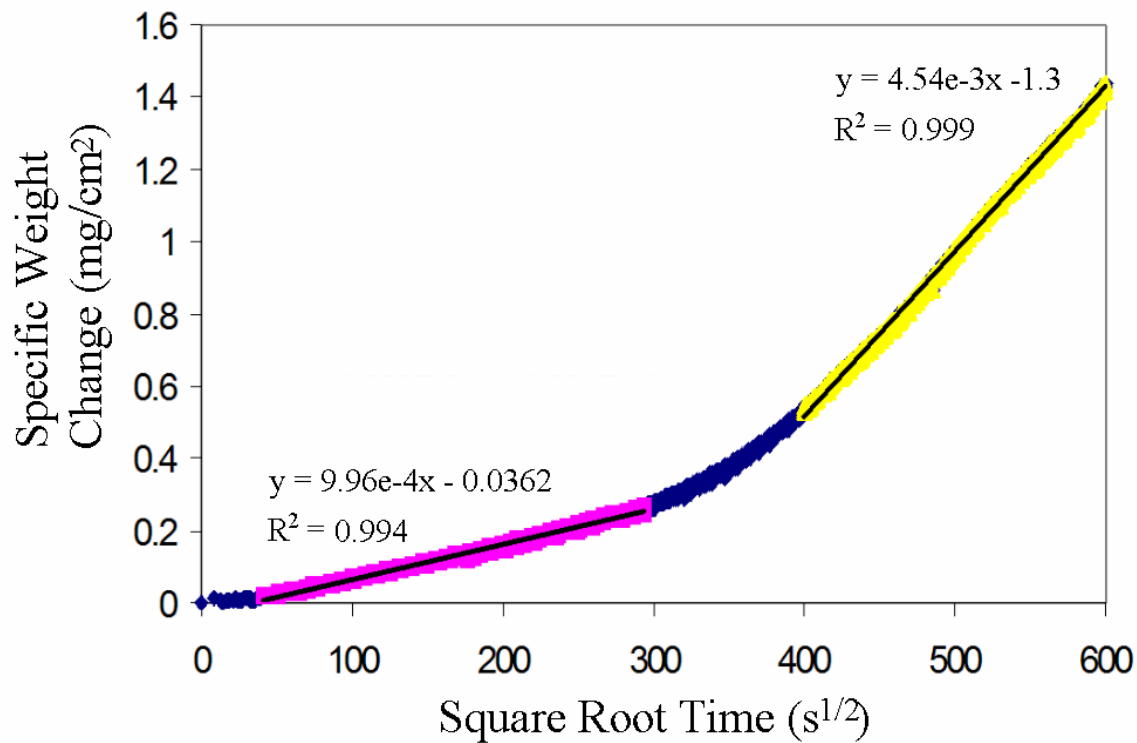


Figure 5-16. Plot of weight change versus square root time for a Ni-8Cr-6Al specimen at 900°C for 100 hr in He + 0.21 O<sub>2</sub> + 0.10 SO<sub>2</sub>. The formulas containing the slopes and the coefficients of determination are listed.

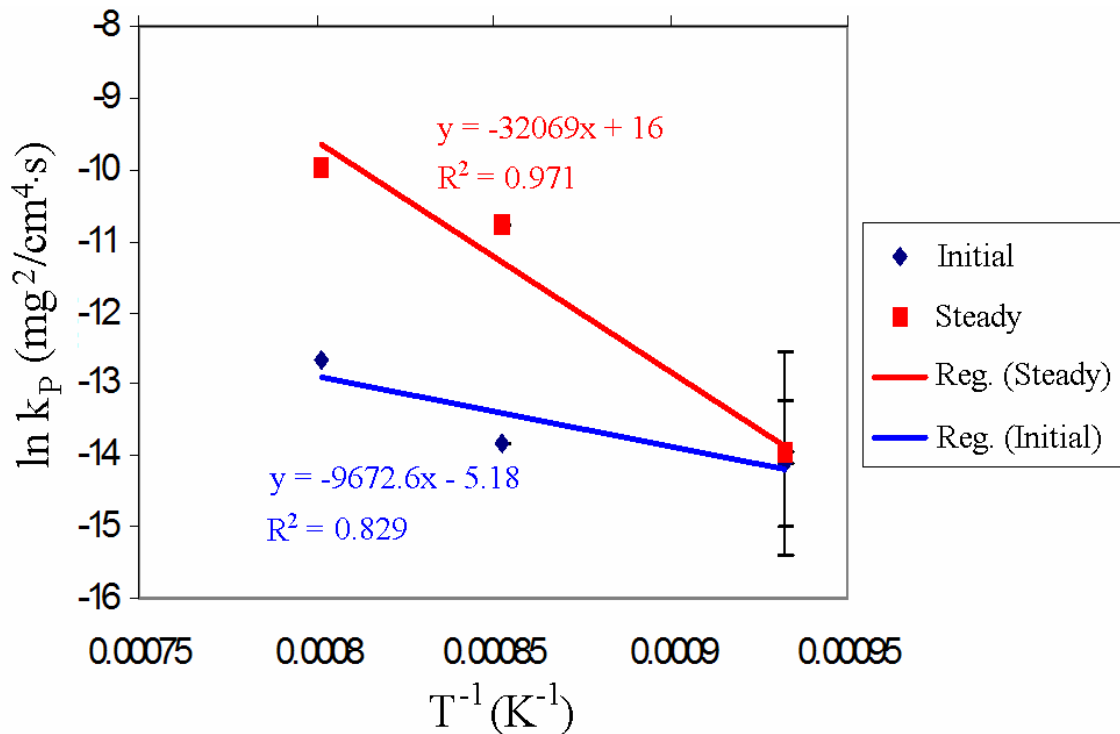


Figure 5-17. Arrhenius plot of the parabolic rate constant versus inverse temperature of Ni-8Cr-6Al oxidized for 100 hr in He + 0.21 O<sub>2</sub> + 0.10 SO<sub>2</sub>. The blue data and regression correspond to the initial oxidation rates, whereas the red data and regression correspond to the later stage oxidation. The formulas containing the slope and the coefficients of determination are listed.

The oxidation curves of Ni-22Cr-11Al alloy in He + 0.21 O<sub>2</sub> + 0.10 SO<sub>2</sub> followed that of the one recorded at 800°C (Figure 5-18)—fast growth that eventually decreases until steady-state parabolic kinetics is observed. An Arrhenius plot of the parabolic rate constants for these experiments is shown in Figure 5-19. The activation energy for the oxidation of Ni-22Cr-11Al in He + 0.21 O<sub>2</sub> + 0.10 SO<sub>2</sub> could be 152.52 kJ/mol, although it is not statistically significant.

Table 5-1 lists the mean parabolic rate constants for all the oxidation and oxidation/sulfidation experiments. Figure 5-20 shows an Arrhenius plot of all the experiments.

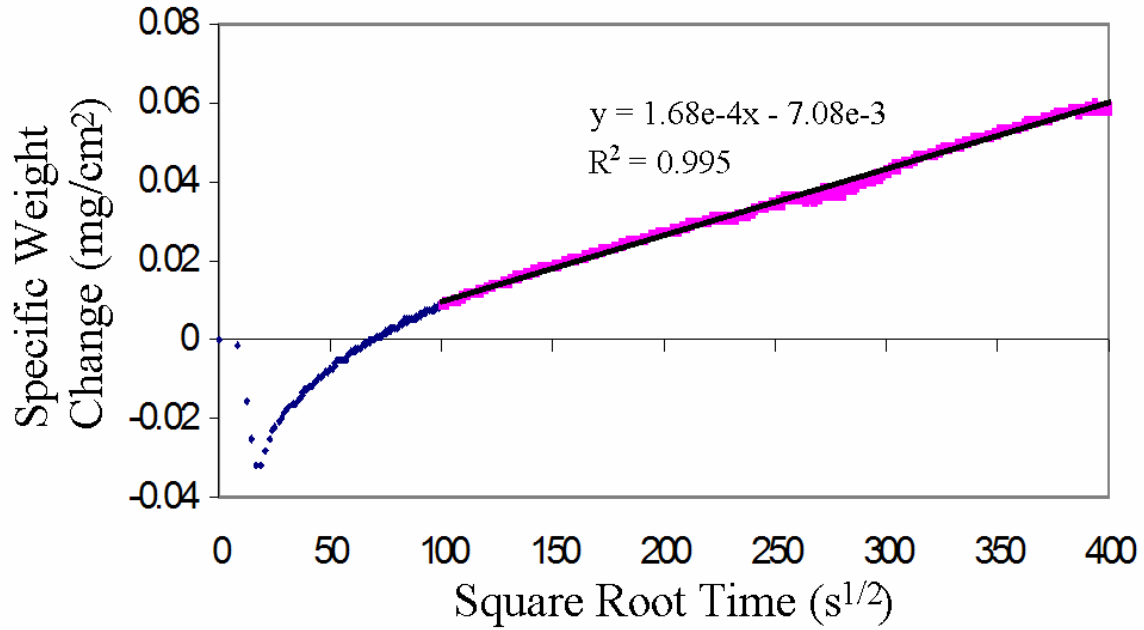


Figure 5-18. Plot of weight change versus square root time for a Ni-22Cr-11Al specimen at 800°C for 100 hr in He + 0.21 O<sub>2</sub> + 0.10 SO<sub>2</sub>. The formula containing the slope and the coefficient of determination are listed.

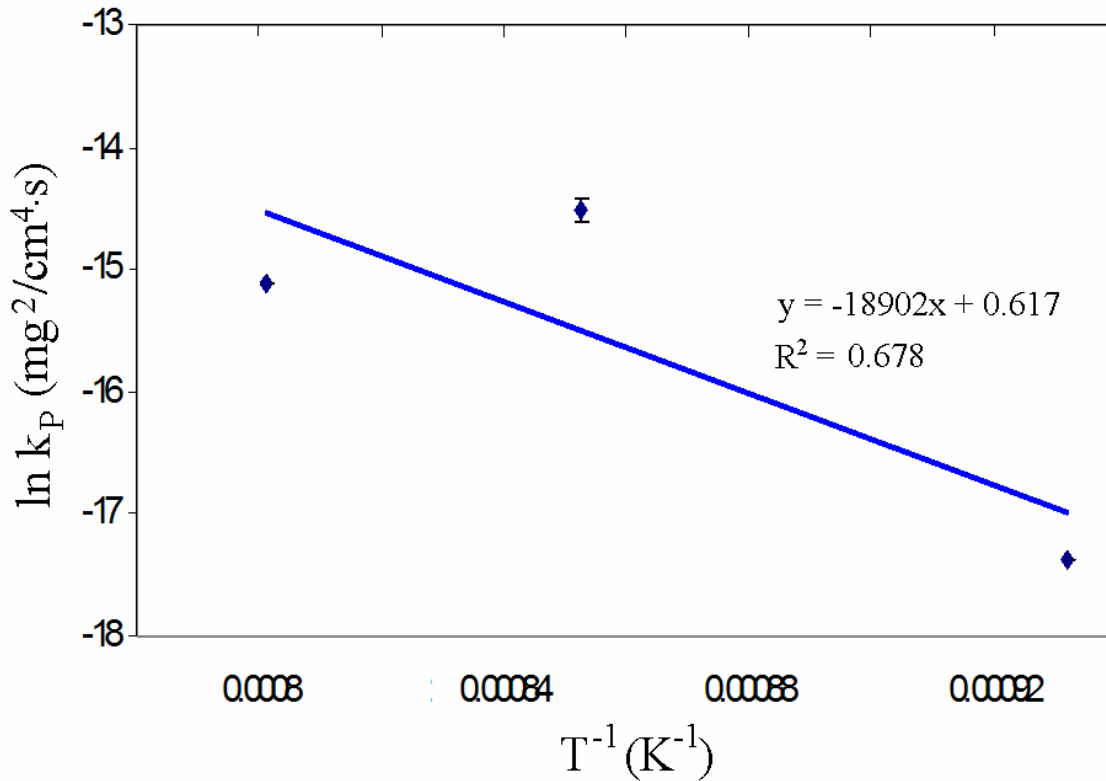


Figure 5-19. Arrhenius plot of the parabolic rate constant versus inverse temperature of Ni-22Cr-11Al oxidized for 100 hr in He + 0.21 O<sub>2</sub> + 0.10 SO<sub>2</sub>. The formula containing the slope and the coefficient of determination are listed.

Table 5-1. List of the parabolic rate constants obtained from steady-state oxidation of Ni, Ni-13.6Al, NiAl, Ni-8Cr-6Al, and Ni-22Cr-11Al alloys.

Alloy Name	Atmosphere (bar)	Temperature (°C)	$k_p$ (mg/cm <sup>2</sup> ·s <sup>1/2</sup> )	$k_p$ (mg <sup>2</sup> /cm <sup>4</sup> ·s)
Ni	Air	800	3.13E-03	9.82E-06
Ni	Air	900	6.42E-03	4.12E-05
Ni	Air	1000	1.20E-02	1.43E-04
Ni	Air	1100	1.97E-02	3.89E-04
Ni-13.6Al	Air	800	1.15E-04	1.31E-08
Ni-13.6Al	Air	900	3.20E-04	1.02E-07
Ni-13.6Al	Air	1000	2.45E-04	6.02E-08
Ni-22Cr-11Al	Air	800	4.08E-04	1.66E-07
Ni-22Cr-11Al	Air	900	6.10E-04	3.72E-07
Ni-22Cr-11Al	Air	1000	5.05E-04	2.55E-07
Ni-22Cr-11Al	He + 0.21 O <sub>2</sub> + 0.02 SO <sub>2</sub>	800	2.28E-04	5.20E-08
Ni-22Cr-11Al	He + 0.21 O <sub>2</sub> + 0.02 SO <sub>2</sub>	900	4.00E-04	1.60E-07
Ni-22Cr-11Al	He + 0.21 O <sub>2</sub> + 0.02 SO <sub>2</sub>	975	5.39E-04	2.91E-07
Ni-22Cr-11Al	He + 0.21 O <sub>2</sub> + 0.10 SO <sub>2</sub>	800	1.68E-04	2.82E-08
Ni-22Cr-11Al	He + 0.21 O <sub>2</sub> + 0.10 SO <sub>2</sub>	900	7.05E-04	4.97E-07
Ni-22Cr-11Al	He + 0.21 O <sub>2</sub> + 0.10 SO <sub>2</sub>	975	5.19E-04	2.69E-07
Ni-31Al	Air	800	4.83E-04	2.33E-07
Ni-31Al	Air	900	1.10E-03	1.20E-06
Ni-31Al	Air	1000	1.95E-03	3.82E-06
Ni-8Cr-6Al	Air	800	1.58E-03	2.50E-06
Ni-8Cr-6Al	Air	900	5.31E-04	2.82E-07
Ni-8Cr-6Al	Air	1000	1.94E-03	3.76E-06
Ni-8Cr-6Al	He + 0.21 O <sub>2</sub> + 0.02 SO <sub>2</sub>	800	1.24E-04	1.54E-08
Ni-8Cr-6Al	He + 0.21 O <sub>2</sub> + 0.02 SO <sub>2</sub>	900	1.32E-03	1.74E-06
Ni-8Cr-6Al	He + 0.21 O <sub>2</sub> + 0.02 SO <sub>2</sub>	975	3.14E-03	9.86E-06
Ni-8Cr-6Al	He + 0.21 O <sub>2</sub> + 0.10 SO <sub>2</sub>	800	9.33E-04	8.70E-07
Ni-8Cr-6Al	He + 0.21 O <sub>2</sub> + 0.10 SO <sub>2</sub>	900	4.54E-03	2.06E-05
Ni-8Cr-6Al	He + 0.21 O <sub>2</sub> + 0.10 SO <sub>2</sub>	975	6.82E-03	4.64E-05

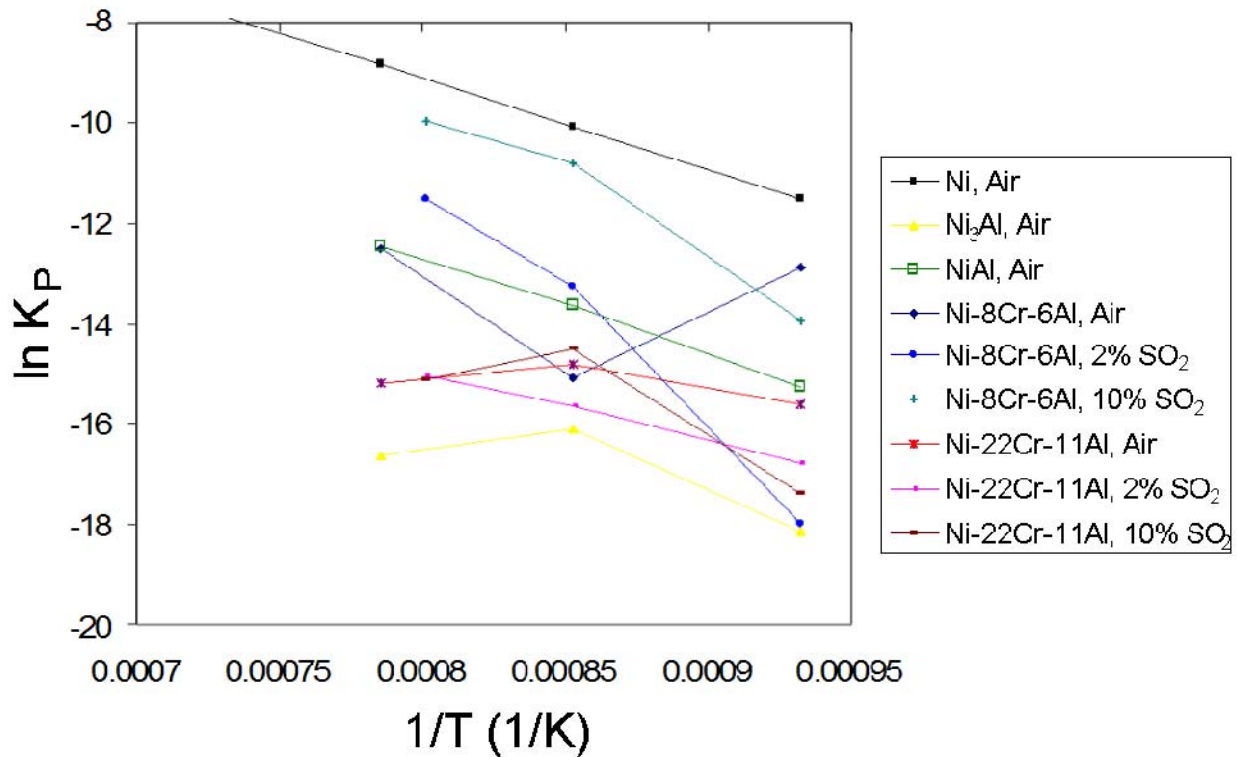


Figure 5-20. Arrhenius plot of alloys isothermally oxidized in this study for 100 hr.

## 5.2 Phase Identification

The identification of phases was performed using the APD3720 XRD and compared the d-spacings of the peak intensities with those of cataloged JCPDS files. This section shows the XRD results from the tests described in Section 5.1 on the Ni-8Cr-6Al and Ni-22Cr-11 Al alloys.

Figure 5-21 shows the XRD results of a polished, heat-treated specimen of Ni-8Cr-6Al. The peaks identified show the presence of Ni, Ni<sub>3</sub>Al, and possibly some Al<sub>2</sub>O<sub>3</sub>. This oxide might be residual from the alumina polished used in sample preparation, as it is not expected. Figures 5-22, 5-23, and 5-24 show the XRD results of Ni-8Cr-6Al oxidized in air for 100 hr at 800, 900, and 1000°C, respectively. Comparing these with Figure 5-21, one can see the emergence of NiO and Al<sub>2</sub>O<sub>3</sub>. All Al<sub>2</sub>O<sub>3</sub> identified from these XRD studies is the stable  $\alpha$  phase. At 800°C, some chromia is seen, and at 1000°C, NiAl<sub>2</sub>O<sub>4</sub> spinel is present. The peak heights of the Ni and  $\gamma'$  fluctuate between all four figures, but they will not be used in this study to

determine the phase percentages. The figures with higher alumina peaks have corresponding higher Ni peaks, and those with lower alumina and/or higher NiO have higher Ni<sub>3</sub>Al peaks. This is likely due to a depletion of one element near the surface if one oxide is more prevalent, and would thus show more of either  $\gamma$  or  $\gamma'$  accordingly.

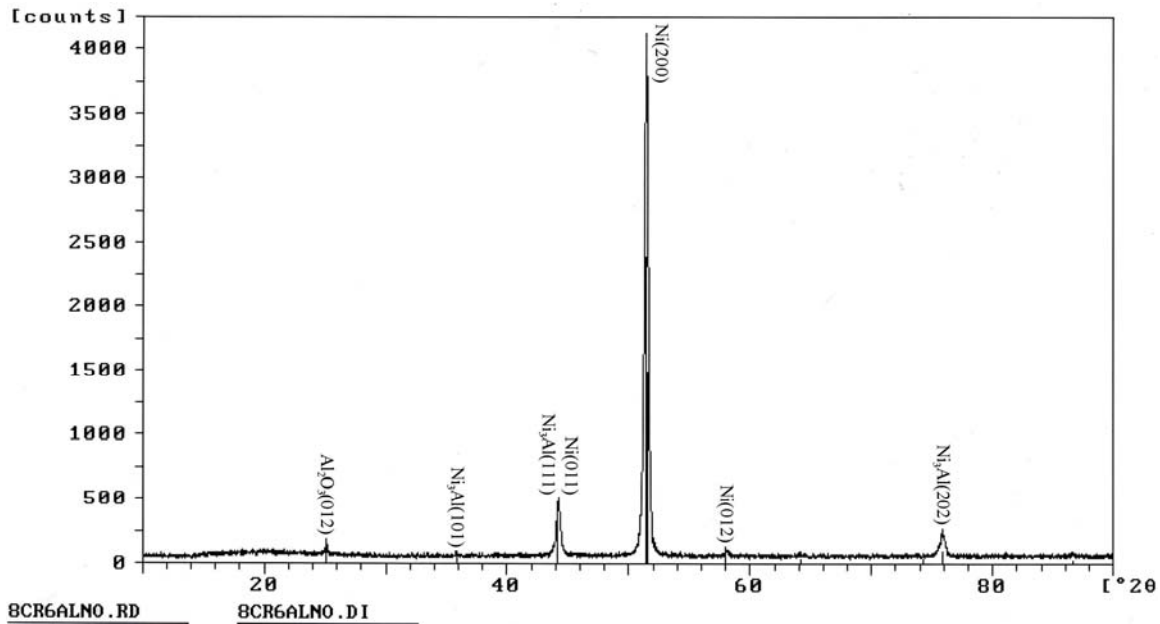


Figure 5-21. Histogram of the peak intensities measured from an XRD analysis of polished, heat treated Ni-8Cr-6Al.

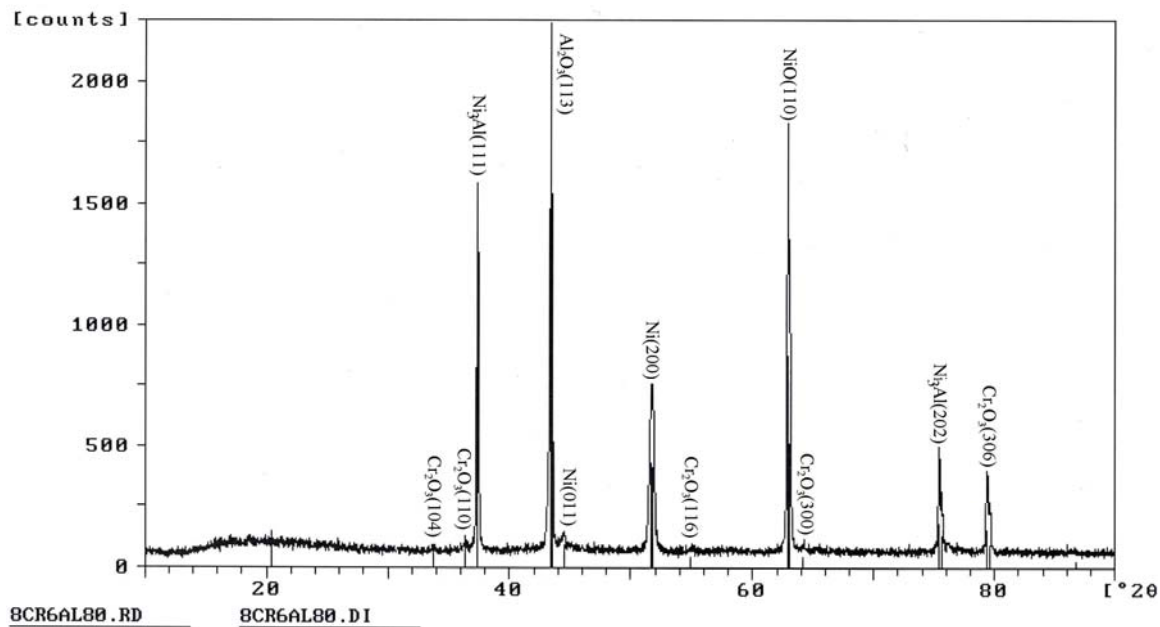


Figure 5-22. Histogram of the peak intensities measured from an XRD analysis of Ni-8Cr-6Al oxidized in air for 100 hr at 800°C.

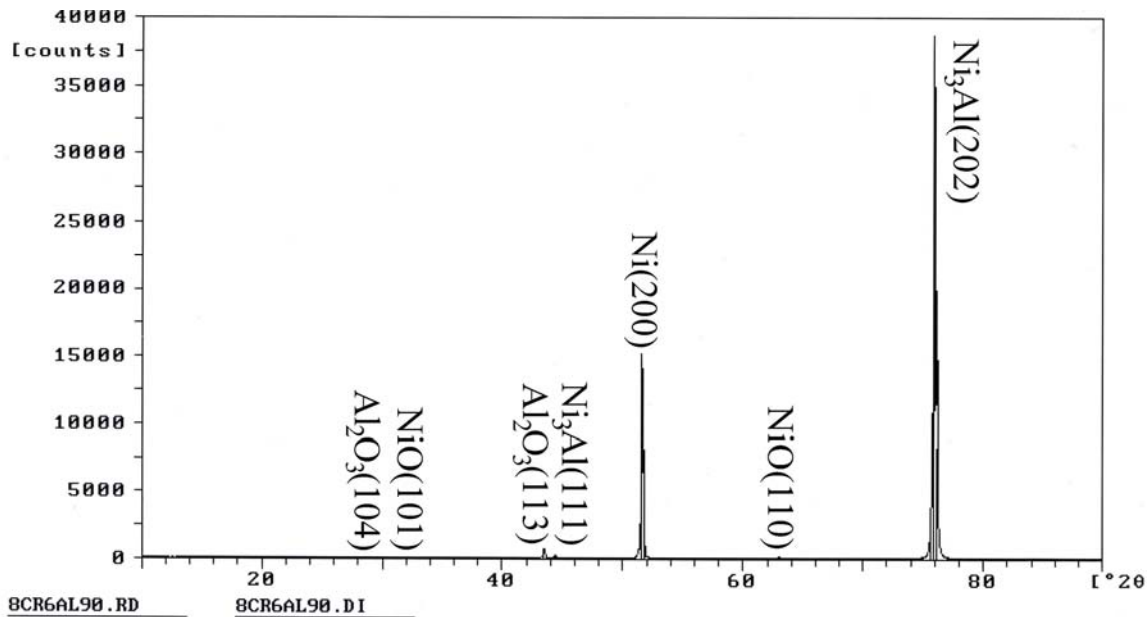


Figure 5-23. Histogram of the peak intensities measured from an XRD analysis of Ni-8Cr-6Al oxidized in air for 100 hr at 900°C.

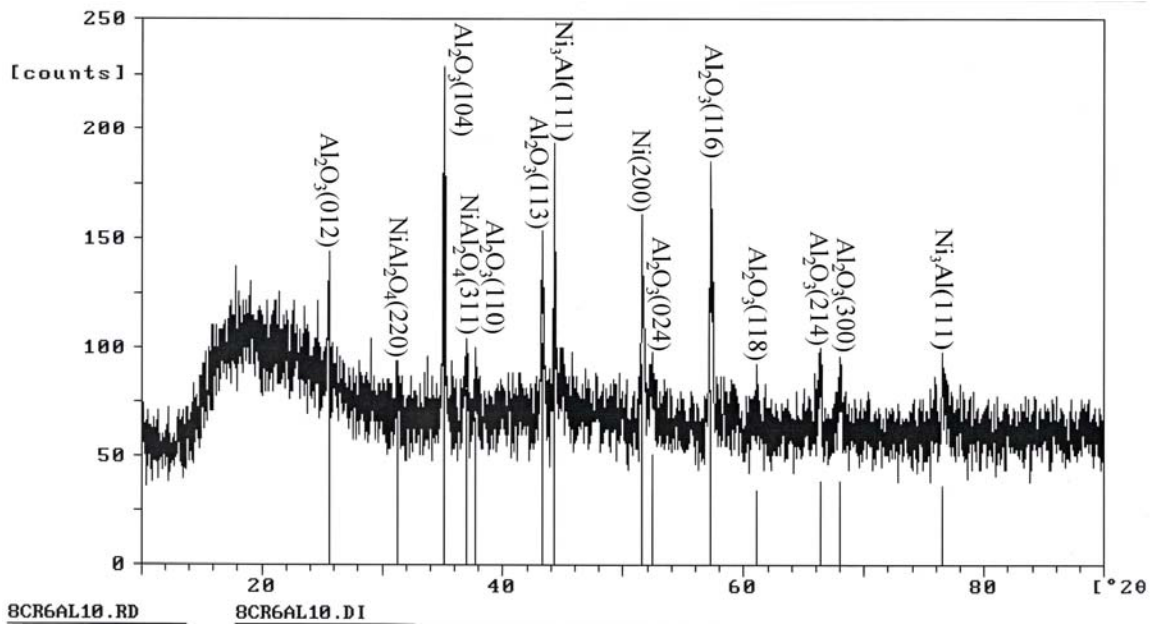


Figure 5-24. Histogram of the peak intensities measured from an XRD analysis of Ni-8Cr-6Al oxidized in air for 100 hr at 1000°C.

Figures 5-25, 5-26, and 5-27 show the XRD data for Ni-8Cr-6Al oxidized in 2% SO<sub>2</sub> for 800, 900, and 975°C, respectively. As with the samples oxidized in air, alumina and NiO are present. However, chromia is present at all temperatures, not just at 800°C. The spinel phase is also shown for the higher temperatures of 900 and 975°C. Those specimens oxidized in 10%

SO<sub>2</sub> show similar results with those oxidized in 2% SO<sub>2</sub>, as shown in Figures 5-28, 5-29, and 5-30 for 800, 900, and 975°C, respectively. However, spinel is only seen on the 900°C sample, and it is the NiCr<sub>2</sub>O<sub>4</sub> (not NiAl<sub>2</sub>O<sub>4</sub>) phase. NiO was found at the lowest temperature, but not at the others. In addition, a sulfide peak (Ni<sub>3</sub>S<sub>2</sub>) may have been detected from the 800°C sample, likely from a spot where the oxide had spalled revealing the interface underneath.

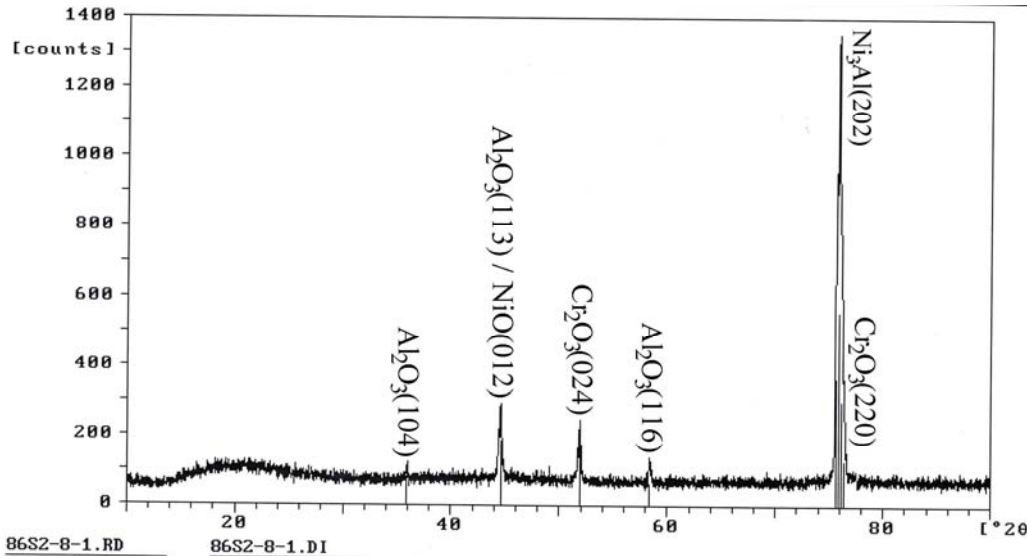


Figure 5-25. Histogram of the peak intensities measured from an XRD analysis of Ni-8Cr-6Al oxidized in He + 0.21 O<sub>2</sub> + 0.02 SO<sub>2</sub> for 100 hr at 800°C.

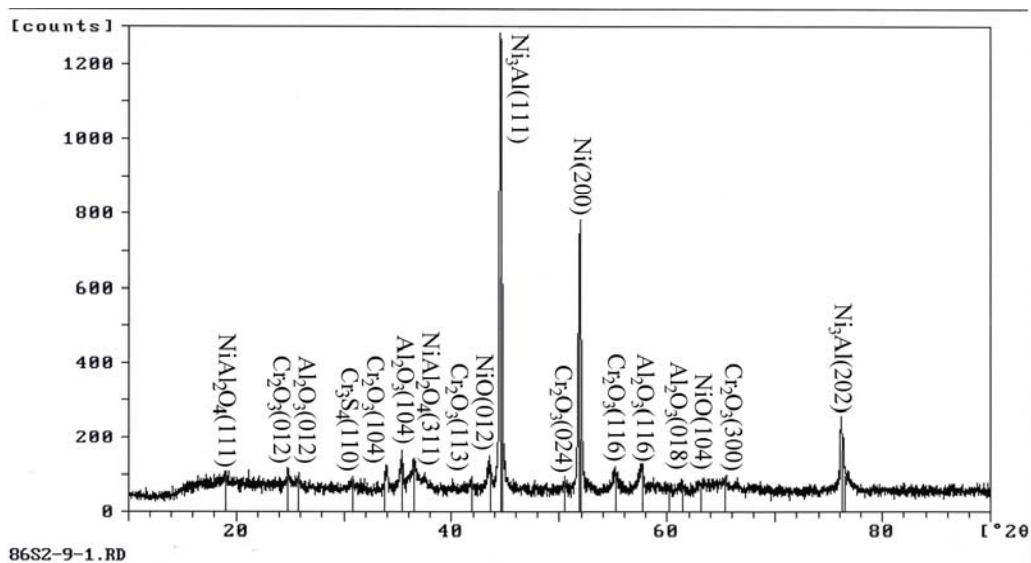


Figure 5-26. Histogram of the peak intensities measured from an XRD analysis of Ni-8Cr-6Al oxidized in He + 0.21 O<sub>2</sub> + 0.02 SO<sub>2</sub> for 100 hr at 900°C.

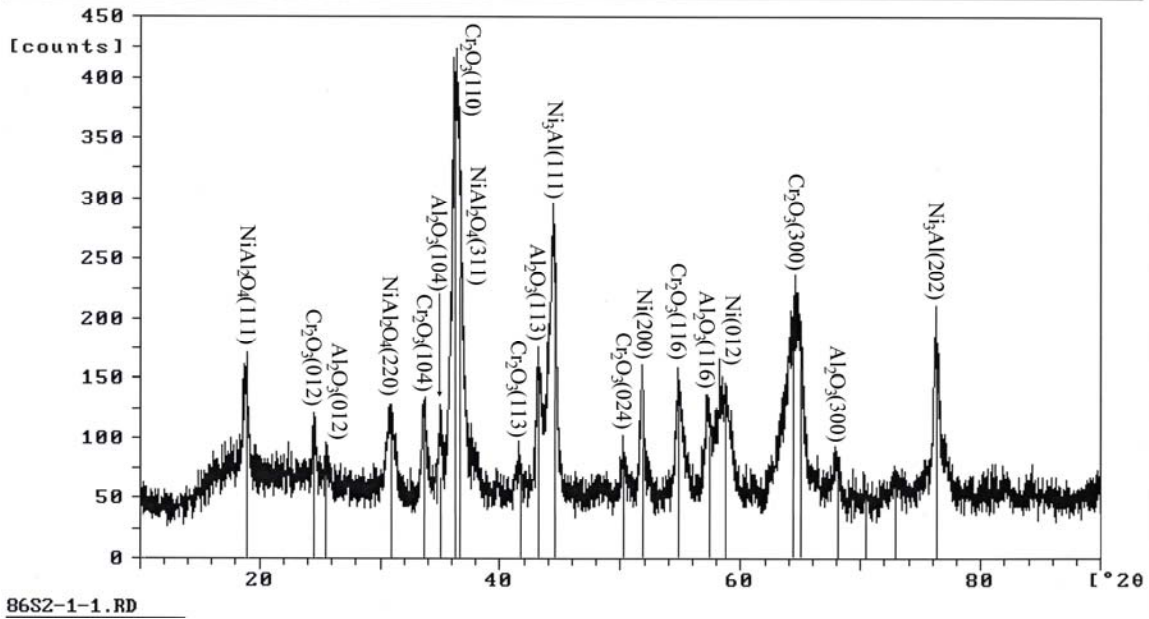


Figure 5-27. Histogram of the peak intensities measured from an XRD analysis of Ni-8Cr-6Al oxidized in He + 0.21 O<sub>2</sub> + 0.02 SO<sub>2</sub> for 100 hr at 975°C.

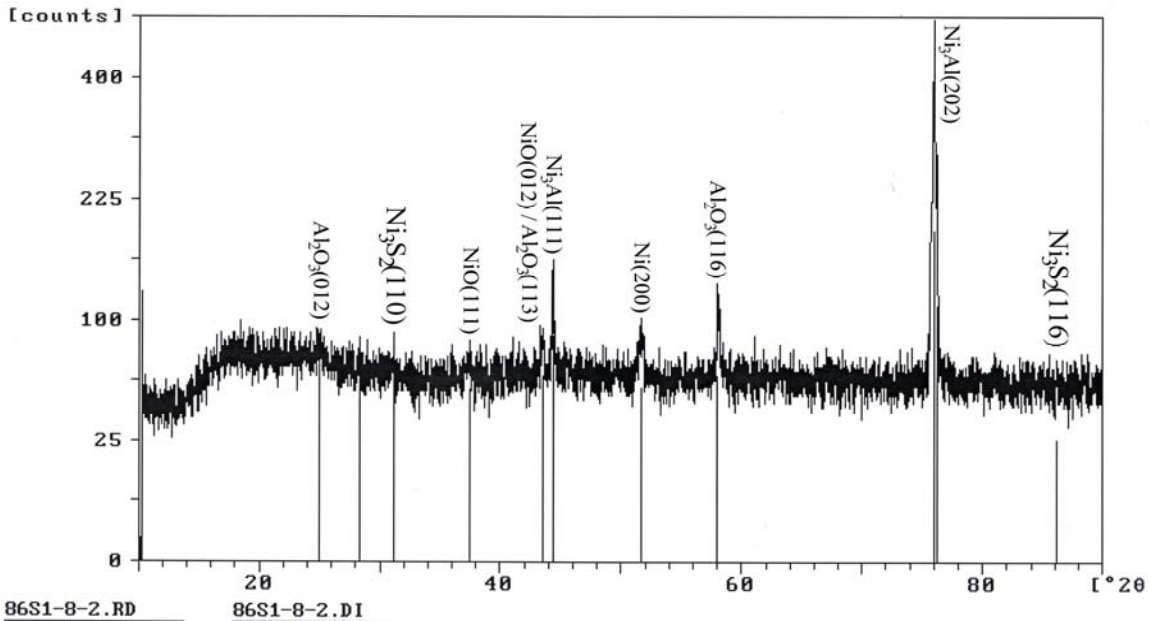


Figure 5-28. Histogram of the peak intensities measured from an XRD analysis of Ni-8Cr-6Al oxidized in He + 0.21 O<sub>2</sub> + 0.10 SO<sub>2</sub> for 100 hr at 800°C.

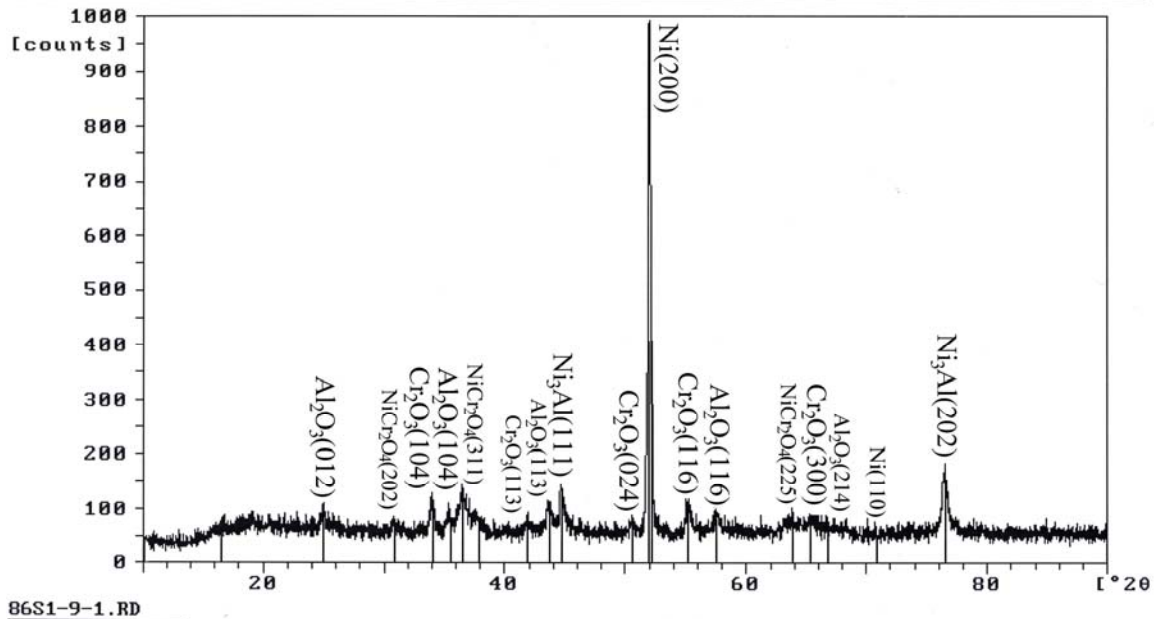


Figure 5-29. Histogram of the peak intensities measured from an XRD analysis of Ni-8Cr-6Al oxidized in He + 0.21 O<sub>2</sub> + 0.10 SO<sub>2</sub> for 100 hr at 900°C.

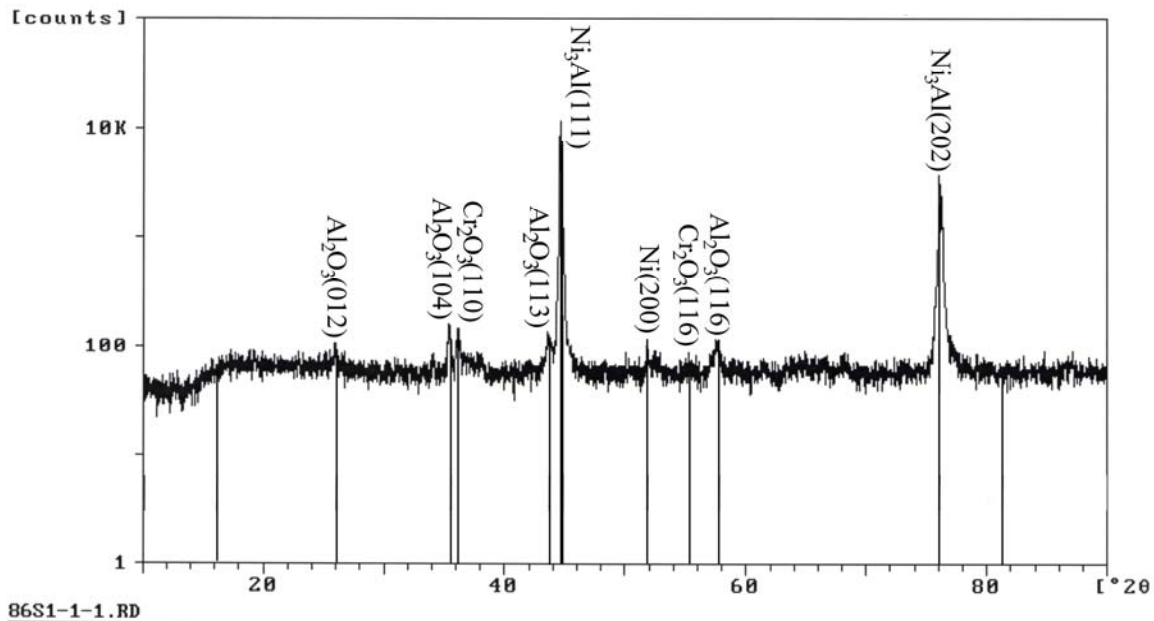


Figure 5-30. Histogram of the peak intensities measured from an XRD analysis of Ni-8Cr-6Al oxidized in He + 0.21 O<sub>2</sub> + 0.10 SO<sub>2</sub> for 100 hr at 975°C.

The XRD data of polished, heat-treated Ni-22Cr-11Al is shown in Figure 5-31, and the samples oxidized in air at 800, 900, and 1000°C are shown in Figures 5-32, 5-33, and 5-34, respectively. The unoxidized specimen of Ni-22Cr-11Al contains Ni, Ni<sub>3</sub>Al, NiAl, and Cr, as well as the one alumina peak. Upon oxidation, chromia and alumina are formed. NiAl<sub>2</sub>O<sub>4</sub> spinel

was also identified for the sample oxidized at 900°C. The formation of Al<sub>2</sub>O<sub>3</sub> corresponded with the loss of NiAl peaks, as this phase was likely consumed during the experiments. Also, the amount of γ' present decreased relative to Ni (except at 1000°C). The addition of 2% SO<sub>2</sub> showed little difference with the XRD data of the oxidized samples, as seen in Figures 5-35, 5-36, and 5-37 for 800, 900, and 975°C, respectively. Two Ni<sub>3</sub>S<sub>2</sub> peaks were observed on the specimen exposed at 975°C, likely from areas of oxide spallation, which was observed on this sample. At 10% SO<sub>2</sub> (as seen in Figures 5-38, 5-39, and 5-40 for 800, 900, and 975°C, respectively), more sulfide peaks were observed. As with the 2%, some Ni<sub>3</sub>S<sub>2</sub> was observed at 800°C, but was a different phase at 900°C—Ni<sub>3</sub>S<sub>4</sub>. At 975°C, Cr sulfide in the form of Cr<sub>3</sub>S<sub>4</sub> was identified. Not all of these samples showed spallation, so some of the sulfides may be present in the oxide or in larger amounts than other sample runs. Table 5-2 summarizes the phases identified from the XRD measurements.

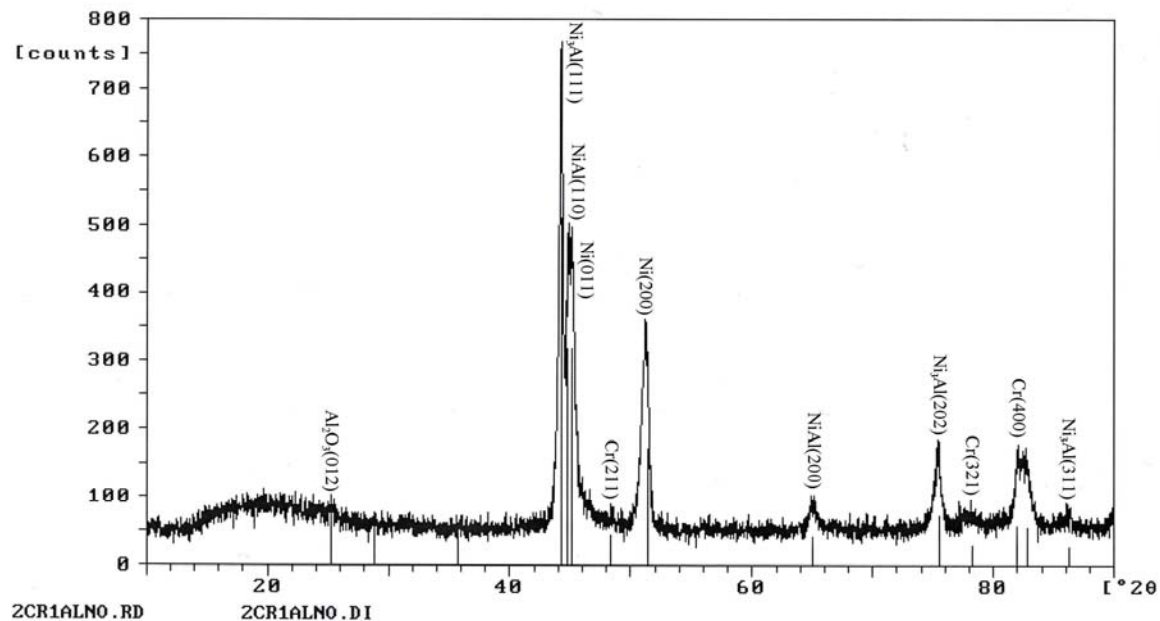


Figure 5-31. Histogram of the peak intensities measured from an XRD analysis of polished, heat treated Ni-22Cr-11Al.

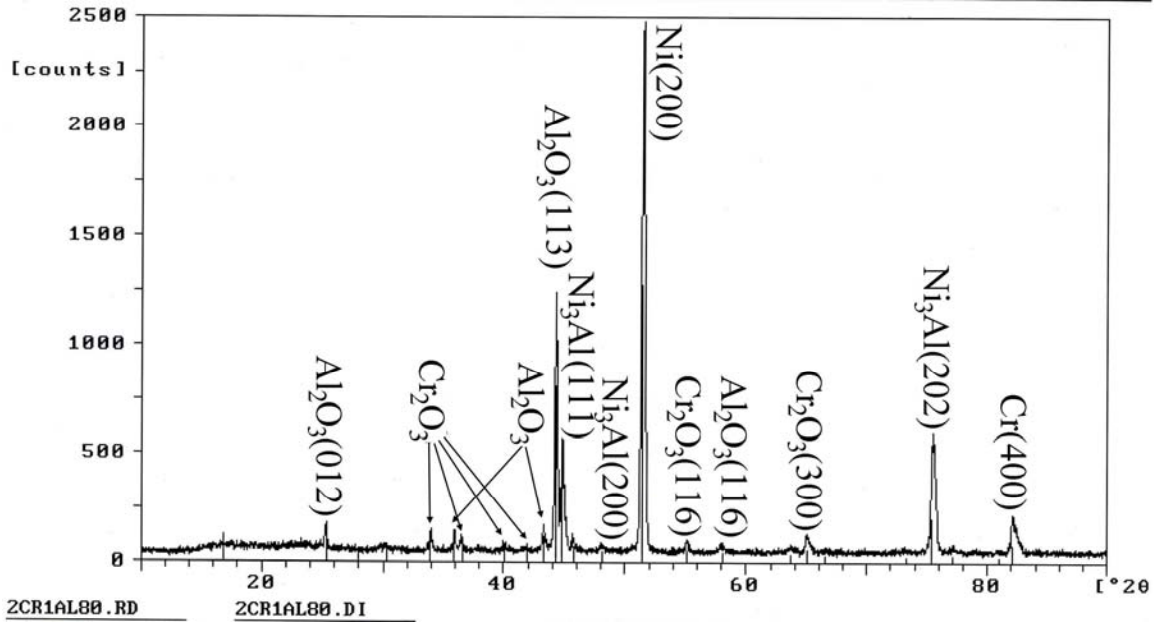


Figure 5-32. Histogram of the peak intensities measured from an XRD analysis of Ni-22Cr-11Al oxidized in air for 100 hr at 800°C.

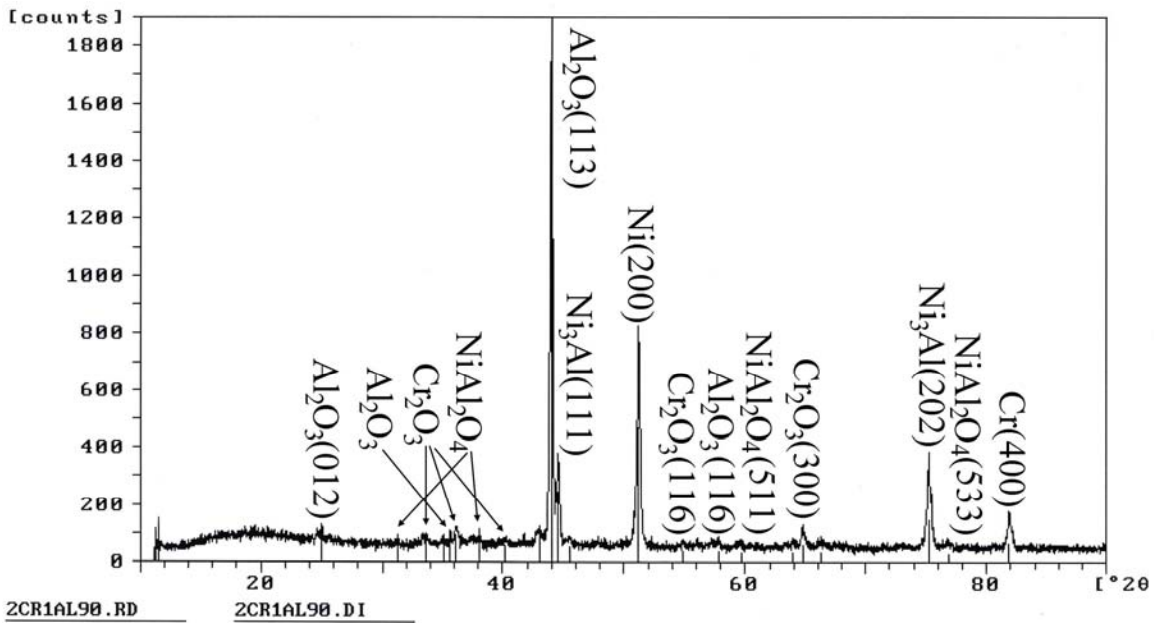


Figure 5-33. Histogram of the peak intensities measured from an XRD analysis of Ni-22Cr-11Al oxidized in air for 100 hr at 900°C.

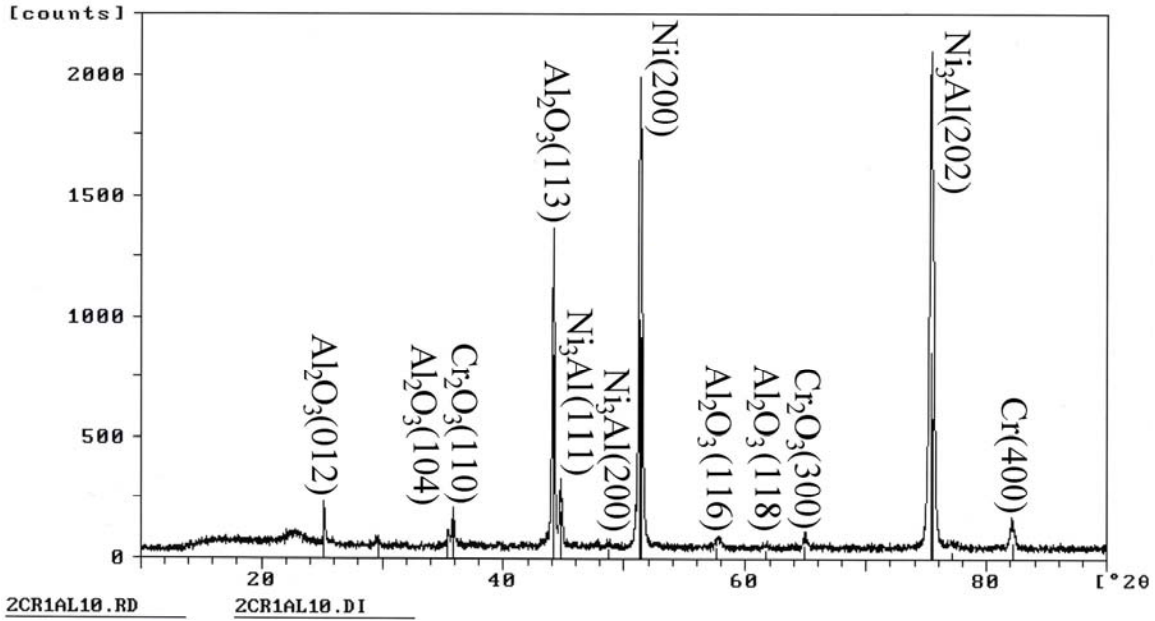


Figure 5-34. Histogram of the peak intensities measured from an XRD analysis of Ni-22Cr-11Al oxidized in air for 100 hr at 1000°C.

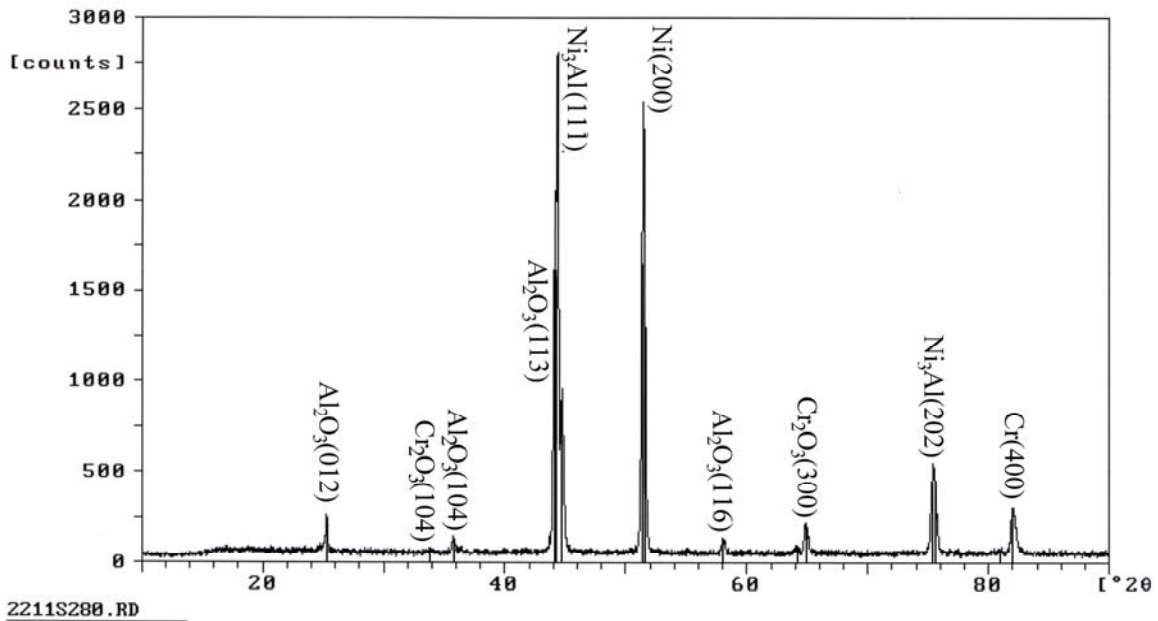


Figure 5-35. Histogram of the peak intensities measured from an XRD analysis of Ni-22Cr-11Al oxidized in He + 0.21 O<sub>2</sub> + 0.02 SO<sub>2</sub> for 100 hr at 800°C.

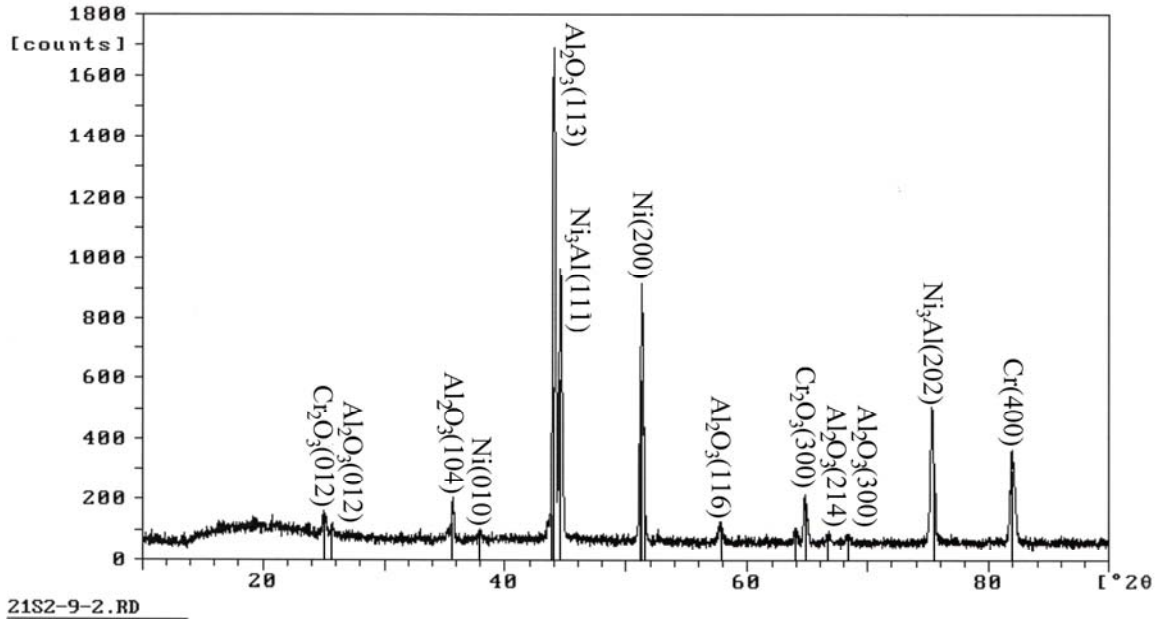


Figure 5-36. Histogram of the peak intensities measured from an XRD analysis of Ni-22Cr-11Al oxidized in He + 0.21 O<sub>2</sub> + 0.02 SO<sub>2</sub> for 100 hr at 900°C.

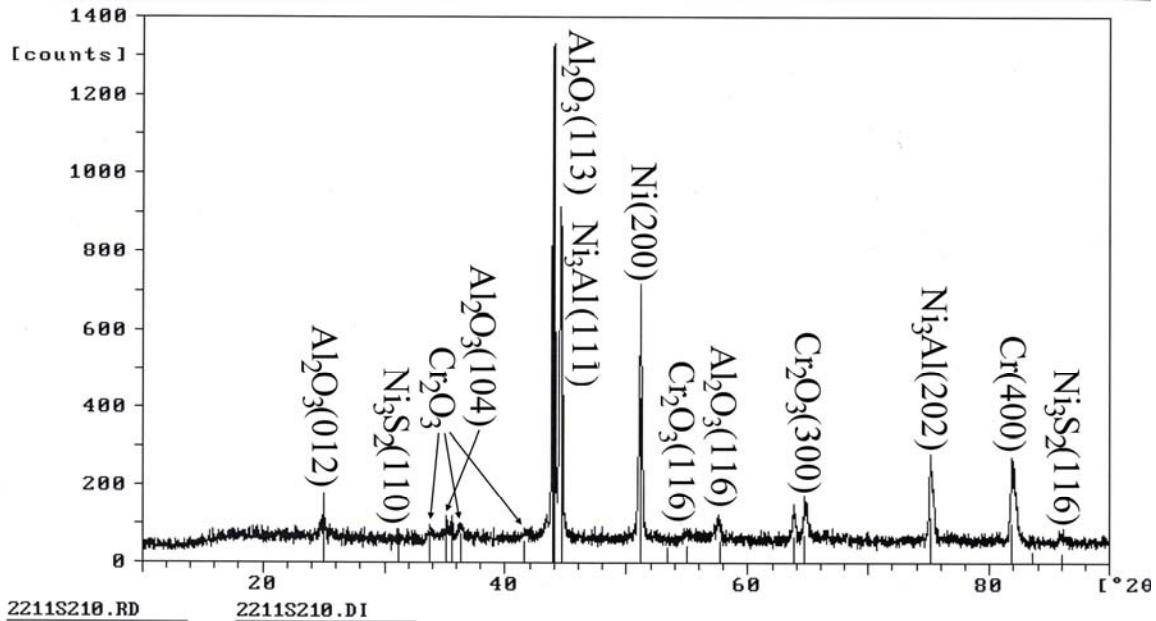


Figure 5-37. Histogram of the peak intensities measured from an XRD analysis of Ni-22Cr-11Al oxidized in He + 0.21 O<sub>2</sub> + 0.02 SO<sub>2</sub> for 100 hr at 975°C.

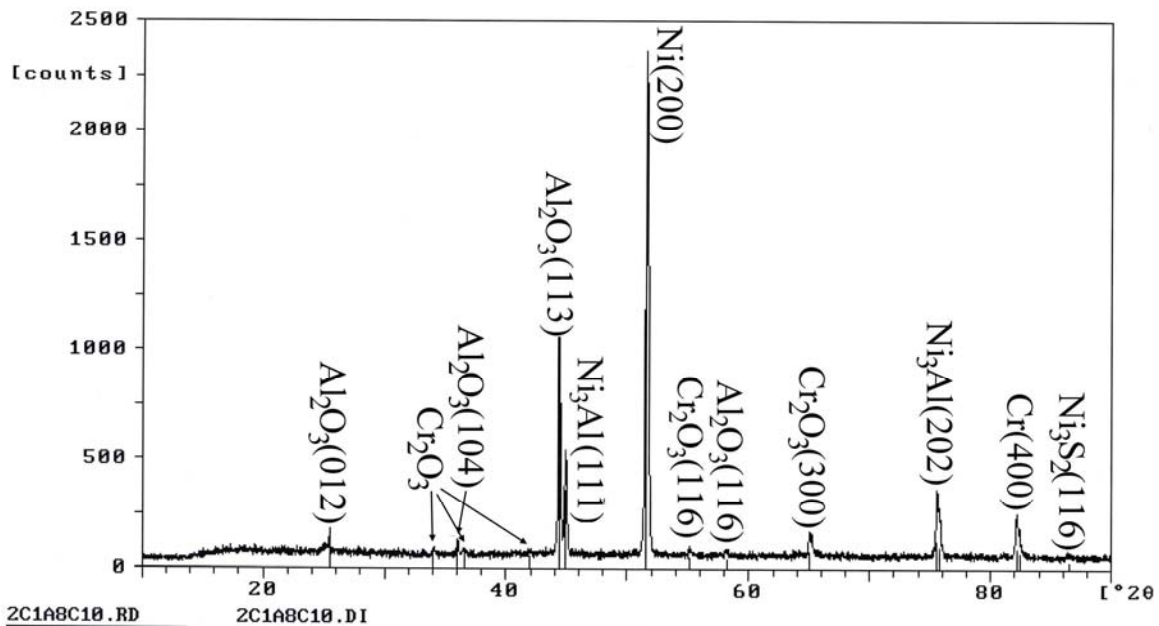


Figure 5-38. Histogram of the peak intensities measured from an XRD analysis of Ni-22Cr-11Al oxidized in He + 0.21 O<sub>2</sub> + 0.10 SO<sub>2</sub> for 100 hr at 800°C.

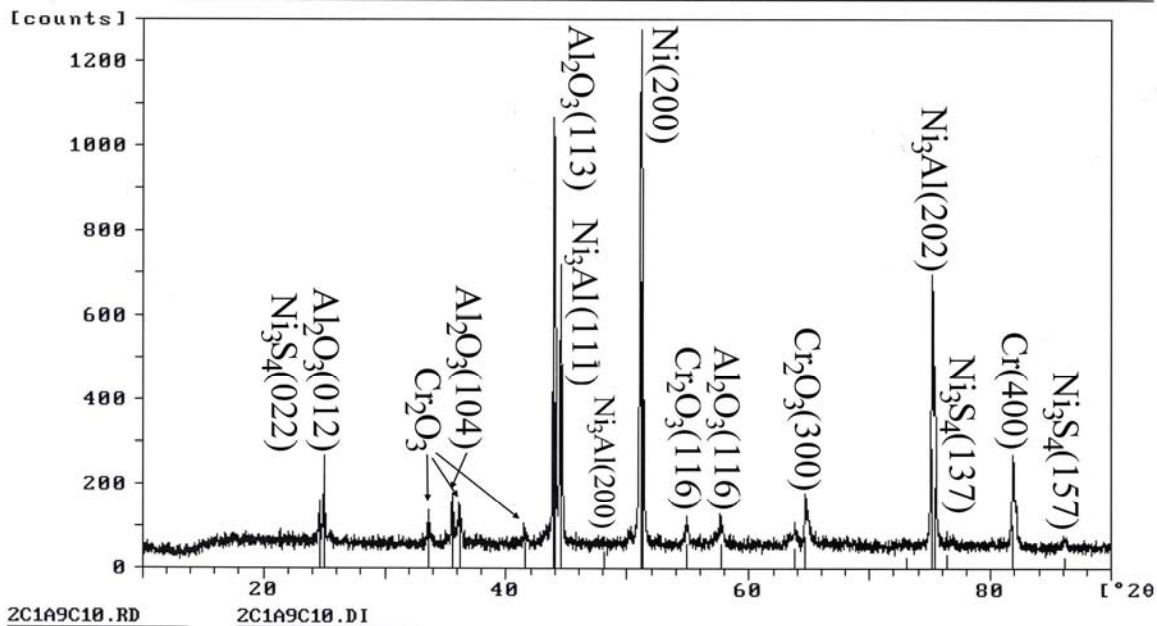


Figure 5-39. Histogram of the peak intensities measured from an XRD analysis of Ni-22Cr-11Al oxidized in He + 0.21 O<sub>2</sub> + 0.10 SO<sub>2</sub> for 100 hr at 900°C.

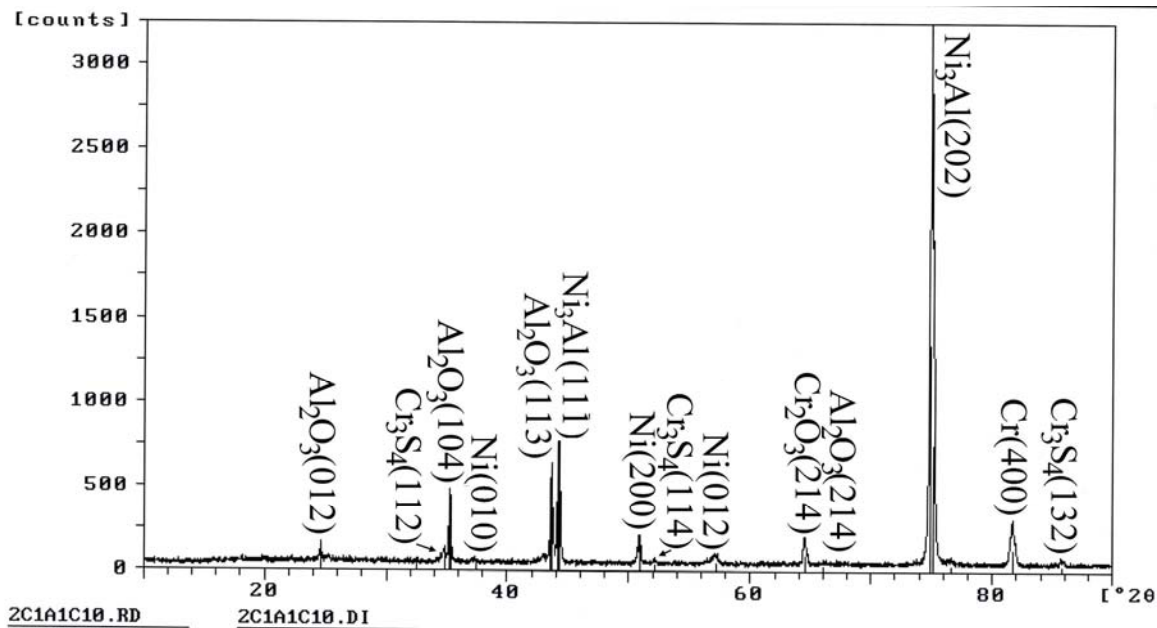


Figure 5-40. Histogram of the peak intensities measured from an XRD analysis of Ni-22Cr-11Al oxidized in He + 0.21 O<sub>2</sub> + 0.10 SO<sub>2</sub> for 100 hr at 975°C.

### 5.3 Surface Imaging

#### 5.3.1 Untested Alloy Specimens

After casting, some of the specimens were inspected using optical and scanning electron microscopy. Figure 5-41 shows an optical micrograph of the microstructure of the Ni-8Cr-6Al composition as cast. Figure 5-42 shows the microstructure of the same composition, but after the 4 hr heat treatment at 1200°C in vacuum. It is clear that the grain size increased due to the heat treatment. Analysis of the grain size showed that the as cast material had a size of  $260 \pm 91 \mu\text{m}$ , and after heat treatment was  $432 \pm 90 \mu\text{m}$ . In addition, there was less porosity seen after heat treatment. From Figures 5-41 and 5-42, it appears as though there the grains are single-phase  $\gamma$ . However, SEM reveals that there are randomly sized precipitates of  $\gamma'$  throughout the microstructure (Figure 5-43), which decreased in size and become cuboidal after heat treatment (Figure 5-44).

Table 5-2. Table summarizing the phases identified using XRD for all cast, heat-treated alloys oxidized.

Alloy	Environment	Temperature (°C)	Metallic Phases	Oxides	Sulfides?
Ni-8Cr-6Al	None	None	Ni, $\gamma'$	Al <sub>2</sub> O <sub>3</sub>	
	Air	800	$\gamma'$ , Ni	Al <sub>2</sub> O <sub>3</sub> , NiO, Cr <sub>2</sub> O <sub>3</sub>	
	Air	900	$\gamma'$ , Ni	Al <sub>2</sub> O <sub>3</sub> , NiO	
	Air	1000	$\gamma'$ , Ni	Al <sub>2</sub> O <sub>3</sub> , NiAl <sub>2</sub> O <sub>4</sub>	
	21% O <sub>2</sub> + 2% SO <sub>2</sub>	800	$\gamma'$	Al <sub>2</sub> O <sub>3</sub> , NiO, Cr <sub>2</sub> O <sub>3</sub>	
	21% O <sub>2</sub> + 2% SO <sub>2</sub>	900	$\gamma'$ , Ni	Al <sub>2</sub> O <sub>3</sub> , NiO, NiAl <sub>2</sub> O <sub>4</sub> , Cr <sub>2</sub> O <sub>3</sub>	Cr <sub>3</sub> S <sub>4</sub>
	21% O <sub>2</sub> + 2% SO <sub>2</sub>	975	$\gamma'$ , Ni	Cr <sub>2</sub> O <sub>3</sub> , NiCr <sub>2</sub> O <sub>4</sub> , Al <sub>2</sub> O <sub>3</sub>	
	21% O <sub>2</sub> + 10% SO <sub>2</sub>	800	$\gamma'$ , Ni	Al <sub>2</sub> O <sub>3</sub> , NiO	Ni <sub>3</sub> S <sub>2</sub>
	21% O <sub>2</sub> + 10% SO <sub>2</sub>	900	$\gamma'$ , Ni	Al <sub>2</sub> O <sub>3</sub> , Cr <sub>2</sub> O <sub>3</sub> , NiCr <sub>2</sub> O <sub>4</sub>	
	21% O <sub>2</sub> + 10% SO <sub>2</sub>	975	$\gamma'$ , Ni	Al <sub>2</sub> O <sub>3</sub> , Cr <sub>2</sub> O <sub>3</sub>	
Ni-22Cr-11Al	None	None	$\gamma'$ , Ni, $\beta$ , Cr	Al <sub>2</sub> O <sub>3</sub>	
	Air	800	Ni, $\gamma'$ , Cr	Al <sub>2</sub> O <sub>3</sub> , Cr <sub>2</sub> O <sub>3</sub>	
	Air	900	Ni, $\gamma'$ , Cr	Al <sub>2</sub> O <sub>3</sub> , Cr <sub>2</sub> O <sub>3</sub>	
	Air	1000	$\gamma'$ , Ni, Cr	Al <sub>2</sub> O <sub>3</sub> , Cr <sub>2</sub> O <sub>3</sub>	
	21% O <sub>2</sub> + 2% SO <sub>2</sub>	800	$\gamma'$ , Ni, Cr	Al <sub>2</sub> O <sub>3</sub> , Cr <sub>2</sub> O <sub>3</sub>	
	21% O <sub>2</sub> + 2% SO <sub>2</sub>	900	$\gamma'$ , Ni, Cr	Al <sub>2</sub> O <sub>3</sub> , Cr <sub>2</sub> O <sub>3</sub>	
	21% O <sub>2</sub> + 2% SO <sub>2</sub>	975	$\gamma'$ , Ni, Cr	Al <sub>2</sub> O <sub>3</sub> , Cr <sub>2</sub> O <sub>3</sub>	Ni <sub>3</sub> S <sub>2</sub>
	21% O <sub>2</sub> + 10% SO <sub>2</sub>	800	Ni, $\gamma'$ , Cr	Al <sub>2</sub> O <sub>3</sub> , Cr <sub>2</sub> O <sub>3</sub>	Ni <sub>3</sub> S <sub>2</sub>
	21% O <sub>2</sub> + 10% SO <sub>2</sub>	900	Ni, $\gamma'$ , Cr	Al <sub>2</sub> O <sub>3</sub> , Cr <sub>2</sub> O <sub>3</sub>	Ni <sub>3</sub> S <sub>4</sub>
	21% O <sub>2</sub> + 10% SO <sub>2</sub>	975	$\gamma'$ , Ni, Cr	Al <sub>2</sub> O <sub>3</sub> , Cr <sub>2</sub> O <sub>3</sub>	Cr <sub>3</sub> S <sub>4</sub>



Figure 5-41. Optical micrograph of as cast Ni-8Cr-6Al at 125X.

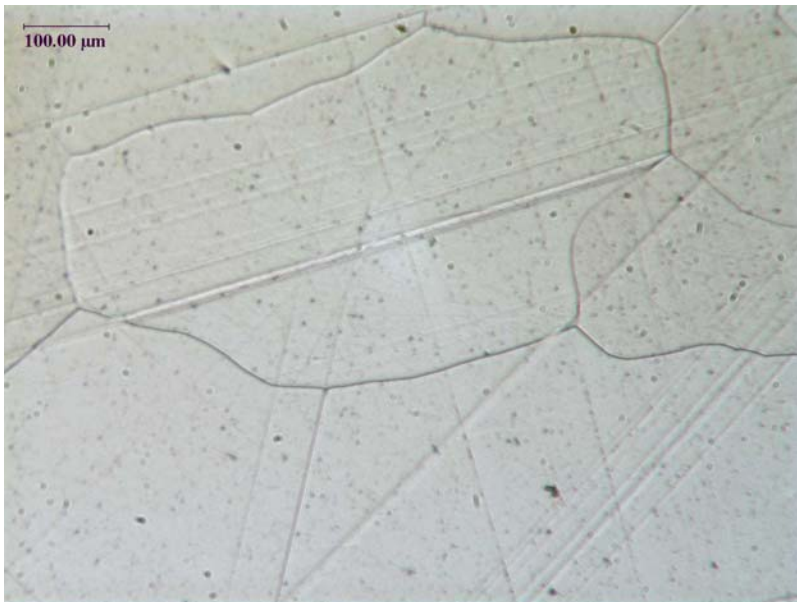


Figure 5-42. Optical micrograph of heat-treated Ni-8Cr-6Al at 125X.

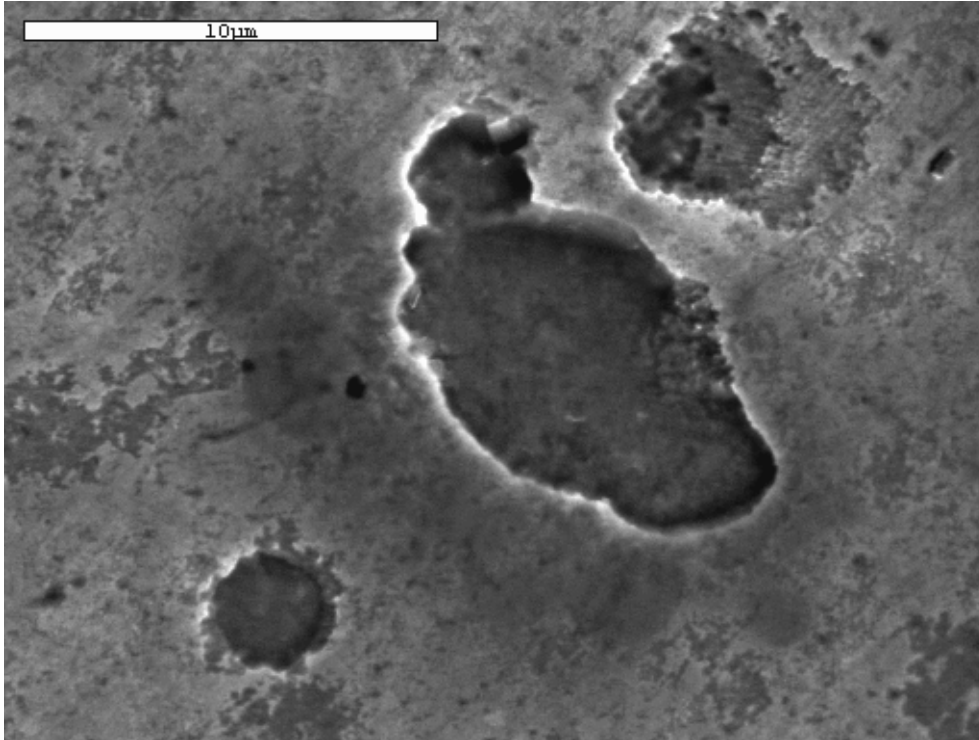


Figure 5-43. Secondary electron (SE) micrograph of as cast Ni-8Cr-6Al microstructure at 5000X.

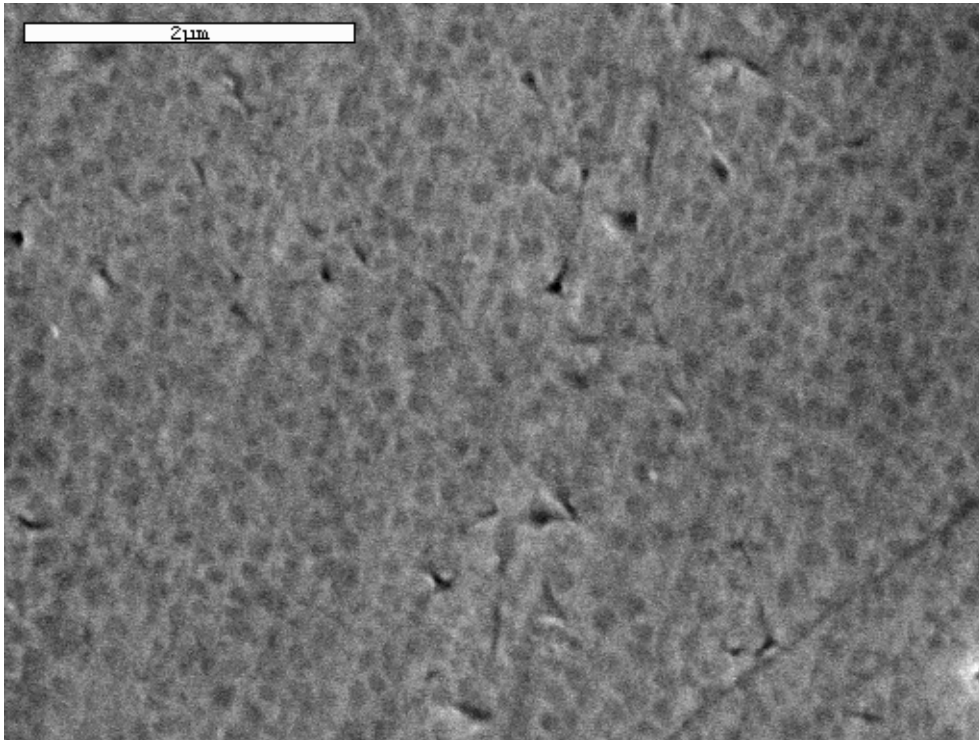


Figure 5-44. SE micrograph of heat-treated Ni-8Cr-6Al microstructure at 20000X.

Figure 5-45 shows the as-cast microstructure of the Ni-22Cr-11Al composition, and Figure 5-46 shows the same alloy composition after heat-treatment. Both figures show a variety of

phases present with a dendritic structure in the as cast specimen. This is ameliorated in the heat-treated specimens and grain growth is observed— $185 \pm 32 \mu\text{m}$  in the as cast versus  $329 \pm 92 \mu\text{m}$  in the heat-treated. From the SE micrographs in Figures 5-47 and 5-48, one can see circular regions with small precipitates surrounded by phase with a different morphology. Heat treatment increased the size of these circular phase regions. As shown by the X-Ray map in Figure 5-49, the circular regions were rich in Ni and Al, while the surrounding phase was rich in Cr. Comparing these results with the XRD micrograph in Figure 5-31 with those obtained from EDS probes of each region, the heat-treated microstructure is one of circular  $\beta$ -NiAl regions containing small, cuboidal  $\text{Ni}_3\text{Al}$  phases surrounded by a Cr-rich  $\gamma$ -Ni matrix.

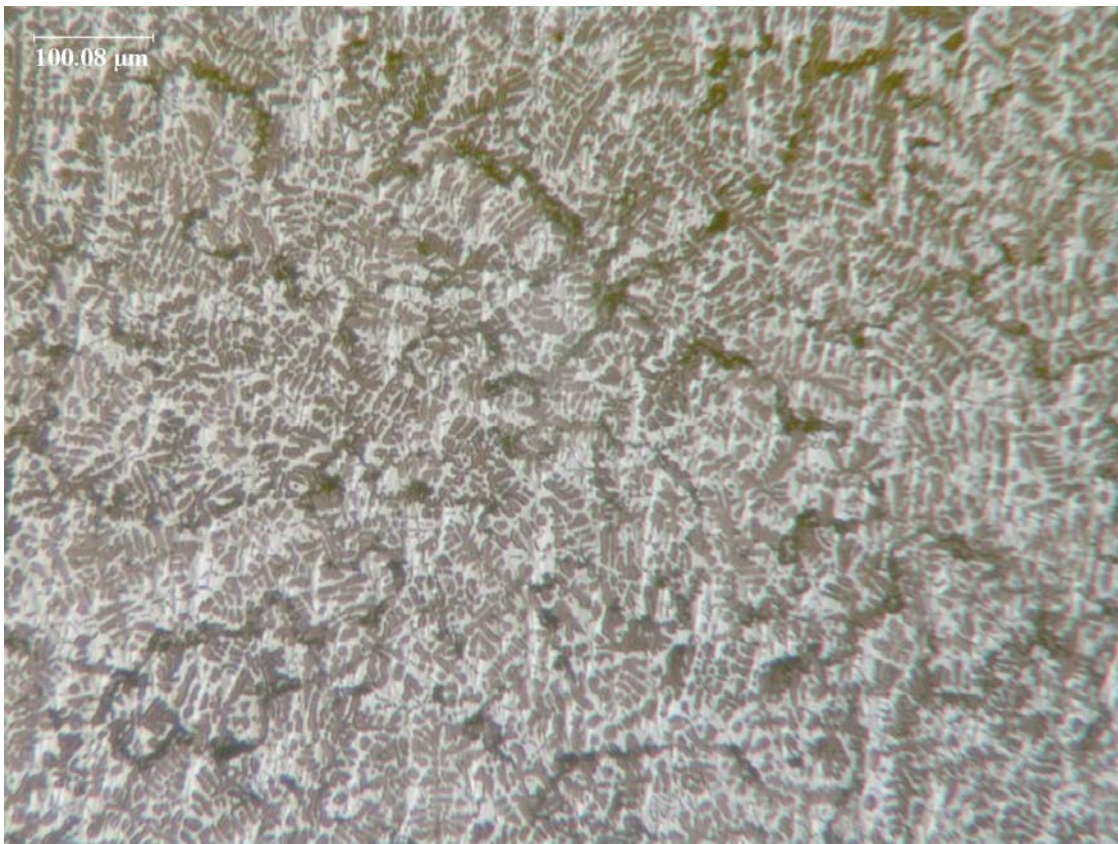


Figure 5-45. Optical micrograph of as cast Ni-22Cr-11Al at 125X.

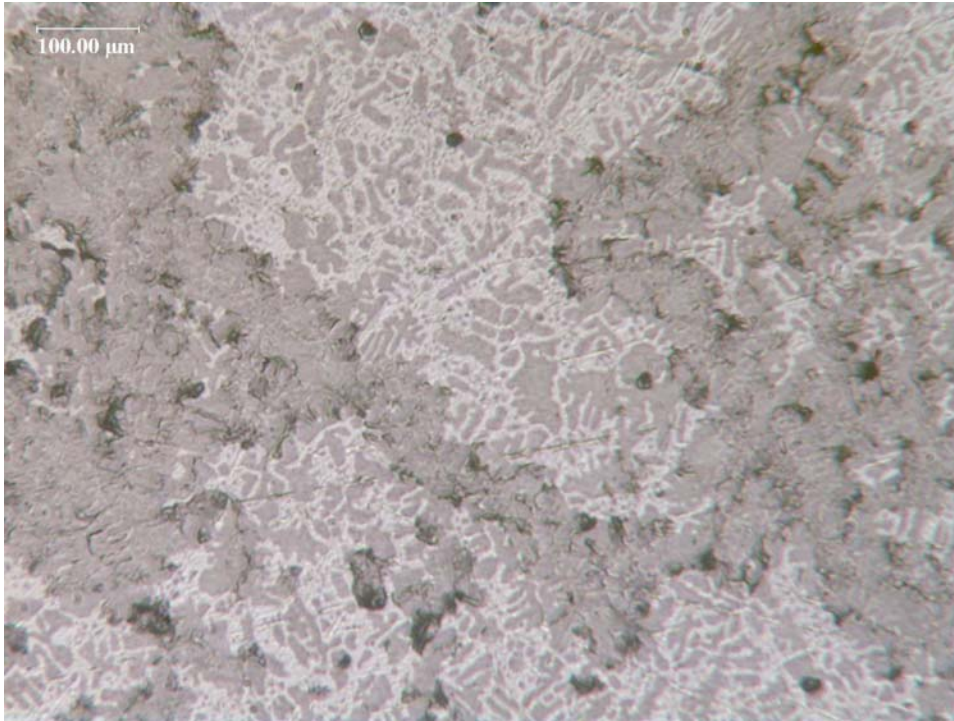


Figure 5-46. Optical micrograph of heat-treated Ni-22Cr-11Al at 125X.

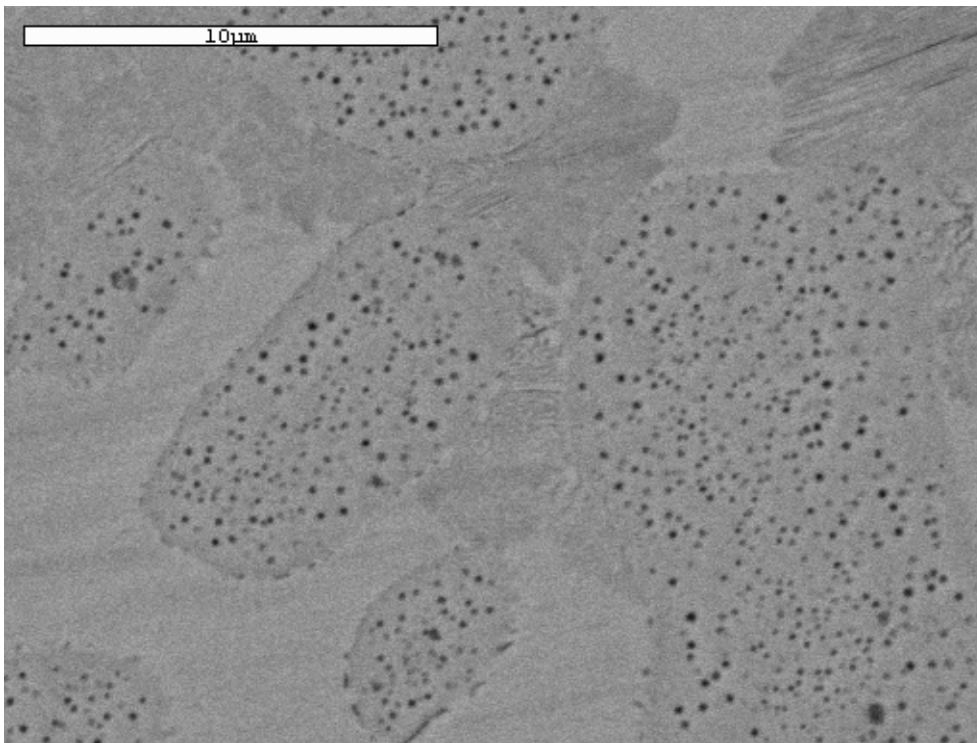


Figure 5-47. Backscattered electron (BSE) micrograph of as cast Ni-22Cr-11Al microstructure at 5000X.

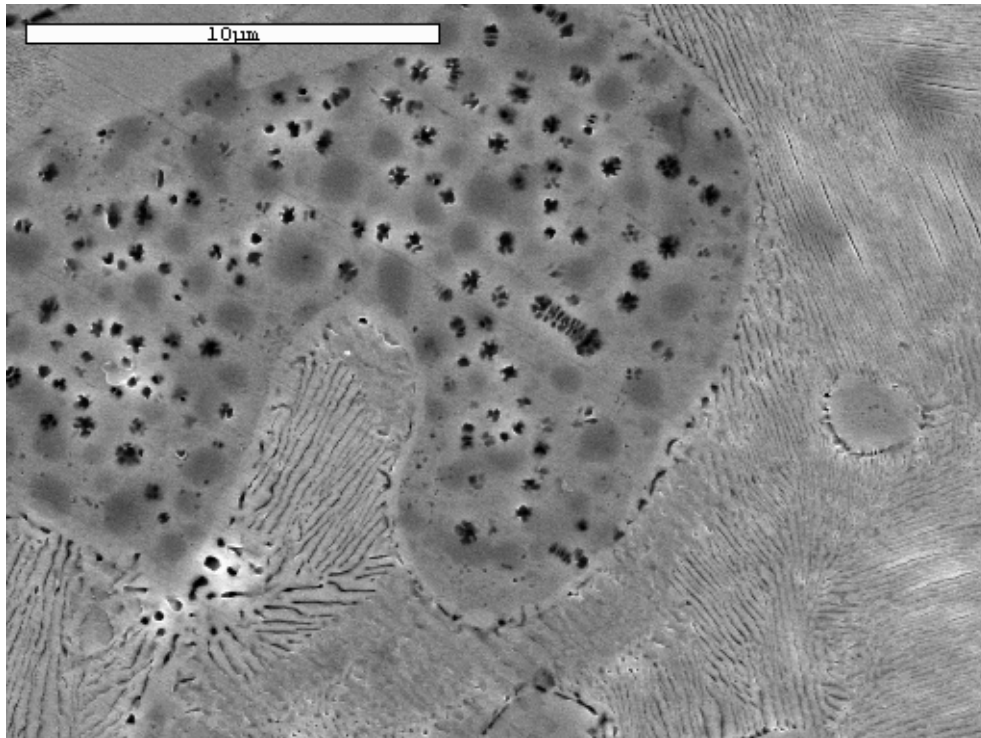


Figure 5-48. Secondary electron (SE) micrograph of heat-treated Ni-22Cr-11Al microstructure at 15000X.

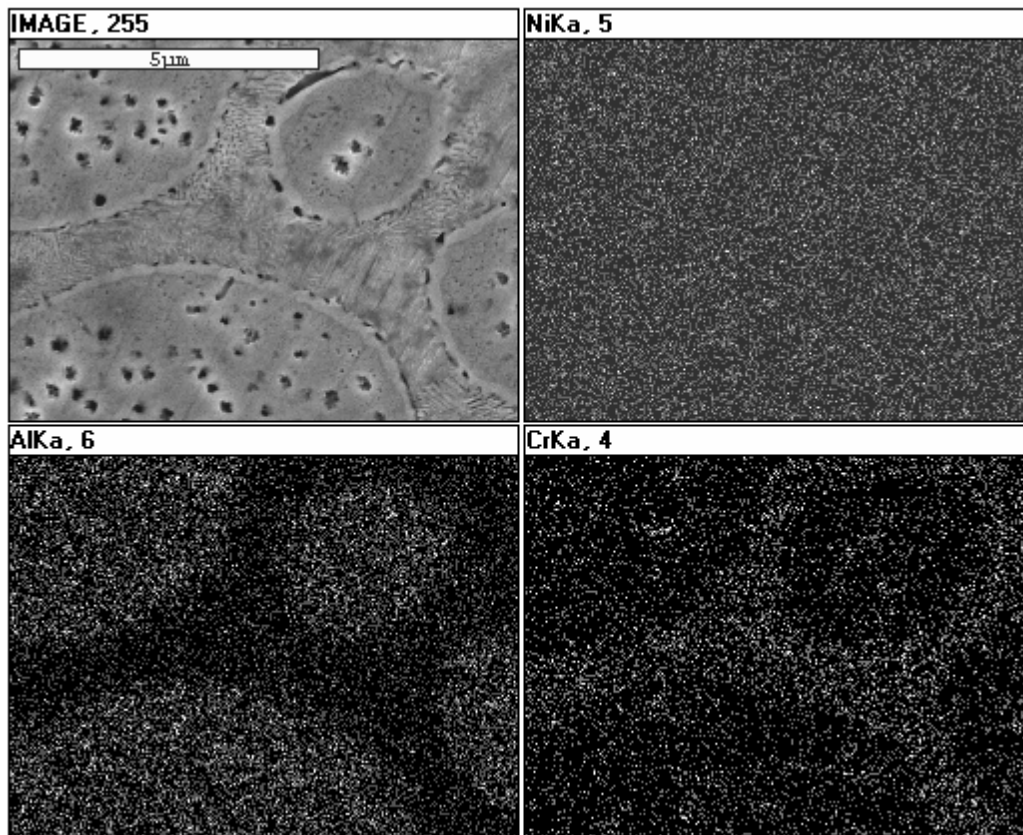


Figure 5-49. X-ray map of the SE micrograph in Figure 5-46.

### 5.3.2 Oxidized Ni and Ni-Al Specimens

The oxide formed on all the Ni specimens was similar to that in Figure 5-50—a triangular shaped layered oxide. The NiAl specimens showed only an external alumina scale that had the appearance of the one showed in Figure 5-51. However, at 1000°C, the morphology changed to a needle- or plate-like pattern (see Figure 5-52). This could indicate transient  $\theta$  or  $\delta$   $\text{Al}_2\text{O}_3$ . The amount of these aluminas was increased above the grain boundaries of the substrate, indicating faster Al transport along the substrate grain boundaries (see Figure 5-53).

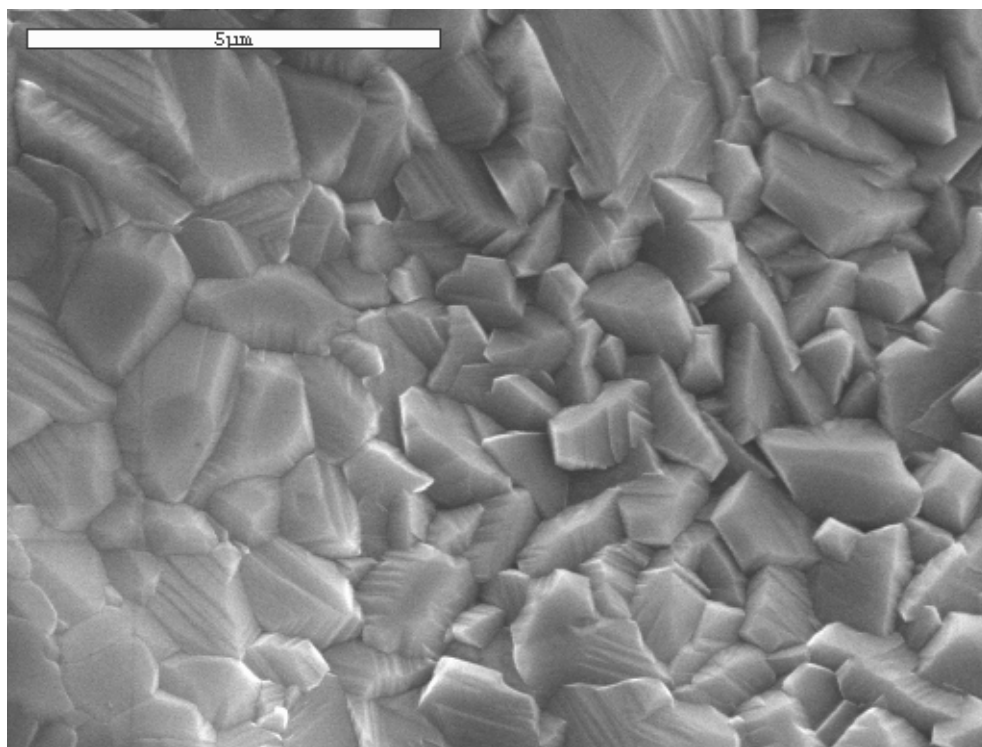


Figure 5-50. SE micrograph of NiO scale Ni oxidized in air at 800°C for 24 hr.

### 5.3.3 Oxidized Ni-8Cr-6Al Specimens

#### 5.3.3.1 Ni-8Cr-6Al Oxidized in Air

The specimens oxidized in air were analyzed using SEM for analysis. All three samples exhibited adherent scales. The specimens oxidized at 800 and 900°C exhibited an almost identical microstructure. Figure 5-54 shows a backscattered electron (BSE) micrograph of one oxidized specimen. The high-Z (atomic number) phase was shown to be NiO, and the low-Z

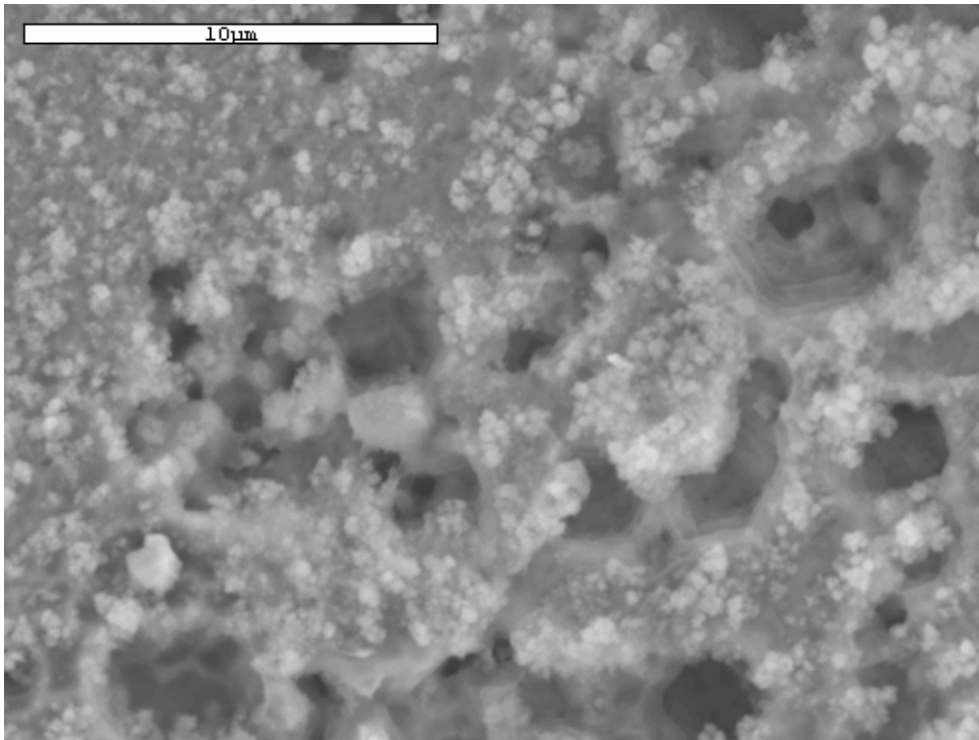


Figure 5-51. SE micrograph of NiAl oxidized at 800°C for 36 hr at 5000X.

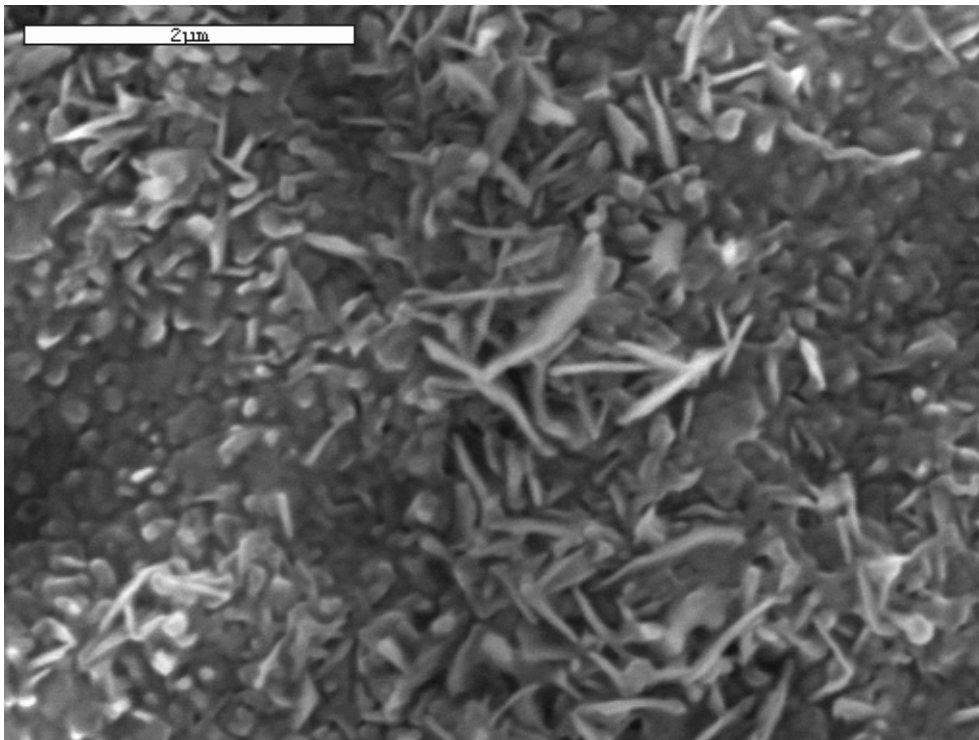


Figure 5-52. SE micrograph of NiAl oxidized at 1000°C for 36 hr at 20000X.

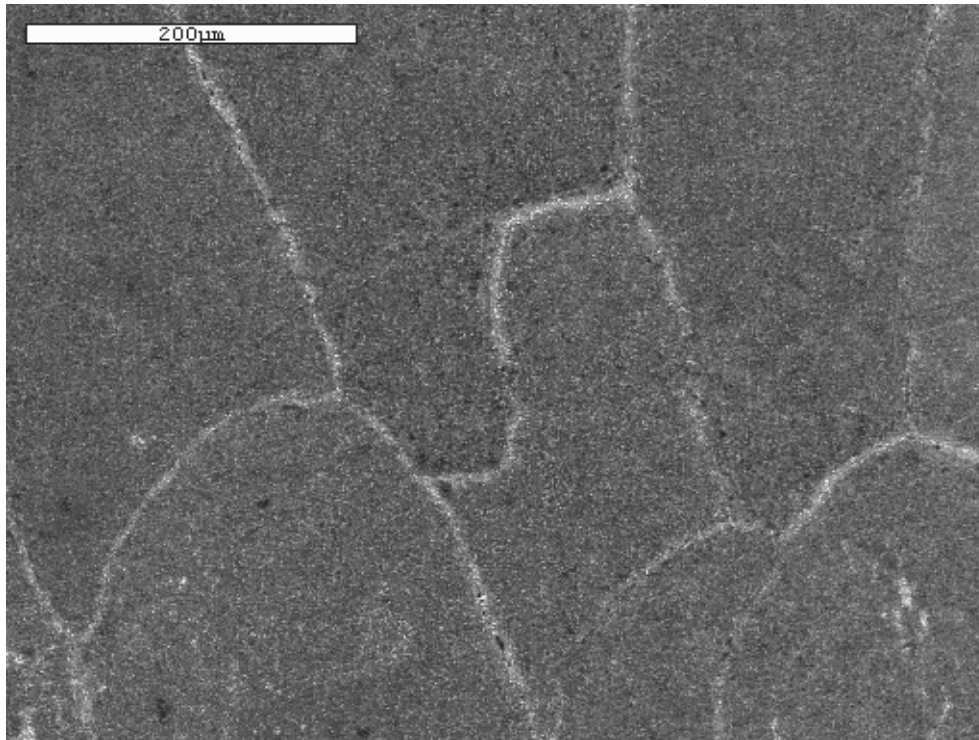


Figure 5-53. SE micrograph of NiAl oxidized at 1000°C for 36 hr at 200X.

phase underneath was alumina (see Figure 5-55). Even though XRD identified chromia in the 800°C specimen, it was not observed on the surface in the SEM. At 1000°C, a different morphology was seen—one with whiskers as seen with the NiAl (see Figures 5-56 and 5-57). BSE imaging, EDS, and XRD showed these whiskers to be  $\alpha$ -Al<sub>2</sub>O<sub>3</sub> (when compared with Figure 5-24) near flaky NiO on top of a mixture of Al<sub>2</sub>O<sub>3</sub> and Ni<sub>2</sub>AlO<sub>4</sub>. Whiskers are not the normal morphology of  $\alpha$ -Al<sub>2</sub>O<sub>3</sub>, but it is likely that prolonged exposure at elevated temperatures converted them from a transient phase to the more stable  $\alpha$ . Oxidation of this alloy for 30 min showed that there had developed a similar scale morphology as shown in Figure 5-51 (see Figure 5-58). The NiO morphology was similar the NiO that grew on pure Ni (see Figure 5-50).

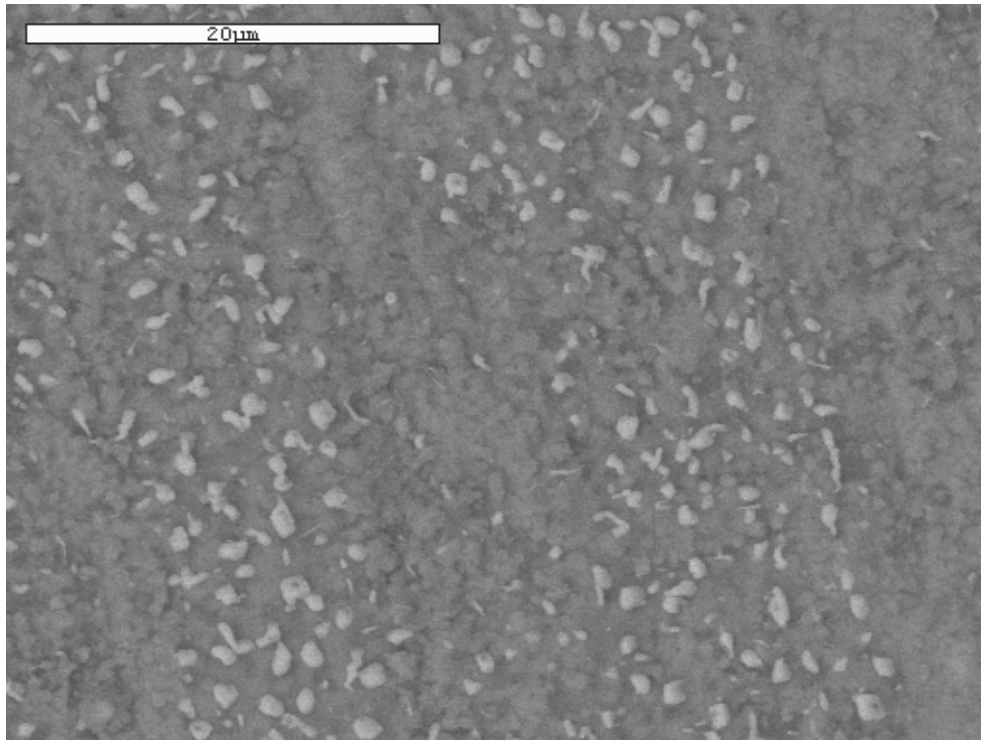


Figure 5-54. Backscattered electron (BSE) micrograph of Ni-8Cr-6Al oxidized in air for 100 hr at 900°C.

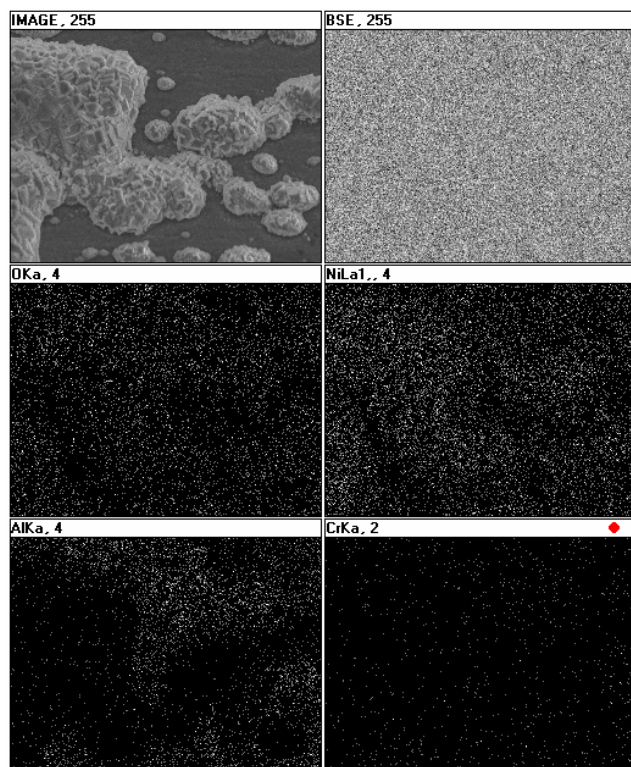


Figure 5-55. X-ray map of SE micrograph at 2500X of Ni-8Cr-6Al oxidized in air for 100 hr at 800°C.

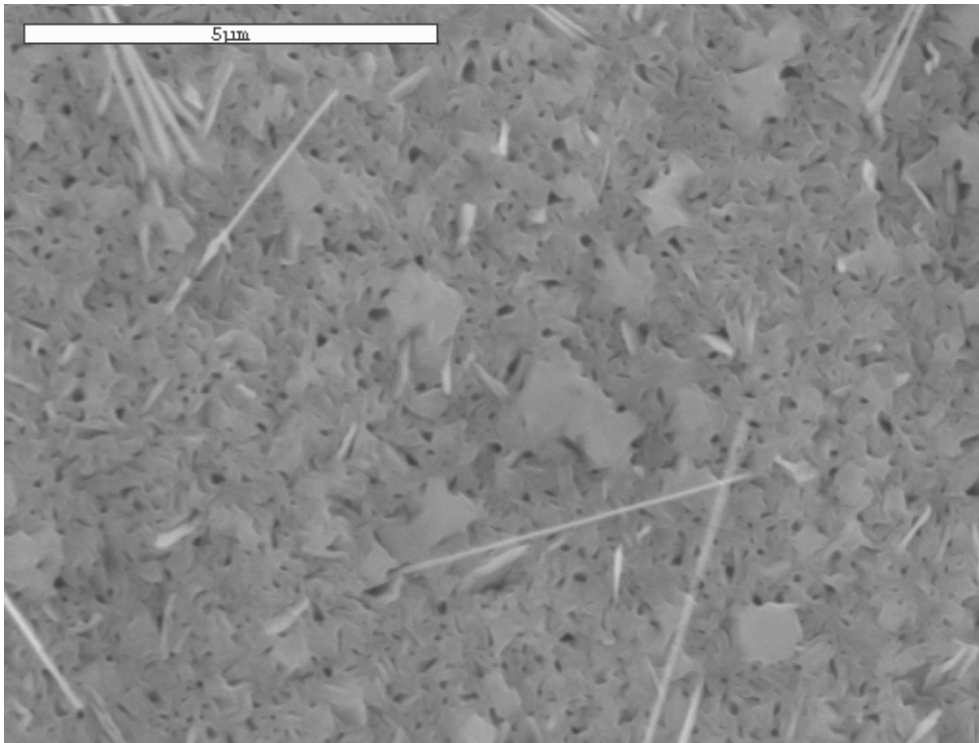


Figure 5-56. SE micrograph of surface of Ni-8Cr-6Al after oxidation in air for 100hr at 1000°C at 10000X

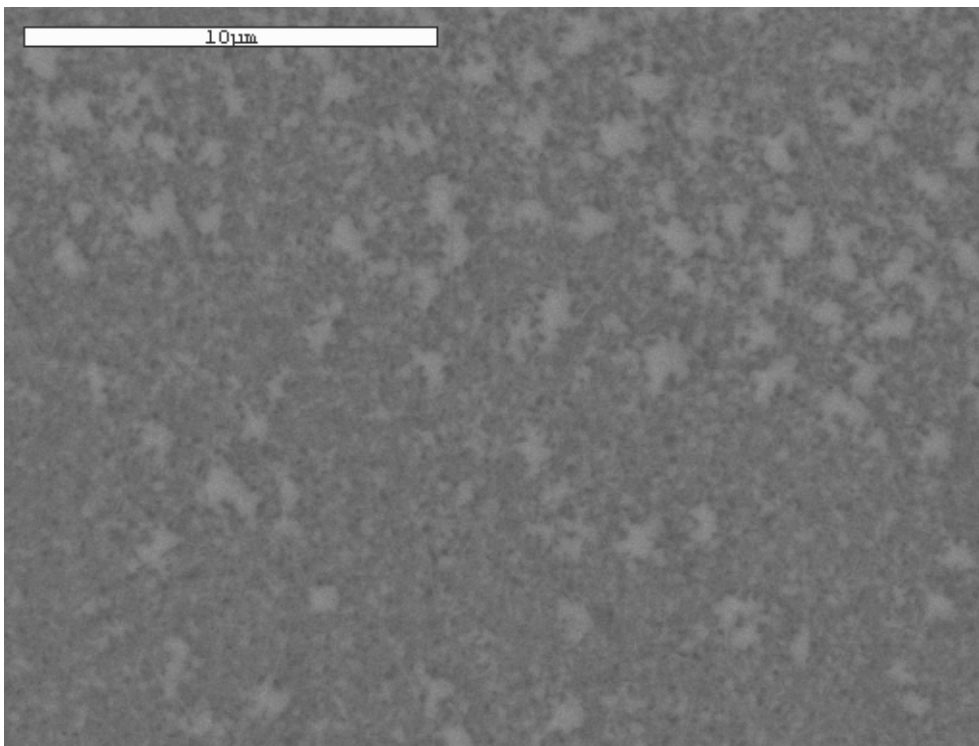


Figure 5-57. BSE micrograph of surface of Ni-8Cr-6Al after oxidation in air for 100hr at 1000°C at 5000X.

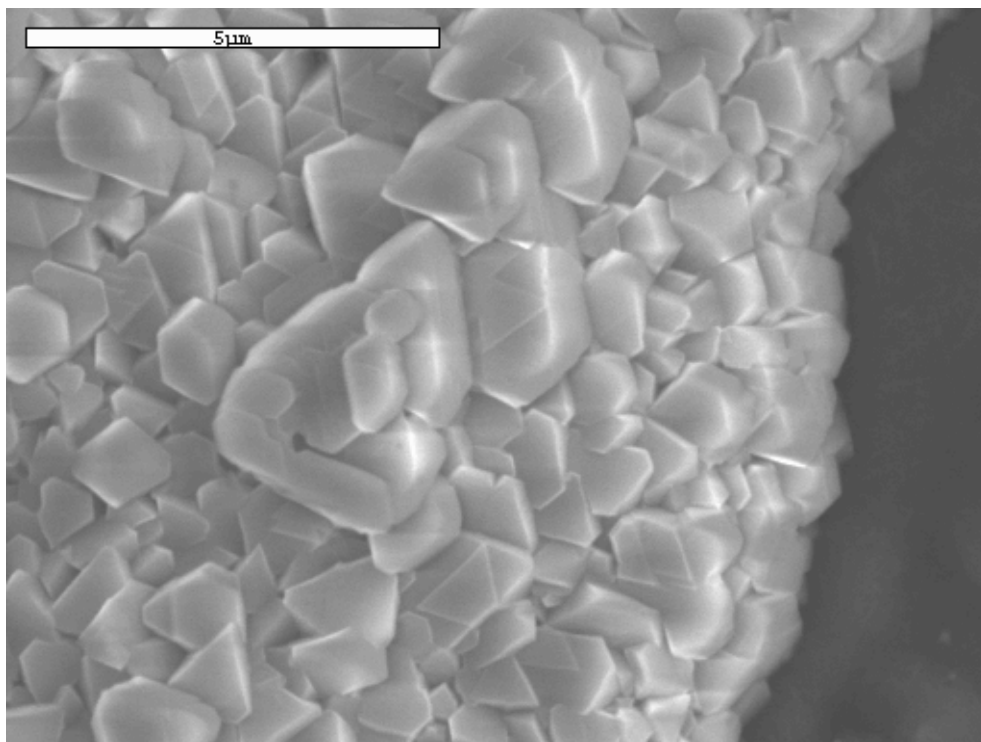


Figure 5-58. SE micrograph of surface of Ni-8Cr-6Al after oxidation in air for 0.5 hr at 800°C at 10000X. The light oxide is NiO and the dark oxide on the right is alumina.

### 5.3.3.2 Ni-8Cr-6Al Oxidized in He + 0.21 O<sub>2</sub> + 0.02 SO<sub>2</sub>

Exposure to SO<sub>2</sub> appeared to stabilize Cr<sub>2</sub>O<sub>3</sub> on Ni-8Cr-6Al samples during oxidation, which was not seen with those oxidized in air. At 800°C, the surface was Al<sub>2</sub>O<sub>3</sub> covered by small rounded Cr<sub>2</sub>O<sub>3</sub> bumps about 2 μm wide with an occasional blocky NiO protrusion on the order of 20 μm wide (see Figure 5-59). At 900°C, there was more NiO coverage of the underlying alumina scale (see Figure 5-60). No spinel or chromia phases were identified from EDS of this specimen, as the low-Z phase was almost all Al and O, while the high-Z was Ni and O. As shown in Figure 5-61, at 975°C the outer scale coverage increased, and it was revealed as an oxide with a mixture of Ni and Cr (corresponding with Figure 5-27). This outer scale tended to spall, and left a bare surface with some small Al oxides, as shown by Figure 5-62. No indication was seen of sulfide or sulfur-bearing phases from the EDS probes of any of these specimens.

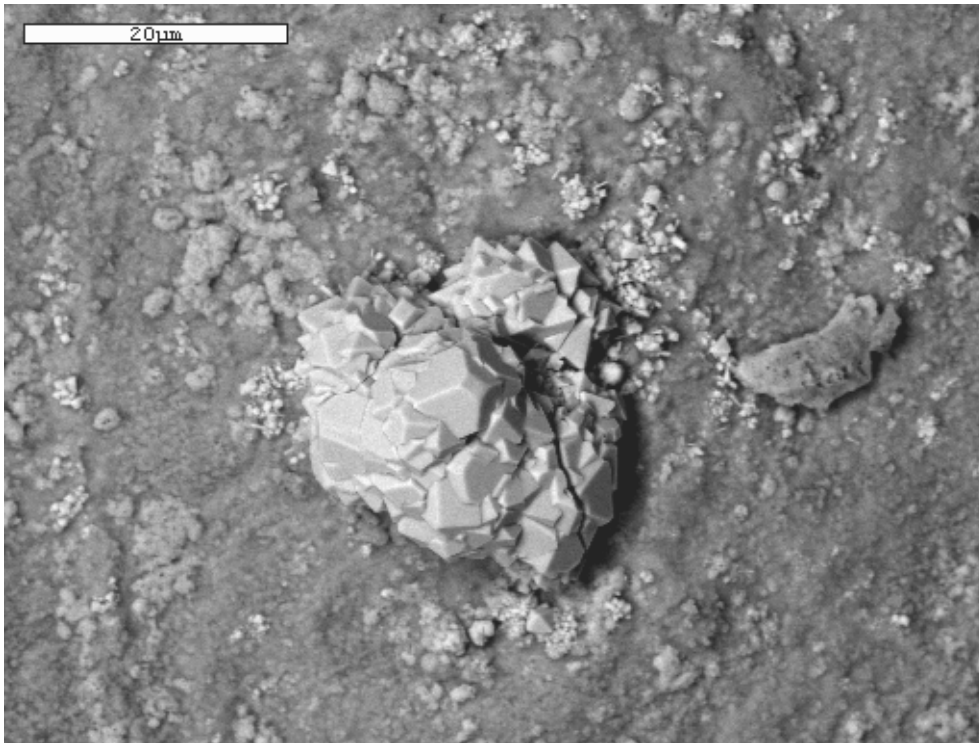


Figure 5-59. BSE micrograph of the surface of Ni-8Cr-6Al oxidized in 2% SO<sub>2</sub> at 800°C for 100 hr at 4000X.

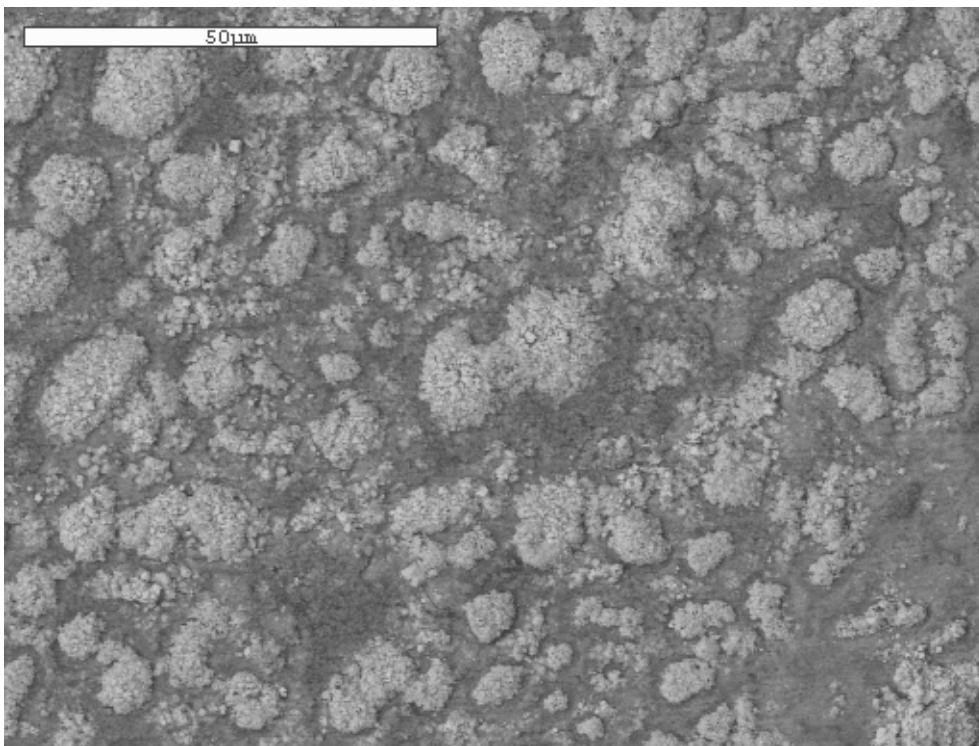


Figure 5-60. BSE micrograph of the surface of Ni-8Cr-6Al oxidized in 2% SO<sub>2</sub> at 900°C for 100 hr at 1000X.

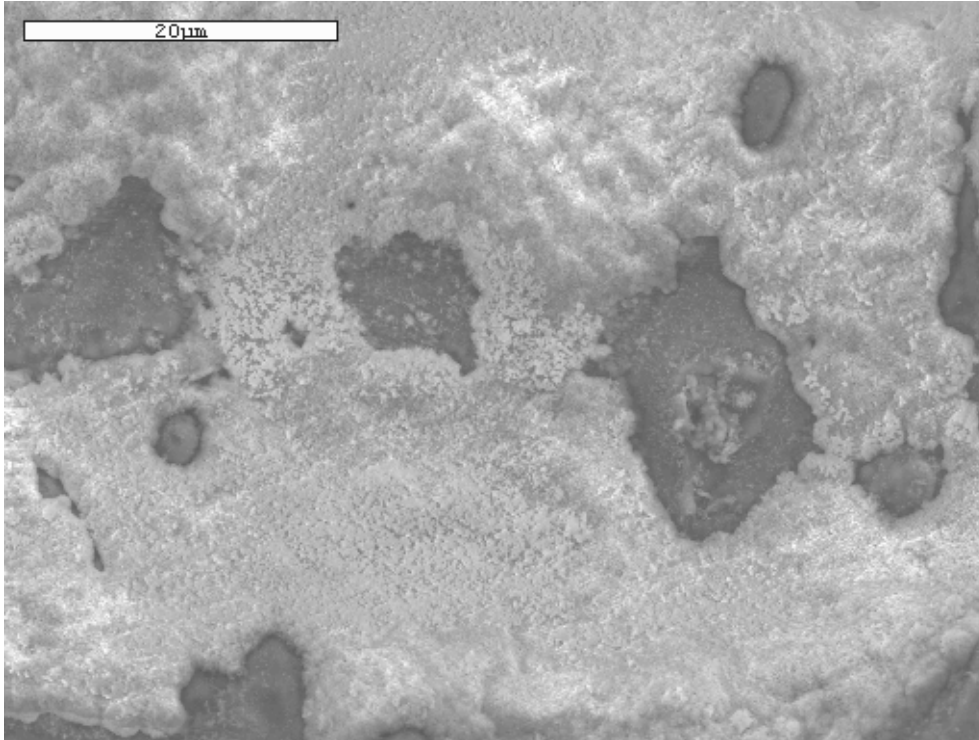


Figure 5-61. SE micrograph of the surface of Ni-8Cr-6Al oxidized in 2% SO<sub>2</sub> at 975°C for 100 hr at 1500X.

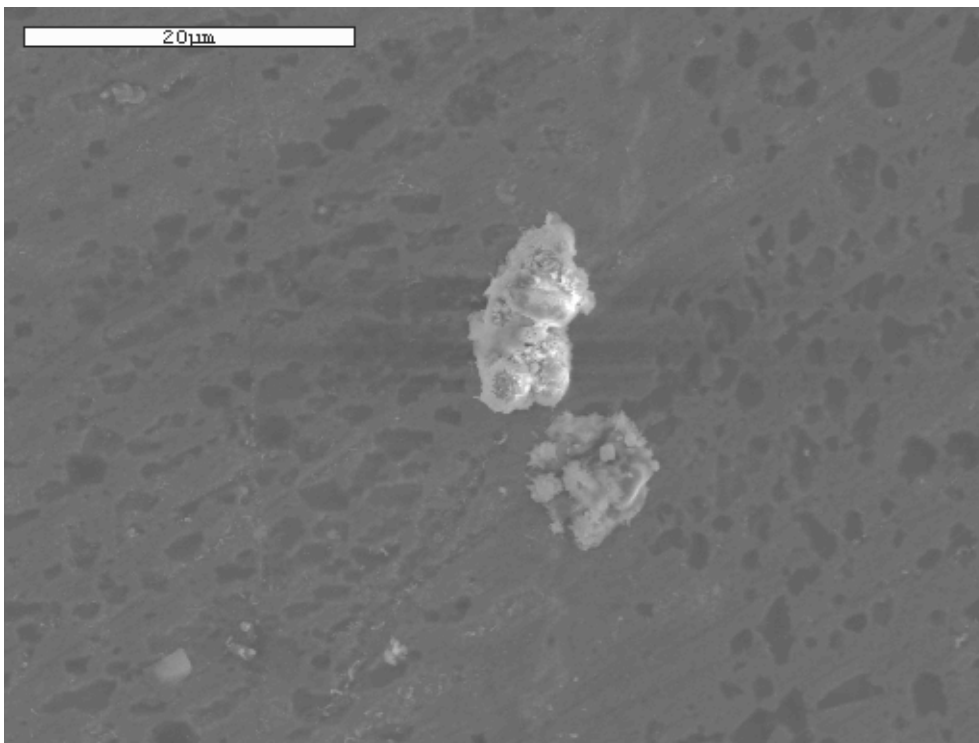


Figure 5-62. SE micrograph of the surface of Ni-8Cr-6Al oxidized in 2% SO<sub>2</sub> at 975°C for 100 hr at 1500X. In this area, the scale has spalled off revealing the bare metal surface.

### 5.3.3.3 Ni-8Cr-6Al Oxidized in He + 0.21 O<sub>2</sub> + 0.10 SO<sub>2</sub>

Analysis of the specimens treated in 10% SO<sub>2</sub> at 800°C showed a continuous Al<sub>2</sub>O<sub>3</sub> oxide covered by small NiO particles with script morphology (see Figure 5-63). In addition, much of the scale had blistered, as can be seen in Figure 5-64. At 900°C, a small script NiO was identified instead of the larger, flat plates of NiCr<sub>2</sub>O<sub>4</sub> spinel (see Figure 5-65) on top of an Al<sub>2</sub>O<sub>3</sub>/Cr<sub>2</sub>O<sub>3</sub> underlying oxide. Also on top of the underlying oxide, was a layer of Al<sub>2</sub>O<sub>3</sub> (the small, lighter phase in Figure 5-65), which showed a small, needlelike morphology, as seen in Figure 5-66. At 975°C, no Ni-oxide phases were observed, and as seen in Figure 5-67, the surface had an Al<sub>2</sub>O<sub>3</sub> oxide covered by intermittent Cr<sub>2</sub>O<sub>3</sub>. This scale combination spalled often, which revealed the underlying metal that that was shown to reoxidize as Al<sub>2</sub>O<sub>3</sub> (see Figure 5-68). Sulfur was detected at levels under 2 wt% where the scale had spalled.

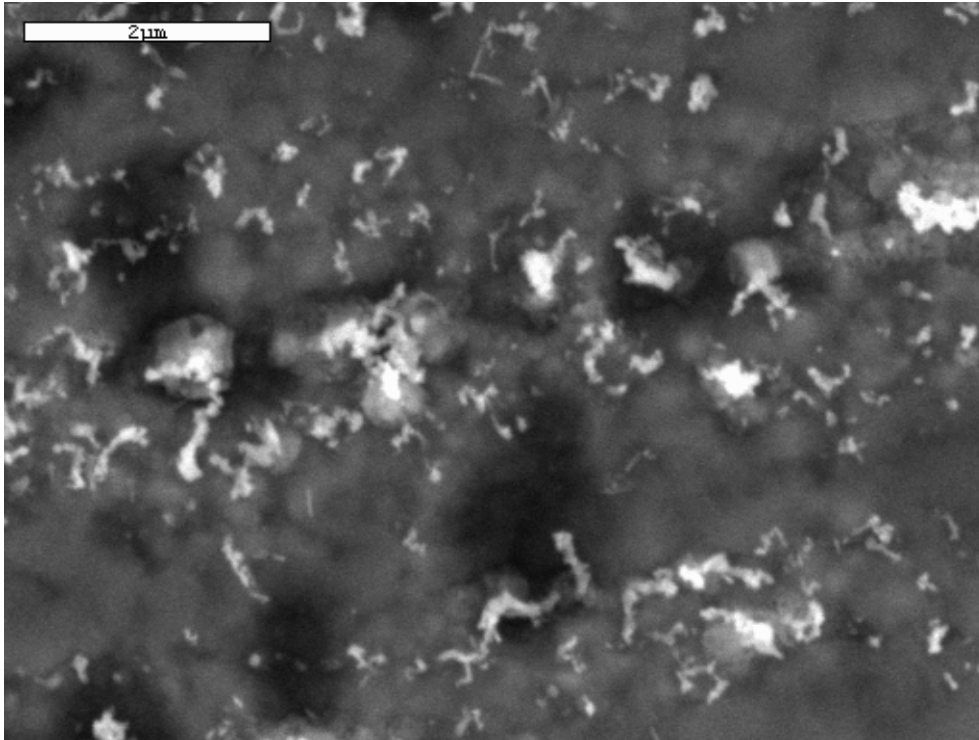


Figure 5-63. SE micrograph of the surface of Ni-8Cr-6Al oxidized in 10% SO<sub>2</sub> at 800°C for 100 hr at 15000X.

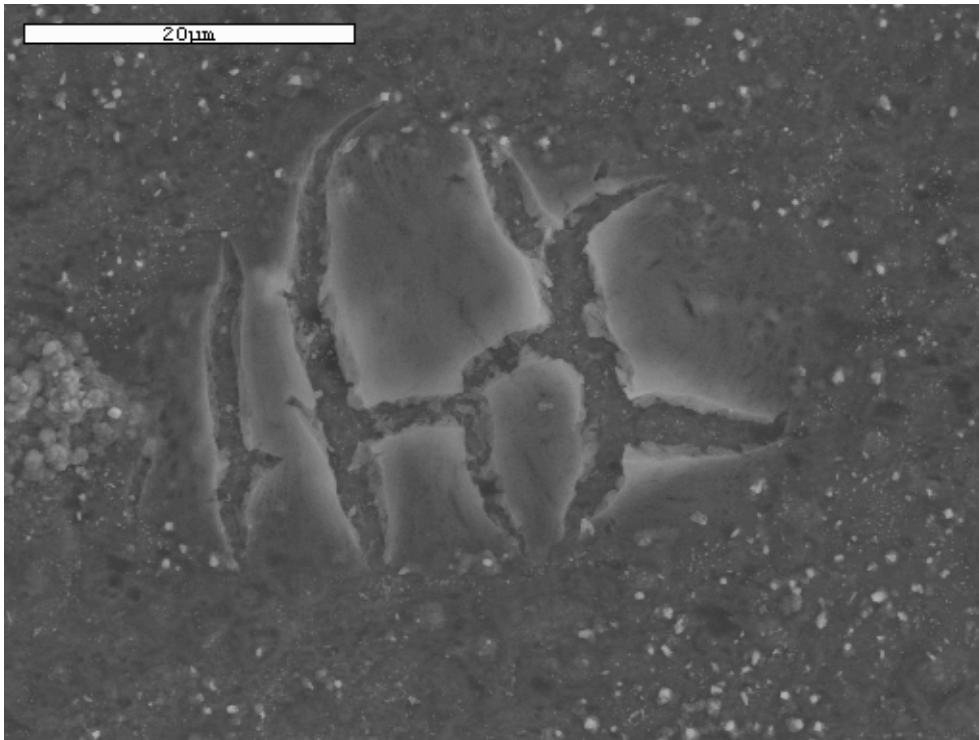


Figure 5-64. SE micrograph of Ni-8Cr-6Al alloy oxidized in 10% SO<sub>2</sub> at 800°C for 100 hr at 1500 showing scale “blisters.”

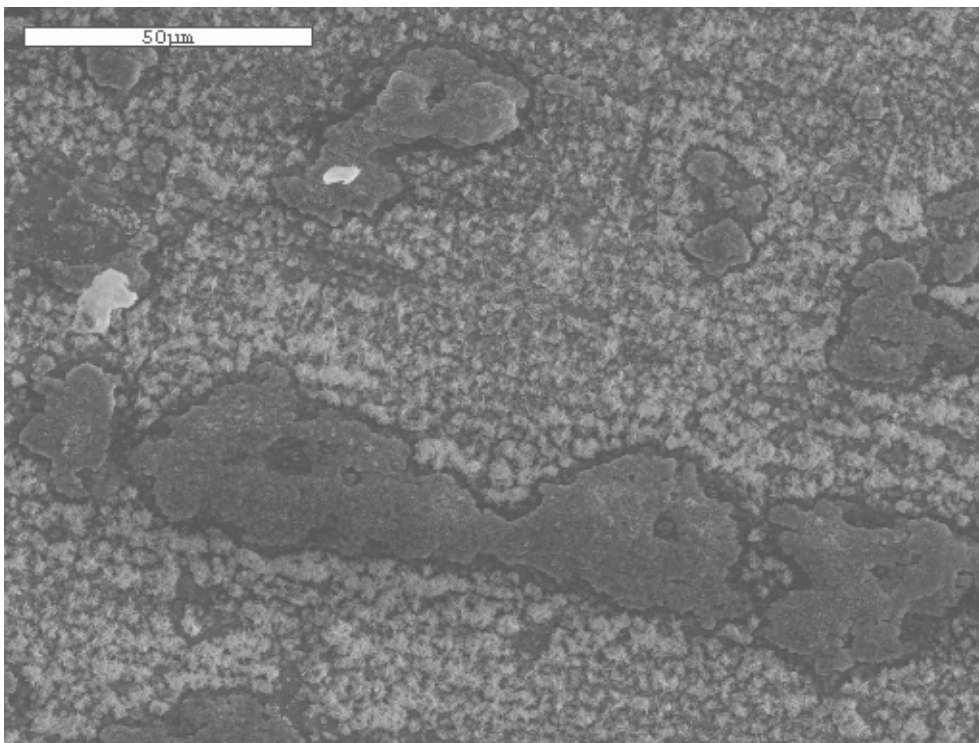


Figure 5-65. SE micrograph of the surface of Ni-8Cr-6Al oxidized in 10% SO<sub>2</sub> at 900°C for 100 hr at 700X.

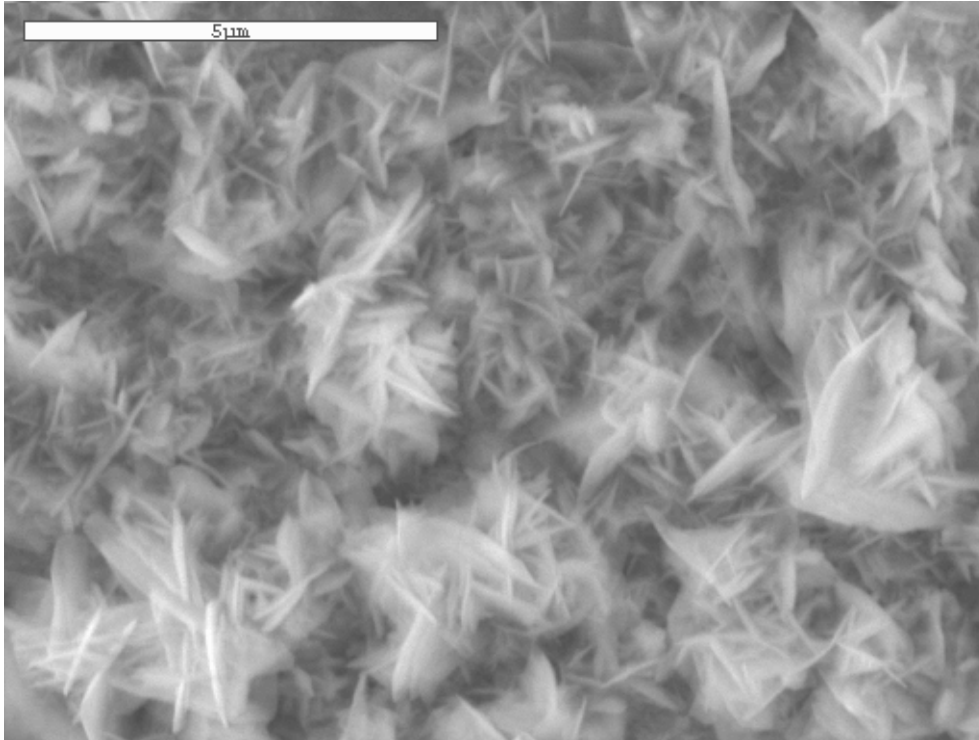


Figure 5-66. SE micrograph of the overlying alumina regions of Ni-8Cr-6Al oxidized in 10% SO<sub>2</sub> at 900°C for 100 hr at 10000X.

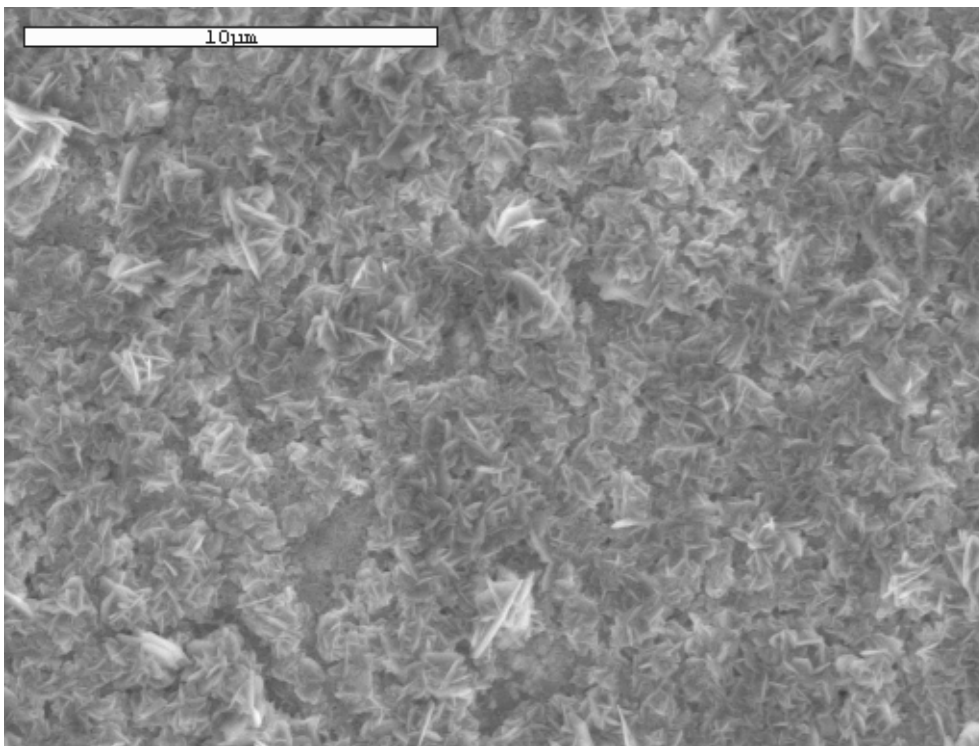


Figure 5-67. SE micrograph of the surface of Ni-8Cr-6Al oxidized in 10% SO<sub>2</sub> at 975°C for 100 hr at 5000X.

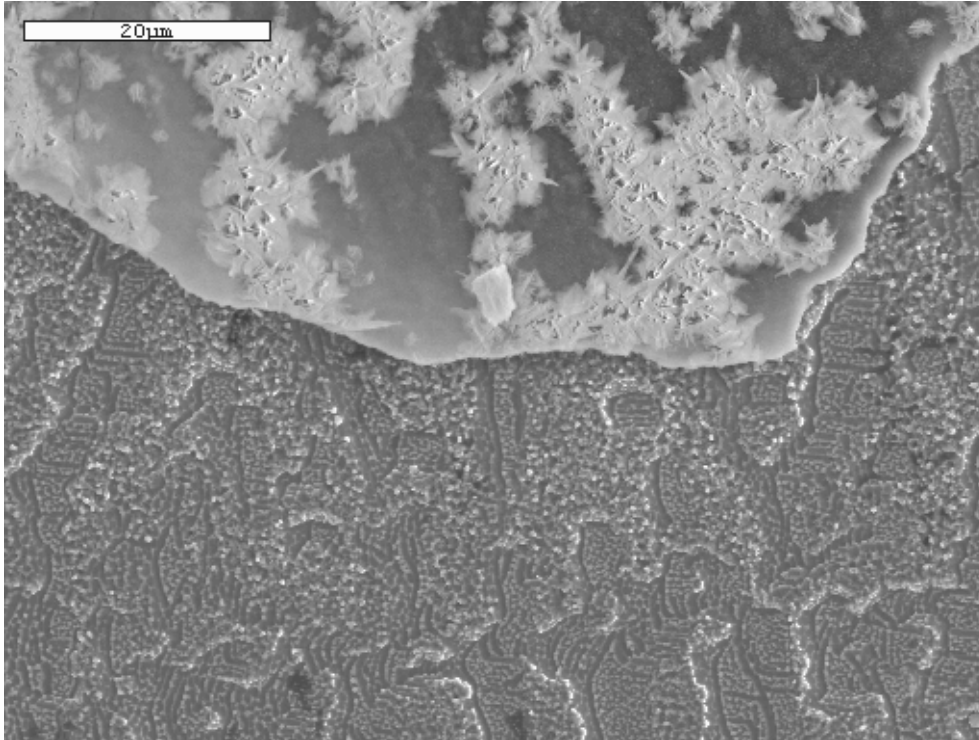


Figure 5-68. SE micrograph of the surface of Ni-8Cr-6Al oxidized in 10% SO<sub>2</sub> at 975°C for 100 hr at 1500X where the scale (top) had spalled off and began to reoxidized (bottom).

### 5.3.4 Oxidized Ni-22Cr-11Al Specimens

#### 5.3.4.1 Ni-22Cr-11Al Oxidized in Air

The scale observed on the Ni-22Cr-11Al alloy consisted of a two-phase microstructure, each in a separate region for all three temperatures (see Figures 5-69, 5-70). The lighter oxide was found to be Cr<sub>2</sub>O<sub>3</sub>, while the darker was Al<sub>2</sub>O<sub>3</sub>. The chromia scale appeared to have grown first, over the regions rich in Cr as seen in Figure 5-49, while the alumina grew over the regions of  $\beta$  and  $\gamma'$ . It cannot be determined from this analysis if the Cr<sub>2</sub>O<sub>3</sub> scale is on top of the Al<sub>2</sub>O<sub>3</sub>, or if it is continuous to the scale metal interface. The specimens oxidized at 1000°C exhibited a different surface morphology than the other two (Figure 5-71). In this situation, an outer scale (shown as dark) was flaking off. This scale was determined to be a mixture of Cr<sub>2</sub>O<sub>3</sub> (lighter on scale) and Al<sub>2</sub>O<sub>3</sub> (darker on scale) with the same pattern as Figure 5-69. This scale flaked off, however, leaving a bare metal surface that grew a thin layer of Al<sub>2</sub>O<sub>3</sub> (the lighter phase).

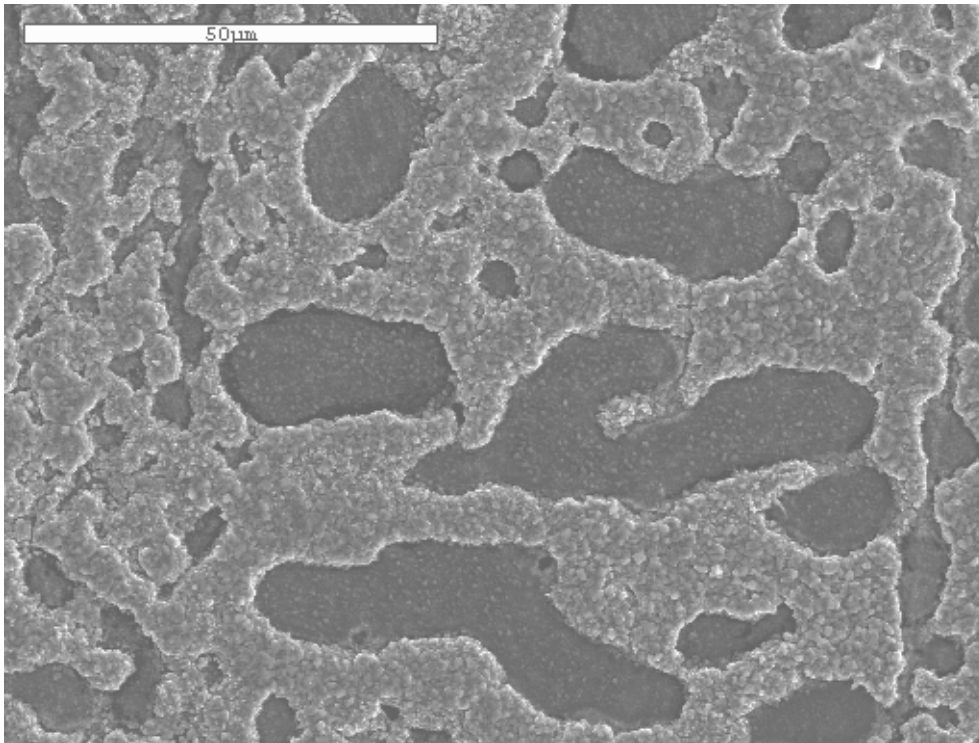


Figure 5-69. SE micrograph of Ni-22Cr-11Al oxidized in air at 800°C for 100 hr at 1000X.

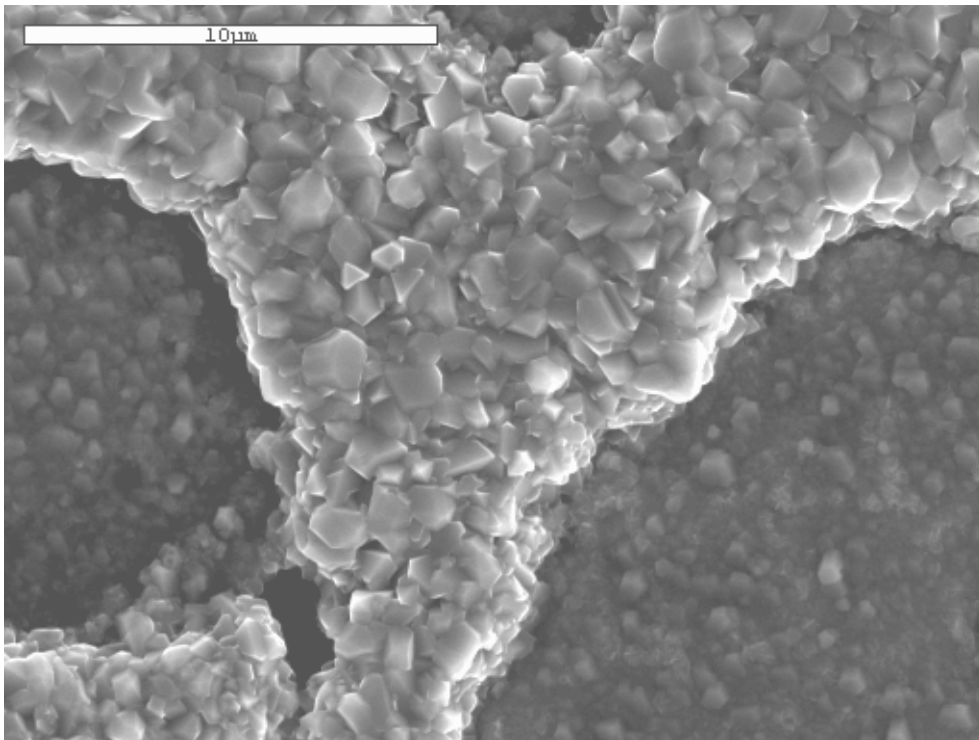


Figure 5-70. SE micrograph of Ni-22Cr-11Al oxidized in air at 800°C for 100 hr at 5000X.

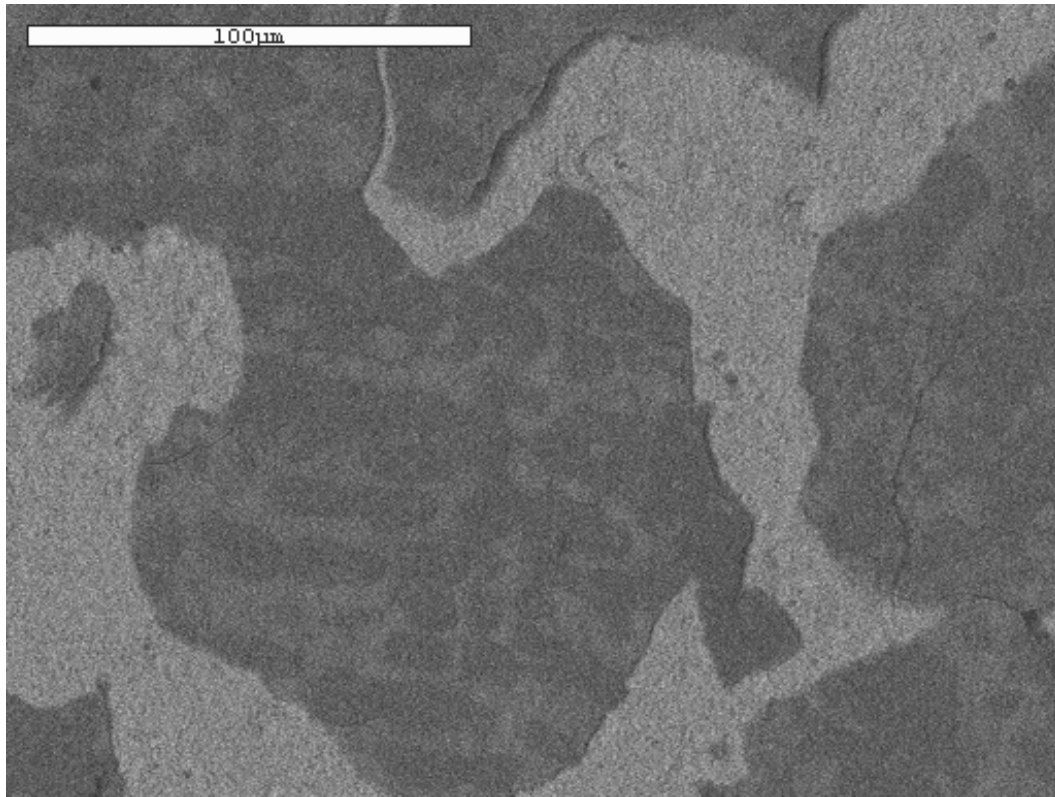


Figure 5-71. BSE micrograph of Ni-22Cr-11Al oxidized in air at 1000°C for 100 hr at 500X.

#### 5.3.4.2 Ni-22Cr-11Al Oxidized in He + 0.21 O<sub>2</sub> + 0.02 SO<sub>2</sub>

The specimens exposed to 2% SO<sub>2</sub> exhibited a similar surface oxide structure with those of the oxidized specimens—Al<sub>2</sub>O<sub>3</sub> was shown to grow over the β areas and Cr<sub>2</sub>O<sub>3</sub> grew over the γ regions (see Figure 5-72). However, on these samples, the Cr<sub>2</sub>O<sub>3</sub> was not a continuous layer, but rather small, spherical blobs between 0.5 and 5 μm in size (see Figure 5-73). Figure 5-74 shows that while the alumina scale was mostly flat, some regions did show a small, needlelike morphology that was also observed on the Ni-8Cr-6Al specimens exposed to 10% SO<sub>2</sub> (see Figure 5-66). Overall, the surface scale for all samples was the same, except for 1000°C, which showed some cracking of the scale (Figure 5-75). Sulfur was detected in these regions of bare metal.

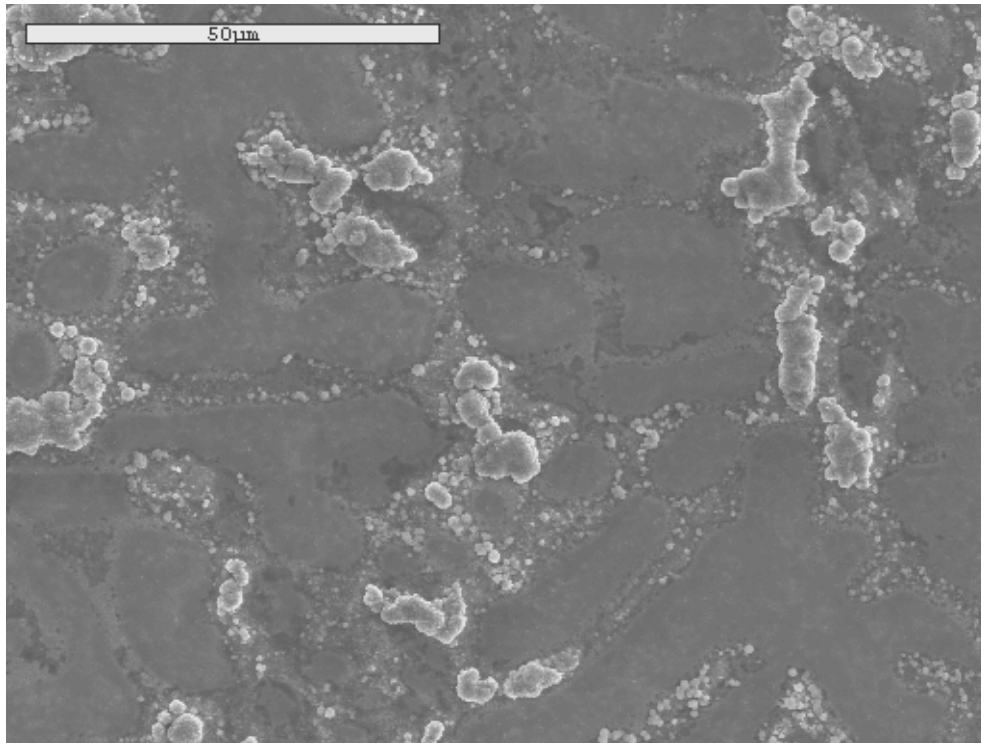


Figure 5-72. SE micrograph of Ni-22Cr-11Al oxidized in 2% SO<sub>2</sub> gas mixture at 800°C for 100 hr at 1000X.

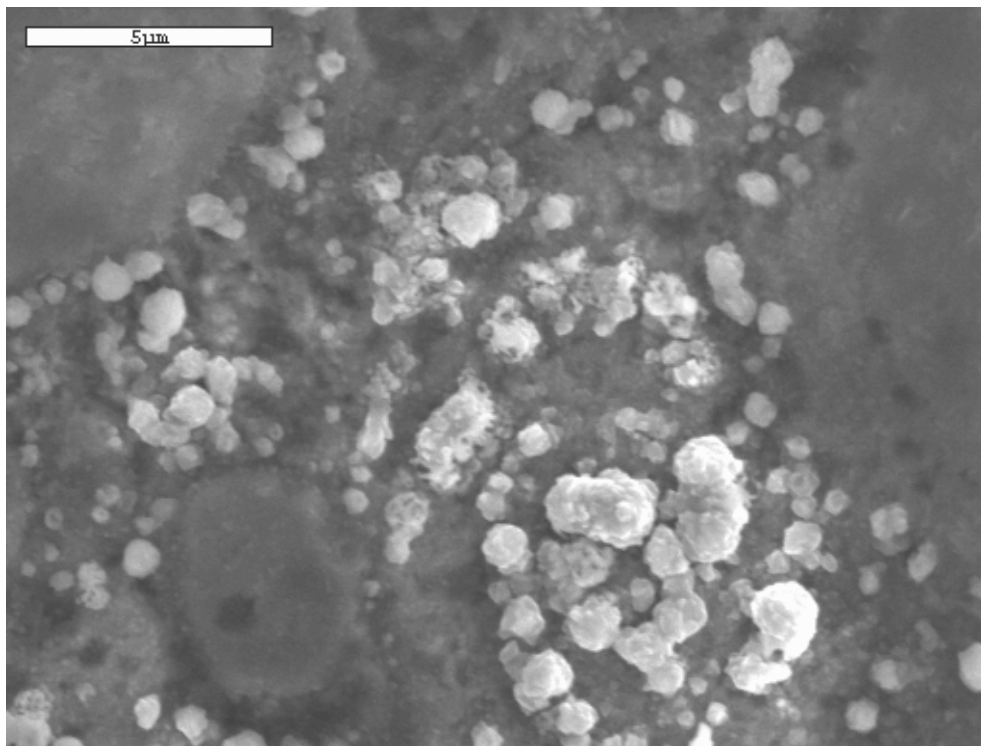


Figure 5-73. SE micrograph of Ni-22Cr-11Al oxidized in 2% SO<sub>2</sub> gas mixture at 900°C for 100 hr at 9000X.

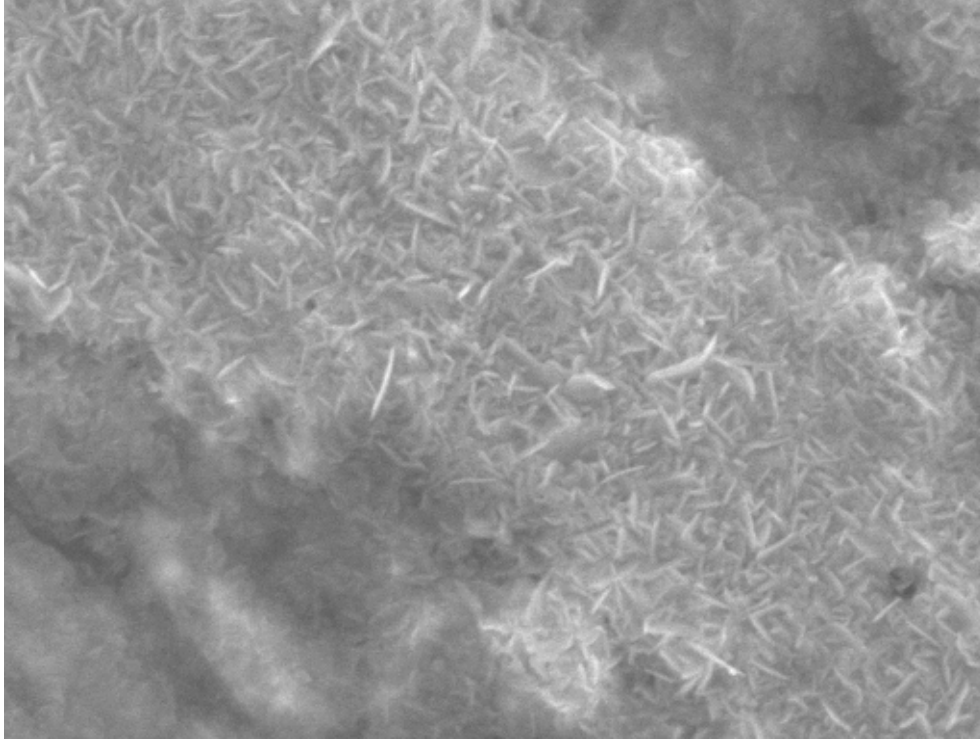


Figure 5-74. SE micrograph of Ni-22Cr-11Al oxidized in 2% SO<sub>2</sub> gas mixture at 900°C for 100 hr at 10000X.

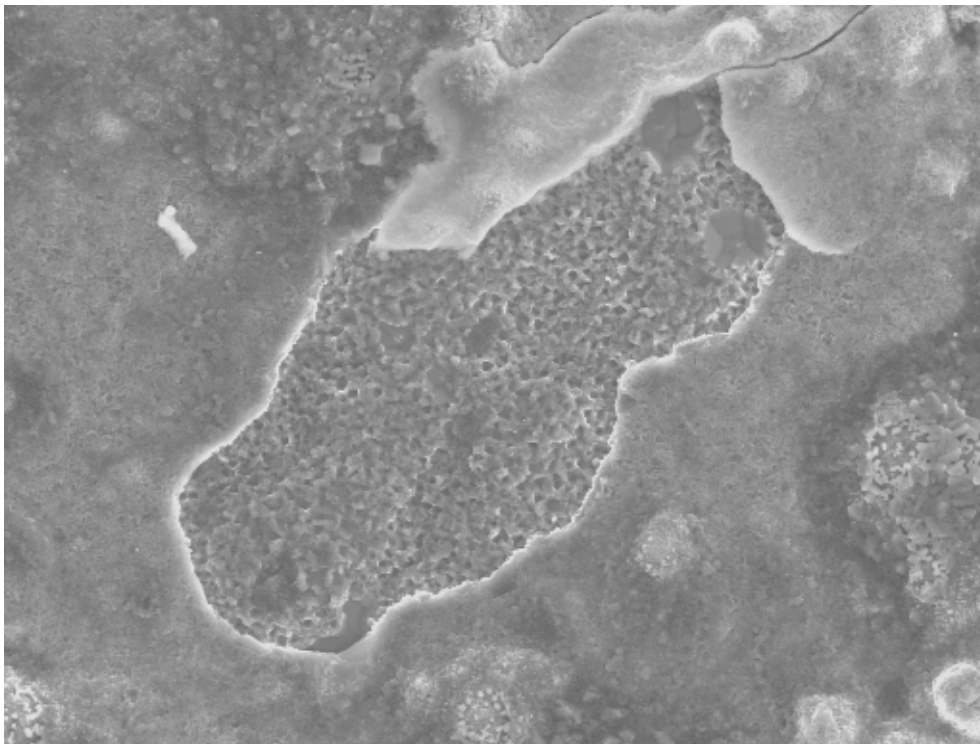


Figure 5-75. SE micrograph of Ni-22Cr-11Al oxidized in 2% SO<sub>2</sub> gas mixture at 1000°C for 100 hr at 1900X.

#### 5.3.4.3 Ni-8Cr-6Al Oxidized in He + 0.21 O<sub>2</sub> + 0.10 SO<sub>2</sub>

The specimens oxidized in 10% SO<sub>2</sub> had a similar morphology with that of those in 2% (see Figure 5-76). The amount and size of the Cr<sub>2</sub>O<sub>3</sub> particles was reduced when compared to the 2% samples, and some of the Cr<sub>2</sub>O<sub>3</sub> spheres had Cr<sub>2</sub>O<sub>3</sub> whiskers, as shown in Figure 5-77. The alumina either had a smoother blocky morphology (Figure 5-76) or would appear as needlelike whiskers (Figure 5-78). All three specimens showed areas of spallation (Figure 5-79), where the metal was exposed. Sulfur-based phases were detected by EDS analyses of these regions and, as detected by XRD (Table 5-2), were found to be Ni-sulfides at 800 and 900°C, and Cr-sulfides at 1000°C.

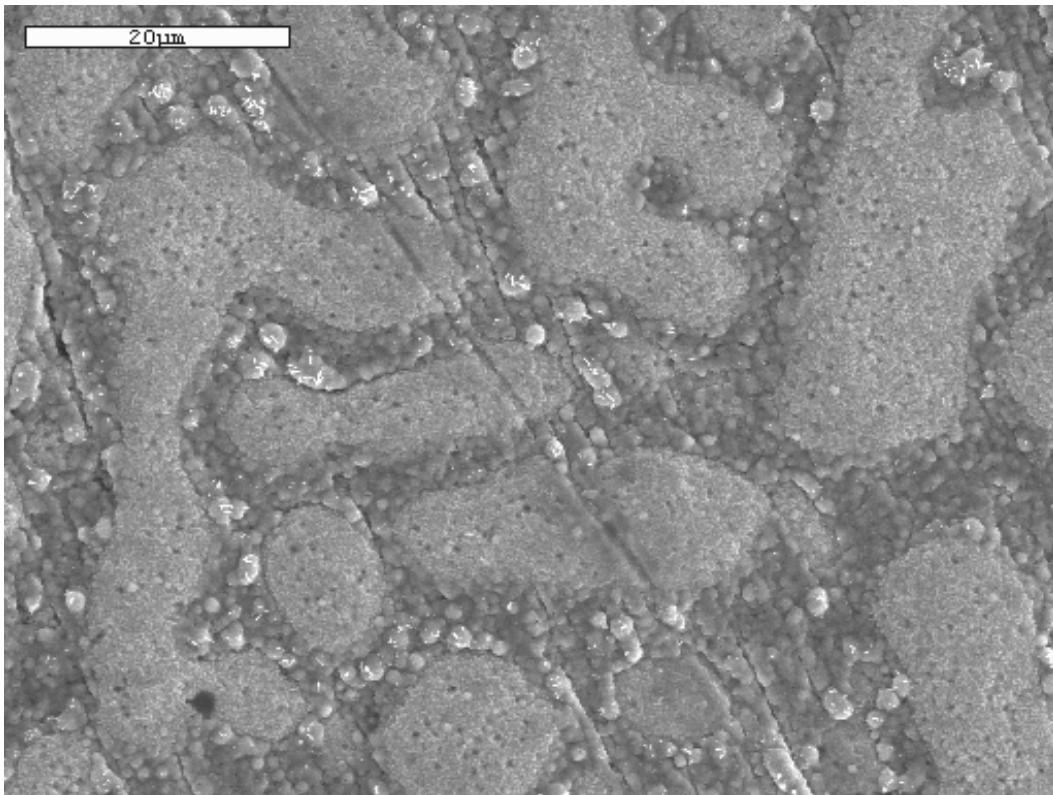


Figure 5-76. SE micrograph of Ni-22Cr-11Al oxidized in 10% SO<sub>2</sub> gas mixture at 800°C for 100 hr at 100X.

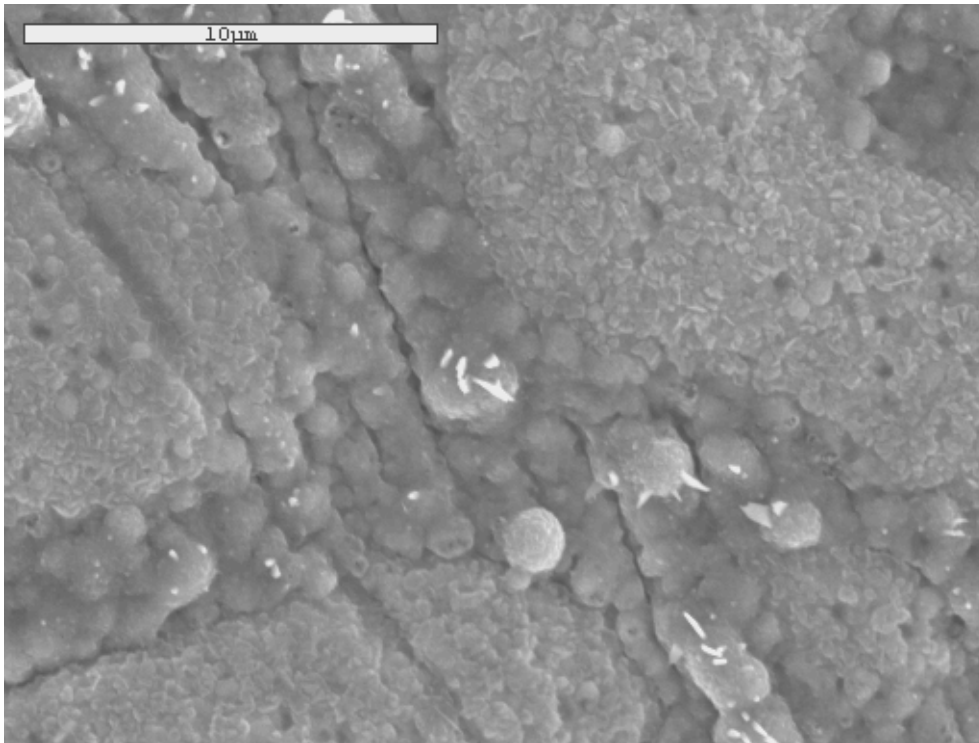


Figure 5-77. SE micrograph of Ni-22Cr-11Al oxidized in 10% SO<sub>2</sub> gas mixture at 800°C for 100 hr at 5000X.

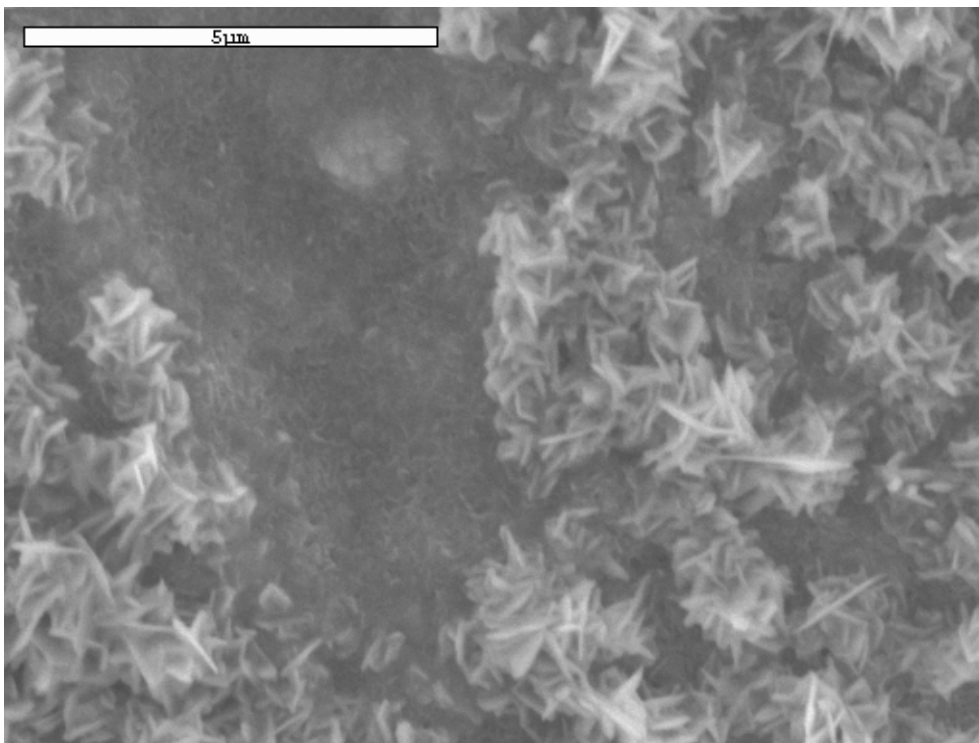


Figure 5-78. SE micrograph of Ni-22Cr-11Al oxidized in 10% SO<sub>2</sub> gas mixture at 1000°C for 100 hr at 10000X.

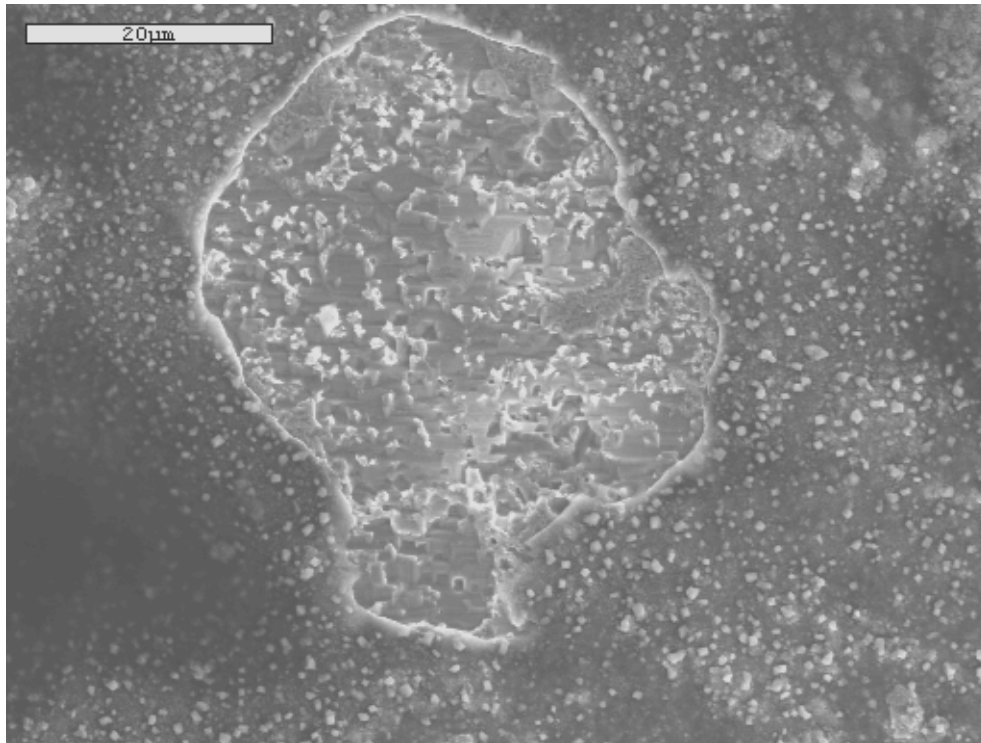


Figure 5-79. SE micrograph of Ni-22Cr-11Al oxidized in 10% SO<sub>2</sub> gas mixture at 900°C for 100 hr at 1500X.

## 5.4 Cross-Sectional Analysis

### 5.4.1 Ni and Ni-Al Specimens

Figure 5-80 shows a cross-section SEM micrograph of an oxidized Ni specimen. The NiO takes a columnar morphology. There appeared to some layers of internal oxidation that may have cracked during sample preparation. Figure 5-81 shows a NiAl sample in cross-section, revealing a layer of Al<sub>2</sub>O<sub>3</sub> alone. There was no depletion layer detected on these samples beneath the scale/alloy interface. However, some Ni-metal areas were observed surrounded by the alumina scale. Due to the lack of phosphorus in these regions, it was concluded that these regions were not from the electroless Ni deposited for edge retention.

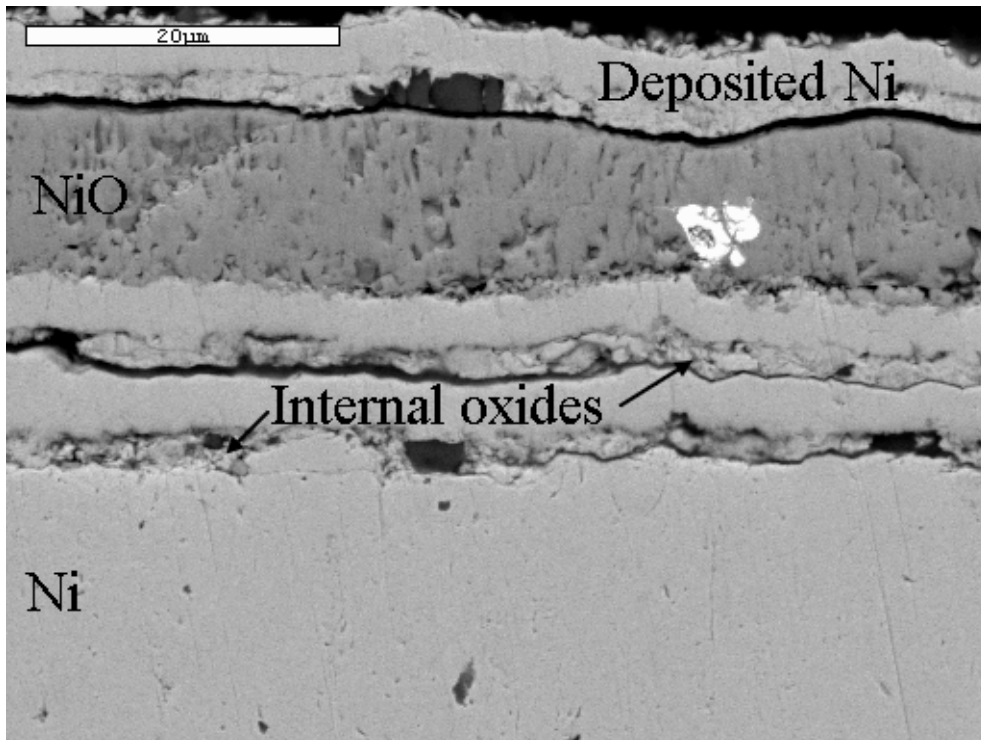


Figure 5-80. BSE micrograph of a Ni specimen oxidized at 800°C for 24 hr at 1900X. The top layer is the electroless Ni layer deposited for edge retention.

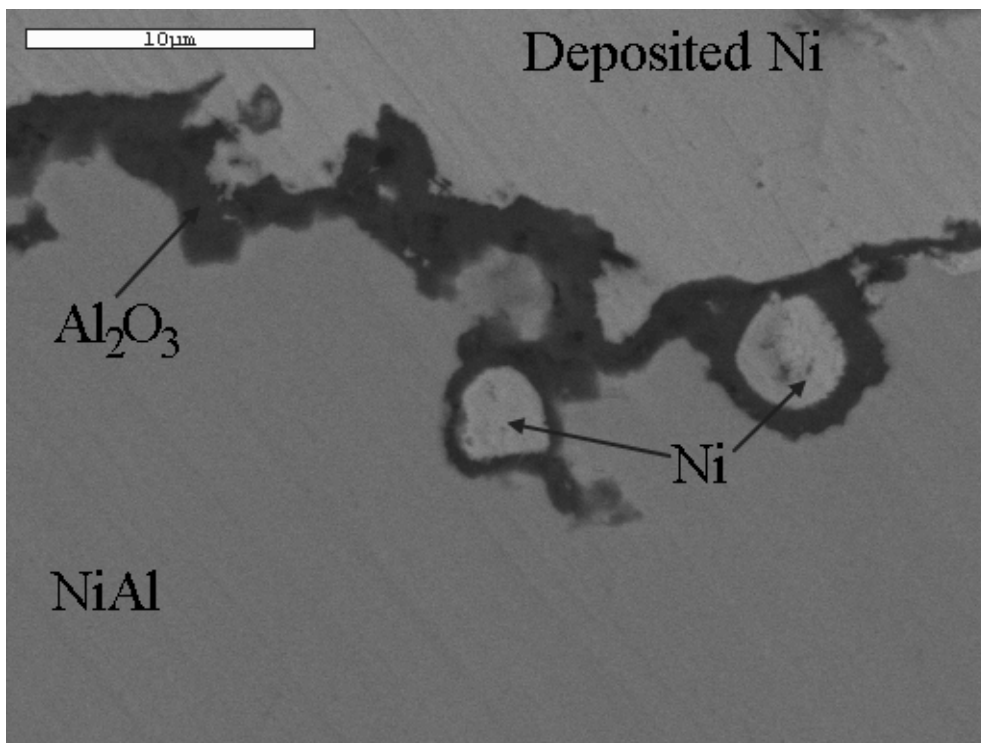


Figure 5-81. BSE micrograph of a NiAl specimen oxidized at 1000°C for 36 hr at 2000X. The top layer is the electroless Ni layer deposited for edge retention.

### 5.4.2 Ni-8Cr-6Al Specimens

Figure 5-82 shows the cross-section of Ni-8Cr-6Al oxidized at 900°C, in which the oxide likely cracked during sample preparation. The outermost oxide was shown to be NiO by EDS, with no solubility for other elements. Beneath that, a mixed Al/Cr oxide was identified with generally the same atomic percent of both Al and Cr. The darker oxide is Al<sub>2</sub>O<sub>3</sub> with only trace amounts of Ni and no other elements. There were small amounts of spinel detected, as well as some of the  $\gamma$ -Ni alloy in oxide itself. This indicates that at least part of the oxide grew into the alloy. Platinum marker tests confirm this, and show that the NiO grew outward from the original alloy/gas interface, while the (Al,Cr)<sub>2</sub>O<sub>3</sub> grew inward. The oxide was approximately 5 to 8  $\mu$ m thick, on average.

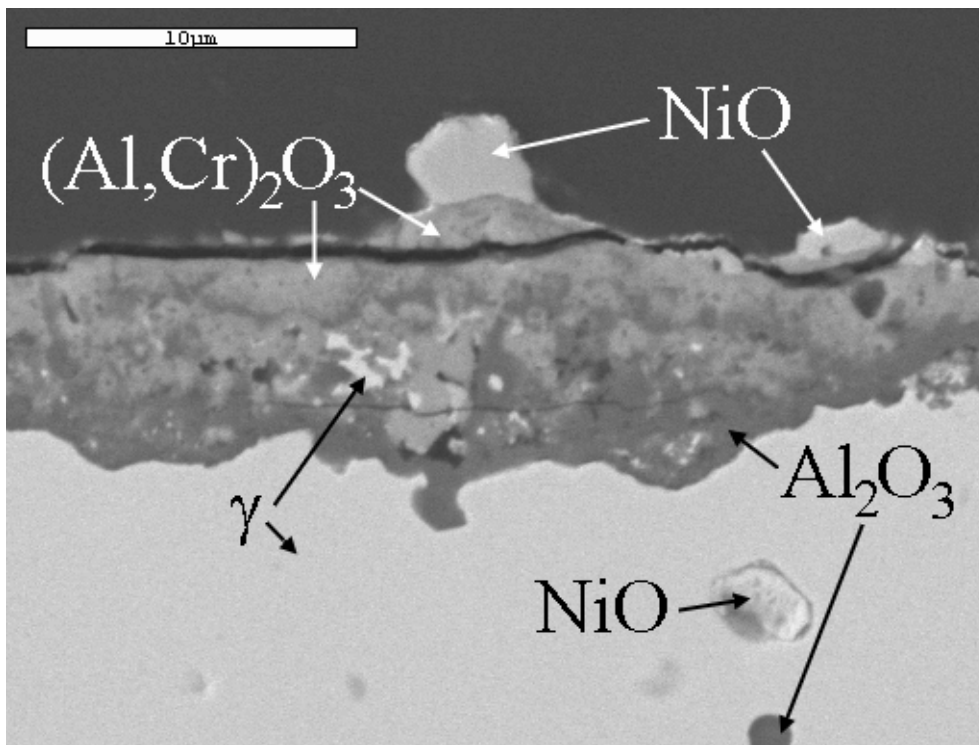


Figure 5-82. BSE micrograph of Ni-8Cr-6Al oxidized at 900°C in cross-section.

Figure 5-83 shows the cross-section of the same alloy oxidized in 2% SO<sub>2</sub> at 800°C. The oxide layer, as with most of the specimens showed a columnar grain morphology. Figure 5-84

shows a 900°C sample and, in contrast with Figure 5-82, there seemed to be no detectable NiO (even though it was seen in XRD), but a nominal amount of Cr<sub>2</sub>O<sub>3</sub> was detected. The top oxide was again (Al,Cr)<sub>2</sub>O<sub>3</sub>, with nearly equal amounts of Cr and Al (by mole). Below this layer was a mix of Cr<sub>2</sub>O<sub>3</sub> and Al<sub>2</sub>O<sub>3</sub> each closer to stoichiometry with solubility for the other elements less than 8 at%. Some Ni(Cr,Al)<sub>2</sub>O<sub>4</sub> spinel phase was observed, particularly at the alloy/scale interface, which had between 1 and 2 at% sulfur. Internally (below the oxide/alloy interface) some Cr sulfides were detected. From the semi-quantitative EDS analyses, their composition was observed as closest to the CrS stoichiometry, as compared to other Cr<sub>x</sub>S<sub>y</sub> sulfides. At a grain boundary, deep penetration of oxide was observed (Figure 5-85). In addition, there were sulfides observed along the grain boundary, which continued into the alloy (see Figure 5-86). These sulfides were also seen at 800°C, which appeared as a mix of Ni and Cr sulfides (see Figure 5-87). Pores were also observed in the oxide and at the oxide/alloy interface. While these could be artifacts, they are likely actual pores due to the observation of good scale adhesion on this specimen.

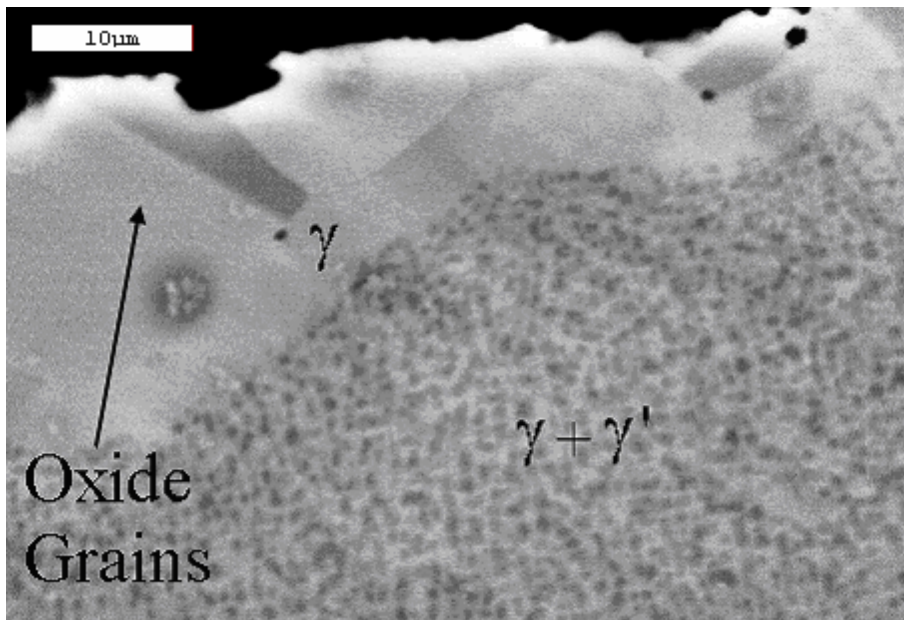


Figure 5-83. SE micrograph of Ni-8Cr-6Al oxidized in 2% SO<sub>2</sub> gas mixture at 800°C for 100hr in cross-section at 10000X.

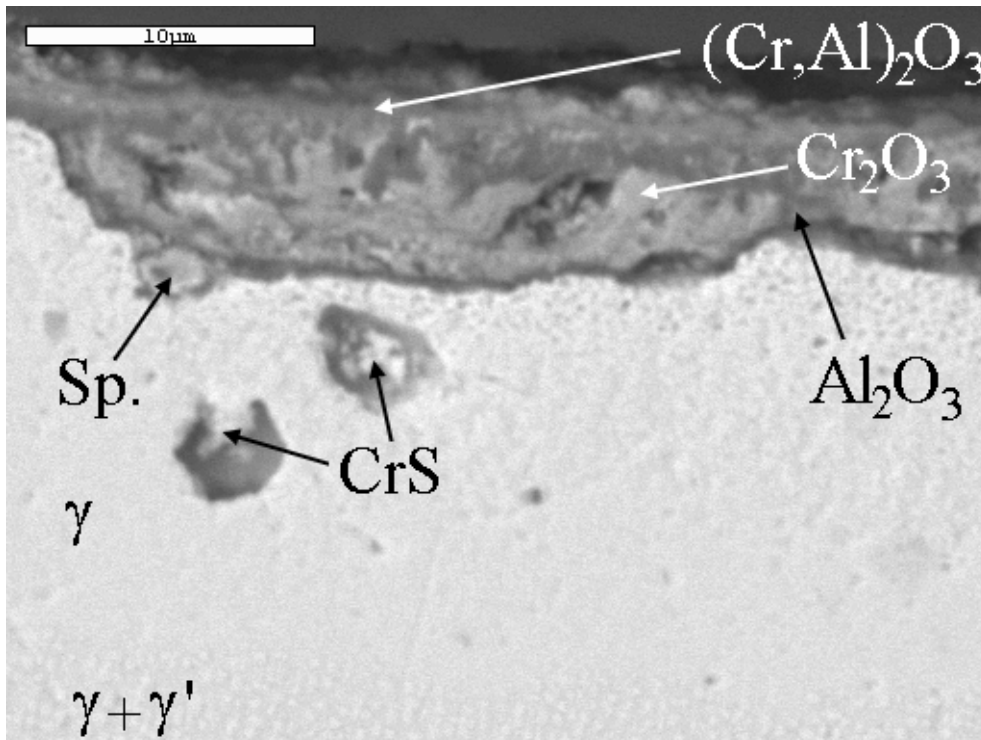


Figure 5-84. BSE micrograph of Ni-8Cr-6Al oxidized in 2% SO<sub>2</sub> gas mixture at 900°C for 100hr in cross-section at 3500X.

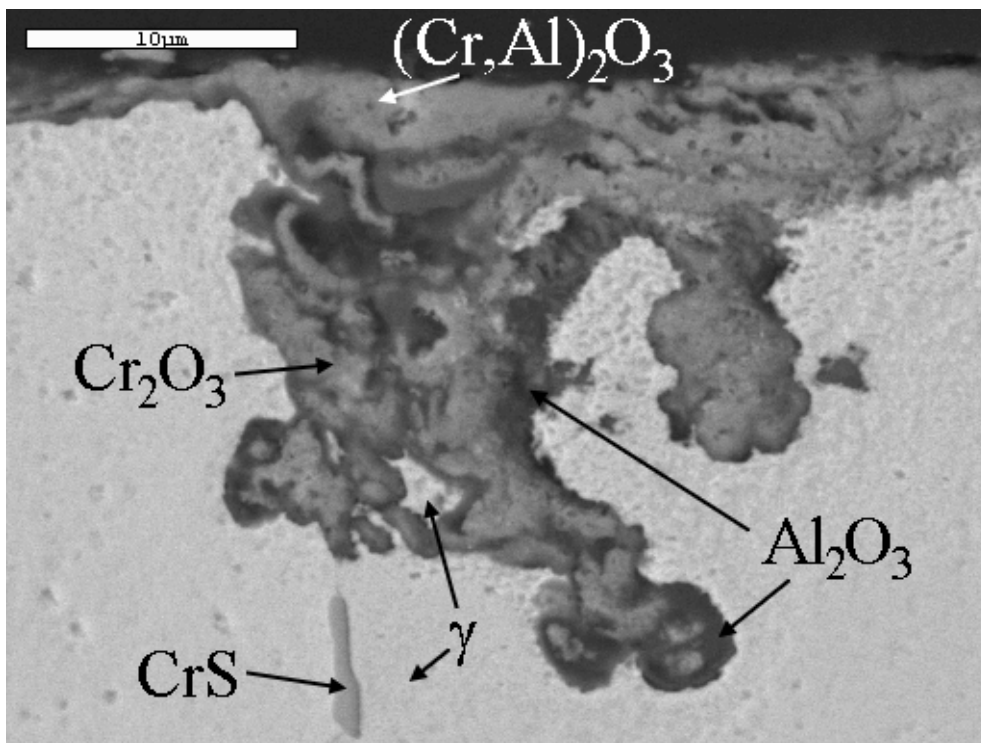


Figure 5-85. BSE micrograph of Ni-8Cr-6Al oxidized in 2% SO<sub>2</sub> gas mixture at 900°C for 100hr in cross-section at 3500X, showing an oxide deeply penetrating along a grain boundary.

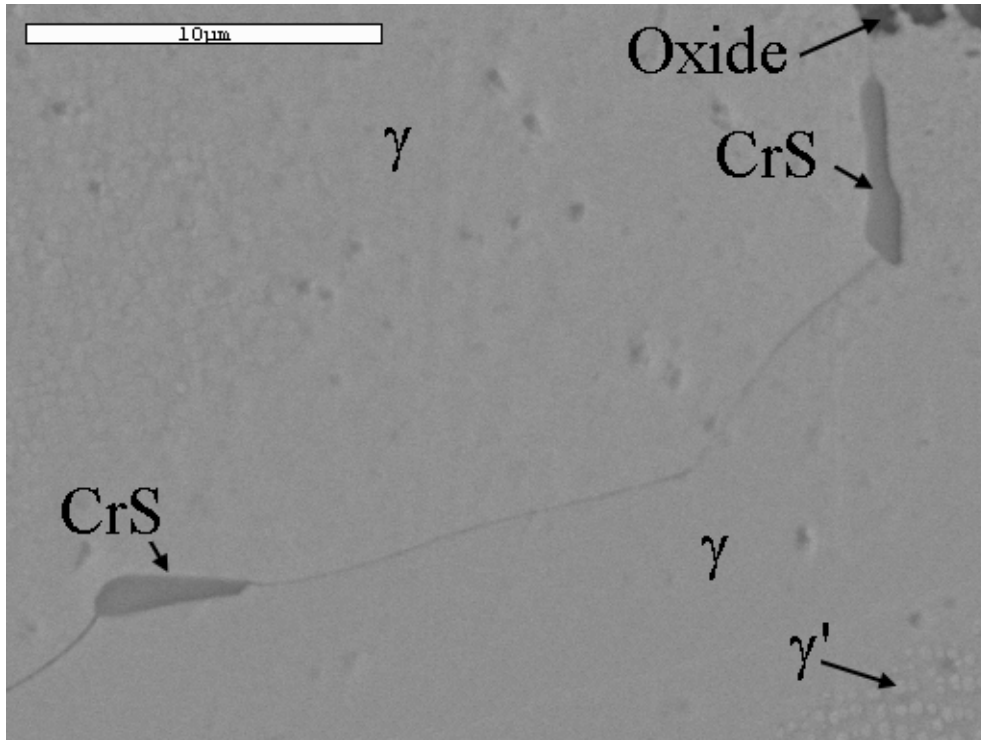


Figure 5-86. BSE micrograph of Ni-8Cr-6Al oxidized in 2% SO<sub>2</sub> gas mixture at 900°C for 100hr in cross-section at 5000X, showing sulfides along a grain boundary.

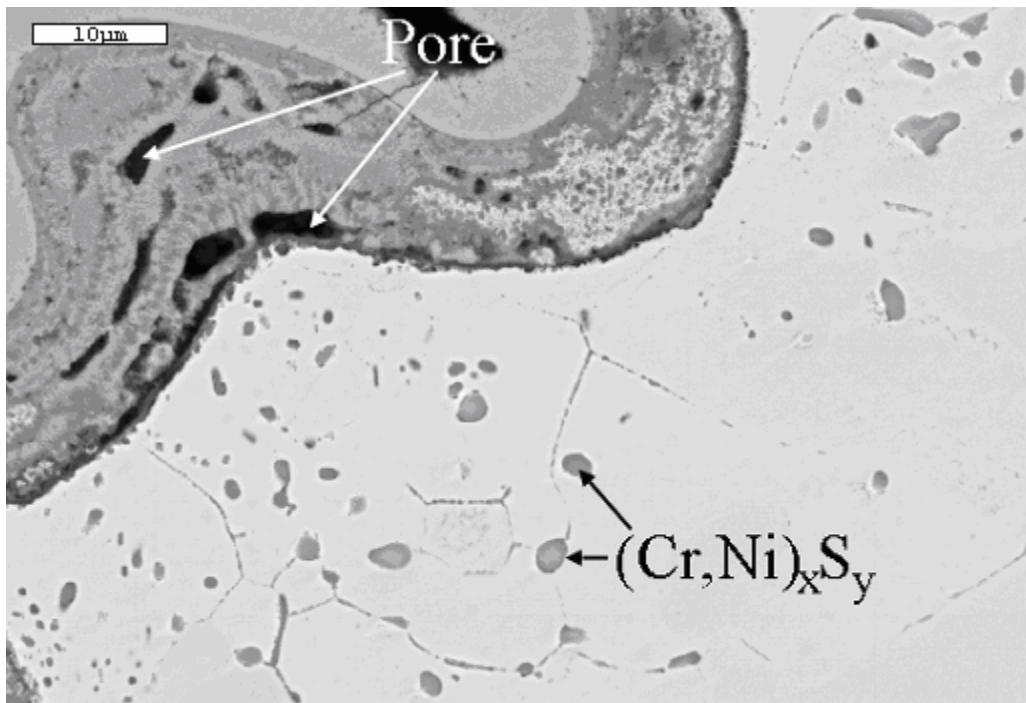


Figure 5-87. SE micrograph of Ni-8Cr-6Al oxidized in 2% SO<sub>2</sub> gas mixture at 800°C for 100hr in cross-section, showing sulfides along grain boundaries and pores in the oxide layer.

As shown in Figure 5-84, several depletion layers existed in the alloy below the scale/alloy interface. The first layer, approximately 1-2  $\mu\text{m}$ , showed a Ni phase with small (less than 4 wt%) amounts of each alloying element, and 6 wt% O, likely from irresolvable internal oxides. The second layer, which was 5  $\mu\text{m}$  thick, was an Al-depletion layer with less than 1 wt% S and 3 wt% O. Lastly, the third layer (5-8  $\mu\text{m}$  thick) was also depleted of Al, but had no S or O. Below that (~12-15  $\mu\text{m}$  under the interface) was the nominal alloy composition with the  $\gamma + \gamma'$  microstructure.

### 5.4.3 Ni-22Cr-11Al Specimens

The Ni-22Cr-11Al oxidized samples showed thinner oxide layers than Ni-8Cr-6Al (between 1-3  $\mu\text{m}$  versus 5-8  $\mu\text{m}$  for the Ni-8Cr-6Al) (see Figure 5-88). The oxide, though showed a similar pattern in that there was an outer layer of  $(\text{Al,Cr})_2\text{O}_3$  and an inner layer of  $\text{Al}_2\text{O}_3$ . At 2%  $\text{SO}_2$ , no sulfides were detected at the oxide/alloy interface, or anywhere else (see Figure 5-89). Low-Z phases were present beneath the interface, which consisted of mostly Al with approximately 11 at% Ni. This would indicate a  $\text{NiAl}_3 + (\text{Al})$  phase, which would be liquid at these oxidizing temperatures. In addition,  $\text{NiAl}_2\text{O}_4$  was often seen near these phases. The most striking difference in the change in microstructure from the unoxidized specimens. If compared to Figure 5-48, there are large areas of  $\beta$ -NiAl and small 2-4  $\mu\text{m}$  precipitates of  $\alpha$ -Cr (see Figure 5-90) surrounded now by a matrix of  $\gamma'$ . However, closest to the surface,  $\beta$  was less likely to be found and there were usually only  $\gamma'$  and  $\alpha$  present. As shown with the surface SEM images, more  $\text{Cr}_2\text{O}_3$  was present above the scale/alloy interface at the lower testing temperatures. One of these samples is shown in Figure 5-89. Beneath this oxide is the  $(\text{Cr,Al})_2\text{O}_3$  which has been seen before, as well as  $\text{NiAl}_2\text{O}_4$  spinel. In all the oxides characterized that were exposed to 2%  $\text{SO}_2$ , no sulfur or sulfide phases were found.

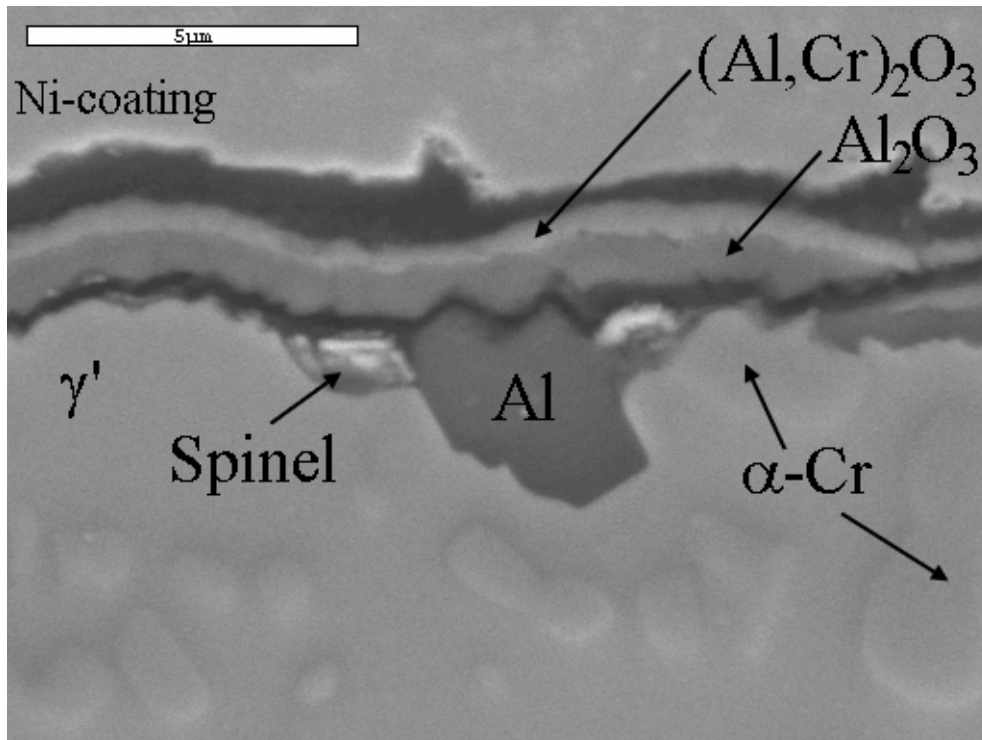


Figure 5-88. BSE micrograph of Ni-22Cr-11Al oxidized in 2% SO<sub>2</sub> gas mixture at 975°C for 100hr in cross-section at 8000X. The top layer is a Ni-coating added for edge retention.

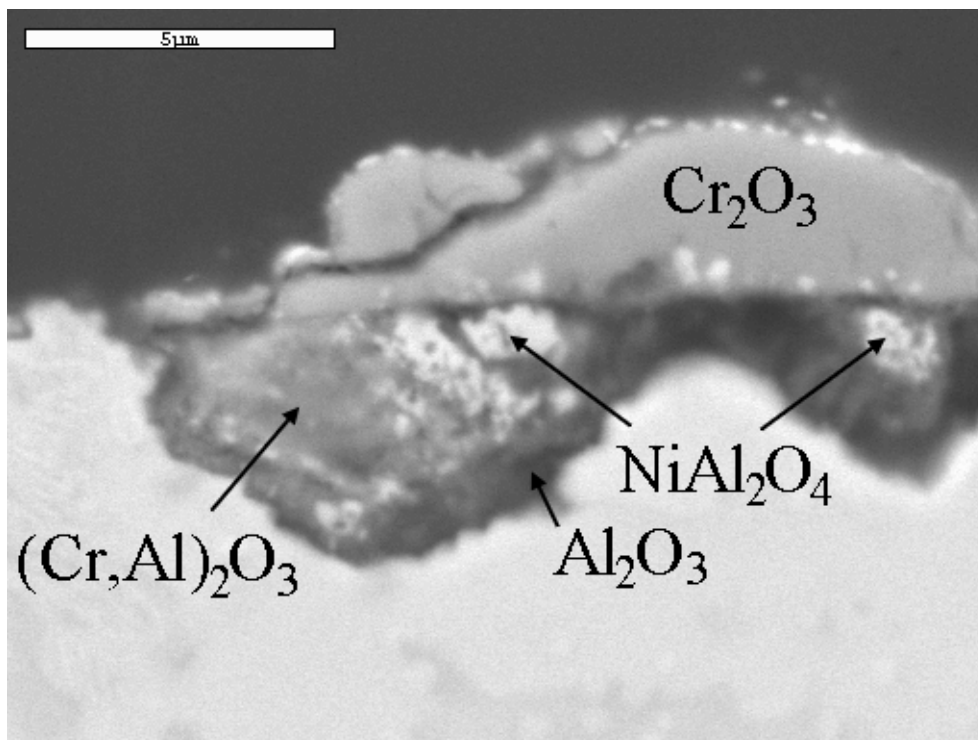


Figure 5-89. BSE micrograph of Ni-22Cr-11Al oxidized in 2% SO<sub>2</sub> gas mixture at 800°C for 100hr in cross-section at 800X.

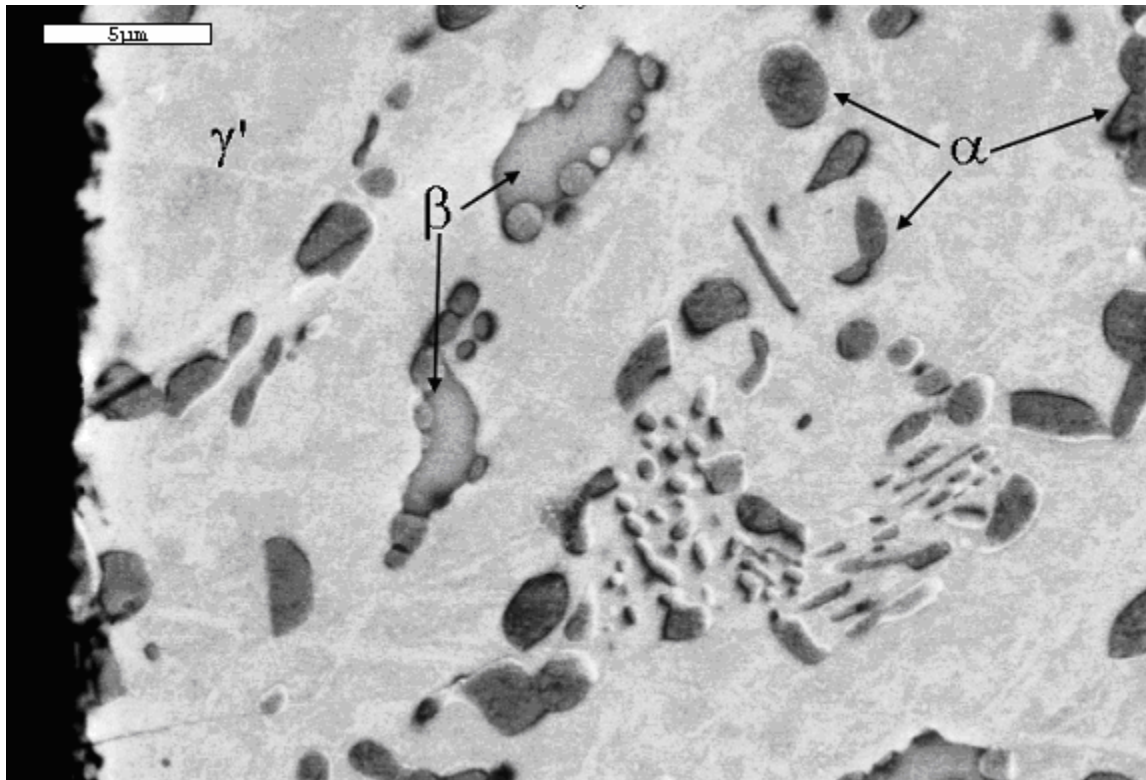


Figure 5-90. BSE micrograph of Ni-22Cr-11Al matrix that was exposed to the 2% SO<sub>2</sub> gas mixture at 975°C for 100hr 2000X. The labeled X-numbers are areas that were probed for EDS.

#### 5.4.4 Electron Microprobe (EPMA) Analysis

The EPMA scans of the cross-sections shown in the previous two sections were performed to determine the extent of sulfur at the scale/alloy interface, as well as the amount of internal oxidation and composition changes in the scale. The major drawback to the EPMA probes, though, were that the X-ray interaction volumes were on the order of 1 μm, and so could not be used accurately for individual phase analysis. However, EPMA was useful in determining the composition changes across a line scanned, as shown in Figures 5-91 through 5-93.

In all three EPMA linescans shown here, the oxide layer is on the left. The interface is located at 5.5 μm, 5.9 μm, and 7.0 μm for Figures 5-91, 5-92, and 5-93, respectively. In Figure 5-86, the outermost layer is Cr<sub>2</sub>O<sub>3</sub>, followed by a spinel phase, and then (Al,Cr)<sub>2</sub>O<sub>3</sub> which becomes leaner in Cr closer to the interface. At the interface, S was detected, upwards of 3.5

wt%. S continued to be found in the alloy, which was depleted in Al up to around 18  $\mu\text{m}$ . With Figure 5-92, the oxide was overall uniformly  $(\text{Cr,Al})_2\text{O}_3$ , except towards the surface which may have been spinel. An  $\alpha$ -Cr precipitate in the matrix near the interface was included in this linescan. This could account for the higher Cr in the oxide since the  $\alpha$  was so close to the interface. The last scan shown here (Figure 5-93) reveals a mostly Al oxide, with one  $\text{NiCr}_2\text{O}_4$  spinel phase in the scan. In both Ni-22Cr-11Al alloy scans show here, the maximum S detected at the interface was 0.3 wt%.

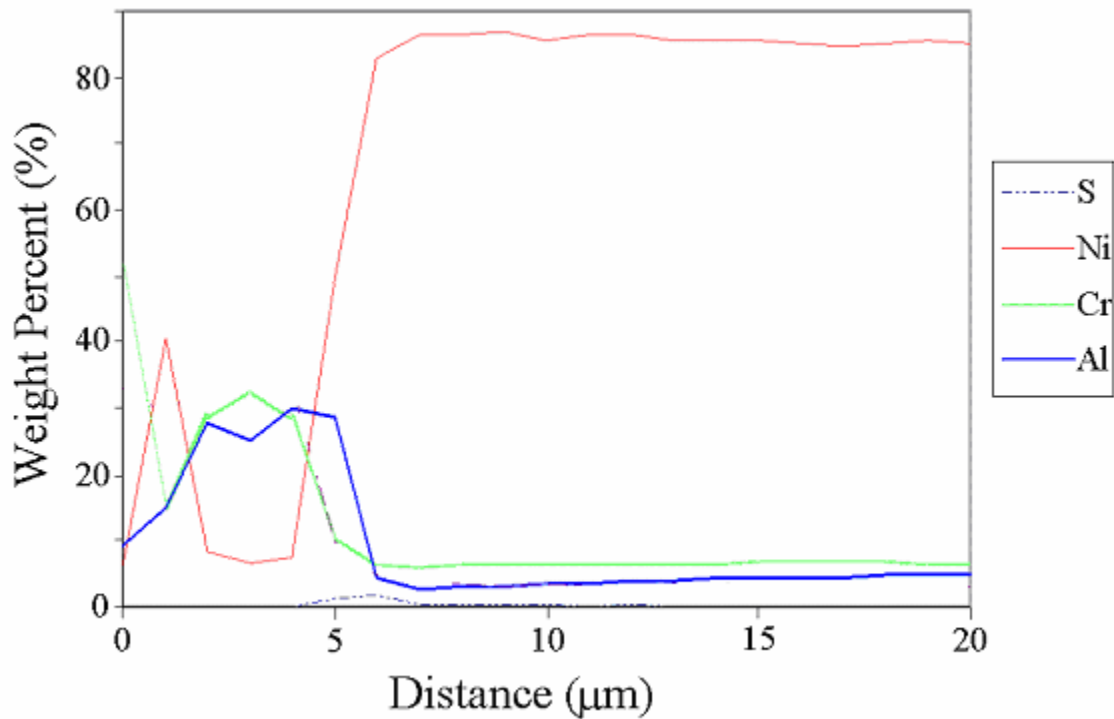


Figure 5-91. EPMA linescan across scale and interface in an Ni-8Cr-6Al alloy oxidized at 900°C in He + 0.21 O<sub>2</sub> + 0.02 SO<sub>2</sub> gas mixture.

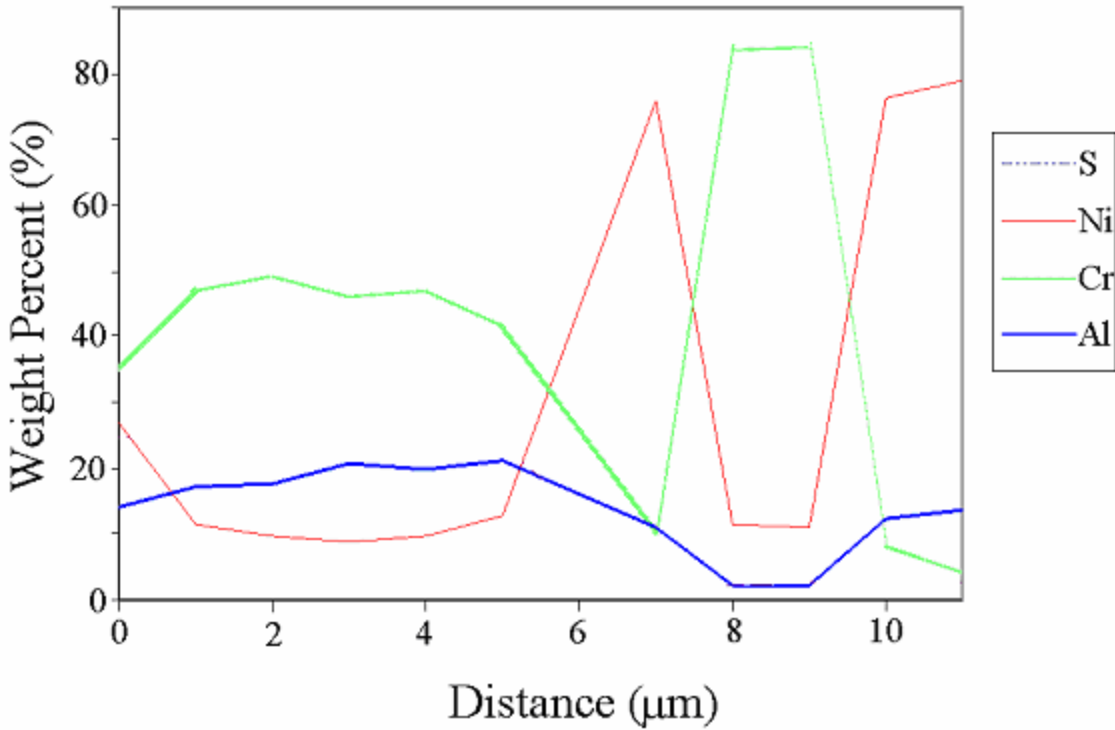


Figure 5-92. EPMA linescan across scale and interface in an Ni-22Cr-11Al alloy oxidized at 800°C in He + 0.21 O<sub>2</sub> + 0.02 SO<sub>2</sub> gas mixture.

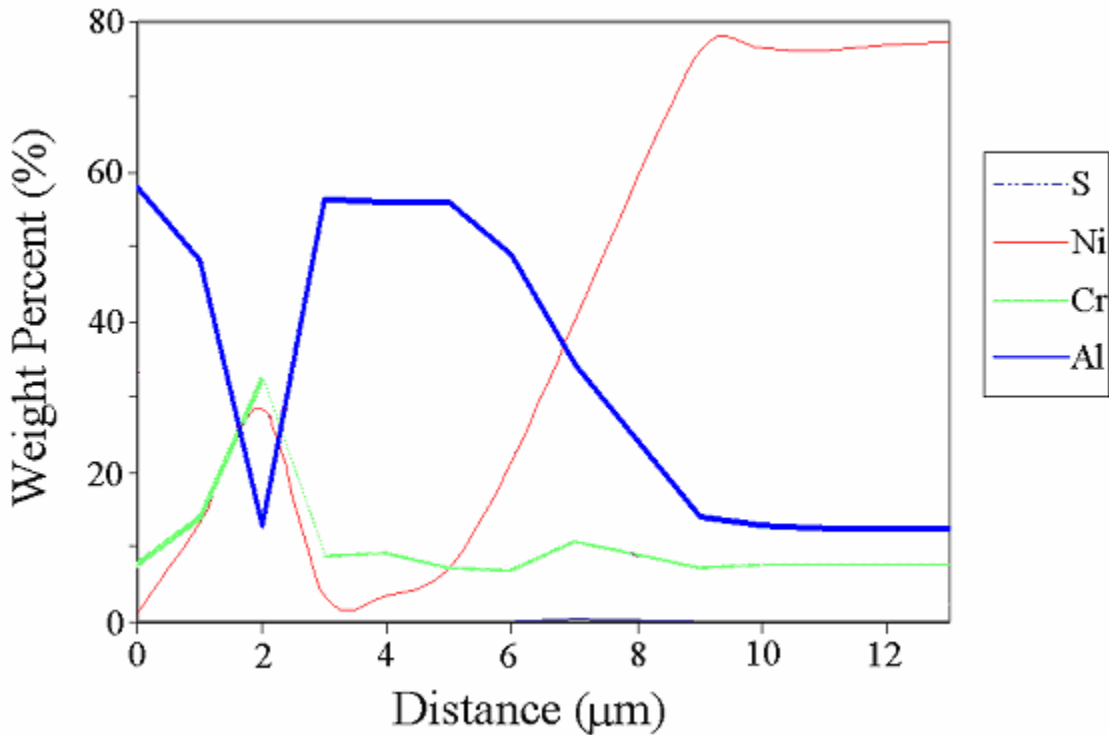


Figure 5-93. EPMA linescan across scale and interface in a Ni-22Cr-11Al alloy oxidized at 975°C in He + 0.21 O<sub>2</sub> + 0.02 SO<sub>2</sub> gas mixture.

## CHAPTER 6 DISCUSSION AND ANALYSIS

### 6.1 Mechanisms of Scale Formation

From the kinetic plot of Figure 5-20, the addition of alloying elements lessens the scale growth in all the oxidizing environments examined. From the XRD and SEM analysis, the following occurred during oxidation:

- Ni oxidized to form NiO
- Ni-8Cr-6Al oxidized to form NiO, NiAl<sub>2</sub>O<sub>4</sub>, Al<sub>2</sub>O<sub>3</sub>, and some (Al,Cr)<sub>2</sub>O<sub>3</sub>
- Ni-8Cr-6Al oxidized with SO<sub>2</sub> to form the same oxides in addition to stabilizing chromia as well as Ni and Cr sulfides
- Ni-22Cr-11Al oxidized to form “pure” Al<sub>2</sub>O<sub>3</sub> and Cr<sub>2</sub>O<sub>3</sub>, as well as an inner layer of (Al,Cr)<sub>2</sub>O<sub>3</sub>. Some spinel was also observed.
- Ni-22Cr-11Al oxidized with SO<sub>2</sub> produced the same oxides and sulfide were detected by XRD but not found from EDS/EPMA analyses.

With the Ni-8Cr-6Al alloys, NiO, spinel, and Al<sub>2</sub>O<sub>3</sub> were observed in SEM. Layers of NiO were observed on top of the Al<sub>2</sub>O<sub>3</sub> scale that lay underneath. This alumina layer with NiO clusters on top was uniform on all specimens tested. The heat-treated samples showed a uniform  $\gamma + \gamma'$  microstructure and this oxidation pattern appears valid, at least on the magnifications afforded via SEM. In addition, it is apparent that the reaction of Ni and O<sub>2</sub> occurs first, and the NiO scale begins to grow by outward cation diffusion of NiO [42-44]. This oxide took triangular plate-like morphology which grew laterally rather than transversely. This structure became layered as new nucleates would form on the transverse surfaces and, matching the substrate coherency, would also grow laterally although no texture was found in the oxides from EBSD.

In addition, Al<sub>2</sub>O<sub>3</sub> would also nucleate on the surface along side the formation of NiO. Spinel was also formed via Equation 2-12, or from Al substituting on the Ni lattice or vice-versa. Previous studies have show that a spinel phase will often form in Ni-Al alloys [76, 78] and from interactions of the NiO and alumina, especially in the initial oxidation [79]. The surface alumina

often appeared, on this alloy and others, as needles or thin plates in random orientations, especially at high temperatures. Previous research has shown that transient aluminas, such as  $\delta$  or  $\theta$ , which are tetragonal and monoclinic respectively, often evolve initially on Al, Ni-Al, and Ni-Cr-Al specimens and grow by outward cation transport [58-59]. However, XRD scans of Ni-8Cr-6Al oxidized at 0.5, 16, and 100 hrs show only the  $\alpha$  corundum phase, which was been shown to grow by inward anion transport [55, 60-61, 89]. Previous publications demonstrated that the transient aluminas will often transform to  $\alpha$  after the formation of a continuous  $\alpha$ -Al<sub>2</sub>O<sub>3</sub> scale [55, 89, 97-98], due to lattice mismatch strains at the differing alumina interfaces [55-56]. This would explain why, if they existed, that the transient alumina phases were not detected.

Cr<sub>2</sub>O<sub>3</sub> or Cr-containing oxides and spinels were not detected on the surface of oxidized Ni-8Cr-6Al specimens. Previous studies of compositions similar to this one by Giggins, Pettit, and other show the formation of NiO and NiCr<sub>2</sub>O<sub>4</sub> at the surface at high oxygen partial pressures (0.2-1 bar) [90, 93, 127]. If not, Cr<sub>2</sub>O<sub>3</sub> stabilized [93, 127]. Cross-sections, however, revealed a (Cr,Al)<sub>2</sub>O<sub>3</sub> layer present underneath, which has been previously observed [86, 97-98]. This would agree with generally accepted mechanism that the formation of NiO (and Al<sub>2</sub>O<sub>3</sub>) on the surface caused the transport of O<sup>2-</sup> anions and metal cations, not the surface metal/chemisorbed oxygen reaction, to be rate limiting, causing a decrease in oxygen activity [48-40]. This allowed for the stabilization of Cr<sub>2</sub>O<sub>3</sub> and Al<sub>2</sub>O<sub>3</sub>, which coalesced into a continuous scale and grew in a steady-state manner, which would be described by the parabolic, steady state growth recorded by the TGA. Since the anion diffusion through alumina scales is slow, it would be rate-limiting [49, 88], and short-circuit processes would dominate at sufficient scale thicknesses [41]. Previous studies, though, commented that this alloy composition might not develop a continuous alumina scale below 1000°C [76, 90, 127], but here was able to form a stable, adherent Al<sub>2</sub>O<sub>3</sub> scale for

100 hrs of isothermal oxidation. There was, however, spallation observed in scales at higher temperatures and in SO<sub>2</sub> gas mixtures. However, TG tests could not confirm an Arrhenius dependence to oxidation in air for either Ni-Cr-Al alloys. Either this is due to measurement/preparation error, steady-state scale growth not being achieved, or complex/competing mechanisms that vary with temperature.

The Ni-22Cr-11Al specimens oxidized and showed only Al<sub>2</sub>O<sub>3</sub> and Cr<sub>2</sub>O<sub>3</sub> on the surface during oxidation. As shown by Figure 5-64, chromia would develop over the Cr-rich  $\gamma$  regions, while Al<sub>2</sub>O<sub>3</sub> would develop over the Al-rich  $\beta + \gamma'$  regions, as had been previously observed in  $\gamma' + \beta$  alloys [96-97]. Comparing Figure 5-48 and 5-49 to the microstructure of the center of the oxidized samples, it can be assumed that the heat-treatment meant to homogenize the Ni-22Cr-11Al arc-melted buttons did not achieve its goal. Unlike the Ni-8Cr-6Al composition, which would solidify as  $\gamma$ -Ni first and then precipitate the  $\gamma'$ , the Ni-22Cr-11Al would solidify as  $\beta$  dendrites, rejecting Cr due to constitutional supercooling. This would push the interdendritic liquid composition closer to the e<sub>3</sub> reaction (see Figures 2-6 and 2-7) in which the liquid would solidify as  $\alpha$  and  $\gamma$ . If the center microstructure of the Ni-22Cr-11Al oxidized specimen is an indication of an equilibrium microstructure, then the heat treatment of 4 hr at 1200°C was neither long enough nor at a high enough temperature to fully equilibrate the microstructure. The oxidized specimens showed, at distances far away from O-penetration, that the equilibrium microstructure is a  $\gamma' + \gamma$  matrix, with semi-spherical  $\beta$  and  $\alpha$  phases dispersed throughout.

Regardless, the Ni-22Cr-11Al specimens that were oxidized showed a faster, outward growing Cr<sub>2</sub>O<sub>3</sub>, and a smoother Al<sub>2</sub>O<sub>3</sub>. This oxidation stage was likely shown as initial parabolic rates of the TG curves for this alloy, which last between two and ten hours, depending on the temperature. No dependence could be found between temperature and this transition time. At

the transition in growth kinetics, spinel may have grown underneath these phases due to the initial depletion of Cr and Al from oxidation. Spinel was detected in some of the samples exposed to SO<sub>2</sub>, but not in the oxidized samples, so it cannot be said whether it existed during this process. This transition process could also indicate the internal oxidation of Cr, which would catalyze the internal oxidation of Al. Like with Ni-8Cr-6Al, and most Ni-Cr-Al alloys with high enough concentrations of Cr and Al, the activity of O was reduced due to the gettering effect of Cr, and a continuous alumina scale formed [85-90]. Cross-sections of the alloy showed this in which the Cr<sub>2</sub>O<sub>3</sub> would appear closest to the gas/scale interface, growing by outward Cr<sup>3+</sup> transport. Underneath a semi-duplex layer of (Al,Cr)<sub>2</sub>O<sub>3</sub> and Al<sub>2</sub>O<sub>3</sub> closest to the scale/alloy interface was observed, which likely grew from internal anion diffusion as it was shown to penetrate into the alloy. Like the Ni-8Cr-6Al specimens, the amount of Cr in the (Al,Cr)<sub>2</sub>O<sub>3</sub> region generally decreased the closer one traced towards the scale/alloy interface, which contained alumina with less than 3 wt% Cr.

The effect of sulfur was one that enhanced the oxidative effects of the atmosphere on the alloys (see Figure 5-20). At the higher temperatures (900 and 975°C), the rate of oxidation increased when SO<sub>2</sub> was added to the gas mixture. This was in spite of the fact that the partial pressure of O<sub>2</sub> may have been decreased due to the formation of SO<sub>3</sub> via Equation 2-16. The partial pressures of O<sub>2</sub>, SO<sub>2</sub>, and SO<sub>3</sub> for the mixed gas experiments are shown in Table 6-1. However, as stated by Luthra, the SO<sub>3</sub> formation is extremely slow and takes extended times to develop—upwards of 90-100 hr, near the length of these tests [128]. No catalyst was used in this test to attempt to have SO<sub>2</sub>, and not SO<sub>3</sub>, be the majority sulfidizing gas. Even with equilibrium achieved, SO<sub>2</sub> was the major sulfidizing gas, particularly at 900 and 975°C. Furthermore, studies have shown that SO<sub>2</sub> is more likely to adsorb on oxide surfaces than SO<sub>3</sub> [128], making

its the reaction-controlling sulfidizing agent. SO<sub>3</sub>, though, was found condensed in the TGA further down the gas stream past the furnace where the gas reached room temperature. SO<sub>3</sub> may have had an effect beyond just lowering the oxygen partial pressure at 800°C (the growth rate was less for SO<sub>2</sub> exposed samples at this temperature). However, no NiSO<sub>4</sub>, or any other sulfates were detected, which are usually signs of an SO<sub>3</sub>-dependent reaction [127, 130-131, 145].

Table 6-1. Table showing the equilibrium partial pressures of gases that evolve upon various mixtures of O<sub>2</sub> and SO<sub>2</sub> at various temperatures, calculated from the SPOT3 database.

Mixture (bar)	Temperature (°C)	P <sub>O<sub>2</sub></sub> (bar)	P <sub>SO<sub>2</sub></sub> (bar)	P <sub>SO<sub>3</sub></sub> (bar)
He + 0.21 O <sub>2</sub> + 0.02 SO <sub>2</sub>	800	0.208	0.015	5.43e-3
He + 0.21 O <sub>2</sub> + 0.02 SO <sub>2</sub>	900	0.209	0.018	2.57e-3
He + 0.21 O <sub>2</sub> + 0.02 SO <sub>2</sub>	975	0.209	0.019	1.50e-3
He + 0.21 O <sub>2</sub> + 0.10 SO <sub>2</sub>	800	0.199	0.074	0.027
He + 0.21 O <sub>2</sub> + 0.10 SO <sub>2</sub>	900	0.205	0.088	0.013
He + 0.21 O <sub>2</sub> + 0.10 SO <sub>2</sub>	975	0.207	0.093	7.49e-3

As stated previously, the effect sulfur plays in the oxidation tests of this study is one of accelerating the oxidation process. This appears to occur in two ways. First, the SO<sub>2</sub> reacts with the metal to form an oxide and free up sulfur in the form of S<sub>2</sub>, as per Equation 2-17 [150]. The second is the faster diffusion of ions through the oxide lattice due to defects created from S impurities [111]. This has been shown to occur from S<sub>2</sub> substituting on the anion lattice, creating cation vacancies [121, 171]:



This free oxygen then creates more cation vacancies (in this case a Ni vacancy) which increases the overall cation diffusion rate:



Similar reactions also occur in Cr<sub>2</sub>O<sub>3</sub>. These vacancies could migrate and be more prevalent at the grain boundaries, increasing diffusion there.

In addition, with the Ni-8Cr-6Al samples, cross-sectional analysis showed the presence of Cr and Ni sulfides along the grain boundaries and phase boundaries in the alloy. There was also a higher concentration of S at the scale/alloy interface than in the matrix or scale. Studies have shown that sulfur and SO<sub>2</sub> are attracted to grain boundaries, pores, and surfaces with higher surface energies [138, 142, 144-145, 151]. In studies with polycrystalline Cr [140] and superalloys [124, 151], at these surfaces, when the P<sub>S<sub>2</sub></sub> is high enough, the SO<sub>2</sub> reacts with Cr in solution to form chromium sulfides beneath the interface (Equation 2-18). The high defect structure of these sulfides affords rapid transport of S<sup>2-</sup>, O<sup>2-</sup>, and cations [119, 148]. Next, with the increasing P<sub>O<sub>2</sub></sub> from the anion influx, the sulfide oxidizes via:



leaving free sulfur to further migrate into the alloy forming more sulfides and repeating this process. This proposed mechanism can explain Figures 5-85 through 5-87 and was observed in previous mixed oxidation/sulfidation studies [115, 133, 137, 140].

In all the SO<sub>2</sub>-exposed samples, Cr<sub>2</sub>O<sub>3</sub> and/or NiCr<sub>2</sub>O<sub>4</sub> were found, and were often more prevalent than NiO. It appears that the presence of sulfur, at these levels, stabilizes the formation of Cr<sub>2</sub>O<sub>3</sub>. This can be attributed to the fact that the presence of sulfur may cause the more rapid growth diffusion of Cr, allowing its oxide to stabilize faster [119].

The mechanism for transport of sulfur through the oxide scale seems more likely to be better described by the transport of sulfur gas molecules. The major criticism to this theory is the inability of the SO<sub>2</sub> molecule to diffuse through a compact scale [117, 122]. However, images of these scales in cross-section show them to be anything but compact: they display pores, cracks,

and scale buckling. It should be noted, though, that some of these observed defects could be preparation artifacts.  $\text{SO}_2$  would easily be able to travel through these paths and react by Equation 2-18 to release S at the scale/alloy interface. While bulk diffusion of  $\text{S}^{2-}$  may be occurring, in these experiments, bulk transport processes would be orders of magnitude slower than grain boundary or free surface diffusion of  $\text{SO}_2$  [112, 117, 133]. Furthermore, the presence of S has been shown to increase the amount of voids present in an oxide scale, which would increase  $\text{SO}_2$  transport [135, 137].

Sulfides were not observed in the Ni-22Cr-11Al samples, although one specimen did show a small sulfur concentration at the scale/metal interface. This is likely due to the fact that the increased concentration of Al and Cr stabilized the protective oxides faster, reducing the rate of sulfur influx. For the length of these tests, the sulfur activity may never reached high enough levels to begin sulfide stabilization. In addition, the grain size of the Ni-22Cr-11Al specimens was smaller than the Ni-8Cr-6Al. Previous research of cast and forged Ni-base superalloys has shown that a finer grain size reduces sulfidation in oxidizing environments [133]. This is due to the faster diffusion of Al and Cr outward along more grain boundary surface area, which forms a protective  $(\text{Al,Cr})_2\text{O}_3$  layer more rapidly.

## **6.2 Comparison of Experimental Results and Calculations**

As shown in Chapter 4, calculations were performed to help predict and explain the processes occurring during the oxidation and sulfidation of the Ni-Cr-Al alloys used in this study. The diagrams calculated for the ternary subsystems of the Ni-Cr-Al-O quaternary system appear to agree well with previous literature, except for one point [6-7, 32]. In previous calculations by Saltykov, the Ni-Al-O and Ni-Cr-O systems produced showed that in the Ni-lean, O-rich sections  $(\text{Al,Cr})_2\text{O}_3$  would always be a two-phase mixture with spinel [6]. However, the results of the calculations (see Figures 4-8, 4-9, and 4-10) in this study show that there is a point

of stoichiometric spinel that decomposes via a peritectoid reaction into (Al/Cr)<sub>2</sub>O<sub>3</sub> and NiO at around 10-14 bar of O<sub>2</sub>. This decomposition reaction is supported by previous studies [121, 171], which were not contradicted by the experiments of this dissertation.

In calculations involving alloys, temperature increases corresponded to the stabilization of oxides that were more stable at lower partial pressures of oxygen. As shown from analysis of the Ni-8Cr-6Al alloy in all environments, NiO was not detected at higher temperatures whereas spinel and chromia (or Cr-rich aluminas) were. This shows that the stability of these oxides increased, causing them to form faster, reducing the amount of NiO that could form. While thermodynamics may play a role, it should be noted that the increase in temperature would have a kinetic effect, allowing faster cation transport that may have aided in the faster formation of the non-Ni oxides.

For most of the calculations involving S, the SPOT3 database was accessed since it had the S descriptions that are unavailable in the SPIN4 database as well as gas phase descriptions for all the S and O gas species. However, the SPOT3 only simulates mechanical mixtures of solid “solutions” and not the actual alloys (no mixing parameters). In spite of this, the phases, activities, and reactions were close in the calculations involving SPIN4 and SPOT3 comparisons (see Table 4-1 and Figure 4-40). The results appeared nearly identical for regions where the (Al,Cr)<sub>2</sub>O<sub>3</sub> oxide was predominant (described as two stoichiometric oxides by SPOT3). Furthermore, the reactions occurring at the scale/alloy interface are stoichiometric themselves and proceed whether the material is an alloy or mechanical mixture. For example, for the formation of Al<sub>2</sub>O<sub>3</sub> from a Ni-Al mixture, the software calculates either:

- Alloy:  $\text{Ni} + 4\text{Al}(\text{soln}) + 3\text{O}_2 \rightarrow \text{Ni} + 2\text{Al}_2\text{O}_3$
- Mixture:  $4\text{Ni}_3\text{Al} + 3\text{O}_2 \rightarrow 12\text{Ni} + 2\text{Al}_2\text{O}_3$

In either case, the net reaction is still that of Al reacting with O<sub>2</sub> to form Al<sub>2</sub>O<sub>3</sub>, with the Ni having no net contribution. Therefore, for the calculation purposes of this dissertation, it is immaterial whether the reacting element is part of a solution or a mechanical mixture, so long as it is the only element reacting with either O<sub>2</sub> or SO<sub>2</sub>. The calculations of SO<sub>2</sub>-O<sub>2</sub> diagrams from this dissertation using this reasoning have already been presented and published [170]. The main discrepancy involves the activity of a component in a particular phase. In addition, the reactions on the potential diagrams calculated for the alloys are identical for the appended SPIN4 database and the SPOT3 database, except were noted on Figures 6-1 and 6-2. This difference is due to an alternate spinel phase description in the SPIN4 database.

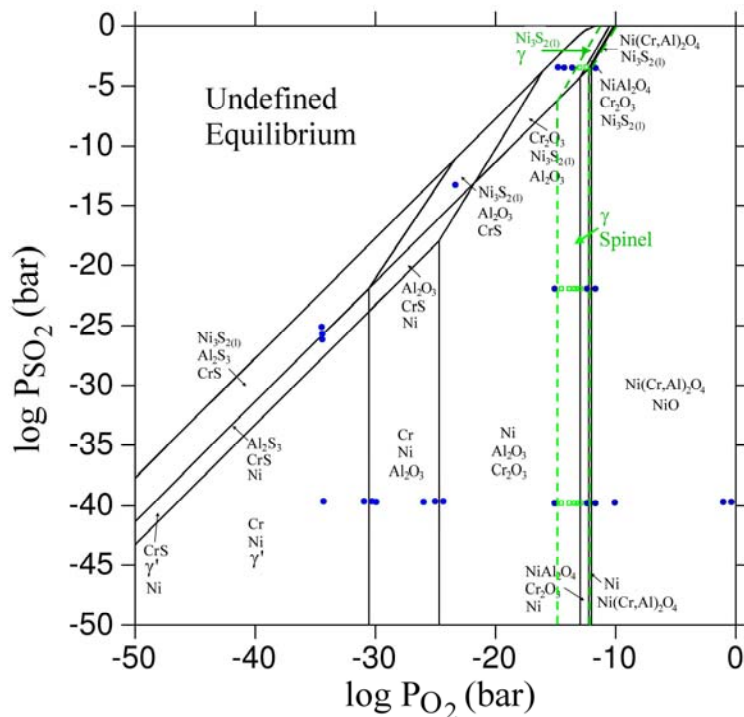


Figure 6-1. Comparison of phases observed in SPIN4 calculations versus an SO<sub>2</sub>-O<sub>2</sub> potential diagram of Ni-8Cr-6Al at 900°C. The blue dots correspond to calculated equilibria where the appended SPIN4 and SPOT3 databases agree. The green cubes correspond to disagreements. The dashed lines represent the alternate reaction lines determined by the appended SPIN4 database.



22Cr-11Al as predicted by a previous work [37]. Lastly, for the Ni-22Cr-11Al alloy, at low enough  $P_{O_2}$ , the  $\beta$ -NiAl phase is stable. The data in this dissertation showed no  $\beta$  near the scale/alloy interface. It should be noted that the oxidation processes described here are ones of a coating in direct contact with a gas atmosphere, and partial pressures of the gas species decreasing as the oxide grows (at the scale/alloy interface). In common service conditions, though, the application of a TBC reduces the  $P_{O_2}$  seen at the scale/alloy interface, causing the (desired) formation of  $(Al,Cr)_2O_3$ . Only after longer service times and more oxygen penetration do spinel and NiO begin to form as part of the TGO [91, 155].

The diagrams calculated and shown in Figures 4-13 through 4-15 were useful in determining the stability of the  $O_2 + SO_2$  gas mixture at various temperatures. The diagrams showed the significance of  $SO_3$  formation and how much of a factor it could be in the sulfidation corrosion observed in the results. Figure 4-14 was also helpful in showing the partial pressure of  $S_2$  in relation to the gas mixture not only at the surface, but also at the scale/alloy interface, where higher sulfur concentrations were discovered from microprobe analyses.

In addition, the high temperatures allowed for sulfide stabilization at higher oxygen partial pressures. The minimal activities of  $SO_2$  gas required to form sulfides varied with the alloy composition, temperature, and oxygen partial pressure. However, the calculations did show that Cr sulfides could form in equilibrium with Ni and  $Al_2O_3$  (at the scale/alloy interface) or in equilibrium with Ni and  $\gamma'$ , which was seen at the grain boundaries in the alloy in Figure 5-86 for the Ni-8Cr-6Al alloy. The Ni-22Cr-11Al alloy, however, showed no real sulfidation at all, being absent of sulfides. The only sulfur found present was at the scale/alloy interface, in amounts of less than 0.30 wt%. From Figures 4-41 and 4-43, the  $P_{S_2}$  required to stabilize sulfides in the oxides could be calculated. At high  $P_{O_2}$  in these alloys, if the  $P_{S_2}$  is too low, the  $SO_2$  will remain

as a gas, or form oxides. Once the  $P_{S_2}$  is high enough, as shown by the  $P_{S_2}$  spikes in Figures 4-41 and 4.43, sulfidation of the alloy can begin. Clearly, the lower the  $P_{O_2}$ , the lower the  $P_{S_2}$  required to for sulfide formation/stabilization. This may explain why, in the Ni-8Cr-6Al alloys oxidized in  $SO_2$ , only Cr-sulfides were observed (see Figures 5-85 through 5-87). Where  $Ni_3S_2$  is stable, the  $P_{O_2}$  may have been too high and the  $P_{S_2}$  too low. However, deeper into the substrate, along the grain boundaries, the  $P_{S_2}$  was adequate to allow for sulfide formation in a lower  $P_{O_2}$  environment.

Figures 6-3 and 6-4 show how activity values calculated from EPMA line scans compared to calculated activities from Section 4.4. In both Figures, there is close agreement between the activities Ni. However, there are discrepancies between the other components. Qualitatively, they all follow the trends calculated—the lowering of  $a_{Cr}$  and  $a_{Al}$  as  $P_{O_2}$  increases. In addition, the activity of  $S_2$  is shown to increase at the scale/alloy interface. Experimentally, activity of  $S_2$  decreases as one moves into the alloy away from the scale/alloy interface. This was not as calculated because the calculations assumed a constant mole fraction of  $SO_2$  gas in the system, which is not the case experimentally. There is also a higher Al activity than calculated. This could be due to the depletion of reacting elements from the alloy near the interface, or the linescans probing certain phases instead of the bulk such a probe of  $\beta$  instead of  $\gamma$ .

The error in correlating the experiments and calculations can come from several sources. First, the activities calculated for the calculations and from the experimental EPMA data are both assumed to be at some equilibrium. The activities calculated from the experimental data assume local equilibrium at the one point, which is likely. However, the calculated diagrams assume equilibrium across a range of  $P_{O_2}$ . This can be problematic, especially when interpreting these diagrams in relation to the actual observed cross-sections. In Figures 5-83 to 5-89, spinel was

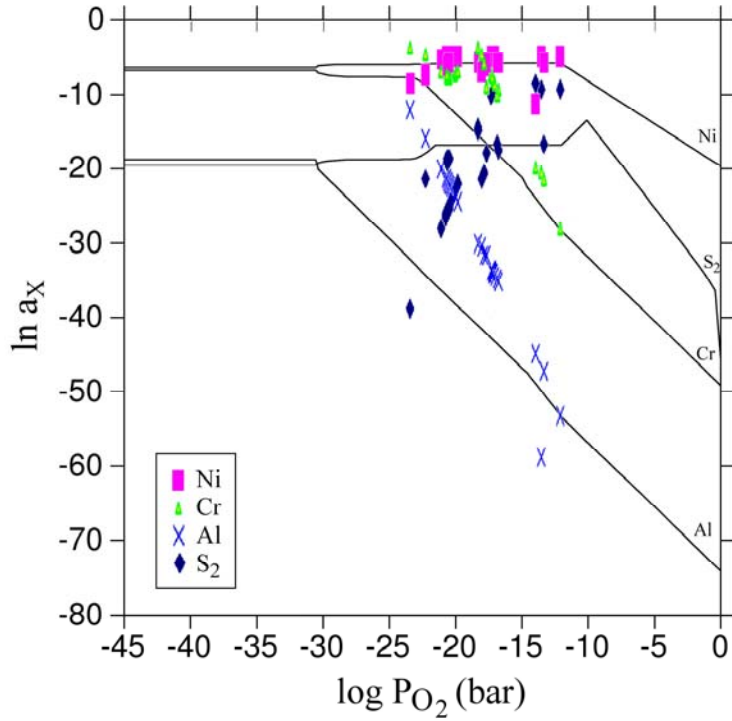


Figure 6-3. Comparison of the calculated activities from microprobe linescans with calculated values using the appended SPIN4 database for a Ni-8Cr-6Al alloy oxidized at 900°C in 0.21 O<sub>2</sub> + 0.02 SO<sub>2</sub>.

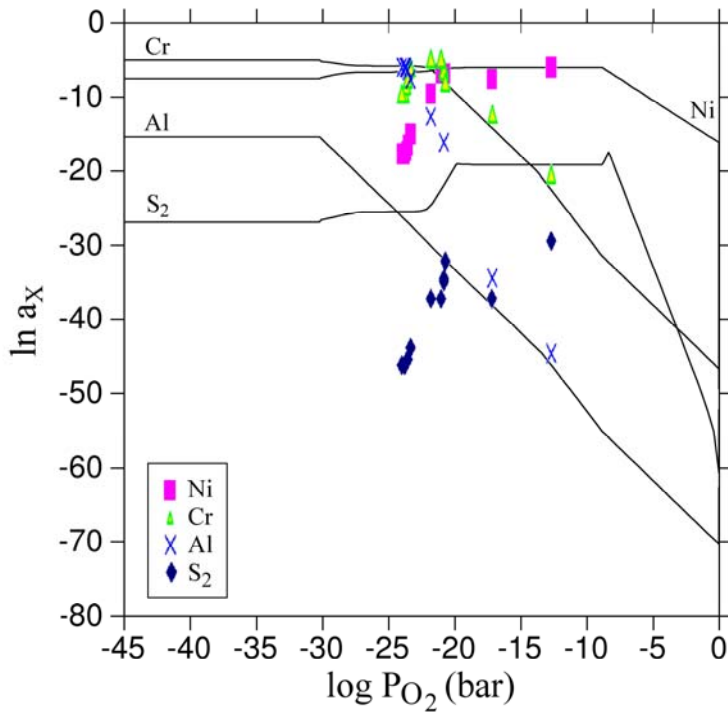


Figure 6-4. Comparison of the calculated activities from microprobe linescans with calculated values using the appended SPIN4 database for a Ni-22Cr-11Al alloy oxidized at 975°C in 0.21 O<sub>2</sub> + 0.02 SO<sub>2</sub>.

only once found in contact with the alloy substrate (usually, this was Al-rich  $\text{Al}_2\text{O}_3$ ). However, the calculations from the SPIN4, as well as SPOT3, databases show a mixture of  $\gamma$  and  $(\text{Al,Cr})_2\text{O}_3$  bounded by  $\gamma$  and spinel. It has been established that the scale/alloy interface is not usually at equilibrium due to slow rate-limiting ion transport that stabilizes  $(\text{Al,Cr})_2\text{O}_3$ , or sulfides in the case of  $\text{SO}_2$  diffusion. Nevertheless, the calculations performed in this dissertation show promise that the Ni-Cr-Al-O-S system can be successfully modeled using thermodynamic calculations. In the future, refinement of the SPIN4 database to allow solution phases of sulfides and sulfates, as well as a sulfur contribution to the ionic liquid phase description and the addition of the additional gas species, will greatly advance the calculations completed here.

## CHAPTER 7 CONCLUSIONS

The purpose of this research study was to calculate the stability of Ni-Cr-Al alloys and their mechanical mixtures in oxidizing and sulfidizing atmospheres. Experiments were also conducted to examine the impact of sulfur on the oxidation of two Ni-Cr-Al alloys. The following conclusions can be drawn from this study:

- The oxidation, and even the simultaneous oxidation/sulfidation, kinetics can be generally described as parabolic in nature. This is due to the nature of this growth mechanism in that the rate of the oxidation reaction is dependent on ionic transport through the oxide scale, which decreases over time as the scale thickens.
- Higher temperatures showed the growth of less NiO and more Al<sub>2</sub>O<sub>3</sub>/Cr<sub>2</sub>O<sub>3</sub> initially, as predicted by thermodynamic calculations of Ni-8Cr-6Al alloys.
- While the morphology of  $\theta$ - and  $\delta$ -Al<sub>2</sub>O<sub>3</sub> was observed, particularly on the surface, XRD could not detect any alumina phases except  $\alpha$ . It is possible that even at short oxidation times, the transient aluminas transform to corundum quickly at these temperatures.
- The addition of SO<sub>2</sub> caused sulfur to accumulate at the scale/alloy interface.
- In the Ni-8Cr-6Al, SO<sub>2</sub> migrated to the scale/alloy interface and oxidized the alloy releasing free sulfur. This sulfur reacted with Cr in solution to form Cr-sulfides at the alloy grain boundaries. These sulfides allowed rapid ion transport due to their high-defect structures, and oxidized themselves allowing sulfur to move further into the alloy, sulfidizing more Cr and repeating the process.
- Cr-containing oxides, which were not detected on Ni-8Cr-6Al in oxidation-only experiments, were detected on the surface when exposed to SO<sub>2</sub>. This was attributed to the vacancy creation of S in the oxide lattice, as well as SO<sub>2</sub> at cracks and grain boundaries allowing faster diffusion of Cr<sup>3+</sup> and was observed as a decreased activation energy.
- For the extent of these tests, the scale formed by the Ni-22Cr-11Al alloys was protective against the formation of internal sulfides.
- The thermodynamic calculations were able to predict the progression of oxidation as well as confirm the phases in equilibrium at various oxygen and sulfur dioxide partial pressures.
- In (Al,Cr)<sub>2</sub>O<sub>3</sub> and NiO, the activities and compositions of the elements were nearly identical for calculations from each database. There were small differences in spinel and the alloy. The activities calculated from the experiments showed qualitative trends with the calculations.

- Combining the results from the two databases used in this dissertation, a more representative  $\text{SO}_2\text{-O}_2$  potential diagram could be calculated.
- This dissertation is a first step in being able to calculate the Al-Cr-Ni-O-S quinary system for describing sulfidation and hot corrosion problems affecting NiCrAlY bond coats.

## LIST OF REFERENCES

1. Department of Energy. *International Energy Outlook 2006*. Report #DOE/EIA-0484 (2006)
2. International Energy Agency. *Monthly Electricity Statistics: November 2006*. (2007)
3. J.P. Longwell, E.S. Rubin, J. Wilson. *Progress in Energy and Combustion Science*. 21 pp. 209-360 (1995)
4. Department of Energy. *Annual Energy Outlook 2007 with Projections to 2030*. Report #DOE/EIA-0383 (2007)
5. H.M. Kvamsel, K. Jordal, O. Bollard. *Energy*. 32 pp. 10-24 (2007)
6. P. Saltykov, O. Fabrichnaya, J. Golczewski, F. Aldinger. *Journal of Alloys and Compounds*. 381 pp. 99-113 (2004)
7. H.J. Seifert, H. Mozaffari, H.L. Lukas, F. Aldinger. "The Oxidation of Ni-Base Alloys—Thermodynamic Modeling and Calculations." *High Temperature Corrosion and Materials Chemistry V: Proceedings of the International Symposium*. E. Opila, J. Fergus, Y. Maruyama, J. Mizusaki, T. Narita, D. Shifler, E. Wuchina, eds. ECS: Pennington, NJ pp. 347-360 (2005)
8. D.J. Srolovitz, T.A. Ramanarayanan. *Oxidation of Metals*. 22 pp. 247-275 (1984)
9. P. Berthod, S. Michon, J. Di Martino, S. Mathieu, S. Noël, R. Podor, C. Rapin. *Calphad*. 27 pp. 279-288 (2003)
10. Y. Tamarin: *Protective Coatings for Turbine Blades*, ASM International, Materials Park, OH (1992) pp. 5-23
11. J.R. Davis, ed. *Heat Resistant Materials*, ASM International: Materials Park, OH (1997) pp. 221-254
12. E. Ross, C.T. Sims, "Nickel-base Alloys," *Superalloys II*. C.T. Sims, N.S. Stolff, W.C. Hagel, eds., John Wiley & Sons: New York (1987) pp. 97-133
13. G.H. Meier, F.S. Pettit. *Materials Science and Engineering A*. 153, pp. 548-560 (1992)
14. P. Kofstad. *High Temperature Oxidation of Metals*. John Wiley & Sons: New York, NY pp. 88-111 (1988)
15. J.L. Smialek, G.M. Meier, "High-Temperature Oxidation," *Superalloys II*. C.T. Sims, N.S. Stolff, W.C. Hagel, eds., John Wiley & Sons: New York pp. 293-326 (1987)
16. D.R. Clarke, C.G. Levi. *Annual Review of Materials Research*. 33 pp. 383-417 (2003)
17. A. Taylor, R.W. Floyd. *Journal of Institute of Metals*. 81 pp. 451-464 (1952)

18. N.C. Oforka, B.B. Argent, *Journal of Less-Common Metals*. 114 pp. 97-109 (1985)
19. J.A. Nesbitt, R.W. Heckel. *Metallurgical Transactions A*. 18A pp. 2061-2073 (1987)
20. J.A. Nesbitt, R.W. Heckel. *Metallurgical Transactions A*. 18A pp. 2087-2094 (1987)
21. Y.M. Hong, Y. Mishima, T. Suzuki. "DTA Measurements of the Ni-Cr-Al Ternary System," *Materials Research Society Symposium Proceedings*. 133 C.T. Liu, A.I. Taub, N.S. Stoloff, C.C. Koch. eds., MRS: Pittsburg, PA pp. 429-440 (1989)
22. C.C. Jia, K. Ishida, T. Nishizawa. *Metallurgical and Materials Transactions A*. 25A pp. 473-485 (1994)
23. L. Kaufman, H. Nesor. *Metallurgical Transactions*. 5 pp. 1623-1629 (1974)
24. S. Ochiai, Y. Oya, T. Suzuki. *Acta Metallurgica*. 32 pp. 289-298 (1984)
25. I. Ansara, B. Sundman, P. Willemin. *Acta Metallurgica*. 36 pp. 977-982 (1988)
26. I. Ansara, N. Dupin, H. L. Lukas, B. Sundman *Journal of Alloys and Compounds*. 247 p. 20-30 (1997)
27. N. Dupin, I. Ansara, B. Sundman. *Calphad*. 25 pp. 279-298 (2001)
28. D.R.G. Achar, R. Munoz-Arroyo, L. Singheiser, W.J. Quadackers, *Surface & Coatings Technology*. 187 pp. 272-283 (2004)
29. P.K. Sung, D.R. Poirier, *Metallurgical and Materials Transactions A*. 30A, pp. 2173-2182 (1999)
30. H. Baker. *ASM Handbook Volume 3—Alloy Phase Diagrams*, ASM International: Materials Park, OH, pp. 43-155 (1992)
31. M. Hillert. *Journal of Alloys and Compounds*. 320 pp. 161-171 (2001)
32. P. Rogl. "Al-Cr-Ni," *Ternary Alloys: A Comprehensive Compendium of Evaluated Constitutional Data and Phase Diagrams: Al-Cd-Ce to Al-Cu-Ru*. 4 pp. 400-415 (1991)
33. R. Bakish, ed. *Introduction to Electron Beam Technology*. John Wiley and Sons: New York, NY (1962) p. 395-422
34. A.M. Dorodnov. *Journal Technical Physics*. 51 pp. 504-524 (1981)
35. R.C. Dykhuizen, M.F. Smith. *Surface and Coatings Technology*. 37 pp. 349-358 (1989)
36. K.G. Schmitt-Thomas, H. Haindl, D. Fu. *Surface and Coatings Technology*. 94-95. pp. 149-154 (1997)

37. Y. Tamarin: *Protective Coatings for Turbine Blades*, ASM International, Materials Park, OH p. 65-67 (1992)
38. S.A. Bradford. "Fundamentals of Corrosion of Gases," *ASM Handbook Volume 13—Corrosion*. ASM International: Materials Park, OH. pp. 61-76 (1992)
39. N. Cabrera, N.F. Mott. *Reports on the Progress of Physics*. 12 pp. 163-184 (1948-1949)
40. C. Wagner. *Zeitschrift für Physikalische Chemie*. B21 pp. 25-41 (1933)
41. D.A. Porter, K.E. Easterling. *Phase Transformations in Metals and Alloys*, 2<sup>nd</sup> Ed. Chapman & Hall: London pp. 98-103 (1993)
42. T. Homma, N.N. Khoi, W.W. Smeltzer, J.D. Embury. *Oxidation of Metals*. 3 pp. 463-473 (1971)
43. J.R. Taylor, A.T. Dinsdale. *Zeitschrift für Metallkunde*. Vol 81, pp. 354-366 (1990)
44. R. Haugrud. *Corrosion Science*. 45. pp 211-235 (2003)
45. H. Hindam, D.P. Whittle. *Oxidation of Metals*. 18 p. 245-284 (1982)
46. M. Schuetze. *Oxidation of Metals*. 44 p. 29-61 (1995)
47. H.V. Atkinson. *Materials Science and Technology*. 4 pp. 1052-1063 (1988)
48. A.W. Harris, A. Atkinson. *Oxidation of Metals*. 34 pp. 229-258 (1990)
49. L.P.H. Jeurgens, W.G. Sloof, F.D. Tichelaar, E.J. Mittemeijer: *Journal of Applied Physics*. 92 pp. 1649-1656 (2002)
50. P. Villars. *Pearson's Handbook: Desk Edition: Crystallographic Data for Intermetallic Phases*. ASM International: Materials Park, OH. (1998)
51. Y.F. Zhukovskii, P.W.M. Jacobs, M. Causa. *Journal of Physics and Chemistry of Solids*. 64 pp. 1317–1331 (2003)
52. L.P.H. Jeurgens, W.G. Sloof, F.D. Tichelaar, E.J. Mittemeijer. *Thin Solid Films*. 418 p. 89-101 (2002)
53. S.R. Pollack, C.E. Morris. *Journal of Applied Physics*. 35 p. 1503-1512 (1964)
54. L.P.H. Jeurgens, W.G. Sloof, F.D. Tichelaar, E.J. Mittemeijer. *Surface Science*. 506 pp. 313–332 (2002)
55. H.J. van Beek, E.J. Mittemeijer. *Thin Solid Films*. 122-151 p. 131 (1984)
56. D. Clemens, V.R. Vosberg, L.W. Hobbs, U. Breuer, W.J. Quadackers, H. Nickel. Fresenius. *Fresenius Journal of Analytical Chemistry*. 355 p. 703-706 (1996)

57. D. Clemens, V.R. Vosberg, H.J. Penkella, U. Breuer, W.J. Quadackers, H. Nickel. Fresenius. *Fresenius Journal of Analytical Chemistry*. 358 p. 122-126 (1997)
58. J.L. Smialek, R. Gibala. *Metallurgical Transactions A*. 14A pp. 2143-2164 (1983)
59. G.C. Rybicki, J.L. Smialek. *Oxidation of Metals*. 31 p. 275-304 (1989)
60. J. Doychak, J.L. Smialek, T.E. Mitchell. *Metallurgical Transactions A*. 20A p. 499-518 (1989)
61. A. Ul-Hamid. *Corrosion Science*. 46 p. 27-36 (2004)
62. R. Prescott, M.J. Graham. *Oxidation of Metals*. 38 p. 223-254 (1992)
63. B. Chattopadhyay, G.C. Wood. *Oxidation of Metals*. 2 p. 373-399 (1970)
64. M.T. Shim, W.J. Moore. *Journal of Chemistry and Physics*. 26 p. 802-832 (1957)
65. D. Caplan, G.I. Sproule. *Oxidation of Metals*. 9 p. 459-472 (1975)
66. A.U. Seybolt. *Journal of the Electrochemical Society*. 107 pp. 147-156 (1960)
67. W.C. Hagel, A.U. Seybolt. *Journal of the Electrochemical Society*. 108 pp. 1146-1152 (1961)
68. S.C. Tsai, A.M. Huntz, C. Dolin. *Oxidation of Metals*. 43 pp. 581-596 (1995)
69. K.P. Lillerud, P. Kofstad. *Journal of the Electrochemical Society*. 127 pp. 2397-2409 (1980)
70. P. Kofstad, K.P. Lillerud. *Journal of the Electrochemical Society*. 127 pp. 2410-2419 (1980)
71. D. Caplan, G.I. Sproule, R.J. Hussey. *Corrosion Science*. 10 pp. 9-17 (1970)
72. M. Skeldon, J.M. Calvert, D.G. Lees. *Oxidation of Metals*. 28 pp. 109-125 (1987)
73. D. Caplan, M. Cohen. *Journal of the Electrochemical Society*. 108 pp. 438-442 (1961)
74. C.A. Stearns, F.J. Kohl, G.C. Fryburg. *Journal of the Electrochemical Society*. 121 pp. 952-961 (1974)
75. T. Sorahan, D.C.L. Burges, L. Hamilton, J.M. Harrington, *Occupational Environmental Medicine*. 55 pp. 236-242 (1998)
76. F.S. Pettit. *Transactions of the AIME*. 239, pp. 1296-1305 (1967)
77. G.C. Wood, F.H. Stott. *British Corrosion Journal*. 6, pp. 247-256 (1971)

78. H.M. Hindam, W.W. Smeltzer. *Journal of the Electrochemical Society*. 127 pp. 1622-1630 (1980)
79. K. Fueki, H. Ishibashi. *Journal of the Electrochemical Society*. 108 pp. 306-311 (1961)
80. R.T. Haasch, A.M. Venezia, C.M. Loxton. *Journal of Materials Research*. 7, pp. 1341-1349 (1992)
81. H.C. Yi, W.W. Smeltzer, A. Petric. *Oxidation of Metals*. 45 pp. 281-299 (1996)
82. S.C. Choi, H.J. Cho, Y.J. Kim, D.B. Lee. *Oxidation of Metals*. 46 pp. 51-72 (1996)
83. H.M. Hindam, W.W. Smeltzer. *Journal of the Electrochemical Society*. 127 pp. 1630-1635 (1980)
84. P.Y. Hou, K. Priimak. *Oxidation of Metals*. 63 pp. 113-130 (2005)
85. J.L. Smialek. *Metallurgical Transactions A*. 9A pp. 309-320 (1978)
86. B.H. Kear, F.S. Pettit, D.E. Fornwalt, L.P. Lemaire. *Oxidation of Metals*. 3 pp. 557-569 (1971)
87. P. Sarrazin, A. Galerie, M. Caillet. *Oxidation of Metals*. 46 pp. 299-312 (1996)
88. S.W. Guan, W.W. Smeltzer. *Oxidation of Metals*. 42 pp. 375-391 (1994)
89. P. Sarrazin, A. Galerie, M. Caillet. *Oxidation of Metals*. 46 pp. 1-17 (1996)
90. C.S. Giggins, F.S. Pettit. *Journal of the Electrochemical Society*. 118 pp. 1782-1790 (1971)
91. F.H. Stott, G.C. Wood, M.G. Hobby. *Oxidation of Metals*. 3 pp. 103-113 (1971)
92. F. Gesmundo, F. Vianni, Y. Niu. *Oxidation of Metals*. 42 pp. 285-301 (1994)
93. G.J. Santoro, D.L. Deadmore, C.E. Lowell. *NASA Technical Note*. TN D-6414 (1971)
94. C.E. Lowell, G.J. Santoro. *NASA Technical Note*. TN D-6838 (1972)
95. F.H. Stott, I.G. Wright, T. Hodgkiess, G.C. Wood. *Oxidation of Metals*. 11 pp. 141-150 (1977)
96. J.L. González Carrasco, P. Adeva, M. Aballe. *Oxidation of Metals*. 33 pp. 1-17 (1990)
97. C.G. Levi, E. Sommer, S.G. Terry, A. Catanoiu, M. Rühle. *Journal of the American Ceramic Society*. 86 pp. 676-685 (2003)
98. W. Brandl, D. Toma, H.J. Grabke. *Surface and Coatings Technology*. 108-109 pp. 10-15 (1998)

99. F.S. Pettit, C.S. Giggins. "Hot Corrosion," *Superalloys II*. C.T. Sims, N.S. Stolff, W.C. Hagel, eds., John Wiley & Sons: New York (1987) pp. 327-358
100. J.A. Goebel, F.S. Pettit. *Metallurgical Transactions*. 1 pp. 1943-1954 (1970)
101. N.S. Bornstein, M.A. DeCrescente. *Metallurgical Transactions*. 2 pp. 2875-2892 (1971)
102. A. Rahmel. *Materials Science and Engineering*. 87 pp. 345-352 (1987)
103. K.L. Luthra, D.A. Shores. *Journal of the Electrochemical Society*. 127 pp. 2202-2210 (1980)
104. K.L. Luthra, O.H. LeBlanc. *Materials Science and Engineering*. 87 pp. 329-335 (1987)
105. D.K. Gupta, R.A. Rapp. *Journal of the Electrochemical Society*. 127 pp. 2194-2202 (1980)
106. R.A. Rapp. *Materials Science and Engineering*. 87 pp. 319-327 (1987)
107. R.A. Rapp. *Corrosion Science*. 44 pp. 209-221 (2002)
108. D.A. Shores. "New Perspectives on Hot Corrosion Mechanisms," *High Temperature Corrosion*. R.A. Rapp, ed. NACE: Houston, TX. p. 493-511 (1983)
109. A.K. Roslik, V.N. Konev, A.M. Maltsev. *Oxidation of Metals*. 43 pp. 59-82 (1995)
110. A. Stokłosa, J. Stringer. *Oxidation of Metals*. 11 pp. 263-276 (1977)
111. A. Stokłosa, J. Stringer. *Oxidation of Metals*. 11 pp. 277-288 (1977)
112. J. Stringer, M.E. El-Dahshan, I.G. Wright. *Oxidation of Metals*. 8 pp. 361-377 (1974)
113. T. Narita, T. Ishikawa, K. Nishida. *Oxidation of Metals*. 27 pp. 221-237 (1987)
114. W. Kai, Y.T. Lin, C.C. Yu, P.C. Chen, C.H. Wu. *Oxidation of Metals*. 61 pp. 507-527 (2004)
115. C.J. Spengler, R. Viswanathan. *Metallurgical Transactions*. 3 pp. 161-166 (1972)
116. P. Singh, N. Birks. *Oxidation of Metals*. 13 pp. 457-474 (1979)
117. C. de Asumndis, F. Gesmundo, C. Bottino. *Oxidation of Metals*. 14 pp. 351-361 (1980)
118. P. Kofstad, G. Åkesson. *Oxidation of Metals*. 13 pp. 57-76 (1979)
119. D.G. Lees. *Oxidation of Metals*. 27 pp. 75-81 (1987)
120. K. Natesan. *Oxidation of Metals*. 30 pp. 53-83 (1988)
121. W.H. Lee. *Materials Chemistry and Physics*. 76 pp. 26-37 (2002)

122. P. Fox, D.G. Lees, G.W. Lorimer. *Oxidation of Metals*. 36 pp. 491-503 (1991)
123. H.J. Grabke, G. Kustonov, H.J. Schmoltzer. *Oxidation of Metals*. 43 pp. 97-114 (1995)
124. Z. Zurek, J. Jedlinski, K. Kowalski, K. Kowalska. *Solid State Ionics*. 101-103 pp. 743-747 (1997)
125. J. Gawel. *Oxidation of Metals*. 30 pp. 139-140 (1988)
126. C. Mathieu, J.P. Larpin, S. Toesca. *Oxidation of Metals*. 39 pp. 211-220 (1993)
127. C.S. Giggins, F.S. Pettit. *Oxidation of Metals*. 14 pp. 363-413 (1980)
128. K.L. Luthra, W.L. Worrell. *Metallurgical Transactions A*. 10A pp. 621-631 (1979)
129. F. Gesmundo, C. de Asumndis, P. Nanni. *Oxidation of Metals*. 20 pp. 217-240 (1983)
130. K.P. Lillerud, B. Haflan, P. Kofstad. *Oxidation of Metals*. 21 pp. 119-134 (1984)
131. A.K. Misra, D.P. Whittle. *Oxidation of Metals*. 22 pp. 1-33 (1984)
132. K.L. Luthra, W.L. Worell. *Metallurgical Transactions A*. 9A pp. 1055-1061 (1978)
133. A.S. Khanna, W.J. Quadackers, X. Yang, H. Schuster. *Oxidation of Metals*. 40 pp. 275-294 (1993)
134. R.E. Lobnig, H.J. Grabke, H.R. Schmidt, K. Hennessen. *Oxidation of Metals*. 39 pp. 353-370 (1993)
135. P.Y. Hou, K. Priimak. *Oxidation of Metals*. 63 pp. 113-130 (2005)
136. P. Kofstad, G. Åkesson. *Oxidation of Metals*. 12 pp. 503-526 (1978)
137. M.H. LaBranche, G.J. Yurek. *Oxidation of Metals*. 28 pp. 78-98 (1987)
138. Z. El-Majid, M. Lambertin. *Oxidation of Metals*. 27 pp. 333-345 (1987)
139. P. Fox, D.G. Lees, G.W. Lorimer. *Oxidation of Metals*. 36 pp. 491-503 (1991)
140. A.G. Andersen, P. Kofstad. *Oxidation of Metals*. 43 pp. 301-315 (1995)
141. P. Singh, N. Birks. *Oxidation of Metals*. 19 pp. 37-52 (1982)
142. D. Wang, D.L. Douglass. *Oxidation of Metals*. 20 pp. 111-146 (1983)
143. M.F. Chen, D.L. Douglass, F. Gesmundo. *Oxidation of Metals*. 33 pp. 399-423 (1990)
144. S.W. Kim, K. Ohla, H. Fischmeister, E. Fromm. *Oxidation of Metals*. 36 pp. 395-407 (1991)

145. A.K. Roslik, V.N. Koner, A.M. Maltsev. *Oxidation of Metals*. 43 pp. 83-95 (1995)
146. Y.R. He, D.L. Douglass. *Oxidation of Metals*. 40, pp. 337-371 (1993)
147. S. Mrowec. *Oxidation of Metals*. 44 pp. 177-209 (1995)
148. E.J. Vineberg, D.L. Douglass. *Oxidation of Metals*. 25 pp. 1-28 (1986)
149. P.Y. Hou, J. Stringer. *Oxidation of Metals*. 38 pp. 323-345 (1992)
150. F. Gesmundo. *Oxidation of Metals*. 13 pp. 237-244 (1979)
151. K. Natesan. *Materials Science and Engineering*. 87 pp. 99-106 (1987)
152. J.H. Wood, E.H. Goldman. "Protective Coatings," *Superalloys II*. C.T. Sims, N.S. Stolff, W.C. Hagel, eds., John Wiley & Sons: New York pp. 359-383 (1987)
153. S. Degterov, A. Pelton. *Journal of Phase Equilibria*. 17 pp. 476-488 (1996)
154. A.D. Pelton, H. Schmalzried, J. Strichner. *Journal of Physics and Chemistry of Solids*. 40 pp. 1103-1122 (1979)
155. H. Mozaffari. Ph.D. Dissertation. Universität Stuttgart (2002)
156. H.L. Lukas, S.G. Fries. *Journal of Phase Equilibria*. 13 pp. 532-541 (1992)
157. L.C. Li, F. Gesmundo, F. Vianni. *Oxidation of Metals*. 40 pp. 395-419 (1993)
158. J.M. Quets, W.H. Dresher. *Journal of Materials*. 4 pp. 583-599 (1969)
159. L.C. Li, F. Gesmundo, F. Vianni, *Materials Engineering*. 4 p. 133-148 (1993)
160. H. Yokokawa, *Journal of Phase Equilibria*. 20 pp. 258-287 (1999)
161. N. Saunders, Z. Guo, X. Li, A.P. Miodownik, J-Ph. Schillé. "Modeling the Materials Properties and Behavior of Ni-Based Superalloys," *Superalloys 2004*. K.A. Green, T.M. Pollock, H. Harada, T.E. Howson, R.C. Reed, J.J. Schirra, S. Watson, eds., TMS: Materials Park, OH. pp. 849-858 (2004)
162. *JANAF Thermochemical Tables, 2<sup>nd</sup> ed.* National Bureau of Standards: Washington, D.C., (1986)
163. B. Bergman, J. Agren. *Journal of the American Ceramics Society*. 68 pp. 444-450 (1985)
164. K.K. Sunil, K.D. Jordan. *Journal of Physical Chemistry*. 92-101 p. 2774 (1988)
165. O. Kubaschewski, C.B. Alcock. *Metallurgical Thermochemistry, 6<sup>th</sup> ed.* Oxford, UK: Pergamon Press (1979)

166. J.M. Larrain. *Calphad*. 4 pp. 155-171 (1980)
167. B. Pieraggi. *Oxidation of Metals*. 64 pp. 397-403 (2005)
168. G.I. Goldstein, D.E. Newbury, P. Echlin, D.C. Joy, A.D. Romig Jr, C.E. Lyman, C. Fiori, E. Lifshin. *Scanning Electron Microscopy and X-Ray Microanalysis*, 2<sup>nd</sup> Ed. Plenum: New York pp. 417-524 (1994)
169. D.V. Ragone. *Thermodynamics of Materials*. J. Wiley & Sons, Inc.: New York (1994)
170. E. Mueller, H. Seifert. "Thermodynamic Calculations of Mixed Sulfidation and Oxidation of Ni-Cr-Al Alloys," *Materials Science and Technology (MS&T) 2006: Fundamentals and Characterization: Vol 2*. Z. Liu, C.E. Campbell, L.Q. Chen, E.B. Damm, J.E. Morral, J.L. Murray, eds. pp. 125-136 (2006)
171. M.C. Pope, N. Birks. *Oxidation of Metals*. 12 pp. 191-204 (1978)

## BIOGRAPHICAL SKETCH

Erik Michael Matthew Mueller was born on July 7, 1978, to Michael J. and Sally Leona Mueller in Jacksonville, FL. There he attended Sacred Heart Elementary and Bishop Kenny High School, where he started at defensive line for the football team and threw shotput and discus for the track team, lettering in both. After graduating in 1996, Erik moved to Gainesville, FL, where he attended the University of Florida. In May 2000, he graduated cum laude with a Bachelor of Science in materials science and engineering with a focus in engineering ceramics, and began an internship at American Technical Ceramics. He entered graduate school later that year at the University of Florida and redirected his focus to metallurgy, electron microscopy, and high-temperature corrosion. He received a Master of Science degree in May 2003, and was admitted to doctoral candidacy in December of 2005. He is currently also captain of University of Florida mascots, who perform at various Gator sporting events, commercial appearances, and charitable festivities. He is also a 3rd degree knight and recorder for the local Knights of Columbus Chapter 13207. In the future, Erik plans to earn his professional engineering license in metallurgical engineering, and to explore the fields of consulting and politics.